



Provided by the author(s) and University of Galway in accordance with publisher policies. Please cite the published version when available.

Title	Experimental and computational investigation of the active force generation of cells subjected to static and dynamic loading
Author(s)	Reynolds, Noel
Publication Date	2016-05-13
Item record	<a href="http://hdl.handle.net/10379/5794">http://hdl.handle.net/10379/5794</a>

Downloaded 2024-04-27T04:33:08Z

Some rights reserved. For more information, please see the item record link above.



Experimental and Computational Investigation of the Active  
Force Generation of Cells Subjected to Static and Dynamic  
Loading

Noel H. Reynolds, B.E.

A thesis submitted to the National University of Ireland as fulfilment  
of the requirements for the Degree of Doctor of Philosophy



Department of Biomedical Engineering  
College of Engineering and Informatics  
National University of Ireland, Galway

2015

Supervisor of Research: Dr. J. P. McGarry

## Abstract

The development of a mechanistic understanding of the processes by which cells sense and actively respond to the mechanical environment would represent a significant advance in the fields of biomechanics and tissue engineering. Investigation at a single cell level is required to obtain new and fundamental insights into this problem. In this thesis a series of experimental tests and cell mechanics models are developed with the aim of advancing the current understanding of cell biomechanics.

Micropipette aspiration (MA) has been used extensively in biomechanical investigations of un-adhered cells suspended in media. However, the MA technique has largely been limited to the investigation of un-adhered cells suspended in media. In the current thesis, a custom MA system is developed to aspirate substrate adhered spread cells. Additionally, the system facilitates immuno-fluorescent imaging of aspirated cells to investigate stress fibre (SF) redistribution and nucleus deformation during MA. In response to an applied pressure, significantly lower aspiration length is observed for untreated contractile cells compared to cells in which actin polymerisation is chemically inhibited, demonstrating the important contribution of SFs in the biomechanical behaviour of spread cells. Additional experiments are performed in which untreated contractile cells are subjected to a range of applied pressures. Computational finite element simulations reveal that a viscoelastic material model for the cell cytoplasm is incapable of accurately predicting the observed aspiration length over the range of applied pressures. It is demonstrated that an active computational framework that incorporates SF remodelling and contractility must be used in order to accurately simulate MA of untreated spread cells. Additionally, the SF distribution observed in immuno-fluorescent experimental images of aspirated cells is accurately predicted using the active SF modelling framework. Finally, a detailed experimental-computational investigation of the nucleus mechanical behaviour demonstrates that the nucleus is highly deformable in cyto, reaching strain levels in excess of 100% during MA.

Previous cell models have assumed that the nucleus is a homogenous material. A new approach to the modelling of the cell nucleus is proposed in this thesis. Greyscale values in confocal z-stacks of nuclear DNA reported in the

experimental study of Henderson et al. (Biophys J; 105:2252-61; 2013) are used to determine the local shear modulus at each material point of a finite element mesh of the nucleus. Simulations reveal that the nucleus is highly heterogeneous with local intra-nuclear shear moduli ranging over two orders of magnitude. Predicted maximum shear strains in the nucleus are five times higher than the macroscopic applied shear strain, as observed experimentally. This demonstrates that mechanical heterogeneity of the nucleus results in significant strain magnification, and suggests that nucleus deformation may play a key role in mechanotransduction and cell sensing of the physical environment.

A novel single cell AFM experimental investigation reveals a complex force-strain response of cells to cyclic loading. The biomechanisms underlying such complex behaviour cannot be fully understood without a detailed mechanistic analysis incorporating the key features of active stress generation and remodelling of the actin cytoskeleton. In order to simulate untreated contractile cells, an active bio-chemo-mechanical model is developed, incorporating the key features of SF remodelling and active tension generation. It is demonstrated that a fading memory SF contractility model accurately captures the transient response of cells to dynamic loading. Simulations reveal that high stretching forces during unloading half-cycles (probe retraction) occur due to tension actively generated by axially oriented SFs. On the other hand, hoop oriented SFs generate tension during loading half-cycles, providing a coherent explanation for the elevated compression resistance of contractile cells. Finally, it is also demonstrated that passive non-linear visco-hyperelastic material laws, traditionally used to simulate cell mechanical behaviour, are not appropriate for untreated contractile cells, and their use should be limited to the simulation of cells in which the active force generation machinery of the actin cytoskeleton has been chemically disrupted. In summary, the active modelling framework provides a coherent understanding of the biomechanisms underlying the complex patterns of experimentally observed single cell force generation presented in the experimental component of this investigation.

In previous studies, systems for mechanical testing of engineered tissue constructs have been limited to uniaxial cyclic stretching. In this thesis a novel experimental system is developed for measurement of cell and tissues forces during both uniaxial and biaxial stretching. In the case of uniaxially constrained tissues

significant tissue deformation occurs due to cell contractility, and the alignment of cells in the stretching direction results in the measurement of a high actively generated cumulative cell force. In the case of biaxially constrained tissues cells are randomly oriented. This results in a lower actively generated cumulative cell force in each stretching direction. The force measured during biaxial cyclic stretching is only ~1.30 times higher than that measured during uniaxial cyclic stretching. When cells are removed from the tissue biaxial forces are ~1.75 times higher than uniaxial forces. Interpretation of experimental results using an active cell contractility model demonstrates that a uniaxial stress state is necessary to achieve a high degree of cell alignment and, consequently, a high actively generated cumulative cell force in the stretching direction.

The novel experimental-computational approaches to investigate the cell responses to static and dynamic loading provide new insights into the complex biomechanical behaviour of the actin cytoskeleton and the cell nucleus. The findings of this thesis may have important implications for understanding in vivo remodelling of cells and tissues during disease progression, such as atherosclerosis and cardiac hypertrophy. The active cell models developed and implemented in this work can potentially be used to guide tissue engineering strategies to control cell behaviour and gene expression.

## Acknowledgments

Firstly, I would like to express my sincerest gratitude to my supervisor Dr. Pat McGarry. Pat has guided, motivated, and inspired me throughout my Ph.D., and as a supervisor he has gone far beyond the call of duty. Not only was his encouragement and guidance throughout the course of this Ph.D. invaluable, but the enthusiasm shown for the work was always refreshing.

I was fortunate to have worked with a fantastic group of research students and postdocs throughout my Ph.D. The daily tea/lunchtime craic was always a delightful respite. In particular, I would like to express my thanks to past and present members of the “McGarry Group”; Eamonn, Emer, Enda, Nicola, Paul W, Will, Fiona G, Brian, Catherine, and Eóin. We’ve come a long way since the Pat Cave! I sincerely thank all the postdocs and technicians in the engineering and anatomy departments who’ve given invaluable help along the way. In particular, David Connolly, Martin Burke, Matthew Haugh, Muriel Voisin, Myles Meehan, Pat Kelly, Peter Owens, and William Kelly. I would also like to thank Dr. Laoise McNamara for the provision of a live cell imaging microscope and Prof. Corey Neu and Soham Ghosh for experimental images.

I wish to thank Science Foundation Ireland – Research Frontiers Programme for funding support during my Ph.D. I also acknowledge the SFI/HEA Irish Centre for High End Computing for the provision of computational facilities and support.

To my family, Sharon, Fintan, Aidan, Ruth, Sarah, Rúairí, and Doireann, going home is always the best way to relax and unwind, so I thank you for that and for your quiet confidence that I’d get there in the end! To Mum and Dad, your love and unrelenting support are what got me there in the end. For the good in me, I owe you both.

What can I say about my one and only desk neighbour Dave Withlan? It appears I had to wait for him before I could submit myself – we ride together, we die together. Completing the circle, the endearment exuding from Lizanne on a daily basis was a constant source of joy. To Meg, thank you for your love and support, particularly in the final days of thesis preparation. When I needed a potato, you were there! Sure don’t I love the whole off ya. Also, the constant source of comic relief provided by James is always essential for evening wind down time.

# Table of Contents

<b>1</b>	<b>Introduction .....</b>	<b>1</b>
1.1	Background .....	1
1.2	Objectives .....	3
1.3	Thesis structure .....	5
1.4	Publications, conference proceedings, and prizes.....	7
1.4.1	Journal publications .....	7
1.4.2	International conference proceedings .....	7
1.4.3	International and national prizes.....	8
1.5	References.....	8
<b>2</b>	<b>Literature review .....</b>	<b>12</b>
2.1	Introduction.....	12
2.2	Cell structure and forces .....	12
2.2.1	The nucleus .....	13
2.2.2	The cytoskeleton.....	15
2.3	Experimental techniques for investigating cell mechanics .....	21
2.3.1	Single cell biomechanics testing.....	21
2.3.2	Mechanical testing of cell populations in 2D .....	32
2.3.2	Cells in 3D .....	33
2.4	Computational modelling of cell mechanics.....	36
2.4.1	Passive cell models .....	37
2.4.2	Active cell models .....	38
2.5	Identified deficits & thesis objectives.....	46
2.6	References.....	49
<b>3</b>	<b>Theory.....</b>	<b>65</b>

3.1	Introduction.....	65
3.2	Continuum mechanics.....	66
3.2.1	Deformation and deformation rate .....	66
3.2.2	Strain and strain rate measures .....	67
3.2.3	Stress measures.....	69
3.3	Constitutive modelling.....	72
3.3.1	Isotropic hyperelasticity .....	72
3.3.2	Visco-hyperelasticity .....	74
3.4	The finite element (FE) method.....	77
3.4.1	Implicit solutions .....	77
3.4.2	Implementation of user defined constitutive laws (UMATs).....	81
3.5	References.....	83
<b>4</b>	<b>On the role of the actin cytoskeleton and nucleus in the biomechanical response of spread cells .....</b>	<b>85</b>
4.1	Introduction.....	85
4.2	Materials and methods .....	87
4.2.1	Sample preparation .....	87
4.2.2	Microscopy and visualisation technique.....	88
4.2.3	Micropipette aspiration rig and data acquisition .....	89
4.2.4	Immuno-fluorescent staining.....	90
4.2.5	Computational methods.....	91
4.2.6	Finite element model development.....	93
4.3	Results.....	95
4.3.1	MA of untreated and cytoD treated adhered cells .....	95
4.3.2	MA of untreated spread adhered cells over a range of applied pressures.....	99
4.3.3	Investigation of nucleus mechanical behaviour.....	104
4.4	Discussion .....	109

Appendix 4.A .....	119
Appendix 4.B.....	120
4.5 References.....	120
<b>5 Investigation of cell nucleus heterogeneity .....</b>	<b>127</b>
5.1 Introduction.....	127
5.2 Model development .....	129
5.2.1 Cartilage representative volume element (RVE).....	129
5.2.2 Greyscale mapping .....	130
5.2.3 Material properties.....	132
5.2.4 Boundary conditions.....	133
5.3 Model predictions .....	134
5.4 Discussion.....	136
5.5 References.....	140
<b>6 Single cell active force generation under dynamic loading – Overview and analysis of AFM experiments .....</b>	<b>143</b>
6.1 Introduction.....	143
6.1.1 Declaration of tasks completed.....	143
6.1.2 Background to AFM cell mechanics experiments.....	145
6.2 Key experimental results.....	147
6.3 Discussion .....	151
6.4 References.....	154
<b>7 Single cell active force generation under dynamic loading – Active modelling insights .....</b>	<b>157</b>
7.1 Introduction.....	157
7.2 Materials and Methods.....	159
7.2.1 Modelling the bio-chemo-mechanical behaviour of the actin cytoskeleton .....	159
7.2.2 Numerical implementation .....	163

7.2.3	Characterising the Passive Response of CytoD Treated Cells during Cyclic Deformation.....	167
7.2.4	FE modelling of cyclic loading .....	168
7.3	Results.....	171
7.3.1	Visco-hyperelastic modelling of cytoD treated cells.....	171
7.3.2	Active SF modelling of untreated cells .....	175
7.3.3	Modelling the transient behaviour of SFs during cyclic loading .....	177
7.3.4	Axial and hoop fibre behaviour during dynamic simulation.....	184
7.3.5	Modelling a realistic cell geometry .....	187
7.4	Discussion.....	189
7.5	References.....	195
<b>8</b>	<b>Investigation of cell behaviour in biaxially and uniaxially constrained tissues subjected to cyclic deformation.....</b>	<b>197</b>
8.1	Introduction.....	197
8.2	Materials and methods .....	199
8.2.1	Sample preparation.....	199
8.2.2	Testing system and experiments.....	201
8.2.3	Immuno-fluorescence .....	203
8.2.4	Finite element (FE) modelling.....	204
8.2.5	FE modelling outputs.....	207
8.3	Results.....	207
8.3.1	Experimental results .....	207
8.3.2	Computational results .....	216
8.4	Discussion.....	219
	Appendix 8.A .....	227
8.5	References.....	227
<b>9</b>	<b>Concluding remarks and future perspectives.....</b>	<b>231</b>

9.1 Summary of key contributions.....	231
9.2 Future perspectives .....	233
9.3 References.....	239

# 1 Introduction

## 1.1 Background

Cell function and tissue maintenance are regulated by a dynamic loading environment. In healthy tissue cells maintain homeostasis by actively sensing and adapting to physical changes. However, irregularities in the *in vivo* physical environment can cause abnormal cell or tissue behaviour (Ingber, 2003), and can lead to, or catalyse, many pathological diseases (Affonce and Lutchen, 2006, Klein-Nulend et al., 2003, Vollrath et al., 2007, Gimbrome et al., 2000, Paszek et al., 2005, Judex et al., 1997, Tan et al., 2006, Heydemann and McNally, 2007, Butcher and Nerem, 2007, Huang, 2014). For example, previous studies have reported dissimilarities in the mechanical properties of normal and diseased cells (Trickey et al., 2000, Jones et al., 1999, Thoumine and Ott, 1997, Guck et al., 2005). Further to diseases themselves, invasive procedures for disease treatment and tissue repair disrupt the local physical environment and alter cell behaviour (Muller et al., 2013, de Billy et al., 2014, Gomez-Barrena et al., 2011, Minami et al., 2013, Wang et al., 2014, Fonseca et al., 2001, Yetkin et al., 2003). The implantation of a stent in a vessel results in artificial stiffening of the vessel, which in turn results in increased proliferation of smooth muscle cells into the lumen – a pathology commonly referred to as *in-stent restenosis* (Hoffmann et al., 1996). Implantation of metallic

stems into the femoral shaft during hip angioplasty results in a reduction of stress in the surrounding bone (referred to as stress shielding), which causes a localised decrease in bone density (Huiskes et al., 1992). Altered mechanical loading of the myocardium (e.g. due to an increased preload caused by hypertension) results in remodelling of cardiomyocyte sarcomeres (e.g. cardiac hypertrophy) (Frey and Olson, 2003). The mechanisms by which cells sense and actively respond to such alterations in the mechanical environment are poorly understood.

Fundamental investigation at a single cell level is required to obtain meaningful insight into the key mechanical processes by which cells actively generate traction and respond to mechanical loading. Therefore, novel in vitro experimental techniques to examine cells under a range of static and dynamic loading modes are of critical importance. Given the complexity of active force generation within cells, and the fact that cells remodel their active force generation machinery in response to applied mechanical loading, experimental results can only be interpreted through computational models that incorporate a mechanistic description of key contractility and remodelling processes. Several simplified models of the cell cytoskeleton are based on the pre-positioning of discrete elastic axial truss elements in finite element meshes (Mohr dieck et al., 2005, Barreto et al., 2013, McGarry and Prendergast, 2004). This ad-hoc approach to matching specific experimental measurements neglects the key intercellular processes that govern active formation, remodelling, and contractility of the actin cytoskeleton. A limited number of models include descriptions of actin cytoskeletal remodelling and contractility (Kaunas and Hsu, 2009, Vernerey and Farsad, 2011, Lee et al., 2012, Qian et al., 2013). However, all such implementations have been limited to 1D or 2D, which dramatically restricts the ability to simulate and interpret a wide range

of experimental tests, not to mention *in vivo* loading conditions. An active stress fibre (SF) framework proposed by Deshpande et al. (2007) (referred to as the bio-chemo-mechanical model) allows for the prediction of the formation, remodelling, and contractility of the actin cytoskeleton. A 2D finite element implementation of this framework (McGarry et al., 2009) accurately predicts distribution of the actin cytoskeleton in cells seeded on micropost arrays, and also predicts the scaling of actively generated cell traction with cell spread area, based on the experiments of Chen and co-workers (Tan et al., 2003). The active SF framework was later expanded into a 3D finite element setting (Ronan et al., 2012) and used to uncover the link between phenotype-specific contractility levels and compression resistance (Ronan et al., 2012, Weafer et al., 2013), and to demonstrate the role of active tension generation in the shear resistance of chondrocytes (Dowling et al., 2012). These studies highlight the critical insights that can be obtained when single cell experimental test data are interpreted through fully predictive 3D models of active SF contractility and remodelling.

## 1.2 Objectives

The overall objective of the current thesis is to provide a new understanding of the active and passive responses of cells to static and dynamic loading. Novel and complex experimental and computational methodologies are developed in this thesis in order to provide new insights into the biomechanical behaviour of cells. In order to make meaningful contributions to the rapidly developing field of cell mechanics, the specific aims are as follows:

1. **Develop a novel approach to micropipette aspiration to perform experiments on spread adhered cell.** Previous micropipette aspiration experiments have largely been limited to testing of cells suspended in

media. However, many of the cell phenotypes in question are adhered to an extracellular matrix (ECM) or substrate *in vivo*, hence mechanical testing of cells in suspension is of limited value, given the importance of cell adhesion and spreading in the active mechanical behaviour of the cell. A system to perform micropipette aspiration of adhered spread cells would represent a significant advance in this branch of single cell experimentation.

2. **Provide a new understanding of SFs and cell mechanics** through a series of micropipette aspiration experiments and interpretation of experimental data through a fully predictive 3D framework for SF contractility and remodelling.
3. **Generate a heterogeneous model for the nucleus to correlate intranuclear strain with local DNA concentrations.** The mechanical behaviour of the nucleus has not been definitively characterised in the literature, with a wide range of elastic properties being defined. Furthermore, previous attempts at modelling the nucleus have assumed that the nucleus is a homogenous isotropic continuum. A detailed and robust methodology for analysis of nucleus heterogeneity would represent a considerable contribution to the field of cell mechanics.
4. **Develop a new multi-axial 3D contractility model for SFs to describe force generation under dynamic loading at a single cell level.** A novel single cell AFM experimental investigation reveals a complex force-strain response of cells to cyclic loading. However, the biomechanisms underlying such complex behaviour are not fully understood. A detailed mechanistic analysis incorporating the key features of active stress generation and remodelling of the actin cytoskeleton would provide valuable insight into the complex patterns of experimentally observed single cell force generation.
5. **Develop a novel experimental technique to compare the active cell mechanical behaviour under dynamic uniaxial and dynamic biaxial loading in a 3D ECM.** In previous studies, systems for mechanical testing of engineered tissue constructs have been limited to uniaxial cyclic stretching without measuring the mechanical response. Given that cells actively respond to loading in the 3D microenvironment, it is important to provide a fundamental mechanistic understanding of the effects of

mechanical conditioning on 3D synthetic tissue constructs. Therefore, the development of a robust system that can apply different uniaxial and biaxial deformation regimes to engineered hydrogel constructs, while measuring the active and passive force, would represent a significant advance in the field of engineered tissue mechanics.

This section provides motivations for each objective in brief. Comprehensive background and motivation is provided for each objective in the literature review and as appropriate throughout this thesis.

## 1.3 Thesis structure

**Chapter 2:** A general literature review on cell mechanics is provided. In particular, a background on intra-cellular structures, in vitro cell mechanics experimental techniques, and computational modelling of cells and the actin cytoskeleton are presented. It should be noted that a critical analysis of relevant literature is also provided throughout the thesis in the context of the findings of each technical chapter (Chapters 4-8).

**Chapter 3:** A background to the theoretical and numerical methods used for computational model development and implementation in this thesis is provided.

**Chapter 4:** An experimental and computational investigation of the mechanical response of spread adhered cells to micropipette aspiration is presented. A custom micropipette aspiration system is developed to aspirate substrate adhered spread cells. Using this system, a series of in vitro experiments are performed in which single cells are subjected to a range of applied aspiration pressures. It is demonstrated that an active computational framework that incorporates SF remodelling and a Hill-type contractility law must be used in order to accurately

simulate micropipette aspiration of untreated spread cells. Finally, a detailed experimental-computational investigation of the nucleus bulk mechanical properties is performed.

**Chapter 5:** A heterogeneous finite element model for the nucleus is created with material properties that span over two orders of magnitude. A correlation between intra-nuclear strain and local DNA concentrations is established.

**Chapter 6:** An overview and analysis of single cell dynamic loading experimental results published recently by Weafer et al. (2015) is presented. These data provide a foundation for novel model development for single cell dynamic loading in Chapter 7.

**Chapter 7:** This chapter presents a novel computational analysis of active cell contractility under dynamic loading conditions. Firstly, the importance of the multiaxial distribution of SFs in the mechanical response of cells to applied loading is uncovered. Deficiencies of a Hill type contractility equation under dynamic conditions are uncovered and a new expression for dynamic contractility is incorporated into the active framework. This new modification provides a significant improvement in the prediction of transient force generation.

**Chapter 8:** A novel experimental system for measurement of cell and tissue forces during uniaxial and biaxial stretching is developed. Tests reveal that a uniaxial stress state results in highly aligned SFs, whereas a biaxial stress state results in randomly aligned SFs. Interpretation of experimental results using the active modelling framework demonstrates the correlation between stress uniaxiality and coordinated SF force generation.

**Chapter 9:** Concluding remarks and future perspectives are provided.

## 1.4 Publications, conference proceedings, and prizes

### 1.4.1 Journal publications

**Chapter 4:** Published in '*Biomaterials*':

Reynolds NH, Ronan W, Dowling EP, Owens P, McMeeking RM, McGarry JP. On the role of the actin cytoskeleton and nucleus in the biomechanical response of spread cells. *Biomaterials* 2014;35:4015-25.

**Chapter 5:** Under preparation for publication in '*Journal of Biomechanics*'.

**Chapter 6:** Contribution to the work of a published paper in which the Ph.D. candidate is a second author is published in '*Acta Biomaterialia*':

Weafer PP, Reynolds NH, Jarvis SP, McGarry JP. Single cell active force generation under dynamic loading – Part I: Experimental AFM measurements. *Acta Biomaterialia* 2015. (doi:10.1016/j.actbio.2015.09.006)

**Chapter 7:** Published in '*Acta Biomaterialia*':

Reynolds NH, McGarry JP. Single cell active force generation under dynamic loading – Part II: Active modelling insights. *Acta Biomaterialia* 2015. (doi:10.1016/j.actbio.2015.09.004)

**Chapter 8:** Under preparation for publication in '*Journal of The Royal Society Interface*'.

### 1.4.2 International conference proceedings

Reynolds, N.H., Ronan, W., Dowling, E.P., Owens, P., McMeeking R.M., McGarry, J.P., 'Investigation of the biomechanical behavior of stress fibers and

nucleus deformation in spread cells using a novel micropipette aspiration technique’, 7th World Congress of Biomechanics, July 2014, Boston, MA, USA.

Reynolds, N.H., Weafer, P.P., Ronan, W, McGarry, J.P., ‘Analysis of the active response of cells to cyclic loading using a modified AFM system’, 19th Congress of the European Society of Biomechanics, August 2013, Patras, Greece.

N. H. Reynolds, W. Ronan, E. P. Dowling, J. P. McGarry, ‘Investigation of the Role of Stress Fiber Contractility and Nucleus Geometry in the Response of Cells to Micropipette Aspiration’, American Society of Mechanical Engineering 2012 Summer Bioengineering Conference, June 2012, Puerto Rico, USA.

N. H. Reynolds, W. Ronan, E. P. Dowling, J. P. McGarry, ‘Contribution of Stress Fiber remodeling to the Response of Cells to Micropipette Aspiration’, Annual Meeting of the Biomedical Engineering Society, October 2011, Connecticut, USA.

### **1.4.3 International and national prizes**

2<sup>nd</sup> overall in the Cellular Biomechanics Ph.D. paper competition at the 7<sup>th</sup> World Congress of Biomechanics in Boston, MA, for paper entitled “*Investigation of the biomechanical behavior of stress fibers and nucleus deformation in spread cells using a novel micropipette aspiration technique*”.

Best overall presentation at the 22<sup>nd</sup> Annual Conference of the Royal Academy of Medicine in Ireland (BINI<sup>22</sup>) in Galway, Ireland, for abstract entitled “*Active dynamic contractility of stress fibres*”.

## **1.5 References**

AFFONCE, D. A. & LUTCHEN, K. R. 2006. New perspectives on the mechanical basis for airway hyperreactivity and airway hypersensitivity in asthma. *J Appl Physiol* (1985), 101, 1710-9.

- BARRETO, S., CLAUSEN, C. H., PERRAULT, C. M., FLETCHER, D. A. & LACROIX, D. 2013. A multi-structural single cell model of force-induced interactions of cytoskeletal components. *Biomaterials*, 34, 6119-6126.
- BUTCHER, J. T. & NEREM, R. M. 2007. Valvular endothelial cells and the mechanoregulation of valvular pathology. *Philosophical Transactions of the Royal Society B: Biological Sciences*, 362, 1445-1457.
- DE BILLY, B., GINDRAUX, F. & LANGLAIS, J. 2014. Osteotomy and fracture fixation in children and teenagers. *Orthop Traumatol Surg Res*, 100, S139-48.
- DESHPANDE, V. S., MCMEEKING, R. M. & EVANS, A. G. 2007. A model for the contractility of the cytoskeleton including the effects of stress-fibre formation and dissociation. *Proc Math Phys Eng Sci*, 463, 787-815.
- DOWLING, E. P., RONAN, W., OFEK, G., DESHPANDE, V. S., MCMEEKING, R. M., ATHANASIOU, K. A. & MCGARRY, J. P. 2012. The effect of remodelling and contractility of the actin cytoskeleton on the shear resistance of single cells: a computational and experimental investigation. *J R Soc Interface*, 9, 3469-79.
- FONSECA, F. A. H., IZAR, M. C. O., FUSTER, V., GALLO, R., PADUREAN, A., FALLON, J. T., SCHACHTER, E. N., CHESEBRO, J. H. & BADIMON, J. J. 2001. Chronic endothelial dysfunction after oversized coronary balloon angioplasty in pigs: a 12-week follow-up of coronary vasoreactivity in vivo and in vitro. *Atherosclerosis*, 154, 61-69.
- FREY, N. & OLSON, E. N. 2003. Cardiac hypertrophy: the good, the bad, and the ugly. *Annu Rev Physiol*, 65, 45-79.
- GIMBRONE, M. A., JR., TOPPER, J. N., NAGEL, T., ANDERSON, K. R. & GARCIA-CARDENA, G. 2000. Endothelial dysfunction, hemodynamic forces, and atherogenesis. *Ann N Y Acad Sci*, 902, 230-9; discussion 239-40.
- GOMEZ-BARRENA, E., ROSSET, P., MULLER, I., GIORDANO, R., BUNU, C., LAYROLLE, P., KONTTINEN, Y. T. & LUYTEN, F. P. 2011. Bone regeneration: stem cell therapies and clinical studies in orthopaedics and traumatology. *J Cell Mol Med*, 15, 1266-86.
- GUCK, J., SCHINKINGER, S., LINCOLN, B., WOTTAWAH, F., EBERT, S., ROMEYKE, M., LENZ, D., ERICKSON, H. M., ANANTHAKRISHNAN, R., MITCHELL, D., KÄS, J., ULVICK, S. & BILBY, C. 2005. Optical Deformability as an Inherent Cell Marker for Testing Malignant Transformation and Metastatic Competence. *Biophysical Journal*, 88, 3689-3698.
- HEYDEMANN, A. & MCNALLY, E. M. 2007. Consequences of disrupting the dystrophin-sarcoglycan complex in cardiac and skeletal myopathy. *Trends Cardiovasc Med*, 17, 55-9.
- HOFFMANN, R., MINTZ, G. S., DUSSAILLANT, G. R., POPMA, J. J., PICHARD, A. D., SATLER, L. F., KENT, K. M., GRIFFIN, J. & LEON, M. B. 1996. Patterns and mechanisms of in-stent restenosis a serial intravascular ultrasound study. *Circulation*, 94, 1247-1254.
- HUANG, G. 2014. Function of Collagens in Energy Metabolism and Metabolic Diseases. *J Cell Sci Ther*, 5, 2.
- HUISKES, R., WEINANS, H. & VAN RIETBERGEN, B. 1992. The relationship between stress shielding and bone resorption around total hip stems and the effects of flexible materials. *Clin Orthop Relat Res*, 124-34.
- INGBER, D. E. 2003. Mechanobiology and diseases of mechanotransduction. *Ann Med*, 35, 564-77.
- JONES, W. R., PING TING-BEALL, H., LEE, G. M., KELLEY, S. S., HOCHMUTH, R. M. & GUILAK, F. 1999. Alterations in the Young's modulus and volumetric properties of

- chondrocytes isolated from normal and osteoarthritic human cartilage. *J Biomech*, 32, 119-127.
- JUDEX, S., GROSS, T. S., BRAY, R. C. & ZERNICKE, R. F. 1997. Adaptation of bone to physiological stimuli. *J Biomech*, 30, 421-9.
- KAUNAS, R. & HSU, H. J. 2009. A kinematic model of stretch-induced stress fiber turnover and reorientation. *J Theor Biol*, 257, 320-30.
- KLEIN-NULEND, J., BACABAC, R. G., VELDHUIJZEN, J. P. & VAN LOON, J. J. 2003. Microgravity and bone cell mechanosensitivity. *Adv Space Res*, 32, 1551-9.
- LEE, S.-L., NEKOUZADEH, A., BUTLER, B., PRYSE, K. M., MCCONNAUGHEY, W. B., NATHAN, A. C., LEGANT, W. R., SCHAEFER, P. M., PLESS, R. B., ELSON, E. L. & GENIN, G. M. 2012. Physically-Induced Cytoskeleton Remodeling of Cells in Three-Dimensional Culture. *PLoS ONE*, 7, e45512.
- MCGARRY, J. G. & PRENDERGAST, P. J. 2004. A three-dimensional finite element model of an adherent eukaryotic cell. *Eur Cell Mater*, 7, 27-33; discussion 33-4.
- MCGARRY, J. P., FU, J., YANG, M. T., CHEN, C. S., MCMEEKING, R. M., EVANS, A. G. & DESHPANDE, V. S. 2009. Simulation of the contractile response of cells on an array of micro-posts. *Philos Trans A Math Phys Eng Sci*, 367, 3477-3497.
- MINAMI, Y., KANEDA, H., INOUE, M., IKUTOMI, M., MORITA, T. & NAKAJIMA, T. 2013. Endothelial dysfunction following drug-eluting stent implantation: A systematic review of the literature. *International Journal of Cardiology*, 165, 222-228.
- MOHRDIECK, C., WANNER, A., ROOS, W., ROTH, A., SACKMANN, E., SPATZ, J. P. & ARZT, E. 2005. A theoretical description of elastic pillar substrates in biophysical experiments. *Chemphyschem*, 6, 1492-8.
- MULLER, B., BOWMAN, K. F., JR. & BEDI, A. 2013. ACL graft healing and biologics. *Clin Sports Med*, 32, 93-109.
- PASZEK, M. J., ZAHIR, N., JOHNSON, K. R., LAKINS, J. N., ROZENBERG, G. I., GEFEN, A., REINHART-KING, C. A., MARGULIES, S. S., DEMBO, M., BOETTIGER, D., HAMMER, D. A. & WEAVER, V. M. 2005. Tensional homeostasis and the malignant phenotype. *Cancer Cell*, 8, 241-54.
- QIAN, J., LIU, H., LIN, Y., CHEN, W. & GAO, H. 2013. A Mechanochemical Model of Cell Reorientation on Substrates under Cyclic Stretch. *PLoS ONE*, 8, e65864.
- RONAN, W., DESHPANDE, V. S., MCMEEKING, R. M. & MCGARRY, J. P. 2012. Numerical investigation of the active role of the actin cytoskeleton in the compression resistance of cells. *J Mech Behav Biomed Mater*, 14, 143-57.
- TAN, J. C., KALAPESI, F. B. & CORONEO, M. T. 2006. Mechanosensitivity and the eye: cells coping with the pressure. *Br J Ophthalmol*, 90, 383-8.
- TAN, J. L., TIEN, J., PIRONE, D. M., GRAY, D. S., BHADRIRAJU, K. & CHEN, C. S. 2003. Cells lying on a bed of microneedles: an approach to isolate mechanical force. *Proc Natl Acad Sci USA*, 100, 1484-9.
- THOUMINE, O. & OTT, A. 1997. Comparison of the mechanical properties of normal and transformed fibroblasts. *Biorheology*, 34, 309-26.
- TRICKEY, W. R., LEE, G. M. & GUILAK, F. 2000. Viscoelastic properties of chondrocytes from normal and osteoarthritic human cartilage. *J Orthop Res*, 18, 891-8.
- VERNEREY, F. J. & FARSAD, M. 2011. A constrained mixture approach to mechano-sensing and force generation in contractile cells. *J Mech Behav Biomed Mater*, 4, 1683-1699.
- VOLLRATH, M. A., KWAN, K. Y. & COREY, D. P. 2007. The micromachinery of mechanotransduction in hair cells. *Annu Rev Neurosci*, 30, 339-65.
- WANG, X., ZACHMAN, A. L., CHUN, Y. W., SHEN, F.-W., HWANG, Y.-S. & SUNG, H.-J. 2014. Polymeric stent materials dysregulate macrophage and endothelial cell functions:

- Implications for coronary artery stent. *International Journal of Cardiology*, 174, 688-695.
- WEAFER, P. P., REYNOLDS, N. H., JARVIS, S. P. & MCGARRY, J. P. 2015. Single cell active force generation under dynamic loading – Part I: AFM experiments. *Acta Biomaterialia*, DOI:dx.doi.org/10.1016/j.actbio.2015.09.006.
- WEAFER, P. P., RONAN, W., JARVIS, S. P. & MCGARRY, J. P. 2013. Experimental and computational investigation of the role of stress fiber contractility in the resistance of osteoblasts to compression. *Bull Math Biol*, 75, 1284-303.
- YETKIN, E., ERBAY, A. R., TURHAN, H., ILERI, M., AYAZ, S., ATAK, R., SENEN, K. & CEHRELI, S. 2003. Decreased platelet activation and endothelial dysfunction after percutaneous mitral balloon valvuloplasty. *International Journal of Cardiology*, 91, 221-225.

## 2 Literature review

### 2.1 Introduction

This chapter presents an overview of literature related to this thesis. In Section 2.2 a background of the key mechanical constituents of cells is presented. In Section 2.3 experimental techniques commonly utilized to investigate cell mechanical behaviour are presented. In Section 2.4 computational modelling approaches for the simulation of the mechanical behaviour of cells and the cytoskeleton are outlined. Throughout this literature review, key deficits/problems in the field of cell mechanics are identified and underlined. In Section 2.5, these deficits are summarised and contextualised in terms of the objectives of this thesis (outlined in Section 1.2 of Chapter 1). In addition to the background literature presented in the current chapter, each technical chapter contains a detailed discussion and analysis of previous studies in the context of the findings of this thesis.

### 2.2 Cell structure and forces

The cell is made up of a vast array of molecules and structures that respond to many different stimuli (Alberts et al., 2002). From a mechanics view point, the cytoskeleton is the key structural component of the cell: which provides resistance

to deformation (Dowling et al., 2012); generates active endogenous forces (Califano and Reinhart-King, 2010); regulates extracellular adhesion, spreading, and migration (Ronan et al., 2014); and is critical for mechanotransduction (Ohashi et al., 2006). The cytoskeleton consists of three components; microtubules, intermediate filaments, and the actin cytoskeleton. In Figure 2.1 fluorescent images of each of these cytoskeletal components is shown. In addition to these cytoskeletal components, the cytoplasm and nucleus also contribute to the mechanical response of cells (Caille et al., 2002), with focal adhesions providing a mechanical connection between the cell and the extracellular matrix (ECM)/substrate (Ronan et al., 2015, Mullen et al., 2014, Riveline et al., 2001).

### **2.2.1 The nucleus**

The main role of the nucleus is to regulate gene expression in cells (Lammerding et al., 2007). The nuclei of endothelial, osteoblast, chondrocyte, and cardiomyocyte cells consist of two main regions: the nucleus interior, which contains DNA and proteins (Henderson et al., 2013), and the nuclear envelope, which is a lipid bilayer (Vaziri et al., 2007, Vaziri and Mofrad, 2007). Nuclei are linked to the surrounding cytoskeletal components via nuclear lamina and chromatin (Lammerding, 2011). Reshaping of the nuclear lamina and chromatin distribution during nucleus deformation has been linked to cell mechanotransduction (Dahl et al., 2008, Rowat et al., 2008, Tsukamoto et al., 2000, Wang et al., 2009). In addition, direct modulation of nuclear shape has been shown to affect the regulation of type II collagen as well as gene expression (Campbell et al., 2007, Shieh and Athanasiou, 2007, Shieh and Athanasiou, 2003, Leipzig and Athanasiou, 2008, Thomas et al., 2002). Given the significant deformation of nuclei observed under physiological load in situ (Henderson et al., 2013, Buschmann et

al., 1996), careful characterisation of nucleus deformation is of critical importance in the development of a fundamental understanding of mechanotransduction.

Numerous studies suggest that nuclei are stiffer than the surrounding cytoplasm (Guilak et al., 2000, Caille et al., 2002, Caille et al., 1998, Maniotis et al., 1997, Jean et al., 2005, Ferko et al., 2007, Deguchi et al., 2007, Ofek et al., 2009a, Knight et al., 2002). In contrast to these findings, Leipzig and Athanasiou (2008) reported that cytoplasm and nucleus strains had a 1:1 ratio during static compression using a piezoelectric actuated probe, suggesting that the stiffness of the cytoplasm and nucleus are similar. However, it should be noted that the extracellular environment in these aforementioned studies is not the same in all cases. It is well known that the “apparent” stiffness of cells can alter due to substrate compliance (Byfield et al., 2009), the level of spreading (Thoumine et al., 1999), and the contractile nature of the cell phenotype in question (Rodriguez et al., 2013, Caille et al., 2002, Peeters et al., 2005, Deng et al., 2010, Ofek et al., 2009b). To overcome this complex factor Deguchi et al. (2005) and Guilak et al. (2000) isolated nuclei from cells before testing. However, it has been suggested that nucleus mechanical behaviour may be altered by the isolation procedure (Guilak et al., 2000). Simulating experiments of isolated nuclei, Vaziri and Mofrad (2007) computed a low nucleus shear modulus of 0.008 kPa. Furthermore, previous experimental studies of micropipette aspiration of suspended cells reveal significant nucleus deformation (Pajerowski et al., 2007, Ribeiro et al., 2012). Pajerowski et al. (2007) reported that permanent visco-plastic deformation of the nucleus occurs due lamin A/C and chromatin remodelling. In summary, the mechanical behaviour of the nucleus has not been definitively characterised in the literature with a wide range of elastic properties being reported. A detailed and robust methodology for

analysis of nucleus biomechanics would represent a considerable contribution to the field of cell mechanics.

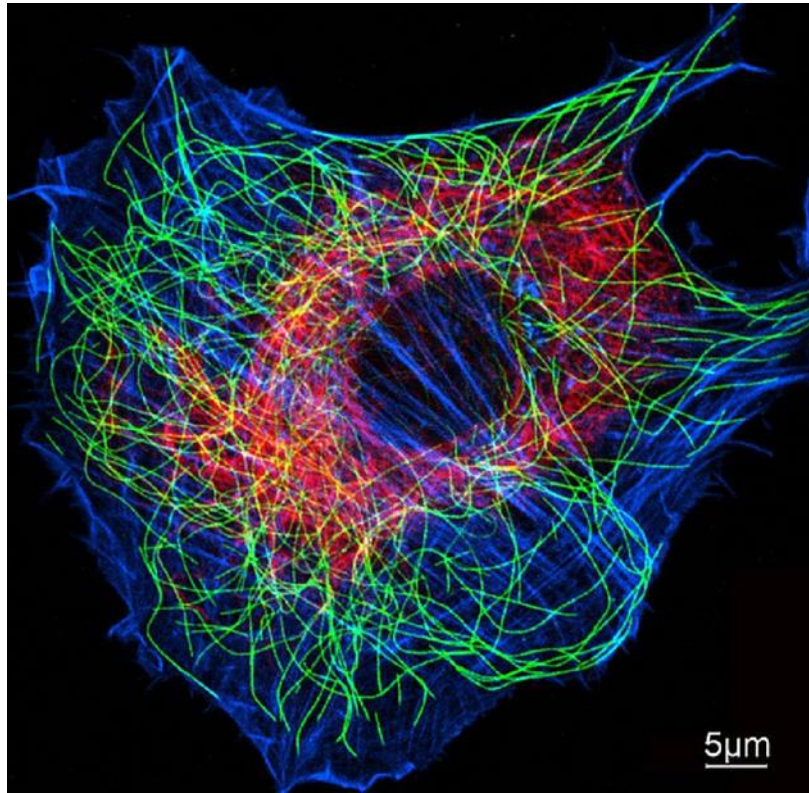


**Figure 2.1:** Fluorescent image of the actin cytoskeleton in a single cell in 2D culture. Intermediate filaments are shown in red, microtubules are shown in green, and actin filaments are shown in blue. Image courtesy of Cora-Ann Schoenenberger and Rosmarie Suetterlin, Biozentrum, University of Basel.

### 2.2.2 The cytoskeleton

The cytoskeleton, which lies within the cytoplasm, is key in maintaining cell structure (Yeung et al., 2005, Dowling et al., 2012, Trickey et al., 2004, Ohashi et al., 2006). The cytoplasm is a crowded environment of proteins and organelles that surround the nucleus (Ethier and Simmons, 2007). As mentioned in the previous section, the cytoskeleton is critical for transmission of mechanical cues to the nucleus as part of mechanotransduction. The cytoskeleton also plays a crucial role in regulating whole cell mechanical response to the extracellular environment (Ingber, 1997, Shieh and Athanasiou, 2003, Wang and Thampatty, 2006, Bader and

Knight, 2008, Fletcher and Mullins, 2010). Furthermore, the cytoskeletal mediated resistance, transmission, and active generation of force dynamically influences cell shape, migration, adhesion, and overall stiffness (Mofrad, 2009, Mann et al., 2012, Lam et al., 2012a). In addition to providing essential structural support and regulation, the cytoskeleton also serves as a transport network for molecular motors to deliver vesicles and other organelles throughout the cell (Hirokawa, 1998). Cytoskeleton components consists of proteins organised into filaments. The cytoskeleton of cells has three main organised protein groups: intermediate filaments, microtubules, and actin filaments (Figure 2.1 and Figure 2.2).

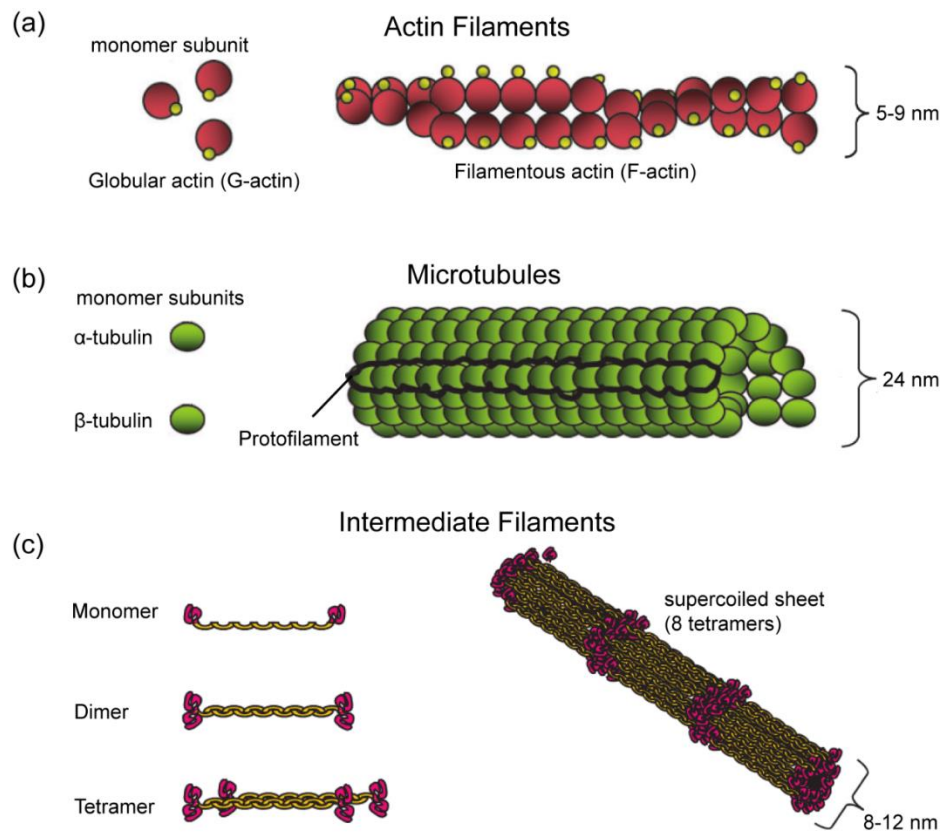


**Figure 2.2: The three filamentous groups that make up the cell cytoskeleton; (a) actin filaments, (b) microtubules, and (c) intermediate filaments. Adapted from (Blain, 2009).**

### 2.2.2.1 Intermediate filaments

Intermediate filaments provide integrity and organisation to both the cell and nucleus (Lodish et al., 2000, Herrmann et al., 2007, Alberts et al., 2002,

Lammerding, 2011). These filaments arrange in a network surrounding the nucleus and are thought to anchor the nucleus within the cell (Dupin et al., 2011). They are 8-12 nm in diameter and are comprised of a series of tetramers which assemble to form a super-coiled sheet (Blain, 2009, Fuchs and Weber, 1994). These tetramer proteins are formed from two coiled dimmers arranged in an anti-parallel manner. The precise function of intermediate filaments is unclear (Eriksson et al., 2009). However, it has been demonstrated experimentally that intermediate filaments have a role in biochemical processes and in the overall response of cells to mechanical load (Ingber, 1997, Durrant et al., 1999, Ofek et al., 2009b, Dowling et al., 2012), particularly during large deformation (Wang and Stamenović, 2000, Stamenovic, 2008).

#### 2.2.2.2 *Microtubules*

Microtubules are key for cellular homeostasis, providing transportation pathways for intercellular delivery of vesicles and organelles (Hirokawa, 1998), separating chromosomes during cell division (Anaphase, 2000, Sharp et al., 2000), and have been linked to synthesis and secretion of proteoglycans and collagen (Jortikka et al., 2000, Poole et al., 2001). Microtubules are assembled from monomers of globular protein,  $\alpha$ -tubulin and  $\beta$ -tubulin, helically wound into protofilaments to form stiff, cylindrical structures (Alberts et al., 2002, Martini, 2004). The largest cytoskeletal component, microtubules have a diameter of ~25 nm and persistence length in the order of millimetres (Lodish et al., 2000, Gittes et al., 1993), and radiate outward from a central organelle (centrosome or microtubule-organising centre) which is located near the nucleus (de Forges et al., 2012). In terms of microtubule contribution to the mechanical response of whole cells, previous in vitro experiments demonstrated that cells treated with colchicine (which

disrupts microtubules) exhibited reduced resistance to applied shear (Dowling et al., 2012). Furthermore, previous studies have demonstrated that microtubules contribute to the cell compression resistance (Ofek et al., 2009b, Brangwynne et al., 2006). However, Trickey et al. (2004) reported no difference between stiffness and viscosity of untreated cells compared to that of colchicine treated cells.

### 2.2.2.3 *Actin filaments*

Of all the cytoskeletal elements, actin filaments are the primary functional component in modulating cell mechanical behaviour (Yeung et al., 2005, Dowling et al., 2012, Trickey et al., 2004, Ohashi et al., 2006). Through interaction with the motor protein myosin, actin filaments are essential for the generation and maintenance of contractile forces required for regulating cell shape/morphology, cell migration, cell adhesion, and whole cell stiffness (Fletcher and Mullins, 2010, Kumar et al., 2006, Sato et al., 2006, De et al., 2010, Blain, 2009, Guilak, 1995, Fernandez et al., 2006). The capability of actin filaments to interact with the myosin motor protein is clearly an important feature. Globular actin (G-actin), which is reported to be the most abundant protein in eukaryotic cells (Alberts et al., 2002), polymerises and coils into a double-helix arrangement to create filamentous actin (F-actin) (Figure 2.2). The polymerised actin filaments have a diameter ranging from 5-9 nm and an elastic modulus of 1-2 GPa (Lodish et al., 2000). Actin filaments continually undergo polymerisation and depolymerisation due to association and dissociation of G-actin at either end. Furthermore, actin filaments can form network branches through Arp2/3 proteins, which assist outward protrusion of the cell membrane during migration and spreading, i.e. lamellipodia and filopodium (Goley and Welch, 2006, Welch, 1999). In a resting state, the cell cytoplasm contains numerous short actin filaments (capped by the protein CapZ)

and inactive state myosin II. In response to an activation signal, calcium ions released from the endoplasmic reticulum into the cell cytosol trigger gelsolin, which cleaves the capped small actin filaments, leading to formation of long actin filaments. These actin filaments and filament complexes bundle together in parallel via  $\alpha$ -actinin (Figure 2.3-B) and fimbrin (Burrige and Wennerberg, 2004). Phosphorylation of the myosin II into the active state can occur due to the activation signal mentioned above (light-chain-kinase) or due to an externally applied load (Rho-kinase). Activated myosin II assembles into bipolar filaments and interacts with the  $\alpha$ -actinin bound actin filament bundles (Figure 2.3-C), to create contractile thread-like structures known as “stress fibres” (Alberts et al., 2002). Fimbrin bound actin filaments bundles are too tightly packed to interact with myosin motor proteins. The contractile behaviour of these formed stress fibres is generated via the crossbridge cycling of the actin filaments and myosin (Figure 2.3-D), which is similar to the well-known behaviour observed for skeletal muscle (Hill, 1938).

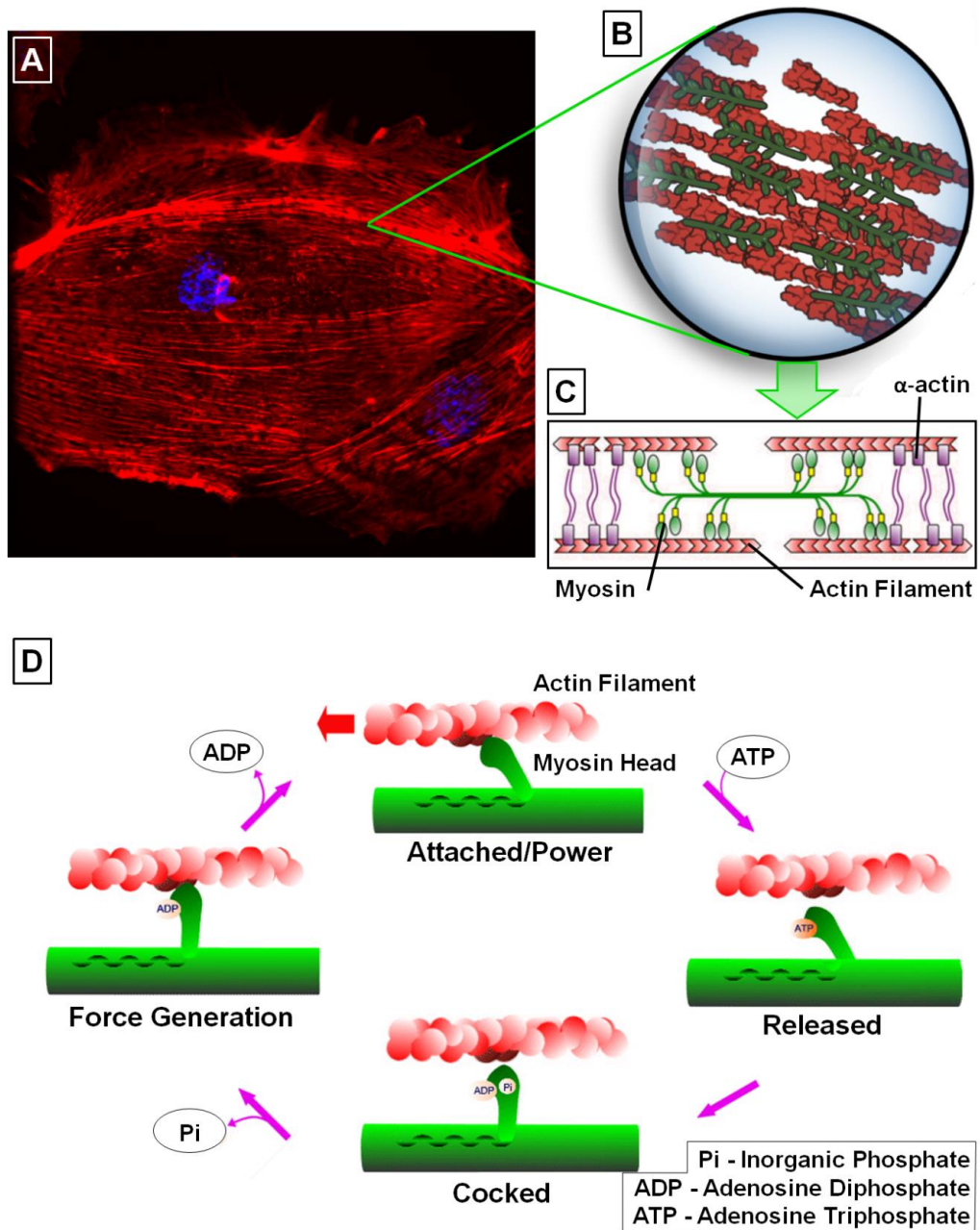


Figure 2.3: (A) fluorescent image of a cell showing nuclei in blue and the actin cytoskeleton in red. (B) Exploded out schematic illustrating bundling of proteins to form stress fibres (adapted from Blanchoin et al. (2014)). (C) Schematic of a single stress fibre unit. (D) Stress fibre contractility is generated by the crossbridge cycling of the actin filaments and myosin.

## 2.3 Experimental techniques for investigating cell mechanics

Cell mechanics has been studied extensively using a wide array of experimental techniques at multiple length scales (Jonas et al., 2008). Investigations at the tissue level (Hillam and Skerry, 1995, Lanyon, 1996, Hsieh and Turner, 2001, Roy et al., 2009), on cell populated 3D constructs (Thavandiran et al., 2013, Wille et al., 2006, Nekouzadeh et al., 2008, Balestrini and Billiar, 2009, Buxboim et al., 2010, Thorpe et al., 2010), on cell populations in 2D (Harris et al., 2012, Kaunas et al., 2005, Barron et al., 2007, Wang et al., 2001b), and on single cells demonstrate alterations in cell structure and function under static and dynamic loading conditions. Single cell investigations are advantageous for understanding changes in cell behaviour in response to a specific stimulus. This may include examination of enzyme and matrix synthesis (Nakano et al., 2011, Ofek and Athanasiou, 2007), gene expression (Tan et al., 2013), cellular signalling (Adachi et al., 2008), and intracellular structural changes, such as cytoskeleton remodelling. Consequently, single cell investigations can be employed to guide the development of mechanical environments that elicit favourable cell responses, hence providing a biomechanistic strategy for tissue engineering (Ofek and Athanasiou, 2007).

### 2.3.1 Single cell biomechanics testing

Given the micro scale size of single cells, and the nano-Newton scale of active force generation, experimental systems used to examine single cell mechanical response must be extremely sensitive. Advances in technologies have facilitated the development or adaptation of a number of different specialised approaches. An overview of these techniques is shown in Figure 2.4 (Rodriguez et

al., 2013). In this section, a brief outline of commonly used techniques, including micropipette aspiration, atomic force microscopy (AFM) indentation, microbead manipulation, uniaxial deformation (compression and tension), microposts force mapping, and traction force microscopy, is presented.

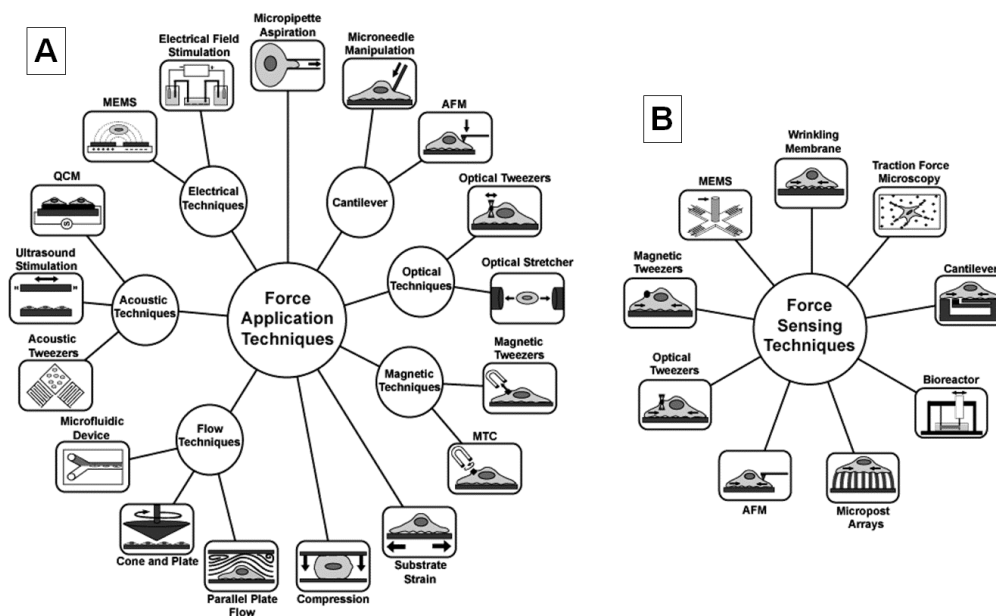


**Figure 2.4: (A) Techniques used apply forces to cells and investigate mechanical response. (B) Techniques used to investigate cell mechanical response in the absence of mechanical loading. Reproduced from Rodriguez et al. (2013).**

**The micropipette aspiration technique** has been used to investigate the mechanical behaviour of whole cells, which have been suspended in media. A micropipette is a small glass capillary with an internal diameter smaller than that of a suspended cell. Micropipette aspiration systems must be mounted on microscope stages to enable cell/micropipette manipulation and monitoring of cell deformation in real time. Suspended cells are drawn to the tip entrance by applying a small negative pressure in the micropipette. Once a tight seal is formed between the cell and the tip entrance, a known negative pressure is applied inside the micropipette, inducing cell deformation or “aspiration” (Figure 2.5-A). If the cell is assumed to

be a homogenous incompressible linear elastic material, the Young's modulus,  $E$ , can be calculated from the following equation (Theret et al., 1988):

$$E = \frac{3a\Delta p}{2\pi L} \Phi \quad (2.1)$$

where  $\Delta p$  is the negative pressure applied inside the micropipette,  $a$  is the internal radius of the micropipette,  $L$  is the length from the tip entrance to the furthestmost point of the cell in the micropipette, and the value for the wall function,  $\Phi$ , can be found in the study of Theret et al. (1988). The model of Theret et al. (1988) was later expanded by Sato et al. (1990) to consider time dependant viscous effects. By assuming that the cell is a standard linear solid viscoelastic material, the aspiration length with respect to time,  $t$ , is given by the following equation:

$$L(t) = \frac{\Phi a \Delta P}{\pi k_1} \left[ 1 - \frac{k_2}{k_1 + k_2} e^{-\frac{t}{\tau}} \right] \quad (2.2)$$

where  $k_1$  and  $k_2$  are spring constants for a standard linear solid model and  $\tau$  is the time constant. Once a close correlation to the experimental length data is obtained using Eqn. (2.2) (Figure 2.5-B), the instantaneous and long term Young's moduli can be determined:

$$E_{\text{instantaneous}} = \frac{3}{2}(k_1 + k_2) \quad ; \quad E_{\text{long term}} = \frac{3}{2}(k_1) \quad (2.3)$$

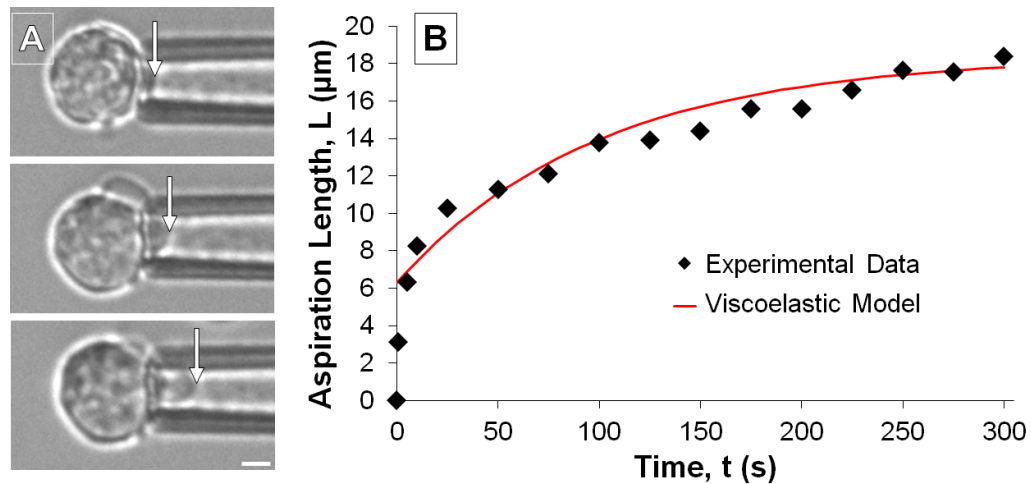


**Figure 2.5:** (A) Selected images from a micropipette aspiration experiment. Arrows indicate the aspiration length. (B) Sample of experimental aspiration length data obtained from experiments. A fit of the experimental data using the viscoelastic model is also shown. Scale bar = 10  $\mu\text{m}$ .

Micropipette aspiration has been used to determine the bulk passive mechanical properties of many cell types in suspension, including leukocytes (Sung et al., 1988, Ting-Beall et al., 1993, Liu et al., 2007, Herant et al., 2005, Evans and Yeung, 1989), red blood cells (Evans, 1973, Hochmuth, 1993, Waugh and Evans, 1979), chondrocytes (Trickey et al., 2006, Trickey et al., 2000, Trickey et al., 2004, Guilak et al., 1999, Jones et al., 1999, Ohashi et al., 2006, Pravin Kumar et al., 2012), platelets (Haga et al., 1998, White et al., 1984, McGrath et al., 2011, Burris et al., 1986), endothelial cells (Sato et al., 1990, Sato et al., 1996, Sato et al., 1987), fibroblasts (Thoumine and Ott, 1997a, Zhou et al., 2010), and stem cells (Tan et al., 2008, Yu et al., 2010, Ribeiro et al., 2012). Micropipette aspiration has been used to compare the stiffness of chondrocytes isolated from healthy and osteoarthritic cartilage (Jones et al., 1999), different types of adult stem cell (Ribeiro et al., 2012), and endothelial cells exposed to varying levels of shear stress (Sato et al., 1996). Furthermore, previous micropipette aspiration studies reported a dramatically reduced stiffness in cells treated with agents to disrupt the actin cytoskeleton (Tan et al., 2008, Trickey et al., 2004, Ohashi et al., 2006). In contrast,

the reduction in stiffness of cells treated with microtubule and intermediate filament disrupting agents was less pronounced (Trickey et al., 2004, Ohashi et al., 2006). It should be noted that a fibrillous contractile actin cytoskeleton is not developed in suspended cells (Sato et al., 1987, Reinhart-King et al., 2005, Haghparast et al., 2013). In contrast, cells adhered to a substrate or ECM develop a highly structured contractile actin cytoskeleton (Munevar et al., 2001, Thoumine and Ott, 1996, Li et al., 2007, Zaleskas et al., 2004, Tan et al., 2003, Lemmon et al., 2005, Tee et al., 2011, Roy et al., 2009). Therefore, the study of un-adhered suspended cells provides limited insight into the behaviour of contractile cells. Finally, the micropipette aspiration technique has also been used to investigate the stiffness of nuclei isolated from the cytoplasm (Guilak et al., 2000, Deguchi et al., 2005).

**Atomic force microscopy (AFM)** is an established technique in cell mechanics that is typically used to probe localised regions of spread adhered cells with unrivalled positional and force precision (Simon and Durrieu, 2006, Colton et al., 1997). The AFM system typically consists of a sharp probing tip attached to a flexible cantilever (Figure 2.6-A). The cantilevers are lowered into the test sample (cells) and the deflection is monitored using a “cantilever deflection detection system”, usually consisting of a laser probe and position sensitive detector (PSD). Sub nano-meter z-axis displacement of the cantilever and sample stage positioning are controlled by piezoelectric actuators. From a cell mechanics perspective, AFMs have been used in investigations of components of the cell nucleus (Hansma et al., 2004, Hirano et al., 2008), cytoskeletal structures (Rotsch et al., 1999, Pesen and Hoh, 2005), and whole cells (Rotsch et al., 1997, Radmacher et al., 1996, Hofmann et al., 1997, Deng et al., 2010, Darling et al., 2008, Prabhune et al., 2012, Jaasma et al., 2007, Lulevich et al., 2006). In addition to force measurement,  $F$ , an

approximation of the Young's modulus,  $E$ , for cells can be calculated by measuring the indentation depth,  $\delta$ , and implementing Hertzian theory (Johnson, 1985, Kuznetsova et al., 2007), where:

$$E = \frac{\pi(1 - \nu^2) F}{2 \tan \alpha \delta^2} \quad (2.4)$$

for a conical tip of half angle,  $\alpha$ , and:

$$E = \frac{3(1 - \nu^2) F}{4\sqrt{a} \sqrt{\delta^3}} \quad (2.5)$$

for a spherical tip of radius,  $a$ .  $\nu$  is the Poisson's ratio for the cell. It should be noted, however, that the Hertzian theory assumes a homogenous linear elastic half-space, and that the indentation depth is much lower than the material thickness.

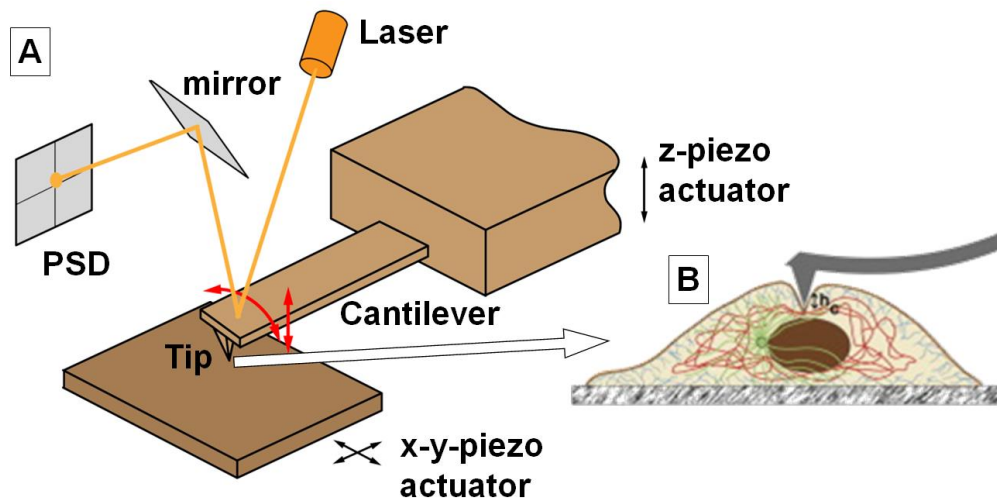


Figure 2.6: (A) Schematic of AFM setup (adapted from Weafer (2012)). (B) Schematic illustrating cell deformation during indentation using a sharp tip (adapted from Plodinec et al. (2011)).

AFM indentation is typically performed on highly localised regions of the cell (Figure 2.6-B). While this is useful for probing individual structures and determining the heterogeneity of the cell, the mechanical response is not established at a whole cell level (Roca-Cusachs et al., 2008, Titushkin and Cho, 2007, Prabhune

et al., 2012, Darling et al., 2008, Bao and Suresh, 2003). Previous studies have attempted overcome this by performing a large number of indentations over the entire cell (Radmacher et al., 1996, Hofmann et al., 1997, Rotsch and Radmacher, 2000, Kelly et al., 2011). However, acquiring data over a large area is time consuming and may occur at a shorter time scale than the intracellular cytoskeletal remodelling itself. Previous studies have replaced the sharp indentation tips attached to the cantilevers with spheres of 60  $\mu\text{m}$  diameter or less (Lehenkari et al., 2000, Lulevich et al., 2006, Jaasma et al., 2006, Zimmer et al., 2012). However, while these spheres are significantly less localised than the sharp tips, the contact region will still be much smaller than the spread cell radius.

Further developing on this approach, Weafer et al. (2012) attached a large sphere with diameter of 150  $\mu\text{m}$  to the end of the flexible cantilever in order to achieve a more uniform strain state in the cell. It was shown that due to the rotation constraint at the sphere-cell interface (due to friction between the sphere and the substrate), the bending profile of the cantilever resembled a double encastre beam. This resulted in an 18-fold underestimation of the material stiffness using standard AFM formulae of deflection, force, and stiffness. Weafer et al. (2012) demonstrated that appropriate correction factors must be used to account for the rotational constraint of the cantilever/sphere. Using this system in a later study, Weafer et al. (2013) demonstrated that untreated cells provide a significantly greater resistance to quasi-static compression compared to cells treated with actin cytoskeleton disrupting agents. Given the size of the sphere attached to the cantilever in the system outlined above, the deformation applied to the cell could be categorised as unconfined whole cell compression.

**Microbead manipulation** is a method whereby small nano- to micron-sized beads are attached to the cell membrane and displaced using optical or magnetic techniques (Laurent et al., 2002). Using the optical technique (Figure 2.7-B and -C), displacement is controlled by directing infrared lasers at the transparent beads. The change in direction of the photons due to refraction results in controlled bead displacement (Lim et al., 2006, Block, 1992, Svoboda and Block, 1994, Neuman and Block, 2004, Fazal and Block, 2011, Titushkin and Cho, 2006, Dao et al., 2003). Using magnetic techniques (Figure 2.7-A), ferromagnetic bead displacements are controlled by the magnetic field gradient produced by an electromagnetic coil (Neuman et al., 2007, Ziemann et al., 1994, Bausch et al., 1999, Bausch et al., 1998, Crick, 1950, Crick and Hughes, 1950). A rotational displacement is often applied to the ferromagnetic beads, known as magnetic twisting cytometry. Microbead manipulation techniques have been used to investigate material properties of the cytoplasm (Crick, 1950, Crick and Hughes, 1950), whole cells (Fabry et al., 2001, Wang et al., 2002, Wang and Ingber, 1995), and cytoskeletal remodelling (Deng et al., 2004, Hu et al., 2004, Hu et al., 2003).

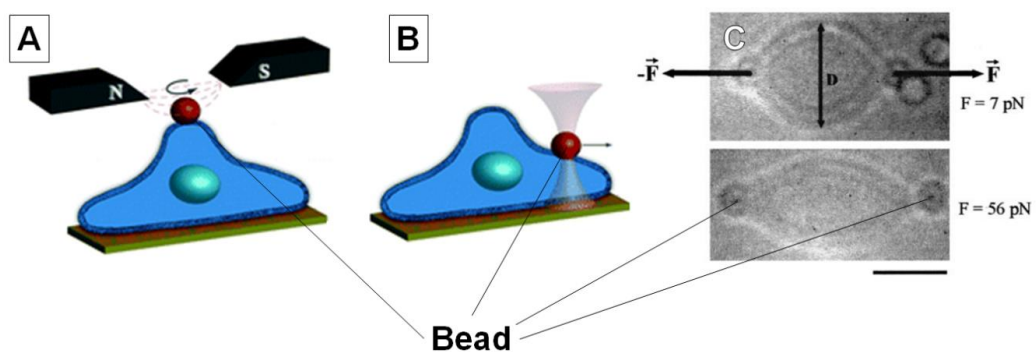


**Figure 2.7:** Schematics of microbead manipulation using (A) magnetic techniques and (B) optical technique (adapted from (Girard et al., 2007)). (C) Microscope image of two optically controlled beads stretching a cell (adapted from (Henon et al., 1999)).

**Whole cell uniaxial deformation** is commonly performed using microplates (Thoumine and Ott, 1997b) or large flat-ended probes (Shin and Athanasiou, 1999). Loading can be applied in a strain controlled (Shieh and Athanasiou, 2006, Ofek et al., 2009b) or force controlled (Leipzig and Athanasiou, 2005, Leipzig and Athanasiou, 2008, Shieh and Athanasiou, 2007) manner. The indenter (probe or microplate) is displaced using a piezoelectric translator while the deflection is monitored using microscopes (Figure 2.8). The force applied by the indenter is determined using cantilever beam theory. These systems are commonly used to subject cells to unconfined compression (Caille et al., 2002, Peeters et al., 2005, Deng et al., 2010, Ofek et al., 2009b) and tension (Thoumine and Ott, 1997b, Micoulet et al., 2005, Fernandez et al., 2006, Mitrossilis et al., 2009). For single cell stretching experiments time is allowed for the cell to adhere to the indenter before the probe is retracted, bringing the cell into a tensile loading regime. An example of the system used by Thoumine and Ott (1997b) is shown in Figure 2.8. To overcome the limitations of optical visualisation of microplate deformation, Weafer et al. (2012) developed a system whereby a large sphere was attached to the end of a flexible AFM cantilever. The loading applied using the large sphere is analogous to the aforementioned uniaxial deformation experiments.

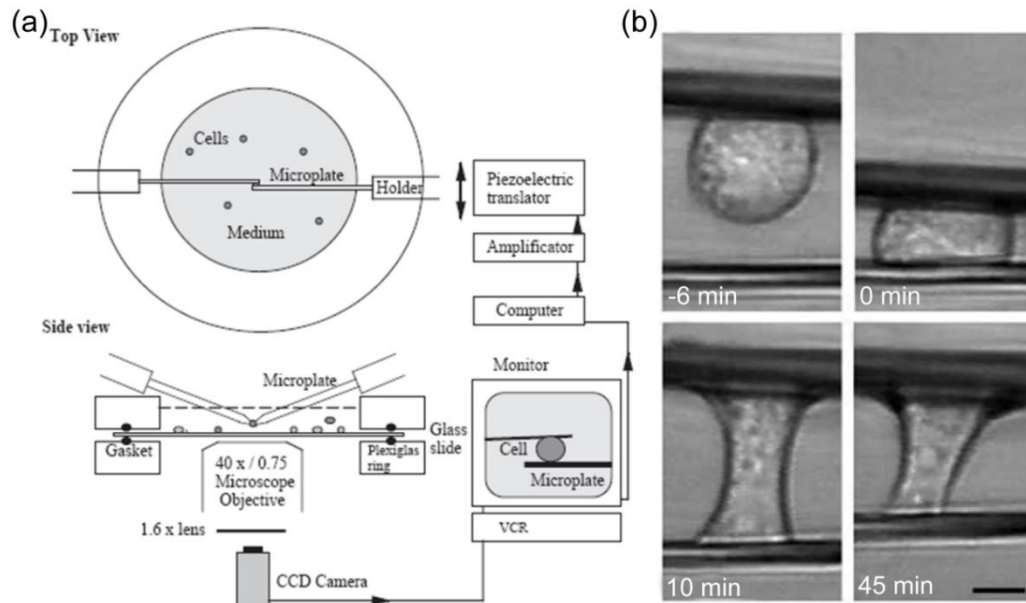


**Figure 2.8: (A) Schematic of the micromanipulation system. (B) Microscope images of a cell between the microplates. Scale bar = 5  $\mu$ m. Adapted from Thoumine and Ott (1997b).**

**Traction force microscopy** is a technique used to determine traction forces exerted by cells to its ECM (Figure 2.9). Cells are seeded on top of (Wang et al., 2002, Doyle and Lee, 2005, Iwadate and Yumura, 2008, Curtze et al., 2004, Tolic-Norrelykke and Wang, 2005, Wang et al., 2005, Lombardi et al., 2007, Chen et al., 2007) or within (Franck et al., 2011, Maskarinec et al., 2009, Legant et al., 2010, Khetan et al., 2013, Legant et al., 2013) compliant gels, which have large numbers of encapsulated microbeads (Sen and Kumar, 2010). By tracking the microbeads displacement (Figure 2.9-B), traction forces generated by the cells (Figure 2.9-C) can be determined using the known stiffness properties of the gel (Van Vliet et al., 2003). For tracking displacement in three dimensions, confocal images of fluorescently labelled beads must be performed (Franck et al., 2011, Maskarinec et al., 2009, Legant et al., 2010, Khetan et al., 2013, Legant et al., 2013). Previous studies have also determined traction forces for cells during substrate deformation (Krishnan et al., 2009, Chen et al., 2010, Walker et al., 2005, Das et al., 2008).

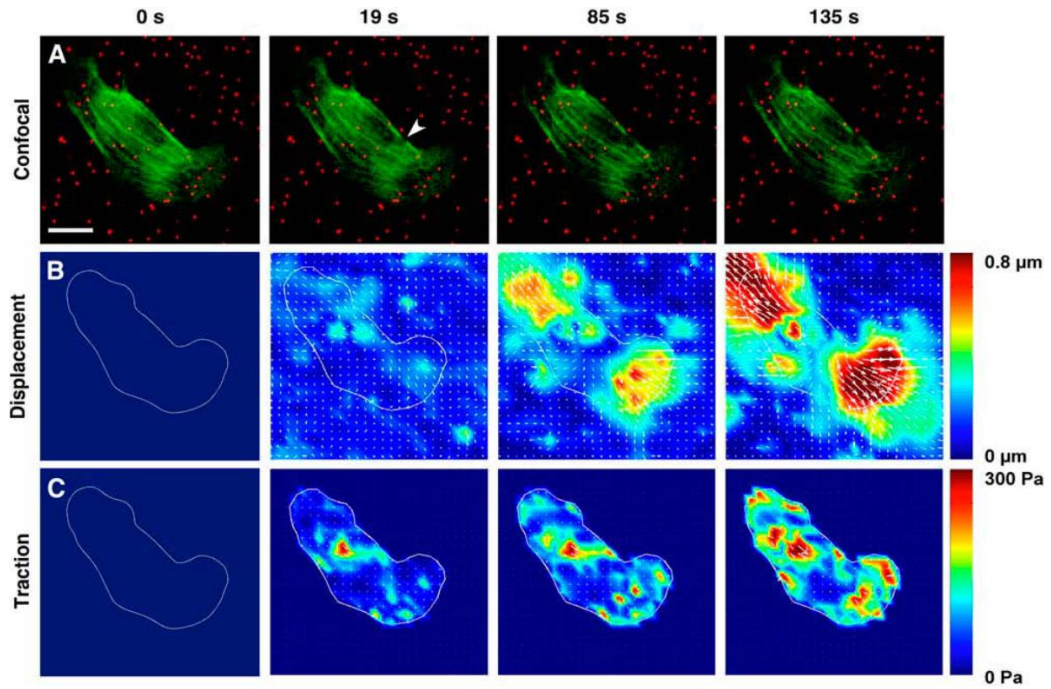


**Figure 2.9: Progression of ECM displacement and cell traction after a stress fibre is severed. (A) Cell in hydrogel with the actin cytoskeleton shown in green and fluorescent beads shown in red. Arrow head indicates point of laser ablation. (B) Contour plot of hydrogel displacement. (C) Contour plot of cell traction forces. Scale bar = 20  $\mu\text{m}$ . Adapted from Kumar et al. (2006).**

**The micropost technique** is another methodology used to measure cell traction forces. A micropost array is a group of upright micron-sized pillars, typically with an even spatial distribution (Figure 2.10-A), to which cells are seeded (Figure 2.10-B). As cells adhere to the microposts the tip becomes deflected (Figure 2.10-C). Using cantilever beam theory the traction force exerted by the cell is determined by measuring the deflection of the tip of each micropost and the following equation:

$$F = \left( \frac{3ED^4}{64L^3} \right) \delta \quad (2.6)$$

where  $E$  is the Young's modulus of the micropost material,  $D$  is the micropost diameter,  $L$  is the length of the micropost, and  $\delta$  is the measured horizontal deflection of the micropost (Schoen et al., 2010). Micropost arrays have been used to investigate cell spreading (Chen et al., 2003, Lemmon et al., 2005), migration

(du Roure et al., 2005) (Sochol et al., 2011) (Ricart et al., 2011), contractility (Rodriguez et al., 2011, Kural and Billiar, 2014, Tan et al., 2003), focal adhesion strength (Fu et al., 2010), and cadherin junction tractions (Ganz et al., 2006, Liu et al., 2010). More recently, studies have investigated cell traction forces during substrate deformation using a silicone-based stretchable micropost arrays (Lam et al., 2012a, Mann et al., 2012). Lam et al. (2012a) seeded single cells on deformable micropost arrays. By tracking the post deflection during stretching the cell stiffness could be approximated. Lam et al. (2012a) reported that cells treated with agents to disrupt the actin cytoskeleton had significantly reduced stiffness properties compared to that of untreated cells.

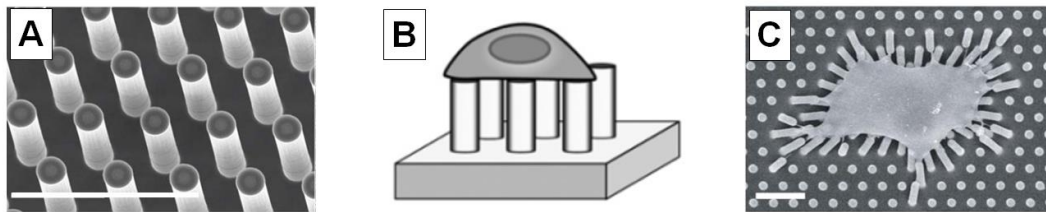


**Figure 2.10: (A) SEM image of micropost array. (B) Schematic of micropost array with a cell seeded on top. (C) SEM image of cell seeded on micropost array with microposts deformed (adapted from Lam et al. (2012b)). Scale bars = 10  $\mu\text{m}$ .**

### 2.3.2 Mechanical testing of cell populations in 2D

In addition to mechanical testing of single cells, a large body of work has been reported in the literature on the testing of cell populations, both in 2D and in 3D. In 2D, individual cells and cell monolayers are seeded on stretchable substrates such as silicone. Substrate stretching involves imposing monotonic or cyclic strain to the cell substrate, typically using a vacuum pump or indenter. Substrates are subjected to stretching in one direction (uniaxial) or in two directions (biaxial). Applied mechanical substrate stretch has been used to investigate cytoskeletal fluidization and resolidification or reinforcement (Krishnan et al., 2008, Krishnan et al., 2009, Chen et al., 2010), actin reorganisation (Chen et al., 2010, DiPaolo et

al., 2010, Kang et al., 2011), ECM protein recruitment and reorganisation (Steward et al., 2011), action potential signalling (Lin et al., 2009), genetic activity (Diederichs et al., 2010), and cell motility (Katsumi et al., 2002). It has been well established that cyclic stretch will change cell morphology and actin cytoskeletal polarisation to the direction of minimal substrate stretch (Kaunas et al., 2005, Barron et al., 2007, Wang et al., 2001b, Neidlinger-Wilke et al., 2001), as demonstrated in Figure 2.11. This polarisation effect has been shown to be strain magnitude (Wang et al., 2015) and strain rate dependant (Lee et al., 2010, Hsu et al., 2010). It should be noted that in these investigations of cell and cytoskeletal re-alignment, forces exerted by the cells have not been measured.

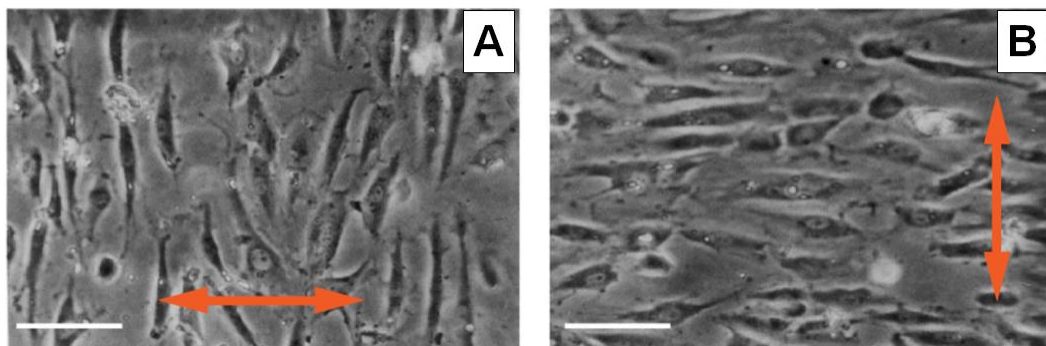


**Figure 2.11: Microscope image of cell orientation after pure uniaxial cyclic substrate stretching in the (A) horizontal direction and in the (B) vertical direction. Arrows indicate stretch direction. Cells reorient parallel to the stretch direction. Scale bars = 100  $\mu\text{m}$ . Adapter from (Wang et al., 2001a).**

### 2.3.2 Cells in 3D

A growing interest in investigating the mechanical response of cells seeded in 3D culture has emerged recently because (i) significantly different behaviour has been observed compared to 2D mechanical testing and (ii) 3D is more representative of physiological conditions. Natural 3D hydrogels such as collagen, fibrin, hyaluronic acid, matrigel, chitosan, and alginate, or non-natural polymer based hydrogels, represent a more physiological environment for cells compared to

2D substrates (Tibbitt and Anseth, 2009). The stiffness of hydrogels can be varied by adjusting the quantity of the coagulating component (Byfield et al., 2009, Legant et al., 2009, Cummings et al., 2004, Wang et al., 2013). Similar to 2D monolayers, cells project filopodia and lamellipodia in 3D culture (Tibbitt and Anseth, 2009). However, unlike 2D monolayers, in 3D culture these processes can penetrate the hydrogel in any direction (Knight and Przyborski, 2014, Legant et al., 2010). Consequently, cytoskeletal behaviour leads to hydrogel contraction or “shrinking” during cell seeding (Kraning-Rush et al., 2011, Wille et al., 2006, Notbohm et al., 2015, West et al., 2013, van Vlimmeren et al., 2012), as shown in Figure 2.12. It should be noted that the time for hydrogel contraction to reach an equilibrium state is in the order of days (Wille et al., 2006, Seliktar et al., 2000, West et al., 2013, Kural and Billiar, 2014, Wang et al., 2013). Previous studies have investigated stress fibre alignment in hydrogels where contraction is prevented in specific directions. If deformation is prevented in a single direction (uniaxial), gel contraction occurs in the laterally and cells polarise between the rigid constrains (Kural and Billiar, 2014, West et al., 2013, Zhao et al., 2013, Legant et al., 2009, Delvoeye et al., 1991, Foolen et al., 2012, Lee et al., 2008, Wang et al., 2013, Wagenseil et al., 2004). In contrast to uniaxially constrained hydrogels, stress fibres in biaxially constraint hydrogels are randomly distributed between the rigid boundaries (Foolen et al., 2014, Thavandiran et al., 2013, Foolen et al., 2012). Further to investigating alignment, the contractile behaviour of engineered cell laden hydrogels has been previously quantified using micropillars. The predetermined mechanical properties of the micropillars can be used to quantify the contractile force exerted by the hydrogel (Legant et al., 2009) and, subsequently, the individual cells (Kural and Billiar, 2014, West et al., 2013). A significantly

reduced level of contractility has been demonstrated in hydrogels cultured in media containing agents to disrupt the actin cytoskeleton, compared to untreated samples (van Vlimmeren et al., 2012, Kraning-Rush et al., 2011, Zhao et al., 2013, West et al., 2013, Legant et al., 2009). It should be noted that in the aforementioned studies, substrate deformation occurred due to active cell contractility, and not due to applied external loading.

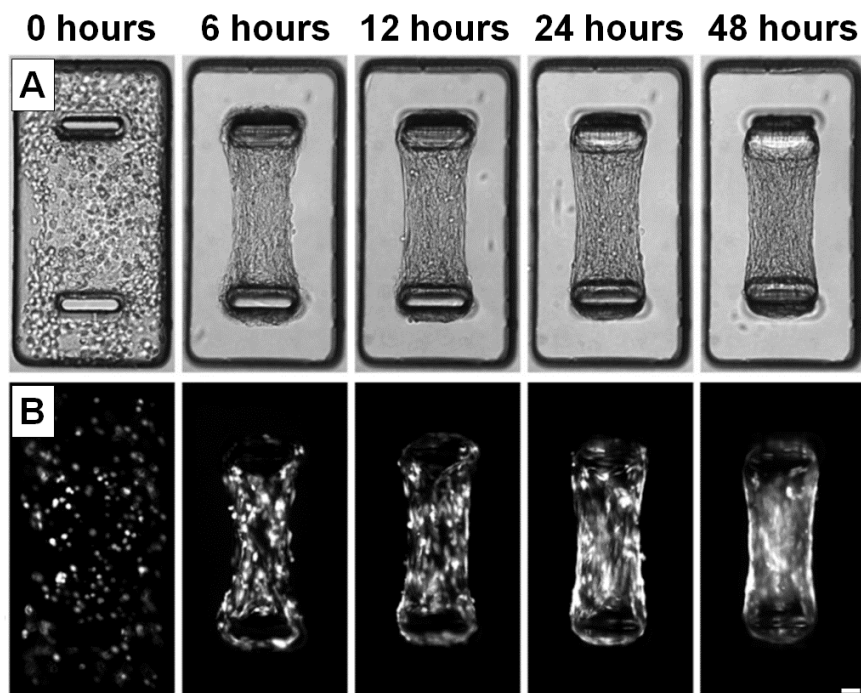


**Figure 2.12: (A) Brightfield and (B) fluorescent images of a hydrogel construct with uniaxial constraints during cell seeding. Whole cells are labelled with green fluorescent protein (GFP) to obtain images shown in (B). Scale bar = 50 $\mu$ m. Adapted from West et al. (2013)**

A number of investigations have applied external uniaxial stretch to hydrogels and monitored various cell responses (Campbell et al., 2007, Gabbay et al., 2006, Foolen et al., 2014, Foolen et al., 2012). The stretch avoidance typically observed for cells in 2D has also been reported in 3D cultures (Foolen et al., 2014). However, it has been more prominently reported that cells align parallel to the direction of stretching in 3D culture (Wille et al., 2006, Foolen et al., 2012, Wakatsuki and Elson, 2002, Zhao et al., 2013, Lee et al., 2008, Nieponice et al.,

2007, Gauvin et al., 2011). Further investigation is required to fully understand this response. Mechanical characterisation of cell laden hydrogels has been performed previously by monotonic or cyclic stretching (Berry et al., 2003, Seliktar et al., 2000, Wagenseil et al., 2003). Advancing on such investigations, active cell force generation during applied stretch was parsed by straining hydrogels following treatment to remove the actin cytoskeleton contribution (Wille et al., 2006, Zhao et al., 2013, Zhao et al., 2014, Wagenseil et al., 2004, Wakatsuki et al., 2000, Wakatsuki et al., 2001). Gels treated to remove the actin cytoskeleton provide lower resistance to deformation in all cases. It should be noted that these studies are limited to uniaxial stretching of the construct. Wagenseil et al. (2004) developed a system which investigated hydrogel vessels using a “pressure-diameter, force-length” test system. Vessels were either inflated to set diameters, or axially deformed, while the internal pressure, axial force, and vessel diameter and length were measured. However, in the study by Wagenseil et al. (2004) hydrogel vessels were fabricated on rigid mandrels and, hence, cells could only be engineered to have circumferential or axial alignment in the vessel. Furthermore, the application of internal pressure and axial deformation was performed in a mutually exclusive manner.

## **2.4 Computational modelling of cell mechanics**

In order to interpret experimental data, a range of computational models for cells have been developed. In this section, a background of relevant models developed to interpret experimental results is given.

### 2.4.1 Passive cell models

Previous studies have used simplified analytical or numerical models to interpret experimentally observed results (Sato et al., 1990, Theret et al., 1988, Jones et al., 1999, Sato et al., 1996, Byfield et al., 2004, Baaijens et al., 2005, Trickey et al., 2006, Jafari Bidhendi and Korhonen, 2012, Zhou et al., 2005, Zhao et al., 2009, Haider and Guilak, 2002, Haider and Guilak, 2000, Leipzig and Athanasiou, 2005, Shieh and Athanasiou, 2006, Koay et al., 2003, Trickey et al., 2000, Guilak et al., 2002, Schmid-Schonbein et al., 1981). These models treat the cell as a passive homogeneous continuum, typically assuming passive constitutive laws that were originally developed for other applications. Furthermore, passive models do not consider the active remodelling of the cell cytoskeletal components and active tension generation of stress fibres. Such constitutive laws include linear-elastic, hyperelastic, viscoelastic, or biphasic formulations. While these models are beneficial for shedding light on certain experimentally observed trends (Trickey et al., 2000), their inadequacy for correctly interpreting cell mechanical response has been demonstrated in numerous previous studies. McGarry and McHugh (2008) demonstrated that if a viscoelastic material model is used for the cytoplasm, stiffness must be artificially altered as a function of spreading in order to capture experimentally observed cell detachment forces. Thoumine et al. (1999) demonstrated that elastic stiffness and viscosity must be significantly altered as a function of the level of cell spreading. Dowling et al. (2012) demonstrated that if the cell is assumed as a hyperelastic solid, the model is not capable of capturing experimentally observed shear force-indentation data. Similar deficiencies in viscoelastic models of spread cells was demonstrated through simulation of parallel plate compression experiments (McGarry, 2009).

In an effort to advance upon the assumption of simple linear elastic or viscoelastic cells, an architectural system of compression-bearing rigid struts and tension-bearing elastic threads in tension have been developed (Figure 2.13), known as the tensegrity model (Ingber, 1993, Ingber, 2003). Compressive elements are claimed to represent microtubules, whereas tensional elements represent stress fibres, actin filaments, and intermediate filaments (Wang et al., 2001c, Ingber, 2003, Brangwynne et al., 2006, Kumar et al., 2006). In previous studies, the tensegrity model required manual allocation of load bearing elements and is often guided by experimental observation of cytoskeletal components. Therefore, a new fibre network must be generated for each cell geometry considered (McGarry and Prendergast, 2004). Furthermore, the tensegrity model assumes stress fibres are supported by microtubules. However, experimental results have shown that microtubule disruption leads to an increase in traction force (Kolodney and Elson, 1995).

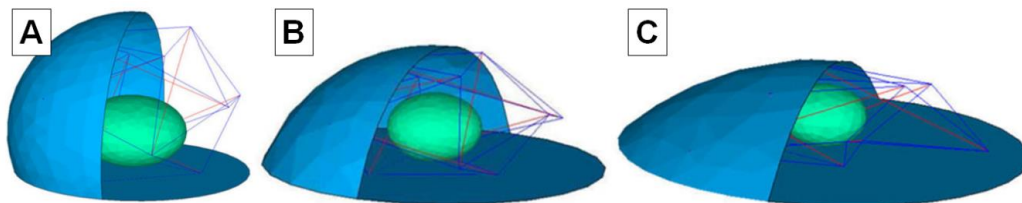


**Figure 2.13:** Tensegrity model as used in (A) rounded cells, (B) partly spread cells and (C) fully spread cells. Each model has a membrane, nucleus, cytoplasm, and cytoskeleton. Red bars represent microtubules and blue bars represent microfilaments. Adapted from McGarry and Prendergast (2004).

#### 2.4.2 Active cell models

In an effort to explain the mechanisms underlying reorientation of cells on 2D substrates subjected to cyclic stretching, Kaunas and Hsu (2009) proposed a model that describes the kinematics of stress fibre remodelling. In this model, fibres are initially randomly distributed throughout the cell and, therefore, “homeostatic”

under static conditions. A 10% pre-strain is also imposed on fibres to mimic cell contractility. Fibres dissociation occurs if the pre-strain is reduced or the fibres are excessively stretched, and these dissociated fibres immediately reform in a random orientation to maintain a constant mass fraction of stress fibres. Simulations provided an accurate prediction of experimental stress fibre orientation redistribution during cyclic deformation. More recently, the model has been improved to include strain dependence of stress fibres tension (Kaunas et al., 2011) and strain rate dependence of fibre dissociation (Kaunas and Deguchi, 2011). Further modifications were made such that fibre dissociation is dependent on sliding velocity in order to investigate the effect of cyclic stretch waveform on fibre orientation (Tondon et al., 2012), as shown in Figure 2.14.

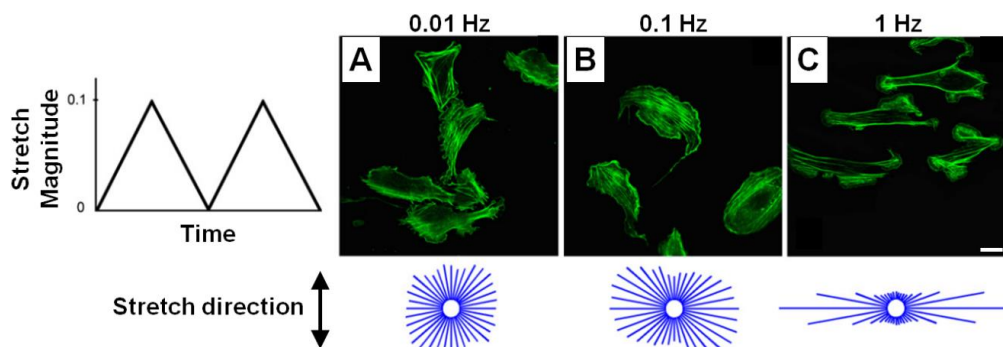


**Figure 2.14:** Kaunas and Hsu (2009) model used to predicted stress fibre orientation distribution during cyclic saw tooth stretch at frequencies of (A) 0.01 Hz, (B) 0.1 Hz, and (C) 1 Hz. Predictions are the blue polar plots below the fluorescent images of the actin cytoskeleton. Scale bar = 25  $\mu\text{m}$ . Adapted from Tondon et al. (2012).

Vernerey and Farsad (2011) developed a multiphasic model based on key cellular mechanical behaviours; (i) actin monomer transport, (ii) cytosol fluid pressure, (iii) mass exchange of cytoskeletal components, and (iv) fibre contraction. In this model, fibre formation is dependent on mechanical stress in a given direction and fibre tension is a function of both strain and strain rate. In addition to stress fibre contractility, this formulation includes mass conservation, osmotic loading,

and transport phenomena. Simulations replicated the dependency of contractility on substrate stiffness and cell shape (see Figure 2.15). A follow-on investigation demonstrated the models capability to predict formation and orientation of stress fibre in cell subjected to cyclic stretch (Foucard and Vernerey, 2012).

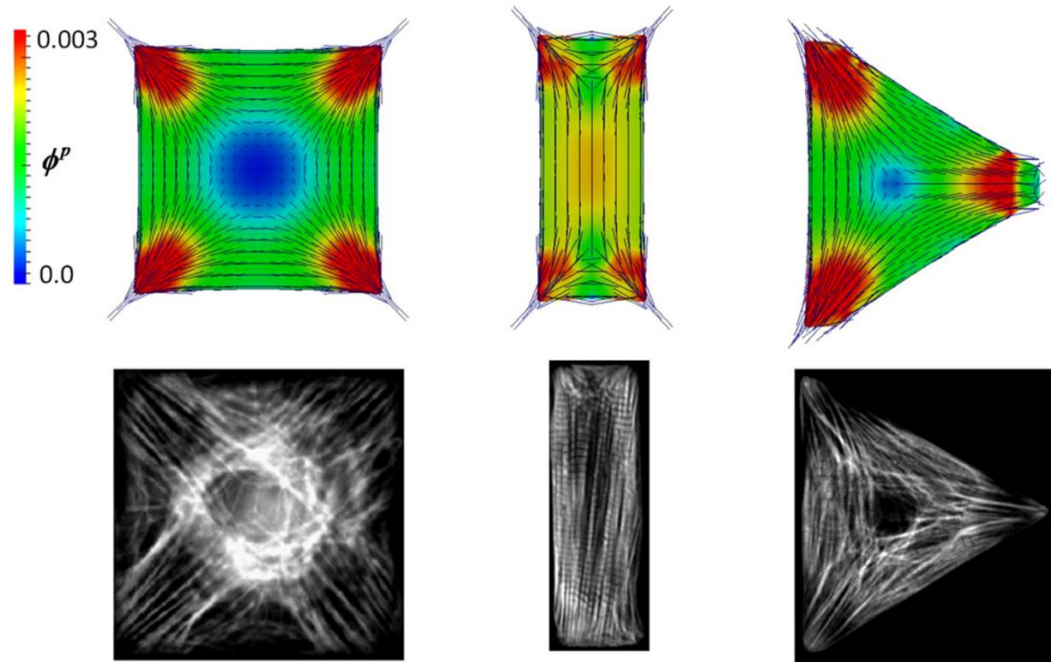


**Figure 2.15:** Prediction (upper panels) of stress fibre orientation (black vectors) and density,  $\phi^P$ , for three different cell shapes (lower panels) using the model proposed by Vernerey and Farsad. Adapted from Vernerey and Farsad (2011).

#### 2.4.2.1 Bio-chemo-mechanical model

A bio-chemo-mechanical model originally developed by Deshpande et al. (2006) considers the biochemistry surrounding; (i) stress fibre formation due to the activation of proteins and signalling molecules in the cell, such as RhoA/Ca<sup>2+</sup> (Wang et al., 2009), (ii) tension dependant stress fibre dissociation, and (iii) strain rate dependant stress fibre tension. A 2D implementation of this formulation accurately predicted the scaling of single cell force with the stiffness of micropost substrates and with cell spreading area. More recently, the 2D finite element model was developed into a full 3D setting by Ronan et al. (2012), greatly increasing the

predictive capability of framework by allowing for the simulation of a wide range of in vitro experiments, in addition to the simulation of cells in vivo/in situ (Dowling et al., 2013). The technical details surrounding the mathematical description of stress fibre behaviour and the numerical finite element implementation are presented later in this thesis in Chapters 4 and 7. In the current section of this literature review an overview of studies in which the bio-chemo-mechanical model was implemented will be presented. In particular, simulations that predicted the behaviour of single cells and cell laden hydrogels experiencing static conditions, monotonic loading, and a dynamic mechanical environment will be summarised.

*Static conditions:* In this section previous studies that implemented the bio-chemo-mechanical model to simulate the response of cells in static culture is presented. In the original study of Deshpande et al. (2006), the 2D model predicted changes in stress fibre formation for cells seeded on supports with different stiffness's, similar to experimental observations (Chen et al., 2003). In a follow on study, a single stress fibre on top of a 1D row of microposts predicted an increase of fibre traction force with increasing post stiffness (Deshpande et al., 2007). In the study of Deshpande et al. (2007), a similar trend was observed for 2D simulations of square cells which were constrained at each corner. The model therefore predicted: the development of cytoskeletal anisotropy with changes in cell shape and boundary conditions; increased fibre formation at attachment points; and enhanced stress fibre development with multiple activation signals. In a later study, McGarry et al. (2009) accurately predicted the mechanical response of cells on an array of microposts, in particular; the force exerted by cells scaling with the number of posts (Figure 2.16-A); actin distributions within the cells, including the rings of

actin around the micro-posts; the curvature of the cell boundaries between the posts; and the higher post forces towards the cell periphery. Furthermore, in the aforementioned study by McGarry et al. (2009) and another study by Weafer et al. (2013), stress fibre alignment distribution in realistic cell geometry were accurately predicted (Figure 2.16-B). In the studies of Thavandiran et al. (2013) and Legant et al. (2009), the bio-chemo-mechanical model was used to predict the response of cell laden hydrogels undergoing constrained contraction. Regions of predicted stress fibre alignment and overall hydrogel deformation were similar to experimental observations.

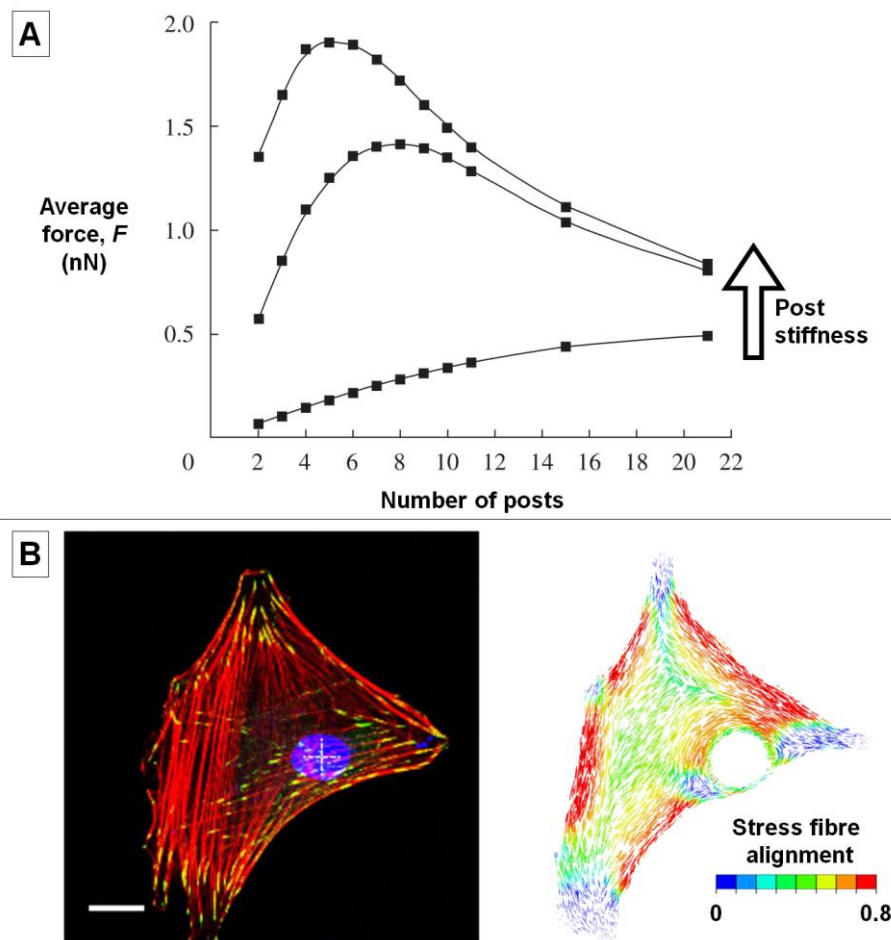


**Figure 2.16:** (A) Predictions of the variation of the normalised average force over all posts,  $F$ , with the number of posts for three choices of post stiffness. (Adapted from McGarry et al. (2009)). (B) Experimental fluorescent images of the actin cytoskeleton and nuclei in cells (left panels). Accompanying predictions of regions of stress fibre alignment obtained using the bio-chemo-mechanical model (right panels). Scale bar = 20  $\mu\text{m}$ . Adapted from Weafer et al. (2013).

In later studies, a focal adhesion model was incorporated into the bio-chemo-mechanical model to account for the effect that cytoskeletal contractile forces have on focal adhesion complexes (Deshpande et al., 2008). In a follow on study, Pathak et al. (2008) demonstrated that the combined model provides an accurate prediction of cell stress fibre distribution and focal adhesion arrangements observed for cells seeded on substrates with V, T, Y, and U shaped micro-patterned ligand patches (They et al., 2006). It was further demonstrated that the combined model captures: focal adhesion concentrations; stress fibre distribution; cell contractility and traction force for cells on micropost arrays; and on compliant substrates (Ronan et al., 2013, Ronan et al., 2014). It should be noted that the micropost arrays and substrates used in these study ranged in stiffness. Interestingly, Ronan et al. (2014) demonstrated that the model predicts increased nucleus stress with increased substrate stiffness. Furthermore, it was also shown that the combined model predicts focal adhesion and stress fibre behaviour during spreading. Ronan et al. (2015) later modified the focal adhesion model to represent cell-cell adhesion or cadherin junctions. It was demonstrated that the modified framework could capture the experimental observations of Liu et al. (2010). In particular, the model predicted that; junction tugging forces increase with junction size; and average cell tractions are unaffected by the presence of a junction.

*Monotonic/quasi-static loading:* In this section previous studies that implemented the bio-chemo-mechanical model to interpret cell mechanical response to monotonic loading are summarised. In a key study, Dowling et al. (2012) demonstrated the important contribution of the actin cytoskeleton in the shear resistance of cells. As the shear indenter deforms the cell, a yield type force-deformation curve is observed (Figure 2.17). By simulating this behaviour using

the bio-chemo-mechanical and a 3D finite element approach, it was revealed that stress fibres at the back of the cell (indenter side) become stretched as the probe displaces into the cell. It was found that this fibre stretching, coupled with stress fibre dissociation at the front edge of the cell led to the distinctive yield-type force-deformation behaviour observed experimentally (Figure 2.17-upper curve). Furthermore, cells treated to remove the actin cytoskeleton exhibited a strain stiffening type force-deformation curve, which resembles a typical response for passive hyperelastic materials (Figure 2.17-lower curve). In a later study, Dowling and McGarry (2013) used the predictive framework to investigate the influence of cell spreading levels on cell detachment. Simulations suggested that a more highly developed contractile actin cytoskeleton increases the spread cell resistance to shear, and consequently, increases the force required initiate rupture, in line with experimental observations.

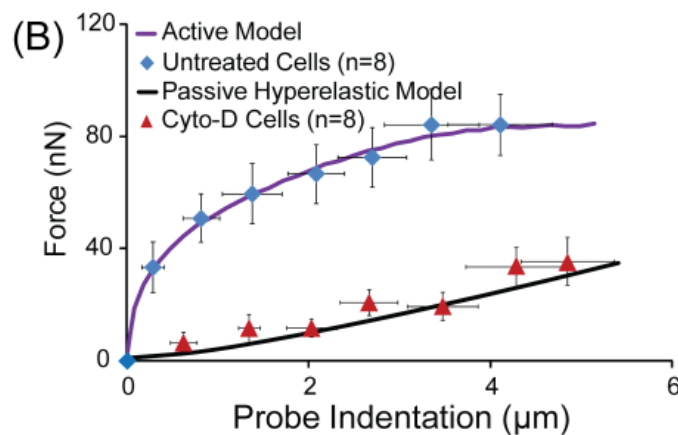


**Figure 2.17: Experimental force-indentation data for shear deformation applied to single cells. Results are shown for untreated cells and cells treated to disrupt the actin cytoskeleton using cytochalasin-D (“cyto-D Cells”). Accurate predictions of untreated cells are obtained using the bio-chemo-mechanical model discussed in the current section. A hyperelastic constitutive formulation accurately captures cyto-D cell results. Adapted from Dowling et al. (2012).**

In simulations by Ronan et al. (2012) it was demonstrated that spread cells, with a well-developed actin cytoskeleton, have a greater resistance to compression

compared to rounded cells, which were predicted to contain fewer stress fibres. Furthermore, highly contractile cell phenotypes provided an increased resistance to compression. It was revealed by Ronan et al. (2012) that as a cell undergoes unconfined compression, dominant fibres groups become stretched, generating tension and, therefore, resist the deformation. This important observation is key in explaining the experimental results of cell compression. Following from this, Weafer et al. (2013) demonstrated that cells treated with agents to disrupt the actin cytoskeleton had a significantly lower resistance to compression than untreated cells. The active bio-chemo-mechanical modelling framework successfully captured this behaviour, as well as the morphological changes observed for cells with and without an intact actin cytoskeleton.

*Dynamic load:* In this section previous studies that used the bio-chemo-mechanical framework to predict cell mechanical behaviour in response to a dynamic loading environment are presented. Wei et al. (2008) simulated cells in 2D culture to uniaxial and equi-biaxial substrate deformation to investigate the ability of the modelling framework to predict stress fibre reorientation during cyclic strain. It was demonstrated that during pure uniaxial strain, where the lateral direction is constrained, stress fibres were predicted to exhibit stretch avoidance and polarised in the direction of minimal stretch. The level of alignment was predicted to increase for higher magnitudes and frequencies of cyclic strain. For unconfined uniaxial strain, cells aligned at  $70^\circ$  to the direction of stretching, i.e. the direction undergoing the least amount of stretching. In contrast, a uniform stress fibre distribution was predicted after equi-biaxial stretching. It should be noted that these predictions are in line with experimentally observed results (Kaunas et al., 2005, Wang et al., 1995, Wang et al., 2001b, Wang et al., 2000).

Dowling et al. (2013) used a representative volume element (RVE) of cartilage tissue to investigate chondrocyte deformation and actin cytoskeleton remodelling during physiological cyclic load. The RVE consisted of an anisotropic ECM, peri-cellular matrix, and a cell. In the presence of a focal defect in the cartilage tissue, it was predicted that cyclic loading induces an altered actin cytoskeleton distribution and an increased nucleus stress compared to cartilage with no defects. Furthermore, cyclic loading caused continuous stress fibre dissociation, whereas the actin cytoskeleton of cells in monotonically deformed RVEs remained relatively intact. This study demonstrated the potential of the bio-chemo-mechanical framework to be used for simulations of in vivo conditions.

The two studies outlined above by Dowling et al. (2013) and Wei et al. (2008) focused on the prediction of stress fibre reorganisation and alignment under dynamic conditions. However, experimental data required to analyse the active force generation of single cells under dynamic loading has not previously been published. In Chapter 7 of this thesis it will be demonstrated that this bio-chemo-mechanical modelling framework provides an inaccurate prediction of transient force-deformation loops during cyclic loading using the recent experimental data of Weafer et al. (2015). A modification to the model will be presented in Chapter 7 of this thesis to overcome this shortcoming.

## **2.5 Identified deficits & thesis objectives**

Over the course of this literature review, specific deficits in the field of cell mechanics were identified and highlighted. Here the deficits are summarised and specific thesis objectives, previously outlined in Chapter 1, are identified to address them.

1. Excerpt from Section 2.2.1: “the mechanical behaviour of the nucleus has not been definitively characterised in the literature with a wide range of elastic properties being reported. A detailed and robust methodology for analysis of nucleus biomechanics would represent a considerable contribution to the field of cell mechanics.”

Objectives 2 (Provide a new understanding of stress fibres and cell mechanics) and 3 (Generate a heterogeneous model for the nucleus to correlate intra-nuclear strain with local DNA concentrations) will aim to address the deficit identified above. Specifically, in Chapter 4 an in-depth computational parametric investigation of nucleus shear and bulk moduli is conducted in order to further the understanding of nucleus mechanical behaviour. Chapter 5 details a methodology of generating a computational finite element mesh that considers the heterogeneity of the nucleus. The model is used to closely predict experimental observations of intra-nucleus deformation.

2. Excerpt from Section 2.3.1: “a fibrillous contractile actin cytoskeleton is not developed in suspended cells (Sato et al., 1987, Reinhart-King et al., 2005, Haghparast et al., 2013). In contrast, cells adhered to a substrate or ECM develop a highly structured contractile actin cytoskeleton (Munevar et al., 2001, Thoumine and Ott, 1996, Li et al., 2007, Zaleskas et al., 2004, Tan et al., 2003, Lemmon et al., 2005, Tee et al., 2011, Roy et al., 2009). Therefore, the study of un-adhered suspended cells provides limited insight into the behaviour of contractile cells.”

Objectives 1 (Develop a novel approach to micropipette aspiration to perform experiments on spread adhered cell) and 2 (Provide a new understanding of stress fibres and cell mechanics) will attempt to address the deficit identified above. Specifically, in Chapter 4 an experimental technique to perform micropipette aspiration on spread adhered cells is developed. The device is used to

investigate the important role of the actin cytoskeleton and nucleus deformation during micropipette aspiration of spread cells.

3. Excerpts from Section 2.3.2: “it has been more prominently reported that cells align parallel to the direction of stretching in 3D culture (Wille et al., 2006, Foolen et al., 2012, Wakatsuki and Elson, 2002, Zhao et al., 2013, Lee et al., 2008, Nieponice et al., 2007, Gauvin et al., 2011). Further investigation is required to fully understand this response” and “these studies are limited to uniaxial stretching of the construct.”

Objectives 2 (Provide a new understanding of stress fibres and cell mechanics) and 5 (Develop a novel experimental technique to compare the active cell mechanical behaviour under dynamic uniaxial and dynamic biaxial loading in a 3D ECM) will attempt to address the deficits identified above. Specifically, in Chapter 8 a novel experimental system for measurement of cell and tissue forces during uniaxial and biaxial stretching is developed. Furthermore, a methodology for generating aligned and un-aligned pseudo-tissues is developed and used to investigate the active and passive mechanical behaviour of these cell-collagen constructs.

4. Excerpt from Section 2.4.2.1: “The two studies outlined above by Dowling et al. (2013) and Wei et al. (2008) focused on the prediction of stress fibre reorganisation and alignment under dynamic conditions. However, experimental data required to analyse the active force generation of single cells under dynamic loading has not previously been published.”

Objectives 2 (Provide a new understanding of stress fibres and cell mechanics) and 4 (Develop a new multi-axial 3D contractility model for stress fibres to describe force generation under dynamic loading at a single cell level) will attempt to address the deficit identified above. Specifically, in Chapter 6 force-deformation data from cyclic compression experiments of single cells is presented.

Experimental results provide new characterisation of the complexity of single cell response to dynamic loading. In Chapter 7, a computational model that provides a coherent insight into the mechanics underlying the complex response of cells undergoing dynamic loading is developed.

## 2.6 References

- ADACHI, T., SATO, K., HIGASHI, N., TOMITA, Y. & HOJO, M. 2008. Simultaneous observation of calcium signaling response and membrane deformation due to localized mechanical stimulus in single osteoblast-like cells. *Journal of the Mechanical Behavior of Biomedical Materials*, 1, 43-50.
- ALBERTS, B., BRAY, D., LEWIS, J., RAFF, M., ROBERTS, K. & WATSON, J. 2002. *Molecular Biology of the Cell*, New York, Garland Publishing Inc.
- ANAPHASE, B. 2000. Microtubule motors in mitosis. *Nature*, 407, 41-47.
- BAAIJENS, F. P. T., TRICKEY, W. R., LAURSEN, T. A. & GUILAK, F. 2005. Large Deformation Finite Element Analysis of Micropipette Aspiration to Determine the Mechanical Properties of the Chondrocyte. *Ann Biomed Eng*, 33, 494-501.
- BADER, D. L. & KNIGHT, M. M. 2008. Biomechanical analysis of structural deformation in living cells. *Med Biol Eng Comput*, 46, 951-63.
- BALESTRINI, J. L. & BILLIAR, K. L. 2009. Magnitude and duration of stretch modulate fibroblast remodeling. *J Biomech Eng*, 131, 051005.
- BAO, G. & SURESH, S. 2003. Cell and molecular mechanics of biological materials. *Nat Mater*, 2, 715-725.
- BARRON, V., BROUGHAM, C., COGHLAN, K., MCLUCAS, E., O'MAHONEY, D., STENSON-COX, C. & MCHUGH, P. E. 2007. The effect of physiological cyclic stretch on the cell morphology, cell orientation and protein expression of endothelial cells. *J Mater Sci Mater Med*, 18, 1973-81.
- BAUSCH, A. R., MOLLER, W. & SACKMANN, E. 1999. Measurement of local viscoelasticity and forces in living cells by magnetic tweezers. *Biophys J*, 76, 573-9.
- BAUSCH, A. R., ZIEMANN, F., BOULBITCH, A. A., JACOBSON, K. & SACKMANN, E. 1998. Local measurements of viscoelastic parameters of adherent cell surfaces by magnetic bead microrheometry. *Biophys J*, 75, 2038-49.
- BERRY, C. C., SHELTON, J. C., BADER, D. L. & LEE, D. A. 2003. Influence of external uniaxial cyclic strain on oriented fibroblast-seeded collagen gels. *Tissue Eng*, 9, 613-24.
- BLAIN, E. J. 2009. Involvement of the cytoskeletal elements in articular cartilage homeostasis and pathology. *International journal of experimental pathology*, 90, 1-15.
- BLANCHOIN, L., BOUJEMAA-PATERSKI, R., SYKES, C. & PLASTINO, J. 2014. Actin dynamics, architecture, and mechanics in cell motility. *Physiol Rev*, 94, 235-63.
- BLOCK, S. M. 1992. Making light work with optical tweezers. *Nature*, 360, 493-5.
- BRANGWYNNE, C. P., MACKINTOSH, F. C., KUMAR, S., GEISSE, N. A., TALBOT, J., MAHADEVAN, L., PARKER, K. K., INGBER, D. E. & WEITZ, D. A. 2006. Microtubules can bear enhanced compressive loads in living cells because of lateral reinforcement. *J Cell Biol*, 173, 733-41.
- BURRIDGE, K. & WENNERBERG, K. 2004. Rho and Rac take center stage. *Cell*, 116, 167-179.

- BURRIS, S. M., SMITH, C. M., 2ND, TUKEY, D. T., CLAWSON, C. C. & WHITE, J. G. 1986. Micropipette aspiration of human platelets after exposure to aggregating agents. *Arteriosclerosis*, 6, 321-5.
- BUSCHMANN, M. D., HUNZIKER, E. B., KIM, Y. J. & GRODZINSKY, A. J. 1996. Altered aggrecan synthesis correlates with cell and nucleus structure in statically compressed cartilage. *J Cell Sci*, 109(Pt 2), 499-508.
- BUXBOIM, A., RAJAGOPAL, K., BROWN, A. E. & DISCHER, D. E. 2010. How deeply cells feel: methods for thin gels. *J Phys Condens Matter*, 22, 194116.
- BYFIELD, F. J., ARANDA-ESPINOZA, H., ROMANENKO, V. G., ROTHBLAT, G. H. & LEVITAN, I. 2004. Cholesterol depletion increases membrane stiffness of aortic endothelial cells. *Biophys J*, 87, 3336-3343.
- BYFIELD, F. J., REEN, R. K., SHENTU, T. P., LEVITAN, I. & GOOCH, K. J. 2009. Endothelial actin and cell stiffness is modulated by substrate stiffness in 2D and 3D. *J Biomech*, 42, 1114-9.
- CAILLE, N., TARDY, Y. & MEISTER, J. J. 1998. Assessment of Strain Field in Endothelial Cells Subjected to Uniaxial Deformation of Their Substrate. *Annals of Biomedical Engineering*, 26, 409-416.
- CAILLE, N., THOUMINE, O., TARDY, Y. & MEISTER, J.-J. 2002. Contribution of the nucleus to the mechanical properties of endothelial cells. *J Biomech*, 35, 177-187.
- CALIFANO, J. P. & REINHART-KING, C. A. 2010. Exogenous and endogenous force regulation of endothelial cell behavior. *Journal of Biomechanics*, 43, 79-86.
- CAMPBELL, J. J., BLAIN, E. J., CHOWDHURY, T. T. & KNIGHT, M. M. 2007. Loading alters actin dynamics and up-regulates cofilin gene expression in chondrocytes. *Biochem Biophys Res Commun*, 361, 329-334.
- CHEN, C., KRISHNAN, R., ZHOU, E., RAMACHANDRAN, A., TAMBE, D., RAJENDRAN, K., ADAM, R. M., DENG, L. & FREDBERG, J. J. 2010. Fluidization and resolidification of the human bladder smooth muscle cell in response to transient stretch. *PLoS One*, 5, e12035.
- CHEN, C. S., TAN, J. L., TIEN, J., PIRONE, D. M., GRAY, D. S. & BHADRIRAJU, K. 2003. Cells lying on a bed of microneedles: An approach to isolate mechanical force. *Proceedings of the National Academy of Sciences of the United States of America*, 100, 1484-1489.
- CHEN, J., LI, H., SUNDARRAJ, N. & WANG, J. H. 2007. Alpha-smooth muscle actin expression enhances cell traction force. *Cell Motil Cytoskeleton*, 64, 248-57.
- COLTON, R. J., BASELT, D. R., DUFRÊNE, Y. F., GREEN, J. B. D. & LEE, G. U. 1997. Scanning probe microscopy. *Current opinion in chemical biology*, 1, 370-377.
- CRICK, F. H. C. 1950. The physical properties of cytoplasm. A study by means of the magnetic particle method. Part 2. Theoretical treatment. *Exp Cell Res*, 1, 505-533.
- CRICK, F. H. C. & HUGHES, A. F. W. 1950. The physical properties of the cytoplasm. A study by means of the magnetic particle method. Part 1. *Exp Cell Res*, 1, 37-80.
- CUMMINGS, C. L., GAWLITTA, D., NEREM, R. M. & STEGEMANN, J. P. 2004. Properties of engineered vascular constructs made from collagen, fibrin, and collagen-fibrin mixtures. *Biomaterials*, 25, 3699-706.
- CURTZE, S., DEMBO, M., MIRON, M. & JONES, D. B. 2004. Dynamic changes in traction forces with DC electric field in osteoblast-like cells. *J Cell Sci*, 117, 2721-9.
- DAHL, K. N., RIBEIRO, A. J. & LAMMERDING, J. 2008. Nuclear shape, mechanics, and mechanotransduction. *Circ Res*, 102, 1307-18.
- DAO, M., LIM, C. T. & SURESH, S. 2003. Mechanics of the human red blood cell deformed by optical tweezers. *Journal of the Mechanics and Physics of Solids*, 51, 2259-2280.

- DARLING, E. M., TOPEL, M., ZAUSCHER, S., VAIL, T. P. & GUILAK, F. 2008. Viscoelastic properties of human mesenchymally-derived stem cells and primary osteoblasts, chondrocytes, and adipocytes. *J Biomech*, 41, 454-64.
- DAS, T., MAITI, T. K. & CHAKRABORTY, S. 2008. Traction force microscopy on-chip: shear deformation of fibroblast cells. *Lab Chip*, 8, 1308-18.
- DE FORGES, H., BOUISSOU, A. & PEREZ, F. 2012. Interplay between microtubule dynamics and intracellular organization. *Int J Biochem Cell Biol*, 44, 266-74.
- DE, R., ZEMEL, A. & SAFRAN, S. A. 2010. Theoretical concepts and models of cellular mechanosensing. *Methods Cell Biol*, 98, 143-75.
- DEGUCHI, S., MAEDA, K., OHASHI, T. & SATO, M. 2005. Flow-induced hardening of endothelial nucleus as an intracellular stress-bearing organelle. *J Biomech*, 38, 1751-1759.
- DEGUCHI, S., YANO, M., HASHIMOTO, K., FUKAMACHI, H., WASHIO, S. & TSUJIOKA, K. 2007. Assessment of the mechanical properties of the nucleus inside a spherical endothelial cell based on microtensile testing. *Journal of Mechanics of Materials and Structures*, 2, 1087-1102.
- DELVOYE, P., WILQUET, P., LEVEQUE, J.-L., NUSGENS, B. V. & LAPIERE, C. M. 1991. Measurement of Mechanical Forces Generated by Skin Fibroblasts Embedded in a Three-Dimensional Collagen Gel. *J Investig Dermatol*, 97, 898-902.
- DENG, L., FAIRBANK, N. J., FABRY, B., SMITH, P. G. & MAKSYM, G. N. 2004. Localized mechanical stress induces time-dependent actin cytoskeletal remodeling and stiffening in cultured airway smooth muscle cells. *Am J Physiol Cell Physiol*, 287, C440-8.
- DENG, Z., LULEVICH, V., LIU, F. T. & LIU, G. Y. 2010. Applications of atomic force microscopy in biophysical chemistry of cells. *J Phys Chem B*, 114, 5971-82.
- DESHPANDE, V. S., MCMEEKING, R. M. & EVANS, A. G. 2006. A bio-chemo-mechanical model for cell contractility. *Proceedings of the National Academy of Sciences of the United States of America*, 103, 14015-14020.
- DESHPANDE, V. S., MCMEEKING, R. M. & EVANS, A. G. 2007. A model for the contractility of the cytoskeleton including the effects of stress-fibre formation and dissociation. *Proc Math Phys Eng Sci*, 463, 787-815.
- DESHPANDE, V. S., MRKSICH, M., MCMEEKING, R. M. & EVANS, A. G. 2008. A bio-mechanical model for coupling cell contractility with focal adhesion formation. *Journal of the Mechanics and Physics of Solids*, 56, 1484-1510.
- DIEDERICHS, S., BOHM, S., PETERBAUER, A., KASPER, C., SCHEPER, T. & VAN GRIENSVEN, M. 2010. Application of different strain regimes in two-dimensional and three-dimensional adipose tissue-derived stem cell cultures induces osteogenesis: implications for bone tissue engineering. *J Biomed Mater Res A*, 94, 927-36.
- DIPAULO, B. C., LENORMAND, G., FREDBERG, J. J. & MARGULIES, S. S. 2010. Stretch magnitude and frequency-dependent actin cytoskeleton remodeling in alveolar epithelia. *Am J Physiol Cell Physiol*, 299, C345-53.
- DOWLING, E. P. & MCGARRY, J. P. 2013. Influence of Spreading and Contractility on Cell Detachment. *Ann Biomed Eng*.
- DOWLING, E. P., RONAN, W. & MCGARRY, J. P. 2013. Computational investigation of in situ chondrocyte deformation and actin cytoskeleton remodelling under physiological loading. *Acta Biomater*, 9, 5943-55.
- DOWLING, E. P., RONAN, W., OFEK, G., DESHPANDE, V. S., MCMEEKING, R. M., ATHANASIOU, K. A. & MCGARRY, J. P. 2012. The effect of remodelling and contractility of the actin cytoskeleton on the shear resistance of single cells: a computational and experimental investigation. *J R Soc Interface*, 9, 3469-79.

- DOYLE, A. D. & LEE, J. 2005. Cyclic changes in keratocyte speed and traction stress arise from Ca<sup>2+</sup>-dependent regulation of cell adhesiveness. *J Cell Sci*, 118, 369-79.
- DU ROURE, O., SAEZ, A., BUGUIN, A., AUSTIN, R. H., CHAVRIER, P., SILBERZAN, P. & LADOUX, B. 2005. Force mapping in epithelial cell migration. *Proc Natl Acad Sci U S A*, 102, 2390-5.
- DUPIN, I., SAKAMOTO, Y. & ETIENNE-MANNEVILLE, S. 2011. Cytoplasmic intermediate filaments mediate actin-driven positioning of the nucleus. *J Cell Sci*, 124, 865-72.
- DURRANT, L. A., ARCHER, C. W., BENJAMIN, M. & RALPHS, J. R. 1999. Organisation of the chondrocyte cytoskeleton and its response to changing mechanical conditions in organ culture. *J Anat*, 194 ( Pt 3), 343-53.
- ERIKSSON, J. E., DECHAT, T., GRIN, B., HELFAND, B., MENDEZ, M., PALLARI, H. M. & GOLDMAN, R. D. 2009. Introducing intermediate filaments: from discovery to disease. *J Clin Invest*, 119, 1763-71.
- ETHIER, C. R. & SIMMONS, C. A. 2007. *Introductory biomechanics: from cells to organisms*, Cambridge University Press.
- EVANS, E. & YEUNG, A. 1989. Apparent viscosity and cortical tension of blood granulocytes determined by micropipet aspiration. *Biophys J*, 56, 151-60.
- EVANS, E. A. 1973. New Membrane Concept Applied to the Analysis of Fluid Shear- and Micropipette-Deformed Red Blood Cells. *Biophysical journal*, 13, 941-954.
- FABRY, B., MAKSYM, G. N., SHORE, S. A., MOORE, P. E., PANETTIERI, R. A., JR., BUTLER, J. P. & FREDBERG, J. J. 2001. Selected contribution: time course and heterogeneity of contractile responses in cultured human airway smooth muscle cells. *J Appl Physiol*, 91, 986-94.
- FAZAL, F. M. & BLOCK, S. M. 2011. Optical tweezers study life under tension. *Nat Photonics*, 5, 318-321.
- FERKO, M. C., BHATNAGAR, A., GARCIA, M. B. & BUTLER, P. J. 2007. Finite-element stress analysis of a multicomponent model of sheared and focally-adhered endothelial cells. *Ann Biomed Eng*, 35, 208-23.
- FERNANDEZ, P., PULLARKAT, P. A. & OTT, A. 2006. A master relation defines the nonlinear viscoelasticity of single fibroblasts. *Biophys J*, 90, 3796-805.
- FLETCHER, D. A. & MULLINS, R. D. 2010. Cell mechanics and the cytoskeleton. *Nature*, 463, 485-92.
- FOOLEN, J., DESHPANDE, V. S., KANTERS, F. M. & BAAIJENS, F. P. 2012. The influence of matrix integrity on stress-fiber remodeling in 3D. *Biomaterials*, 33, 7508-18.
- FOOLEN, J., JANSSEN-VAN DEN BROEK, M. W. & BAAIJENS, F. P. 2014. Synergy between Rho signaling and matrix density in cyclic stretch-induced stress fiber organization. *Acta Biomater*, 10, 1876-85.
- FOUCARD, L. & VERNEREY, F. J. 2012. A thermodynamical model for stress-fiber organization in contractile cells. *Applied Physics Letters*, 100.
- FRANCK, C., MASKARINEC, S. A., TIRRELL, D. A. & RAVICHANDRAN, G. 2011. Three-dimensional traction force microscopy: a new tool for quantifying cell-matrix interactions. *PLoS One*, 6, e17833.
- FU, J., WANG, Y. K., YANG, M. T., DESAI, R. A., YU, X., LIU, Z. & CHEN, C. S. 2010. Mechanical regulation of cell function with geometrically modulated elastomeric substrates. *Nat Methods*, 7, 733-6.
- FUCHS, E. & WEBER, K. 1994. Intermediate filaments: structure, dynamics, function, and disease. *Annu Rev Biochem*, 63, 345-82.
- GABBAY, J. S., ZUK, P. A., TAHERNIA, A., ASKARI, M., O'HARA, C. M., KARTHIKEYAN, T., AZARI, K., HOLLINGER, J. O. & BRADLEY, J. P. 2006. In vitro microdistraction of preosteoblasts: distraction promotes proliferation and oscillation promotes differentiation. *Tissue Eng*, 12, 3055-65.

- GANZ, A., LAMBERT, M., SAEZ, A., SILBERZAN, P., BUGUIN, A., MEGE, R. M. & LADOUX, B. 2006. Traction forces exerted through N-cadherin contacts. *Biology of the Cell*, 98, 721-730.
- GAUVIN, R., PARENTEAU-BAREIL, R., LAROUCHE, D., MARCOUX, H., BISSON, F., BONNET, A., AUGER, F. A., BOLDUC, S. & GERMAIN, L. 2011. Dynamic mechanical stimulations induce anisotropy and improve the tensile properties of engineered tissues produced without exogenous scaffolding. *Acta Biomater*, 7, 3294-301.
- GIRARD, P. P., CAVALCANTI-ADAM, E. A., KEMKEMER, R. & SPATZ, J. P. 2007. Cellular chemomechanics at interfaces: sensing, integration and response. *Soft Matter*, 3, 307-326.
- GITTES, F., MICKEY, B., NETTLETON, J. & HOWARD, J. 1993. Flexural rigidity of microtubules and actin filaments measured from thermal fluctuations in shape. *J Cell Biol*, 120, 923-34.
- GOLEY, E. D. & WELCH, M. D. 2006. The ARP2/3 complex: an actin nucleator comes of age. *Nat Rev Mol Cell Biol*, 7, 713-26.
- GUILAK, F. 1995. Compression-induced changes in the shape and volume of the chondrocyte nucleus. *Journal of Biomechanics*, 28, 1529-1541.
- GUILAK, F., ERICKSON, G. R. & TING-BEALL, H. P. 2002. The effects of osmotic stress on the viscoelastic and physical properties of articular chondrocytes. *Biophys J*, 82, 720-7.
- GUILAK, F., JONES, W. R., TING-BEALL, H. P. & LEE, G. M. 1999. The deformation behavior and mechanical properties of chondrocytes in articular cartilage. *Osteoarthritis Cartilage*, 7, 59-70.
- GUILAK, F., TEDROW, J. R. & BURBKART, R. 2000. Viscoelastic properties of the cell nucleus. *Biochem Biophys Res Commun*, 269, 781-786.
- HAGA, J. H., BEAUDOIN, A. J., WHITE, J. G. & STRONG, J. 1998. Quantification of the passive mechanical properties of the resting platelet. *Ann Biomed Eng*, 26, 268-77.
- HAGHPARAST, S. M. A., KIHARA, T., SHIMIZU, Y., YUBA, S. & MIYAKE, J. 2013. Actin-based biomechanical features of suspended normal and cancer cells. *J Biosci Bioeng*, 116, 380-385.
- HAIDER, M. A. & GUILAK, F. 2000. An axisymmetric boundary integral model for incompressible linear viscoelasticity: application to the micropipette aspiration contact problem. *J Biomech Eng*, 122, 236-244.
- HAIDER, M. A. & GUILAK, F. 2002. An axisymmetric boundary integral model for assessing elastic cell properties in the micropipette aspiration contact problem. *J Biomech Eng*, 124, 586-95.
- HANSMA, H. G., KASUYA, K. & OROUDJEV, E. 2004. Atomic force microscopy imaging and pulling of nucleic acids. *Curr Opin Struct Biol*, 14, 380-5.
- HARRIS, A. R., PETER, L., BELLIS, J., BAUM, B., KABLA, A. J. & CHARRAS, G. T. 2012. Characterizing the mechanics of cultured cell monolayers. *Proceedings of the National Academy of Sciences*, 109, 16449-16454.
- HENDERSON, J. T., SHANNON, G., VERESS, A. I. & NEU, C. P. 2013. Direct measurement of intranuclear strain distributions and RNA synthesis in single cells embedded within native tissue. *Biophys J*, 105, 2252-2261.
- HENON, S., LENORMAND, G., RICHERT, A. & GALLET, F. 1999. A new determination of the shear modulus of the human erythrocyte membrane using optical tweezers. *Biophysical Journal*, 76, 1145-1151.
- HERANT, M., HEINRICH, V. & DEMBO, M. 2005. Mechanics of neutrophil phagocytosis: behavior of the cortical tension. *J Cell Sci*, 118, 1789-97.

- HERRMANN, H., BAR, H., KREPLAK, L., STRELKOV, S. V. & AEBI, U. 2007. Intermediate filaments: from cell architecture to nanomechanics. *Nat Rev Mol Cell Biol*, 8, 562-73.
- HILL, A. V. 1938. The Heat of Shortening and the Dynamic Constants of Muscle. *Philos Trans R Soc Lond B Biol Sci*, 126, 136-195.
- HILLAM, R. A. & SKERRY, T. M. 1995. Inhibition of bone resorption and stimulation of formation by mechanical loading of the modeling rat ulna in vivo. *Journal of Bone and Mineral Research*, 10, 683-689.
- HIRANO, Y., TAKAHASHI, H., KUMETA, M., HIZUME, K., HIRAI, Y., OTSUKA, S., YOSHIMURA, S. H. & TAKEYASU, K. 2008. Nuclear architecture and chromatin dynamics revealed by atomic force microscopy in combination with biochemistry and cell biology. *Pflugers Arch*, 456, 139-53.
- HIROKAWA, N. 1998. Kinesin and dynein superfamily proteins and the mechanism of organelle transport. *Science*, 279, 519-26.
- HOCHMUTH, R. M. 1993. Measuring the mechanical properties of individual human blood cells. *J Biomech Eng*, 115, 515-9.
- HOFMANN, U. G., ROTSCH, C., PARAK, W. J. & RADMACHER, M. 1997. Investigating the cytoskeleton of chicken cardiocytes with the atomic force microscope. *J Struct Biol*, 119, 84-91.
- HSIEH, Y. F. & TURNER, C. H. 2001. Effects of loading frequency on mechanically induced bone formation. *Journal of Bone and Mineral Research*, 16, 918-924.
- HSU, H. J., LEE, C. F., LOCKE, A., VANDERZYL, S. Q. & KAUNAS, R. 2010. Stretch-Induced Stress Fiber Remodeling and the Activations of JNK and ERK Depend on Mechanical Strain Rate, but Not FAK. *PLoS One*, 5.
- HU, S., CHEN, J., FABRY, B., NUMAGUCHI, Y., GOULDSTONE, A., INGBER, D. E., FREDBERG, J. J., BUTLER, J. P. & WANG, N. 2003. Intracellular stress tomography reveals stress focusing and structural anisotropy in cytoskeleton of living cells. *Am J Physiol Cell Physiol*, 285, C1082-90.
- HU, S., EBERHARD, L., CHEN, J., LOVE, J. C., BUTLER, J. P., FREDBERG, J. J., WHITESIDES, G. M. & WANG, N. 2004. Mechanical anisotropy of adherent cells probed by a three-dimensional magnetic twisting device. *Am J Physiol Cell Physiol*, 287, C1184-91.
- INGBER, D. E. 1993. Cellular Tensegrity - Defining New Rules of Biological Design That Govern the Cytoskeleton. *Journal of Cell Science*, 104, 613-627.
- INGBER, D. E. 1997. Tensegrity: The architectural basis of cellular mechanotransduction. *Annual Review of Physiology*, 59, 575-599.
- INGBER, D. E. 2003. Tensegrity I. Cell structure and hierarchical systems biology. *Journal of Cell Science*, 116, 1157-1173.
- IWADATE, Y. & YUMURA, S. 2008. Actin-based propulsive forces and myosin-II-based contractile forces in migrating Dictyostelium cells. *J Cell Sci*, 121, 1314-24.
- JAASMA, M. J., JACKSON, W. M. & KEAVENY, T. M. 2006. Measurement and characterization of whole-cell mechanical behavior. *Annals of biomedical engineering*, 34, 748-758.
- JAASMA, M. J., JACKSON, W. M., TANG, R. Y. & KEAVENY, T. M. 2007. Adaptation of cellular mechanical behavior to mechanical loading for osteoblastic cells. *Journal of Biomechanics*, 40, 1938-1945.
- JAFARI BIDHENDI, A. & KORHONEN, R. K. 2012. A Finite Element Study of Micropipette Aspiration of Single Cells: Effect of Compressibility. *Comput Math Method M*, 2012, 192618.
- JEAN, R. P., CHEN, C. S. & SPECTOR, A. A. 2005. Finite-element analysis of the adhesion-cytoskeleton-nucleus mechanotransduction pathway during endothelial cell rounding: axisymmetric model. *J Biomech Eng*, 127, 594-600.

- JOHNSON, K. 1985. *Contact Mechanics*, Cambridge University Press,.
- JONAS, M., SO, P. T. & HUANG, H. 2008. Cell mechanics at multiple scales. *Methods Enzymol*, 443, 177-98.
- JONES, W. R., PING TING-BEALL, H., LEE, G. M., KELLEY, S. S., HOCHMUTH, R. M. & GUILAK, F. 1999. Alterations in the Young's modulus and volumetric properties of chondrocytes isolated from normal and osteoarthritic human cartilage. *J Biomech*, 32, 119-127.
- JORTIKKA, M. O., PARKKINEN, J. J., INKINEN, R. I., KARNER, J., JARVELAINEN, H. T., NELIMARKKA, L. O., TAMMI, M. I. & LAMMI, M. J. 2000. The role of microtubules in the regulation of proteoglycan synthesis in chondrocytes under hydrostatic pressure. *Arch Biochem Biophys*, 374, 172-80.
- KANG, J., STEWARD, R. L., KIM, Y., SCHWARTZ, R. S., LEDUC, P. R. & PUSKAR, K. M. 2011. Response of an actin filament network model under cyclic stretching through a coarse grained Monte Carlo approach. *J Theor Biol*, 274, 109-19.
- KATSUMI, A., MILANINI, J., KIOSSES, W. B., DEL POZO, M. A., KAUNAS, R., CHIEN, S., HAHN, K. M. & SCHWARTZ, M. A. 2002. Effects of cell tension on the small GTPase Rac. *J Cell Biol*, 158, 153-64.
- KAUNAS, R. & DEGUCHI, S. 2011. Multiple Roles for Myosin II in Tensional Homeostasis Under Mechanical Loading. *Cellular and Molecular Bioengineering*, 4, 182-191.
- KAUNAS, R., HSU, H.-J. & DEGUCHI, S. 2011. Sarcomeric model of stretch-induced stress fiber reorganization. *Cell Health and Cytoskeleton*, 3.
- KAUNAS, R. & HSU, H. J. 2009. A kinematic model of stretch-induced stress fiber turnover and reorientation. *J Theor Biol*, 257, 320-30.
- KAUNAS, R., NGUYEN, P., USAMI, S. & CHIEN, S. 2005. Cooperative effects of Rho and mechanical stretch on stress fiber organization. *Proceedings of the National Academy of Sciences of the United States of America*, 102, 15895-15900.
- KELLY, G. M., KILPATRICK, J. I., VAN ES, M. H., WEAFFER, P. P., PRENDERGAST, P. J. & JARVIS, S. P. 2011. Bone cell elasticity and morphology changes during the cell cycle. *J Biomech.*, 44, 1484-1490.
- KHETAN, S., GUVENDIREN, M., LEGANT, W. R., COHEN, D. M., CHEN, C. S. & BURDICK, J. A. 2013. Degradation-mediated cellular traction directs stem cell fate in covalently crosslinked three-dimensional hydrogels. *Nat Mater*, 12, 458-65.
- KNIGHT, E. & PRZYBORSKI, S. 2014. Advances in 3D cell culture technologies enabling tissue-like structures to be created in vitro. *J Anat*.
- KNIGHT, M. M., VAN DE BREEVAART BRAVENBOER, J., LEE, D. A., VAN OSCH, G. J. V. M., WEINANS, H. & BADER, D. L. 2002. Cell and nucleus deformation in compressed chondrocyte-alginate constructs: temporal changes and calculation of cell modulus. *Biochimica et Biophysica Acta (BBA) - General Subjects*, 1570, 1-8.
- KOAY, E. J., SHIEH, A. C. & ATHANASIOU, K. A. 2003. Creep indentation of single cells. *J Biomech Eng*, 125, 334-41.
- KOLODNEY, M. S. & ELSON, E. L. 1995. Contraction due to microtubule disruption is associated with increased phosphorylation of myosin regulatory light chain. *Proc Natl Acad Sci U S A*, 92, 10252-6.
- KRANING-RUSH, C. M., CAREY, S. P., CALIFANO, J. P., SMITH, B. N. & REINHART-KING, C. A. 2011. The role of the cytoskeleton in cellular force generation in 2D and 3D environments. *Phys Biol*, 8, 015009.
- KRISHNAN, R., PARK, C. Y., LIN, Y. C., MEAD, J., JASPERS, R. T., TREPAT, X., LENORMAND, G., TAMBE, D., SMOLENSKY, A. V. & KNOLL, A. H. 2009. Reinforcement versus fluidization in cytoskeletal mechanoresponsiveness. *PLoS One*, 4, e5486.

- KRISHNAN, R., TREPAT, X., NGUYEN, T. T., LENORMAND, G., OLIVER, M. & FREDBERG, J. J. 2008. Airway smooth muscle and bronchospasm: fluctuating, fluidizing, freezing. *Respir Physiol Neurobiol*, 163, 17-24.
- KUMAR, S., MAXWELL, I. Z., HEISTERKAMP, A., POLTE, T. R., LELE, T. P., SALANGA, M., MAZUR, E. & INGBER, D. E. 2006. Viscoelastic Retraction of Single Living Stress Fibers and Its Impact on Cell Shape, Cytoskeletal Organization, and Extracellular Matrix Mechanics. *Biophysical journal*, 90, 3762-3773.
- KURAL, M. H. & BILLIAR, K. L. 2014. Mechanoregulation of valvular interstitial cell phenotype in the third dimension. *Biomaterials*, 35, 1128-1137.
- KUZNETSOVA, T. G., STARODUBTSEVA, M. N., YEGORENKOV, N. I., CHIZHIK, S. A. & ZHDANOV, R. I. 2007. Atomic force microscopy probing of cell elasticity. *Micron*, 38, 824-33.
- LAM, R. H., WENG, S., LU, W. & FU, J. 2012a. Live-cell subcellular measurement of cell stiffness using a microengineered stretchable micropost array membrane. *Integr Biol (Camb)*, 4, 1289-98.
- LAM, R. H. W., SUN, Y. B., CHEN, W. Q. & FU, J. P. 2012b. Elastomeric microposts integrated into microfluidics for flow-mediated endothelial mechanotransduction analysis. *Lab on a Chip*, 12, 1865-1873.
- LAMMERDING, J. 2011. Mechanics of the nucleus. *Compr Physiol*, 1, 783-807.
- LAMMERDING, J., DAHL, K. N., DISCHER, D. E. & KAMM, R. D. 2007. Nuclear Mechanics and Methods. In: YU-LI, W. & DENNIS, E. D. (eds.) *Methods in Cell Biology*. Academic Press.
- LANYON, L. 1996. Using functional loading to influence bone mass and architecture: objectives, mechanisms, and relationship with estrogen of the mechanically adaptive process in bone. *Bone*, 18, S37-S43.
- LAURENT, V. R. M., HÉNON, S., PLANUS, E., FODIL, R., BALLAND, M., ISABEY, D. & GALLET, F. O. 2002. Assessment of Mechanical Properties of Adherent Living Cells by Bead Micromanipulation: Comparison of Magnetic Twisting Cytometry vs Optical Tweezers. *Journal of Biomechanical Engineering*, 124, 408-421.
- LEE, C. F., HAASE, C., DEGUCCI, S. & KAUNAS, R. 2010. Cyclic stretch-induced stress fiber dynamics - dependence on strain rate, Rho-kinase and MLCK. *Biochem Biophys Res Commun*, 401, 344-9.
- LEE, E. J., HOLMES, J. W. & COSTA, K. D. 2008. Remodeling of Engineered Tissue Anisotropy in Response to Altered Loading Conditions. *Annals of biomedical engineering*, 36, 1322-1334.
- LEGANT, W. R., CHOI, C. K., MILLER, J. S., SHAO, L., GAO, L., BETZIG, E. & CHEN, C. S. 2013. Multidimensional traction force microscopy reveals out-of-plane rotational moments about focal adhesions. *Proc Natl Acad Sci U S A*, 110, 881-6.
- LEGANT, W. R., MILLER, J. S., BLAKELY, B. L., COHEN, D. M., GENIN, G. M. & CHEN, C. S. 2010. Measurement of mechanical tractions exerted by cells in three-dimensional matrices. *Nat Methods*, 7, 969-71.
- LEGANT, W. R., PATHAK, A., YANG, M. T., DESHPANDE, V. S., MCMEEKING, R. M. & CHEN, C. S. 2009. Microfabricated tissue gauges to measure and manipulate forces from 3D microtissues. *Proc Natl Acad Sci U S A*, 106, 10097-102.
- LEHENKARI, P. P., CHARRAS, G. T., NYKANEN, A. & HORTON, M. A. 2000. Adapting atomic force microscopy for cell biology. *Ultramicroscopy*, 82, 289-95.
- LEIPZIG, N. D. & ATHANASIOU, K. A. 2005. Unconfined creep compression of chondrocytes. *J Biomech*, 38, 77-85.
- LEIPZIG, N. D. & ATHANASIOU, K. A. 2008. Static compression of single chondrocytes catabolically modifies single-cell gene expression. *Biophys J*, 94, 2412-22.

- LEMMON, C. A., SNIADOCKI, N. J., RUIZ, S. A., TAN, J. L., ROMER, L. H. & CHEN, C. S. 2005. Shear force at the cell-matrix interface: enhanced analysis for microfabricated post array detectors. *Mech Chem Biosyst*, 2, 1-16.
- LI, B., XIE, L., STARR, Z. C., YANG, Z., LIN, J.-S. & WANG, J. H. C. 2007. Development of micropost force sensor array with culture experiments for determination of cell traction forces. *Cell Motil Cytoskeleton*, 64, 509-518.
- LIM, C. T., ZHOU, E. H., LI, A., VEDULA, S. R. K. & FU, H. X. 2006. Experimental techniques for single cell and single molecule biomechanics. *Materials Science & Engineering C-Biomimetic and Supramolecular Systems*, 26, 1278-1288.
- LIN, Y. W., CHENG, C. M., LEDUC, P. R. & CHEN, C. C. 2009. Understanding sensory nerve mechanotransduction through localized elastomeric matrix control. *PLoS One*, 4, e4293.
- LIU, B., GOERGEN, C. J. & SHAO, J. Y. 2007. Effect of temperature on tether extraction, surface protrusion, and cortical tension of human neutrophils. *Biophys J*, 93, 2923-33.
- LIU, Z., TAN, J. L., COHEN, D. M., YANG, M. T., SNIADOCKI, N. J., RUIZ, S. A., NELSON, C. M. & CHEN, C. S. 2010. Mechanical tugging force regulates the size of cell-cell junctions. *Proc Natl Acad Sci U S A*, 107, 9944-9.
- LODISH, H., BERK, A., ZIPURSKY, S. L., MATSUDAIRA, P., BALTIMORE, D. & DARNELL, J. 2000. *Molecular Cell Biology*, New York, W. H. Freeman.
- LOMBARDI, M. L., KNECHT, D. A., DEMBO, M. & LEE, J. 2007. Traction force microscopy in Dictyostelium reveals distinct roles for myosin II motor and actin-crosslinking activity in polarized cell movement. *J Cell Sci*, 120, 1624-34.
- LULEVICH, V., ZINK, T., CHEN, H. Y., LIU, F. T. & LIU, G. 2006. Cell mechanics using atomic force microscopy-based single-cell compression. *Langmuir*, 22, 8151-8155.
- MANIOTIS, A. J., CHEN, C. S. & INGBER, D. E. 1997. Demonstration of mechanical connections between integrins, cytoskeletal filaments, and nucleoplasm that stabilize nuclear structure. *Proc Natl Acad Sci USA*, 94, 849-854.
- MANN, J. M., LAM, R. H., WENG, S., SUN, Y. & FU, J. 2012. A silicone-based stretchable micropost array membrane for monitoring live-cell subcellular cytoskeletal response. *Lab Chip*, 12, 731-40.
- MARTINI, F. H. 2004. *Fundamentals of Anatomy and Physiology*, San Francisco, Benjamin Cummings Inc.
- MASKARINEC, S. A., FRANCK, C., TIRRELL, D. A. & RAVICHANDRAN, G. 2009. Quantifying cellular traction forces in three dimensions. *Proc Natl Acad Sci U S A*, 106, 22108-13.
- MATSUI, T. S., KAUNAS, R., KANZAKI, M., SATO, M. & DEGUCHI, S. 2011. Non-muscle myosin II induces disassembly of actin stress fibres independently of myosin light chain dephosphorylation. *Interface Focus*, 1, 754-766.
- MCGARRY, J. G. & PRENDERGAST, P. J. 2004. A three-dimensional finite element model of an adherent eukaryotic cell. *Eur Cell Mater*, 7, 27-33; discussion 33-4.
- MCGARRY, J. P. 2009. Characterization of cell mechanical properties by computational modeling of parallel plate compression. *Ann Biomed Eng*, 37, 2317-25.
- MCGARRY, J. P., FU, J., YANG, M. T., CHEN, C. S., MCMEEKING, R. M., EVANS, A. G. & DESHPANDE, V. S. 2009. Simulation of the contractile response of cells on an array of micro-posts. *Philos Trans A Math Phys Eng Sci*, 367, 3477-3497.
- MCGARRY, J. P. & MCHUGH, P. E. 2008. Modelling of in vitro chondrocyte detachment. *J Mech Phys Solids*, 56, 1554-1565.
- MCGRATH, B., MEALING, G. & LABROSSE, M. R. 2011. A mechanobiological investigation of platelets. *Biomech Model Mechanobiol*, 10, 473-84.

- MICOULET, A., SPATZ, J. P. & OTT, A. 2005. Mechanical response analysis and power generation by single-cell stretching. *Chemphyschem*, 6, 663-70.
- MITROSSILIS, D., FOUCHARD, J., GUIROY, A., DESPRAT, N., RODRIGUEZ, N., FABRY, B. & ASNACIOS, A. 2009. Single-cell response to stiffness exhibits muscle-like behavior. *Proceedings of the National Academy of Sciences*, 106, 18243-18248.
- MOFRAD, M. R. K. 2009. Rheology of the Cytoskeleton. *Annual Review of Fluid Mechanics*, 41, 433-453.
- MULLEN, C. A., VAUGHAN, T. J., VOISIN, M. C., BRENNAN, M. A., LAYROLLE, P. & MCNAMARA, L. M. 2014. Cell morphology and focal adhesion location alters internal cell stress. *Journal of The Royal Society Interface*, 11.
- MUNEVAR, S., WANG, Y.-L. & DEMBO, M. 2001. Traction Force Microscopy of Migrating Normal and H-ras Transformed 3T3 Fibroblasts. *Biophys J*, 80, 1744-1757.
- NAKANO, M., IMAMURA, H., NAGAI, T. & NOJI, H. 2011. Ca<sup>2+</sup>(+) regulation of mitochondrial ATP synthesis visualized at the single cell level. *ACS Chem Biol*, 6, 709-15.
- NEIDLINGER-WILKE, C., GROOD, E. S., WANG, J.-C., BRAND, R. A. & CLAES, L. 2001. Cell alignment is induced by cyclic changes in cell length: studies of cells grown in cyclically stretched substrates. *J Orthop Res*, 19, 286-93.
- NEKOUZADEH, A., PRYSE, K. M., ELSON, E. L. & GENIN, G. M. 2008. Stretch-activated force shedding, force recovery, and cytoskeletal remodeling in contractile fibroblasts. *Journal of Biomechanics*, 41, 2964-2971.
- NEUMAN, K. C. & BLOCK, S. M. 2004. Optical trapping. *Rev Sci Instrum*, 75, 2787-809.
- NEUMAN, K. C., LIONNET, T. & ALLEMAND, J. F. 2007. Single-molecule micromanipulation techniques. *Annual Review of Materials Research*, 37, 33-67.
- NIEPONICE, A., MAUL, T. M., CUMER, J. M., SOLETTI, L. & VORP, D. A. 2007. Mechanical stimulation induces morphological and phenotypic changes in bone marrow-derived progenitor cells within a three-dimensional fibrin matrix. *J Biomed Mater Res A*, 81, 523-30.
- NOTBOHM, J., LESMAN, A., TIRRELL, D. A. & RAVICHANDRAN, G. 2015. Quantifying cell-induced matrix deformation in three dimensions based on imaging matrix fibers. *Integrative Biology*.
- OFEK, G. & ATHANASIOU, K. 2007. Micromechanical properties of chondrocytes and chondrons: relevance to articular cartilage tissue engineering. *Journal of Mechanics of Materials and Structures*, 2, 1059-1086.
- OFEK, G., NATOLI, R. M. & ATHANASIOU, K. A. 2009a. In situ mechanical properties of the chondrocyte cytoplasm and nucleus. *J Biomech*, 42, 873-7.
- OFEK, G., WILTZ, D. C. & ATHANASIOU, K. A. 2009b. Contribution of the cytoskeleton to the compressive properties and recovery behavior of single cells. *Biophys J*, 97, 1873-82.
- OHASHI, T., HAGIWARA, M., BADER, D. L. & KNIGHT, M. M. 2006. Intracellular mechanics and mechanotransduction associated with chondrocyte deformation during pipette aspiration. *Biorheology*, 43, 201-14.
- PAJEROWSKI, J. D., DAHL, K. N., ZHONG, F. L., SAMMAK, P. J. & DISCHER, D. E. 2007. Physical plasticity of the nucleus in stem cell differentiation. *Proc Natl Acad Sci USA*, 104, 15619-15624.
- PATHAK, A., DESHPANDE, V. S., MCMEEKING, R. M. & EVANS, A. G. 2008. The simulation of stress fibre and focal adhesion development in cells on patterned substrates. *Journal of The Royal Society Interface*, 5, 507-524.
- PEETERS, E. A., OOMENS, C. W., BOUTEN, C. V., BADER, D. L. & BAAIJENS, F. P. 2005. Mechanical and failure properties of single attached cells under compression. *J Biomech*, 38, 1685-93.

- PESEN, D. & HOH, J. H. 2005. Micromechanical architecture of the endothelial cell cortex. *Biophys J*, 88, 670-9.
- PLODINEC, M., LOPARIC, M., SUETTERLIN, R., HERRMANN, H., AEBI, U. & SCHOENENBERGER, C.-A. 2011. The nanomechanical properties of rat fibroblasts are modulated by interfering with the vimentin intermediate filament system. *Journal of Structural Biology*, 174, 476-484.
- POOLE, C. A., ZHANG, Z.-J. & ROSS, J. M. 2001. The differential distribution of acetylated and detyrosinated alpha-tubulin in the microtubular cytoskeleton and primary cilia of hyaline cartilage chondrocytes. *Journal of Anatomy*, 199, 393-405.
- PRABHUNE, M., BELGE, G., DOTZAUER, A., BULLERDIEK, J. & RADMACHER, M. 2012. Comparison of mechanical properties of normal and malignant thyroid cells. *Micron*, 43, 1267-1272.
- PRAVINCUMAR, P., BADER, D. L. & KNIGHT, M. M. 2012. Viscoelastic cell mechanics and actin remodelling are dependent on the rate of applied pressure. *PLoS ONE*, 7, e43938.
- RADMACHER, M., FRITZ, M., KACHER, C. M., CLEVELAND, J. P. & HANSMA, P. K. 1996. Measuring the viscoelastic properties of human platelets with the atomic force microscope. *Biophys J*, 70, 556-67.
- REINHART-KING, C. A., DEMBO, M. & HAMMER, D. A. 2005. The dynamics and mechanics of endothelial cell spreading. *Biophys J*, 89, 676-689.
- RIBEIRO, A. J., TOTTEY, S., TAYLOR, R. W., BISE, R., KANADE, T., BADYLAK, S. F. & DAHL, K. N. 2012. Mechanical characterization of adult stem cells from bone marrow and perivascular niches. *J Biomech*, 45, 1280-7.
- RICART, B. G., YANG, M. T., HUNTER, C. A., CHEN, C. S. & HAMMER, D. A. 2011. Measuring traction forces of motile dendritic cells on micropost arrays. *Biophys J*, 101, 2620-8.
- RIVELINE, D., ZAMIR, E., BALABAN, N. Q., SCHWARZ, U. S., ISHIZAKI, T., NARUMIYA, S., KAM, Z., GEIGER, B. & BERSHADSKY, A. D. 2001. Focal contacts as mechanosensors: externally applied local mechanical force induces growth of focal contacts by an mDia1-dependent and ROCK-independent mechanism. *J Cell Biol*, 153, 1175-86.
- ROCA-CUSACHS, P., ALCARAZ, J., SUNYER, R., SAMITIER, J., FARRE, R. & NAVAJAS, D. 2008. Micropatterning of single endothelial cell shape reveals a tight coupling between nuclear volume in G1 and proliferation. *Biophys J*, 94, 4984-95.
- RODRIGUEZ, A. G., HAN, S. J., REGNIER, M. & SNIADOCKI, N. J. 2011. Substrate Stiffness Increases Twitch Power of Neonatal Cardiomyocytes in Correlation with Changes in Myofibril Structure and Intracellular Calcium. *Biophys J*, 101, 2455-2464.
- RODRIGUEZ, M. L., MCGARRY, P. J. & SNIADOCKI, N. J. 2013. Review on cell mechanics: experimental and modeling approaches. *Appl Mech Rev*, 65, 060801.
- RONAN, W., DESHPANDE, V. S., MCMEEKING, R. M. & MCGARRY, J. P. 2012. Numerical investigation of the active role of the actin cytoskeleton in the compression resistance of cells. *J Mech Behav Biomed Mater*, 14, 143-57.
- RONAN, W., DESHPANDE, V. S., MCMEEKING, R. M. & MCGARRY, J. P. 2014. Cellular contractility and substrate elasticity: a numerical investigation of the actin cytoskeleton and cell adhesion. *Biomech Model Mechanobiol*, 13, 417-435.
- RONAN, W., MCMEEKING, R. M., CHEN, C. S., MCGARRY, J. P. & DESHPANDE, V. S. 2015. Cooperative contractility: the role of stress fibres in the regulation of cell-cell junctions. *J Biomech*, 48, 520-8.
- RONAN, W., PATHAK, A., DESHPANDE, V. S., MCMEEKING, R. M. & MCGARRY, J. P. 2013. Simulation of the Mechanical Response of Cells on Micropost Substrates. *J Biomech Eng*, 135, 101012.

- ROTSCH, C., BRAET, F., WISSE, E. & RADMACHER, M. 1997. AFM imaging and elasticity measurements on living rat liver macrophages. *Cell Biol Int*, 21, 685-96.
- ROTSCH, C., JACOBSON, K. & RADMACHER, M. 1999. Dimensional and mechanical dynamics of active and stable edges in motile fibroblasts investigated by using atomic force microscopy. *Proc Natl Acad Sci U S A*, 96, 921-6.
- ROTSCH, C. & RADMACHER, M. 2000. Drug-induced changes of cytoskeletal structure and mechanics in fibroblasts: an atomic force microscopy study. *Biophys J*, 78, 520-35.
- ROWAT, A. C., LAMMERDING, J., HERRMANN, H. & AEBI, U. 2008. Towards an integrated understanding of the structure and mechanics of the cell nucleus. *Bioessays*, 30, 226-36.
- ROY, S., THACHER, T., SILACCI, P. & STERGIOPULOS, N. 2009. Arterial biomechanics after destruction of cytoskeleton by cytochalasin D. *J Biomech*, 42, 2562-2568.
- SATO, K., ADACHI, T., SHIRAI, Y., SAITO, N. & TOMITA, Y. 2006. Local disassembly of actin stress fibers induced by selected release of intracellular tension in osteoblastic cell. *Journal of Biomechanical Science and Engineering*, 1, 204-214.
- SATO, M., LEVESQUE, M. J. & NEREM, R. M. 1987. Micropipette aspiration of cultured bovine aortic endothelial cells exposed to shear stress. *Arteriosclerosis*, 7, 276-86.
- SATO, M., OHSHIMA, N. & NEREM, R. M. 1996. Viscoelastic properties of cultured porcine aortic endothelial cells exposed to shear stress. *J Biomech*, 29, 461-467.
- SATO, M., THERET, D. P., WHEELER, L. T., OHSHIMA, N. & NEREM, R. M. 1990. Application of the micropipette technique to the measurement of cultured porcine aortic endothelial cell viscoelastic properties. *J Biomech Eng*, 112, 263-8.
- SCHMID-SCHONBEIN, G. W., SUNG, K. L., TOZEREN, H., SKALAK, R. & CHIEN, S. 1981. Passive mechanical properties of human leukocytes. *Biophys J*, 36, 243-56.
- SCHOEN, I., HU, W., KLOTZSCH, E. & VOGEL, V. 2010. Probing cellular traction forces by micropillar arrays: contribution of substrate warping to pillar deflection. *Nano Lett*, 10, 1823-30.
- SELIKAR, D., BLACK, R. A., VITO, R. P. & NEREM, R. M. 2000. Dynamic mechanical conditioning of collagen-gel blood vessel constructs induces remodeling in vitro. *Ann Biomed Eng*, 28, 351-62.
- SEN, S. & KUMAR, S. 2010. Combining mechanical and optical approaches to dissect cellular mechanobiology. *J Biomech*, 43, 45-54.
- SHARP, D. J., ROGERS, G. C. & SCHOLEY, J. M. 2000. Microtubule motors in mitosis. *Nature*, 407, 41-7.
- SHIEH, A. C. & ATHANASIOU, K. A. 2003. Principles of cell mechanics for cartilage tissue engineering. *Ann Biomed Eng*, 31, 1-11.
- SHIEH, A. C. & ATHANASIOU, K. A. 2006. Biomechanics of single zonal chondrocytes. *J Biomech*, 39, 1595-602.
- SHIEH, A. C. & ATHANASIOU, K. A. 2007. Dynamic compression of single cells. *Osteoarthritis Cartilage*, 15, 328-334.
- SHIN, D. & ATHANASIOU, K. 1999. Cytoindentation for obtaining cell biomechanical properties. *J Orthop Res*, 17, 880-90.
- SIMON, A. & DURRIEU, M. C. 2006. Strategies and results of atomic force microscopy in the study of cellular adhesion. *Micron*, 37, 1-13.
- SNIADACKI, N. J. & CHEN, C. S. 2007. Microfabricated Silicone Elastomeric Post Arrays for Measuring Traction Forces of Adherent Cells. In: WANG, Y. & DISCHER, D. E. (eds.) *Methods in Cell Biology: Cell Mechanics*. San Diego, CA: Elsevier Inc.
- SOCHOL, R. D., HIGA, A. T., JANAIRO, R. R. R., LI, S. & LIN, L. 2011. Effects of micropost spacing and stiffness on cell motility. *Micro & Nano Letters*, 6, 323-326.
- STAMENOVIC, D. 2008. Rheological behavior of mammalian cells. *Cell Mol Life Sci*, 65, 3592-605.

- STEWART, R. L., CHENG, C. M., YE, J. D., BELLIN, R. M. & LEDUC, P. R. 2011. Mechanical stretch and shear flow induced reorganization and recruitment of fibronectin in fibroblasts. *Sci Rep*, 1, 147.
- SUNG, K. L., DONG, C., SCHMID-SCHONBEIN, G. W., CHIEN, S. & SKALAK, R. 1988. Leukocyte relaxation properties. *Biophys J*, 54, 331-6.
- SVOBODA, K. & BLOCK, S. M. 1994. Biological applications of optical forces. *Annu Rev Biophys Biomol Struct*, 23, 247-85.
- TAN, D. W., JENSEN, K. B., TROTTER, M. W., CONNELLY, J. T., BROAD, S. & WATT, F. M. 2013. Single-cell gene expression profiling reveals functional heterogeneity of undifferentiated human epidermal cells. *Development*, 140, 1433-44.
- TAN, J. L., TIEN, J., PIRONE, D. M., GRAY, D. S., BHADRIRAJU, K. & CHEN, C. S. 2003. Cells lying on a bed of microneedles: an approach to isolate mechanical force. *Proc Natl Acad Sci USA*, 100, 1484-9.
- TAN, S. C., PAN, W. X., MA, G., CAI, N., LEONG, K. W. & LIAO, K. 2008. Viscoelastic behaviour of human mesenchymal stem cells. *BMC Cell Biol*, 9, 40.
- TEE, S.-Y., FU, J., CHEN, CHRISTOPHER S. & JANMEY, PAUL A. 2011. Cell Shape and Substrate Rigidity Both Regulate Cell Stiffness. *Biophys J*, 100, L25-L27.
- THAVANDIRAN, N., DUBOIS, N., MIKRYUKOV, A., MASSÉ, S., BECA, B., SIMMONS, C. A., DESHPANDE, V. S., MCGARRY, J. P., CHEN, C. S., NANTHAKUMAR, K., KELLER, G. M., RADISIC, M. & ZANDSTRA, P. W. 2013. Design and formulation of functional pluripotent stem cell-derived cardiac microtissues. *Proc Natl Acad Sci USA*, 110, 4698-4707.
- THERET, D. P., LEVESQUE, M. J., SATO, M., NEREM, R. M. & WHEELER, L. T. 1988. The Application of a Homogeneous Half-Space Model in the Analysis of Endothelial Cell Micropipette Measurements. *J Biomech Eng*, 110, 190-199.
- THERY, M., PEPIN, A., DRESSAIRE, E., CHEN, Y. & BORNENS, M. 2006. Cell distribution of stress fibres in response to the geometry of the adhesive environment. *Cell Motil Cytoskeleton*, 63, 341-55.
- THOMAS, C. H., COLLIER, J. H., SFEIR, C. S. & HEALY, K. E. 2002. Engineering gene expression and protein synthesis by modulation of nuclear shape. *Proc Natl Acad Sci USA*, 99, 1972-1977.
- THORPE, S. D., BUCKLEY, C. T., VINARDELL, T., O'BRIEN, F. J., CAMPBELL, V. A. & KELLY, D. J. 2010. The response of bone marrow-derived mesenchymal stem cells to dynamic compression following TGF- $\beta$ 3 induced chondrogenic differentiation. *Annals of biomedical engineering*, 38, 2896-2909.
- THOUMINE, O., CARDOSO, O. & MEISTER, J.-J. 1999. Changes in the mechanical properties of fibroblasts during spreading: a micromanipulation study. *Eur Biophys J*, 28, 222-234.
- THOUMINE, O. & OTT, A. 1996. Influence of adhesion and cytoskeletal integrity on fibroblast traction. *Cell Motil Cytoskeleton*, 35, 269-80.
- THOUMINE, O. & OTT, A. 1997a. Comparison of the mechanical properties of normal and transformed fibroblasts. *Biorheology*, 34, 309-26.
- THOUMINE, O. & OTT, A. 1997b. Time scale dependent viscoelastic and contractile regimes in fibroblasts probed by microplate manipulation. *J Cell Sci*, 110 ( Pt 17), 2109-16.
- TIBBITT, M. W. & ANSETH, K. S. 2009. Hydrogels as extracellular matrix mimics for 3D cell culture. *Biotechnol Bioeng*, 103, 655-63.
- TING-BEALL, H. P., NEEDHAM, D. & HOCHMUTH, R. M. 1993. Volume and osmotic properties of human neutrophils. *Blood*, 81, 2774-80.

- TITUSHKIN, I. & CHO, M. 2006. Distinct membrane mechanical properties of human mesenchymal stem cells determined using laser optical tweezers. *Biophys J*, 90, 2582-91.
- TITUSHKIN, I. & CHO, M. 2007. Modulation of cellular mechanics during osteogenic differentiation of human mesenchymal stem cells. *Biophysical Journal*, 93, 3693-3702.
- TOLIC-NORRELYKKE, I. M. & WANG, N. 2005. Traction in smooth muscle cells varies with cell spreading. *J Biomech*, 38, 1405-12.
- TONDON, A., HSU, H. J. & KAUNAS, R. 2012. Dependence of cyclic stretch-induced stress fiber reorientation on stretch waveform. *J Biomech*, 45, 728-35.
- TRICKEY, W. R., BAAIJENS, F. P., LAURSEN, T. A., ALEXOPOULOS, L. G. & GUILAK, F. 2006. Determination of the Poisson's ratio of the cell: recovery properties of chondrocytes after release from complete micropipette aspiration. *J Biomech*, 39, 78-87.
- TRICKEY, W. R., LEE, G. M. & GUILAK, F. 2000. Viscoelastic properties of chondrocytes from normal and osteoarthritic human cartilage. *J Orthop Res*, 18, 891-8.
- TRICKEY, W. R., VAIL, T. P. & GUILAK, F. 2004. The role of the cytoskeleton in the viscoelastic properties of human articular chondrocytes. *J Orthop Res*, 22, 131-9.
- TSUKAMOTO, T., HASHIGUCHI, N., JANICKI, S. M., TUMBAR, T., BELMONT, A. S. & SPECTOR, D. L. 2000. Visualization of gene activity in living cells. *Nat Cell Biol*, 2, 871-8.
- VAN VLIET, K., BAO, G. & SURESH, S. 2003. The biomechanics toolbox: experimental approaches for living cells and biomolecules. *Acta Materialia*, 51, 5881-5905.
- VAN VLIMMEREN, M. A., DRIESSEN-MOL, A., OOMENS, C. J. & BAAIJENS, F. T. 2012. Passive and active contributions to generated force and retraction in heart valve tissue engineering. *Biomechanics and Modeling in Mechanobiology*, 11, 1015-1027.
- VAZIRI, A., GOPINATH, A. & DESHPANDE, V. S. 2007. Continuum-based computational models for cell and nuclear mechanics. *Journal of the Mechanics of Materials and Structures*, 2, 1169-1191.
- VAZIRI, A. & MOFRAD, M. R. 2007. Mechanics and deformation of the nucleus in micropipette aspiration experiment. *J Biomech*, 40, 2053-62.
- VERNERY, F. J. & FARSAD, M. 2011. A constrained mixture approach to mechano-sensing and force generation in contractile cells. *J Mech Behav Biomed Mater*, 4, 1683-1699.
- WAGENSEIL, J. E., ELSON, E. L. & OKAMOTO, R. J. 2004. Cell orientation influences the biaxial mechanical properties of fibroblast populated collagen vessels. *Ann Biomed Eng*, 32, 720-31.
- WAGENSEIL, J. E., WAKATSUKI, T., OKAMOTO, R. J., ZAHALAK, G. I. & ELSON, E. L. 2003. One-dimensional viscoelastic behavior of fibroblast populated collagen matrices. *J Biomech Eng*, 125, 719-25.
- WAKATSUKI, T. & ELSON, E. L. 2002. Reciprocal interactions between cells and extracellular matrix during remodeling of tissue constructs. *Biophysical Chemistry*, 100, 593-605.
- WAKATSUKI, T., KOLODNEY, M. S., ZAHALAK, G. I. & ELSON, E. L. 2000. Cell mechanics studied by a reconstituted model tissue. *Biophysical Journal*, 79, 2353-2368.
- WAKATSUKI, T., SCHWAB, B., THOMPSON, N. C. & ELSON, E. L. 2001. Effects of cytochalasin D and latrunculin B on mechanical properties of cells. *J Cell Sci*, 114, 1025-36.

- WALKER, G. M., SAI, J., RICHMOND, A., STREMLER, M., CHUNG, C. Y. & WIKSWO, J. P. 2005. Effects of flow and diffusion on chemotaxis studies in a microfabricated gradient generator. *Lab Chip*, 5, 611-8.
- WANG, H., IP, W., BOISSY, R. & GROOD, E. S. 1995. Cell orientation response to cyclically deformed substrates: experimental validation of a cell model. *J Biomech*, 28, 1543-52.
- WANG, H., SVORONOS, A. A., BOUDOU, T., SAKAR, M. S., SCHELL, J. Y., MORGAN, J. R., CHEN, C. S. & SHENOY, V. B. 2013. Necking and failure of constrained 3D microtissues induced by cellular tension. *Proceedings of the National Academy of Sciences*, 110, 20923-20928.
- WANG, J. C. & THAMPATTY, B. P. 2006. An Introductory Review of Cell Mechanobiology. *Biomechanics and Modeling in Mechanobiology*, 5, 1-16.
- WANG, J. H., GOLDSCHMIDT-CLERMONT, P. & YIN, F. C. 2000. Contractility affects stress fiber remodeling and reorientation of endothelial cells subjected to cyclic mechanical stretching. *Ann Biomed Eng*, 28, 1165-71.
- WANG, J. H. C., GOLDSCHMIDT-CLERMONT, P., WILLE, J. & YIN, F. C. P. 2001a. Specificity of endothelial cell reorientation in response to cyclic mechanical stretching. *J. Biomech.*, 34, 1563-1572.
- WANG, J. H. C., GOLDSCHMIDT-CLERMONT, P., WILLE, J. & YIN, F. C. P. 2001b. Specificity of endothelial cell reorientation in response to cyclic mechanical stretching. *Journal of Biomechanics*, 34, 1563-1572.
- WANG, L., LI, Y., CHEN, B., LIU, S., LI, M., ZHENG, L., WANG, P., LU, T. J. & XU, F. 2015. Patterning Cellular Alignment through Stretching Hydrogels with Programmable Strain Gradients. *ACS Applied Materials & Interfaces*, 7, 15088-15097.
- WANG, N. & INGBER, D. E. 1995. Probing transmembrane mechanical coupling and cytomechanics using magnetic twisting cytometry. *Biochem Cell Biol*, 73, 327-35.
- WANG, N., NARUSE, K., STAMENOVIC, D., FREDBERG, J. J., MIJAILOVICH, S. M., TOLIC-NORRELYKKE, I. M., POLTE, T., MANNIX, R. & INGBER, D. E. 2001c. Mechanical behavior in living cells consistent with the tensegrity model. *Proc Natl Acad Sci U S A*, 98, 7765-70.
- WANG, N. & STAMENOVIĆ, D. 2000. Contribution of intermediate filaments to cell stiffness, stiffening, and growth. *American Journal of Physiology-Cell Physiology*, 279, C188-C194.
- WANG, N., TOLIC-NORRELYKKE, I. M., CHEN, J., MIJAILOVICH, S. M., BUTLER, J. P., FREDBERG, J. J. & STAMENOVIC, D. 2002. Cell prestress. I. Stiffness and prestress are closely associated in adherent contractile cells. *Am J Physiol Cell Physiol*, 282, C606-16.
- WANG, N., TYTELL, J. D. & INGBER, D. E. 2009. Mechanotransduction at a distance: mechanically coupling the extracellular matrix with the nucleus. *Nature Reviews Molecular Cell Biology*, 10, 75-82.
- WANG, Y., BOTVINICK, E. L., ZHAO, Y., BERNS, M. W., USAMI, S., TSIEN, R. Y. & CHIEN, S. 2005. Visualizing the mechanical activation of Src. *Nature*, 434, 1040-5.
- WAUGH, R. & EVANS, E. A. 1979. Thermoelasticity of red blood cell membrane. *Biophys J*, 26, 115-31.
- WEAFER, P. 2012. *Experimental Investigation of the Response of Osteoblasts to Static and Dynamic Loading using a Modified Atomic Force Microscope*. Ph.D Thesis, National University of Ireland Galway.
- WEAFER, P. P., MCGARRY, J. P., VAN ES, M. H., KILPATRICK, J. I., RONAN, W., NOLAN, D. R. & JARVIS, S. P. 2012. Stability enhancement of an atomic force microscope for long-term force measurement including cantilever modification for whole cell deformation. *Rev Sci Instrum*, 83, 093709.

- WEAFER, P. P., REYNOLDS, N. H., JARVIS, S. P. & MCGARRY, J. P. 2015. Single cell active force generation under dynamic loading – Part I: AFM experiments. *Acta Biomaterialia*, DOI:dx.doi.org/10.1016/j.actbio.2015.09.006.
- WEAFER, P. P., RONAN, W., JARVIS, S. P. & MCGARRY, J. P. 2013. Experimental and computational investigation of the role of stress fiber contractility in the resistance of osteoblasts to compression. *Bull Math Biol*, 75, 1284-303.
- WEI, Z., DESHPANDE, V. S., MCMEEKING, R. M. & EVANS, A. G. 2008. Analysis and interpretation of stress fiber organization in cells subject to cyclic stretch. *J Biomech Eng*, 130, 031009.
- WELCH, M. D. 1999. The world according to Arp: regulation of actin nucleation by the Arp2/3 complex. *Trends Cell Biol*, 9, 423-7.
- WEST, A. R., ZAMAN, N., COLE, D. J., WALKER, M. J., LEGANT, W. R., BOUDOU, T., CHEN, C. S., FAVREAU, J. T., GAUDETTE, G. R., COWLEY, E. A. & MAKSYM, G. N. 2013. Development and characterization of a 3D multicell microtissue culture model of airway smooth muscle. *Am J Physiol Lung Cell Mol Physiol*, 304, L4-16.
- WHITE, J. G., BURRIS, S. M., TUKEY, D., SMITH, C., 2ND & CLAWSON, C. C. 1984. Micropipette aspiration of human platelets: influence of microtubules and actin filaments on deformability. *Blood*, 64, 210-4.
- WILLE, J., ELSON, E. & OKAMOTO, R. 2006. Cellular and Matrix Mechanics of Bioartificial Tissues During Continuous Cyclic Stretch. *Annals of Biomedical Engineering*, 34, 1678-1690.
- YEUNG, T., GEORGES, P. C., FLANAGAN, L. A., MARG, B., ORTIZ, M., FUNAKI, M., ZAHIR, N., MING, W., WEAVER, V. & JANMEY, P. A. 2005. Effects of substrate stiffness on cell morphology, cytoskeletal structure, and adhesion. *Cell Motil Cytoskeleton*, 60, 24-34.
- YU, H., TAY, C. Y., LEONG, W. S., TAN, S. C. W., LIAO, K. & TAN, L. P. 2010. Mechanical behavior of human mesenchymal stem cells during adipogenic and osteogenic differentiation. *Biochem Biophys Res Commun*, 393, 150-155.
- ZALESKAS, J. M., KINNER, B., FREYMAN, T. M., YANNAS, I. V., GIBSON, L. J. & SPECTOR, M. 2004. Contractile forces generated by articular chondrocytes in collagen-glycosaminoglycan matrices. *Biomaterials*, 25, 1299-1308.
- ZHAO, R., BOUDOU, T., WANG, W. G., CHEN, C. S. & REICH, D. H. 2013. Decoupling cell and matrix mechanics in engineered microtissues using magnetically actuated microcantilevers. *Adv Mater*, 25, 1699-705.
- ZHAO, R., CHEN, C. S. & REICH, D. H. 2014. Force-driven evolution of mesoscale structure in engineered 3D microtissues and the modulation of tissue stiffening. *Biomaterials*, 35, 5056-5064.
- ZHAO, R., WYSS, K. & SIMMONS, C. A. 2009. Comparison of analytical and inverse finite element approaches to estimate cell viscoelastic properties by micropipette aspiration. *J Biomech*, 42, 2768-73.
- ZHOU, E., QUEK, S. & LIM, C. 2010. Power-law rheology analysis of cells undergoing micropipette aspiration. *Biomech Model Mechanobiol*, 9, 563-572.
- ZHOU, E. H., LIM, C. T. & QUEK, S. T. 2005. Finite Element Simulation of the Micropipette Aspiration of a Living Cell Undergoing Large Viscoelastic Deformation. *Mech Adv Mater Struct*, 12, 501-512.
- ZIEMANN, F., RADLER, J. & SACKMANN, E. 1994. Local measurements of viscoelastic moduli of entangled actin networks using an oscillating magnetic bead micro-rheometer. *Biophys J*, 66, 2210-6.
- ZIMMER, C. C., SHI, L. F., SHIH, Y. P., LI, J. R., JIN, L. W., LO, S. H. & LIU, G. Y. 2012. F-Actin reassembly during focal adhesion impacts single cell mechanics and nanoscale membrane structure. *Science China Chemistry*, 1-11.

# 3 Theory

## 3.1 Introduction

In this chapter theoretical and numerical methods that form the basis of the computational models used in this thesis are described. A background on continuum mechanics and solid mechanics is presented in Section 3.2. In particular, finite deformation kinematics, strain measures, and stress measures are discussed.

An overview of hyperelastic and viscoelastic constitutive laws is presented in Section 3.3. Such formulations are used in this thesis to model passive components of the cell. It should be noted that the development and implementation of active biomechanical constitutive law for stress fibre contractility and remodelling are not presented in this chapter. Rather, this complex framework is presented in Chapters 4 and 7.

The finite element (FE) method is outlined in Section 3.4, with a focus on the non-linear implicit solution schemes used in this thesis. A brief outline of the general implementation of user defined material subroutines is also presented, with reference to the commercial FE code, Abaqus (Simula, RI, USA). The active constitutive laws presented in Chapters 4 and 7 are coded into Fortran UMATs, as described in Sections 3.4.1 and 3.4.2.

## 3.2 Continuum mechanics

As a background to this section, the reader should note that the notation is such that matrices, tensors and vectors are denoted by bold typeface. Scalars and individual components of tensors and matrices are in italicised non-boldface font. Index notation convention is illustrated below where the dot product of two 3D vectors ( $\mathbf{u}, \mathbf{v}$ ). This is the summation of its component parts, such that:

$$\mathbf{u} \cdot \mathbf{v} = u_1 v_1 + u_2 v_2 + u_3 v_3 = \sum_i^3 u_i v_i = u_i v_i \quad (3.1)$$

where  $i = 1, 2, 3$ . Second order tensors have nine components in 3D (3x3). The location of each component of a tensor is defined by subscripts,  $i$  and  $j$ , where  $i, j = 1, 2, 3$ . For example, component  $A_{ij}$  is a value in the  $i^{\text{th}}$  row and the  $j^{\text{th}}$  column of tensor  $\mathbf{A}$ .

### 3.2.1 Deformation and deformation rate

Consider the deformation of the body in Figure 3.1. The body in the reference configuration,  $\Gamma_0$ , undergoes motion,  $\chi$ , to the deformed configuration,  $\Gamma$ . Now consider a point in this body,  $p$ , during motion. The position of  $p$  relative to the fixed origin,  $O$ , is given by the vector,  $\mathbf{X}$ , in the reference configuration and  $\mathbf{x} = \chi(\mathbf{X}, t)$  in the current configuration. For the point,  $p$ ,  $\mathbf{X}$  defines the material coordinates and  $\mathbf{x}$  describes spatial coordinates. Therefore,  $p$  is displaced by  $\mathbf{u}$  between the reference and current configuration, such that  $\mathbf{u} = \mathbf{x} - \mathbf{X}$ . An infinitesimal line element in the reference configuration,  $d\mathbf{X}$ , bound by the points  $p$  and  $q$ , transforms to  $d\mathbf{x}$  in the current configuration through the deformation gradient tensor,  $\mathbf{F}$ , such that:

$$\mathbf{F} = \frac{\partial \mathbf{x}}{\partial \mathbf{X}} \text{ or } F_{ij} = \frac{\partial x_i}{\partial X_j} \quad (3.2)$$

The velocity,  $\mathbf{v}$ , of the material point,  $p$ , is given as:

$$\mathbf{v} = \frac{\partial \mathbf{x}}{\partial t} \quad (3.3)$$

The spatial velocity gradient tensor,  $\mathbf{L}$ , is then:

$$\mathbf{L} = \frac{\partial \mathbf{v}}{\partial \mathbf{x}} = \frac{\partial \mathbf{v}}{\partial \mathbf{X}} \cdot \frac{\partial \mathbf{X}}{\partial \mathbf{x}} = \frac{\partial \mathbf{F}}{\partial t} \cdot \mathbf{F}^{-1} = \dot{\mathbf{F}} \cdot \mathbf{F}^{-1} \quad (3.4)$$

where  $\mathbf{F}^{-1}$  is the inverse of  $\mathbf{F}$ .

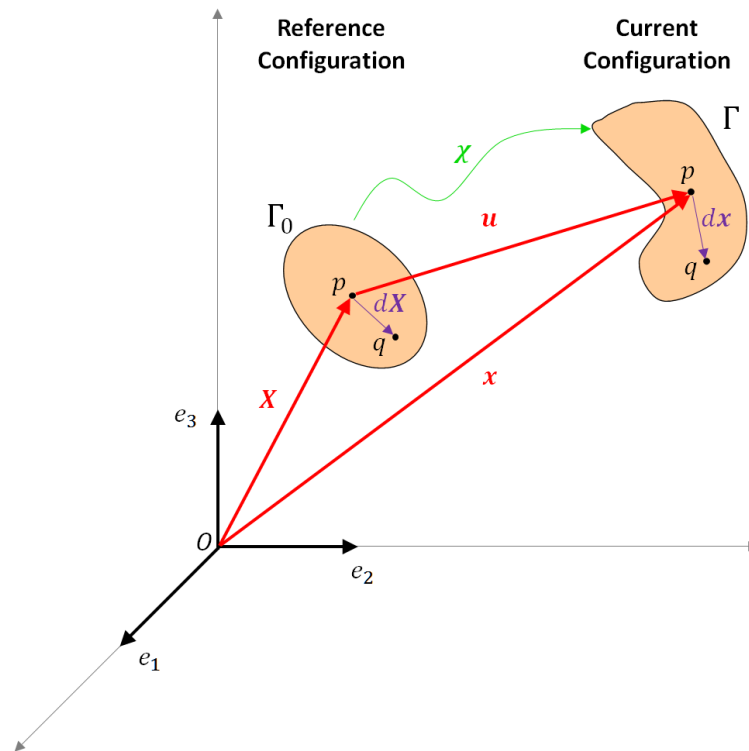


Figure 3.1: Schematic of a body undergoing motion from the reference configuration to the current configuration.

### 3.2.2 Strain and strain rate measures

The deformation gradient tensor is used to define key strain measures. The Green-Lagrange strain,  $\mathbf{E}$ , is given as:

$$\mathbf{E} = \frac{1}{2}(\mathbf{F}^T \cdot \mathbf{F} - \mathbf{I}) = \frac{1}{2}(\nabla \mathbf{u} + \nabla \mathbf{u}^T + \nabla \mathbf{u} \cdot \nabla \mathbf{u}^T) \quad (3.5)$$

where  $\mathbf{F}^T$  is the transpose of the  $\mathbf{F}$  and  $\mathbf{I}$  is the identity tensor. The infinitesimal (small) strain tensor can be found from the Green-Lagrange strain by assuming that the product of the infinitesimals is zero ( $\nabla \mathbf{u} \cdot \nabla \mathbf{u}^T \approx 0$ ), giving:

$$\boldsymbol{\epsilon} = \frac{1}{2}(\nabla \mathbf{u} + \nabla \mathbf{u}^T) \quad (3.6)$$

The left and right Cauchy-Green strain tensors are given by:

$$\mathbf{B} = \mathbf{F} \cdot \mathbf{F}^T \text{ and } \mathbf{C} = \mathbf{F}^T \cdot \mathbf{F} \quad (3.7)$$

respectively. Given that the deformation gradient tensor,  $\mathbf{F}$ , is a well-defined second-order tensor, it can be decomposed into an orthogonal rotation tensor,  $\mathbf{R}$ , and symmetric spatial and material stretch tensors,  $\mathbf{V}$  and  $\mathbf{U}$ , respectively, using polar decomposition:

$$\mathbf{F} = \mathbf{R} \cdot \mathbf{U} = \mathbf{V} \cdot \mathbf{R} \quad (3.8)$$

Therefore, deformation can be considered as a rotation followed by a stretch ( $\mathbf{F} = \mathbf{R} \cdot \mathbf{U}$ ) or vice versa ( $\mathbf{F} = \mathbf{V} \cdot \mathbf{R}$ ). The eigenvalues of  $\mathbf{U}$  are known as the principal stretches,  $\bar{\lambda}_{i=1,2,3}$  and the logarithmic strain can be found from  $\mathbf{V}$ :

$$\boldsymbol{\varepsilon} = \ln(\mathbf{V}) \quad (3.9)$$

Decomposition of the spatial velocity gradient,  $\mathbf{L}$ , gives the symmetric rate of deformation,  $\mathbf{D}$ , and the anti-symmetric spin tensor,  $\mathbf{W}$ :

$$\begin{aligned} \mathbf{D} &= \text{sym}(\mathbf{L}) = \frac{1}{2}(\mathbf{L} + \mathbf{L}^T) \\ \mathbf{W} &= \text{asym}(\mathbf{L}) = \frac{1}{2}(\mathbf{L} - \mathbf{L}^T) \end{aligned} \quad (3.10)$$

Based on the definition that  $\mathbf{D}$  is the rate of true strain, the logarithmic strain rate,  $\dot{\boldsymbol{\varepsilon}}$ , is given as:

$$\dot{\boldsymbol{\varepsilon}} = \mathbf{D} \quad (3.11)$$

Therefore, the logarithmic strain can also be determined by integrating the rate of deformation tensor with respect to time:

$$\boldsymbol{\varepsilon} = \int_0^t \mathbf{D} dt \quad (3.12)$$

where the principal referential axes remain fixed with respect to the material coordinates.

### 3.2.3 Stress measures

Considering a volume  $\Gamma$  in Figure 3.2, the traction,  $\mathbf{t}$ , is the force per unit area that acts on an infinitesimal surface element in the vicinity of a point  $p$  in the current configuration. The traction vector is related to the normal  $\mathbf{n}$  at  $p$  by Cauchy's theorem:

$$\mathbf{t} = \boldsymbol{\sigma} \cdot \mathbf{n} \quad (3.13)$$

where  $\boldsymbol{\sigma}$  is the symmetric Cauchy stress tensor. The Kirchhoff stress,  $\boldsymbol{\tau}$ , is defined as:

$$\boldsymbol{\tau} = J\boldsymbol{\sigma} \quad (3.14)$$

where  $J = d\Gamma/d\Gamma_0$  is the volume ratio of the current and reference configuration in the vicinity of  $p$ . The first Piola-Kirchhoff stress,  $\mathbf{P}$ , (or nominal stress,  $\mathbf{N}$ ) is given by:

$$\mathbf{N}^T = \mathbf{P} = \boldsymbol{\tau} \cdot \mathbf{F}^{-T} \quad (3.15)$$

These stress tensors are not necessarily symmetric. The second Piola-Kirchhoff stress,  $\mathbf{p}^{2nd}$ , is defined as:

$$\mathbf{p}^{2nd} = \mathbf{F}^{-1} \cdot \boldsymbol{\tau} \cdot \mathbf{F}^{-T} \quad (3.16)$$

In order to visualise stress in real geometries, stress states that are independent of the coordinate system orientation are useful. Consider again the Cauchy (true) stress tensor. When a material body is subjected to external stresses it deforms. The 3D stress state of the material is represented by the Cauchy stress tensor, as follows:

$$\boldsymbol{\sigma} = \begin{bmatrix} \sigma_{11} & \sigma_{12} & \sigma_{13} \\ \sigma_{21} & \sigma_{22} & \sigma_{23} \\ \sigma_{31} & \sigma_{32} & \sigma_{33} \end{bmatrix} \quad (3.17)$$

The Cauchy stress tensor is symmetric such that,  $\sigma_{ij} = \sigma_{ji}$ . Therefore, six component represent the stress state in 3D. The eigenvalue problem,  $\text{Det}[\boldsymbol{\sigma} - \lambda \mathbf{I}] = 0$ , leads to the following characteristic equation:

$$\lambda^3 - I_1(\sigma_{ij})\lambda^2 + I_2(\sigma_{ij})\lambda - I_3(\sigma_{ij}) = 0 \quad (3.18)$$

Where the invariants of the stress tensor are given as:

$$I_1 = \text{trace}(\boldsymbol{\sigma}) = \sum_{i=1}^3 \sigma_{ii} \quad (3.19)$$

$$I_2 = \sigma_{11}\sigma_{22} + \sigma_{22}\sigma_{33} + \sigma_{11}\sigma_{33} - \sigma_{12}^2 - \sigma_{13}^2 - \sigma_{23}^2 \quad (3.20)$$

$$I_3 = \text{Det}[\sigma_{ij}] \quad (3.21)$$

The values of these invariants are independent of the coordinate system used. Therefore, they may also be written in terms of the roots of the characteristic equation, i.e. the principal stresses:

$$I_1 = \sigma_1 + \sigma_2 + \sigma_3 \quad (3.22)$$

$$I_2 = \sigma_1\sigma_2 + \sigma_2\sigma_3 + \sigma_1\sigma_3 \quad (3.23)$$

$$I_3 = \sigma_1 \sigma_2 \sigma_3 \quad (3.24)$$

A stress tensor in which the principal directions are aligned with the global coordinate system is given as:

$$\sigma_{ij} = \begin{bmatrix} \sigma_1 & 0 & 0 \\ 0 & \sigma_2 & 0 \\ 0 & 0 & \sigma_3 \end{bmatrix} \quad (3.25)$$

The Cauchy stress tensor is also commonly expressed in terms of a hydrostatic stress,  $\sigma_h$ , and a deviatoric stress,  $\mathbf{S}$ , or the stress due to shape changes:

$$\sigma_h = \frac{-\text{Trace}(\boldsymbol{\sigma})}{3} \quad (3.26)$$

$$\mathbf{S} = \boldsymbol{\sigma} - \sigma_h \mathbf{I} \quad (3.27)$$

A practical tensile equivalent stress, on von Mises stress, is commonly used:

$$\sigma_{vm} = \sqrt{\frac{3}{2} S_{ij} S_{ij}} \quad (3.28)$$

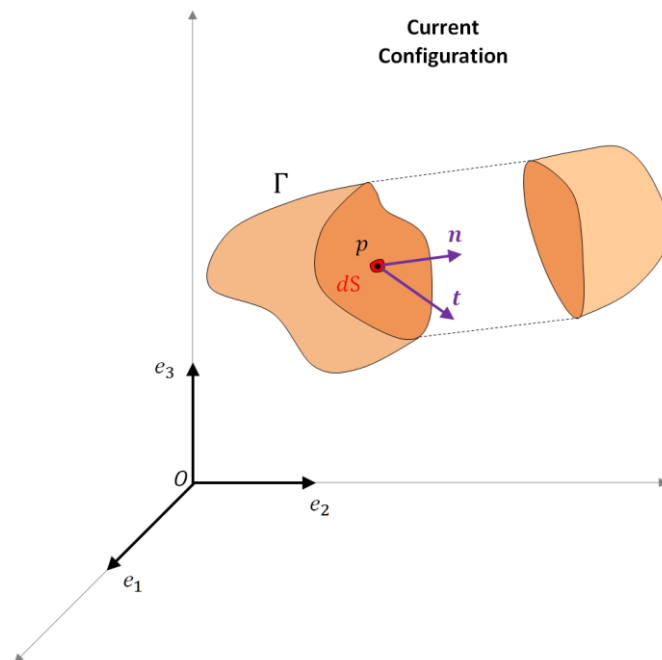


Figure 3.2: Schematic of the traction vector,  $t$ , on an internal surface of a body cut by a plane with normal,  $n$ , in the current configuration.

### 3.3 Constitutive modelling

Numerous investigations have focused on the passive mechanical behaviour of biological soft tissues and cells. Linear-elastic (Ofek et al., 2009a), hyperelastic (Nolan et al., 2014, Vaughan et al., 2015), and viscoelastic (Jafari Bidhendi and Korhonen, 2012) constitutive models are frequently used. However, linear elasticity is only applicable for small strain deformation (<2%). In general, soft tissue and cell mechanics experience much larger strains in vivo. Non-linear hyperelastic and viscoelastic constitutive laws are discussed in this section. As will be demonstrated in Chapter 4 and 7, such formulations are suitable for the passive components of biological cells. Once again it should be noted that the development and implementation of active biomechanical constitutive law for stress fibre contractility and remodelling are not presented in this chapter. Rather, this complex framework is presented in Chapters 4 and 7.

#### 3.3.1 Isotropic hyperelasticity

Hyperelastic constitutive formulations are employed to model the large strain deformation of “rubber-like” materials and are widely used to describe the mechanical behaviour soft tissues. Hyperelastic formulations are defined in terms of a strain energy function,  $\Psi$ , which defines the strain energy stored in a material per unit volume as a function of deformation. In general:

$$\mathbf{P} = \frac{\partial \Psi(\mathbf{F})}{\partial \mathbf{F}} \quad (3.29)$$

Therefore, based on equations (3.14) and (3.15), the Cauchy stress is given as:

$$\boldsymbol{\sigma} = \frac{1}{J} \mathbf{F} \cdot \frac{\partial \Psi(\mathbf{F})}{\partial \mathbf{F}} \quad (3.30)$$

It should be recalled that,  $J$ , is the Jacobian of the deformation gradient tensor,  $\mathbf{F}$ .

The volume preserving part of the deformation gradient tensor is given as:

$$\bar{\mathbf{F}} = J^{-\frac{1}{3}}\mathbf{F} \quad (3.31)$$

Therefore, isotropic hyperelastic materials can be described in terms of the distortional part of the left Cauchy-Green tensor,  $\bar{\mathbf{B}}$ :

$$\bar{\mathbf{B}} = J^{-\frac{2}{3}}\mathbf{B} \text{ or } \bar{\mathbf{B}} = \bar{\mathbf{F}} \cdot \bar{\mathbf{F}}^T \quad (3.32)$$

Considering this and the right Cauchy-Green strain tensor,  $\mathbf{C}$ , the stress invariants can be written in terms of the principal stretches  $\lambda_1, \lambda_2, \lambda_3$ . The invariants can be defined in terms of the principal stretches:

$$I_1 = \lambda_1^2 + \lambda_2^2 + \lambda_3^2 \quad (3.33)$$

$$I_2 = \lambda_1^2\lambda_2^2 + \lambda_1^2\lambda_3^2 + \lambda_2^2\lambda_3^2 \quad (3.34)$$

$$I_3 = \lambda_1^2\lambda_2^2\lambda_3^2 \quad (3.35)$$

Based on the equation (3.30) and  $\Psi = \Psi(\bar{I}_1, \bar{I}_2, \bar{I}_3, J)$ , the Cauchy stress is given as:

$$\boldsymbol{\sigma} = \frac{2}{J} \left( \frac{\partial \Psi}{\partial \bar{I}_1} + \bar{I}_1 \frac{\partial \Psi}{\partial \bar{I}_2} \right) \bar{\mathbf{B}} - \frac{2}{J} \frac{\partial \Psi}{\partial \bar{I}_1} \bar{\mathbf{B}} \cdot \bar{\mathbf{B}} + 2J \frac{\partial \Psi}{\partial I_3} \mathbf{I} \quad (3.36)$$

The following reduced order polynomial form of the strain energy density for compressible isotropic hyperelastic materials is given as:

$$\Psi = \sum_{m=1}^6 C_{m0} \frac{2}{J} (\bar{I}_1 - 3)^m + \frac{1}{D_m} (J - 1)^{2m} \quad (3.37)$$

where  $\bar{I}_1$  is a modified version of  $I_1$  such that,  $\bar{I}_1 = I_1/J^{\frac{2}{3}}$ , and  $C_{m0}$  and  $D_m$  are material constants. The hyperelastic material models used for work carried out in this thesis are described Chapters 4 and 7.

### 3.3.2 Visco-hyperelasticity

In viscoelastic materials, the stress is a function of strain and time. Mathematical models of linear-viscoelasticity consist of spring and dashpot elements to represent the elastic and viscous components, respectively. Viscous material behaviour in this thesis is implemented as a non-linear solid model, consisting of a non-linear spring and dashpot in series, which is in parallel with another non-linear spring (Figure 3.3-A). This approach can be thought of as a non-linear extension of the widely used standard linear solid (SLS) model (Figure 3.3-B).

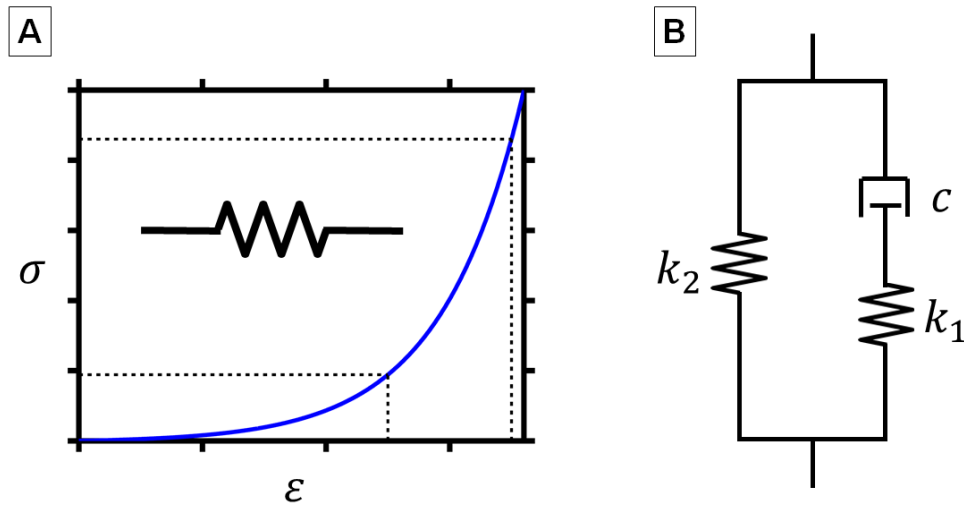


Figure 3.3: (A) Graphical representation of the stress-strain curve for a non-linear spring element. (B) Standard linear solid (SLS) mathematical model for viscoelasticity.

The non-linear visco-hyperelastic formulations used in this thesis are time domain generalisations of the hyperelastic constitutive models. The instantaneous Kirchhoff stress,  $\boldsymbol{\tau}_0$ , of a compressible material is given as:

$$\boldsymbol{\tau}_0(t) = \boldsymbol{\tau}_0^D(\bar{\mathbf{F}}(t)) + \boldsymbol{\tau}_0^H(t) \quad (3.38)$$

where,  $\boldsymbol{\tau}_0^D$  and  $\boldsymbol{\tau}_0^H$ , are the deviatoric and hydrostatic parts of  $\boldsymbol{\tau}_0$ , respectively. Using the hereditary integral in the reference configuration for large strain materials, and

then using a standard push forward operator, the following equations for the current configuration can be obtained:

$$\begin{aligned}\boldsymbol{\tau}^D(t) &= \boldsymbol{\tau}_0^D(t) + \text{Dev} \left[ \int_0^\tau \frac{\dot{G}(\tau')}{G_0} \bar{\mathbf{F}}_t^{-1}(t-t') \cdot \boldsymbol{\tau}_0^D(t-t') \cdot \bar{\mathbf{F}}_t^{-T}(t-t') d\tau' \right] \\ \boldsymbol{\tau}^H(t) &= \boldsymbol{\tau}_0^H(t) + \int_0^\tau \frac{\dot{K}(\tau')}{K_0} \boldsymbol{\tau}_0^H(t-t') d\tau'\end{aligned}\quad (3.39)$$

where,  $\tau$ , is the reduced time,  $\text{Dev}(\blacksquare) = (\blacksquare) - (1/3)\text{trace}(\blacksquare):\mathbf{I}$ ,  $\bar{\mathbf{F}}_t(t-t')$  is the distortional deformation gradient of the state at  $t-t'$  relative to  $t$ ,  $G_0$  and  $K_0$  are the instantaneous small-strain shear and bulk moduli, respectively,  $\dot{G}(\tau') = dG(\tau')/d\tau'$ , and  $\dot{K}(\tau') = dK(\tau')/d\tau'$ . Note that the reduced time represents a shift in time with temperature,  $\theta$ , and is related to the actual time through:

$$d\tau' = \frac{dt'}{A_\theta(\theta(t'))} \quad \text{or} \quad \frac{d\tau}{dt} = \frac{1}{A_\theta(\theta(t))} \quad (3.40)$$

where  $A_\theta$  is the Williams-Landell-Ferry shift function. Therefore, the internal stresses associated with each term are as follows:

$$\begin{aligned}\boldsymbol{\tau}_i^D(t) &= \frac{g_i}{\tau_i} \int_0^\tau \bar{\mathbf{F}}_t^{-1}(t-t') \cdot \boldsymbol{\tau}_0^D(t-t') \cdot \bar{\mathbf{F}}_t^{-T}(t-t') e^{-\frac{\tau'}{\tau_i}} d\tau' \\ \boldsymbol{\tau}_i^H(t) &= \frac{k_i}{\tau_i} \int_0^\tau \boldsymbol{\tau}_0^H(t-t') e^{-\frac{\tau'}{\tau_i}} d\tau'\end{aligned}\quad (3.41)$$

where  $g_i$ ,  $k_i$ , and  $\tau_i$  are Prony series parameters relating the instantaneous shear and bulk moduli to their associated time dependant terms,  $G(t)$  and  $K(t)$ , respectively.

Assuming the solution is known at time,  $t$ , these stresses can be integrated forward in time and used to construct the solution at  $t + \Delta t$ . It follows then that:

$$\begin{aligned} \boldsymbol{\tau}_i^D(t + \Delta t) &= \frac{g_i}{\tau_i} \int_0^{\tau + \Delta \tau} \bar{\mathbf{F}}_{t+\Delta t}^{-1}(t + \Delta t - t') \cdot \boldsymbol{\tau}_0^D(t + \Delta t - t') \\ &\quad \cdot \bar{\mathbf{F}}_{t+\Delta t}^{-T}(t + \Delta t - t') e^{-\frac{t'}{\tau_i}} d\tau' \end{aligned} \quad (3.42)$$

$$\boldsymbol{\tau}_i^H(t + \Delta t) = \frac{k_i}{\tau_i} \int_0^{\tau + \Delta \tau} \boldsymbol{\tau}_0^H(t + \Delta t - t') e^{-\frac{t'}{\tau_i}} d\tau'$$

By assumption that  $\boldsymbol{\tau}_0^D(t + \Delta t - t')$  and  $\boldsymbol{\tau}_0^H(t + \Delta t - t')$  varies linearly with  $t' - \Delta t$  over the increment, it can be deduced that:

$$\boldsymbol{\tau}_i^D(t + \Delta t) = \alpha_i g_i \boldsymbol{\tau}_0^D(t - \Delta t) + \beta_i g_i \hat{\boldsymbol{\tau}}_0^D(t) + \gamma_i \hat{\boldsymbol{\tau}}_i^D(t) \quad (3.43)$$

$$\boldsymbol{\tau}_i^H(t + \Delta t) = \alpha_i g_i \boldsymbol{\tau}_0^H(t - \Delta t) + \beta_i g_i \boldsymbol{\tau}_0^H(t) + \gamma_i \boldsymbol{\tau}_i^H(t)$$

where  $\gamma_i = e^{-\frac{\Delta \tau}{\tau_i}}$ ,  $\alpha_i = 1 - \frac{\tau_i}{\Delta \tau} (1 - \gamma_i)$ ,  $\beta_i = \frac{\tau_i}{\Delta \tau} (1 - \gamma_i) - \gamma_i$ , and:

$$\hat{\boldsymbol{\tau}}_0^D(t) = \Delta \bar{\mathbf{F}} \cdot \boldsymbol{\tau}_0^D(t) \cdot \Delta \bar{\mathbf{F}}^T \quad (3.44)$$

$$\hat{\boldsymbol{\tau}}_i^D(t) = \Delta \bar{\mathbf{F}} \cdot \boldsymbol{\tau}_i^D(t) \cdot \Delta \bar{\mathbf{F}}^T$$

The total stress at the end of the increment then becomes:

$$\boldsymbol{\tau}(t + \Delta t) = \boldsymbol{\tau}_0(t + \Delta t) - \sum_{i=1}^N \boldsymbol{\tau}_i^D(t + \Delta t) - \sum_{i=1}^N \boldsymbol{\tau}_i^H(t + \Delta t) \quad (3.45)$$

Furthermore, the Cauchy stress can be given as:

$$\begin{aligned} \boldsymbol{\sigma}(t + \Delta t) &= \boldsymbol{\sigma}_0(t + \Delta t) - \sum_{i=1}^N \text{Dev}(\mathbf{S}_i(t + \Delta t)) \\ &\quad - \sum_{i=1}^N \sigma_{h_i}(t + \Delta t) \mathbf{I} \end{aligned} \quad (3.46)$$

where the deviatoric and hydrostatic internal stresses,  $\mathbf{S}_i$  and  $\sigma_{h_i}$ , can be determined in a similar fashion as  $\boldsymbol{\tau}_i^D$  and  $\boldsymbol{\tau}_i^H$  above. This set of equations describes the full implementation of the visco-hyperelastic model.

## 3.4 The finite element (FE) method

The numerical solutions of continuum mechanics problems presented in this thesis are obtained using the FE method, as implemented in the commercial FE software, Abaqus (DS Simulia, RI, USA). In this section a brief background to implicit FE solution schemes is given. Furthermore, a brief summary of user defined material subroutines and their implementation into the Abaqus numerical scheme is presented.

### 3.4.1 Implicit solutions

Implicit FE method incrementally updates the stress state in the body. In this type of solution scheme after the deformation has been applied, the stress state at  $t + \Delta t$  is solved iteratively by converging a residual force vector to zero. The Abaqus/Standard implicit solver, uses the Newton-Raphson method to minimise the residual forces in order to converge on stress equilibrium in the body. Considering once again Figure 3.2: the principle of virtual work provides the fundamental equation for the FE method:

$$\int_{\Gamma} \delta \boldsymbol{\varepsilon}^T \boldsymbol{\sigma} d\Gamma = \int_S \delta \mathbf{u}^T \mathbf{t} dS \quad (3.47)$$

where,  $\Gamma$ , is the reference volume bounded by a surface,  $S$ ,  $\boldsymbol{\sigma}$  and  $\mathbf{t}$  are the stress and surface traction vectors, respectively, and  $\delta \boldsymbol{\varepsilon}$  and  $\delta \mathbf{u}$  are the virtual strains and virtual displacements of the equilibrium equation. The FE approximation can now be introduced over each element ( $e$ ) of volume ( $\Gamma_e$ ) and surface ( $S_e$ ):

$$\delta \boldsymbol{\varepsilon} = \widehat{\mathbf{B}}_e \delta \mathbf{u}_e \quad (3.48)$$

$$\delta \mathbf{u} = \widehat{\mathbf{N}}_e \delta \mathbf{u}_e \quad (3.49)$$

where  $\hat{\mathbf{N}}_e$  is the global shape function matrix,  $\hat{\mathbf{B}}_e$  is the elemental shape function gradient matrix, and  $\delta \mathbf{u}_e$  are the nodal displacements. Then, by substituting equations (3.48) and (3.49) into (3.47), the principal of virtual work becomes:

$$\begin{aligned} \sum_e \int_{\Gamma_e} \delta \mathbf{u}_e^T \hat{\mathbf{B}}_e^T \boldsymbol{\sigma}(\mathbf{u}_e) d\Gamma &= \sum_e \int_{S_e} \delta \mathbf{u}_e^T \hat{\mathbf{N}}_e^T \mathbf{t} dS \\ \delta \mathbf{u}^T \int_{\Gamma} \hat{\mathbf{B}}^T \boldsymbol{\sigma}(\mathbf{u}) d\Gamma - \delta \mathbf{u}_e^T \int_S \hat{\mathbf{N}}^T \mathbf{t} dS &= 0 \\ \delta \mathbf{u}^T \left( \int_{\Gamma} \hat{\mathbf{B}}^T \boldsymbol{\sigma}(\mathbf{u}) d\Gamma - \int_S \hat{\mathbf{N}}^T \mathbf{t} dS \right) &= 0 \end{aligned} \quad (3.50)$$

Given that the virtual displacement,  $\delta \mathbf{u}$ , is arbitrary, it follows that:

$$\int_{\Gamma} \hat{\mathbf{B}}^T \boldsymbol{\sigma}(\mathbf{u}) d\Gamma - \int_S \hat{\mathbf{N}}^T \mathbf{t} dS = 0 \quad (3.51)$$

Considering linear elasticity:

$$\boldsymbol{\sigma} = \mathbf{D}\boldsymbol{\varepsilon} = \mathbf{D}\hat{\mathbf{B}}\mathbf{u}_e \quad (3.52)$$

where,  $\mathbf{D}$ , in this case is a fourth order elasticity tensor. Therefore, where the external force vector,  $\mathbf{F}_{ext}$ , can be defined as:

$$\mathbf{F}_{ext} = \int_S \hat{\mathbf{N}}^T \mathbf{t} dS \quad (3.53)$$

the linear elasticity case of the principal of virtual work can be rewritten as:

$$\begin{aligned} \int_{\Gamma} \hat{\mathbf{B}}^T \mathbf{D}\hat{\mathbf{B}}\mathbf{u}_e d\Gamma - \mathbf{F}_{ext} &= 0 \\ \left( \int_{\Gamma} \hat{\mathbf{B}}^T \mathbf{D}\hat{\mathbf{B}} d\Gamma \right) \mathbf{u}_e - \mathbf{F}_{ext} &= 0 \\ \mathbf{K}\mathbf{u}_e &= \mathbf{F}_{ext} \end{aligned} \quad (3.54)$$

Where,  $\mathbf{K}$ , is the familiar form of the global FE characteristic/stiffness matrix. Returning to the general case in equation (3.51), a set of global equations in  $\mathbf{u}$  for the out of balance residual force,  $\mathbf{G}$ , can then be assembled and solved as:

$$\mathbf{G}(\mathbf{u}) = \int_{\Gamma} \hat{\mathbf{B}}^T \boldsymbol{\sigma}(\mathbf{u}) d\Gamma - \int_S \hat{\mathbf{N}}^T \mathbf{t} dS \quad (3.55)$$

Therefore, in order to achieve an equilibrium stress state in the body, the non-linear set of equations must be solved for convergence, such that:

$$\mathbf{G}(\mathbf{u}) = 0 \quad (3.56)$$

In general, for boundary value problems involving non-linear geometries, constitutive laws, and/or boundary conditions, the residual force vector is initially non-zero at  $t + \Delta t$  and, therefore, minimisation must be performed iteratively. At  $t + \Delta t$ , the loads/displacements may have caused geometry deviations and equation (3.50) must be updated to reflect this.

The Newton-Raphson method is an iterative process whereby a tangent to the function,  $f(x)$ , in the current solution is used to approximate to a closer, more accurate solution:

$$x_{i+1} = x_i - \left[ \frac{df}{dx} \right]^{-1} \cdot f(x_i) \quad (3.57)$$

This process continues iteratively until a tolerance is achieved such that an accurate approximation is obtained:

$$|x_{i+1} - x_i| < \text{Tolerance} \quad (3.58)$$

Within the increment of an implicit analysis, after an initial guess,  $\mathbf{u}_i^{t+\Delta t}$ , the Newton-Raphson numerical scheme iterates from time  $t$  to  $t + \Delta t$  for all nodal displacements,  $\mathbf{u}_{i+1}^{t+\Delta t}$ , until an equilibrium between internal forces and externally

applied loads/displacements reach a stable equilibrium, i.e. equation (3.56).

Therefore, the Newton-Raphson minimisation process is applied to the residual force vector:

$$\mathbf{G}(\mathbf{u}^{t+\Delta t}) = 0 \quad (3.59)$$

For the  $i^{\text{th}}$  iteration:

$$\mathbf{u}_{i+1}^{t+\Delta t} = \mathbf{u}_i^{t+\Delta t} - \left[ \frac{\partial \mathbf{G}(\mathbf{u}_i^{t+\Delta t})}{\partial \mathbf{u}} \right]^{-1} \mathbf{G}(\mathbf{u}_i^{t+\Delta t}) \quad (3.60)$$

Therefore the change in nodal displacements gives:

$$\partial \mathbf{u}_{i+1} = \mathbf{u}_{i+1}^{t+\Delta t} - \mathbf{u}_i^{t+\Delta t} = \left[ \frac{\partial \mathbf{G}(\mathbf{u}_i^{t+\Delta t})}{\partial \mathbf{u}} \right]^{-1} \mathbf{G}(\mathbf{u}_i^{t+\Delta t}) \quad (3.61)$$

which can be written in terms of the tangent stiffness matrix,  $\bar{\mathbf{K}}$ , to form the linear equation for the problem:

$$\begin{aligned} \bar{\mathbf{K}}(\mathbf{u}_i^{t+\Delta t}) &= \frac{\partial \mathbf{G}(\mathbf{u}_i^{t+\Delta t})}{\partial \mathbf{u}} \\ \bar{\mathbf{K}}(\mathbf{u}_i^{t+\Delta t}) \partial \mathbf{u}_{i+1} &= -\mathbf{G}(\mathbf{u}_i^{t+\Delta t}) \end{aligned} \quad (3.62)$$

These are the FE equations that must be solved for in each iteration in the process, such that now:

$$|\mathbf{G}(\mathbf{u}_{i+1}^{t+\Delta t})| < \text{Tolerance} \quad (3.63)$$

In contrast to the linear elastic form given in equation (3.54), in the non-linear implicit solution scheme the solution variable must be incrementally displaced.

Finally, the tangent stiffness matrix is expressed as:

$$\begin{aligned}
\bar{\mathbf{K}}(\mathbf{u}) &= \frac{\partial \mathbf{G}(\mathbf{u})}{\partial \mathbf{u}} = \frac{\partial}{\partial \mathbf{u}} \left( \int_{\Gamma} \hat{\mathbf{B}}^T \boldsymbol{\sigma}(\mathbf{u}) d\Gamma - \mathbf{F} \right) \\
&= \frac{\partial}{\partial \mathbf{u}} \left( \int_{\Gamma} \hat{\mathbf{B}}^T \boldsymbol{\sigma}(\mathbf{u}) d\Gamma \right) = \int_{\Gamma} \hat{\mathbf{B}}^T \frac{\partial \boldsymbol{\sigma}(\mathbf{u})}{\partial \mathbf{u}} d\Gamma \\
&= \int_{\Gamma} \hat{\mathbf{B}}^T \frac{\partial \boldsymbol{\sigma}(\mathbf{u})}{\partial \boldsymbol{\varepsilon}} \frac{\partial \boldsymbol{\varepsilon}}{\partial \mathbf{u}} d\Gamma = \int_{\Gamma} \hat{\mathbf{B}}^T \frac{\partial \boldsymbol{\sigma}(\boldsymbol{\varepsilon})}{\partial \boldsymbol{\varepsilon}} \hat{\mathbf{B}} d\Gamma \\
\bar{\mathbf{K}}(\mathbf{u}) &= \int_{\Gamma} \hat{\mathbf{B}}^T \mathbf{D}^{tan} \hat{\mathbf{B}} d\Gamma
\end{aligned} \tag{3.64}$$

where the consistent tangent matrix,  $\mathbf{D}^{tan}$ , is the Jacobian of the constitutive law:

$$\mathbf{D}^{tan} = \frac{\partial \boldsymbol{\sigma}(\boldsymbol{\varepsilon})}{\partial \boldsymbol{\varepsilon}} \tag{3.65}$$

It should be noted that for each Newton-Raphson iteration, it is necessary to calculate and invert tangent stiffness matrix,  $\bar{\mathbf{K}}$ . While this is computationally expensive, it ensures an accuracy solution. Furthermore, compared to other solution techniques such as the “explicit” method, it facilitates the use of relatively large time steps.

### 3.4.2 Implementation of user defined constitutive laws (UMATs)

Abaqus has numerous in-built material constitutive formulations pre-coded in the program library which allow for the simulation of a wide range of materials. Abaqus also provides the ability for the user to define a new constitutive formulation through a user defined material subroutine (UMAT). For each time increment and Newton-Raphson iteration, the UMAT is called by the main program at each integration point to define the mechanical behaviour. The UMAT must calculate the stress state at the end of the increment/iteration using the deformation state and time increment as input. Furthermore, a consistent tangent matrix (material Jacobian),  $\mathbb{C}^{(ij)}$ , must be computed.

The material Jacobian defines the change in stress at the end of the time increment caused by the infinitesimal perturbation of strain. In the Abaqus code, the material Jacobian is defined as:

$$\mathbb{C}^{(ij)} = \frac{\partial \Delta \boldsymbol{\sigma}}{\partial \Delta \boldsymbol{\varepsilon}} \quad (3.66)$$

In this thesis, a perturbation method, previously described by Miehe (1996) and later used in non-linear hyperelasticity implementations by Sun et al. (2008) and Nolan et al. (2014), is employed to create a numerical approximation of the material Jacobian. This approximation uses a linearized incremental form of the tangent modulus tensor for the Jaumann rate of the Kirchhoff stress,  $\mathbb{C}^{\tau J}$ :

$$\Delta \boldsymbol{\tau} - \Delta \mathbf{W} \boldsymbol{\tau} - \boldsymbol{\tau} \Delta \mathbf{W}^T = \mathbb{C}^{\tau J} : \Delta \mathbf{D} \quad (3.67)$$

where  $\boldsymbol{\tau}$  is the Kirchhoff stress.  $\mathbf{W}$  and  $\mathbf{D}$  are the antisymmetric and symmetric parts of the spatial velocity gradient,  $\mathbf{L}$ , respectively, described previously in equations (3.10). Recall that  $\Delta \mathbf{L} = \Delta \mathbf{F} \mathbf{F}^{-1}$  and  $\mathbf{F}$  is the deformation gradient. By perturbing the deformation gradient on the above linearized form, the tangent moduli can be approximated by a forward difference of the associated Kirchhoff stresses. The perturbation is performed on each of the degrees of freedom in the simulation. For a full 3D case this requires perturbing the deformation gradient six times, once for each component of  $\Delta \mathbf{D}$ :

$$\Delta \mathbf{F}^{(ij)} = \frac{\epsilon}{2} (\mathbf{e}_i \otimes \mathbf{e}_j \mathbf{F} + \mathbf{e}_j \otimes \mathbf{e}_i \mathbf{F}) \quad (3.68)$$

where  $\epsilon$  is a small perturbation parameter and  $\{\mathbf{e}_i\}_{i=1,2,3}$  denotes the basis vector in the spatial description. Thus, the material Jacobian,  $\mathbb{C}^{(ij)}$ , obtained from the perturbation of  $\Delta \mathbf{F}^{(ij)}$  is given as:

$$\mathbb{C} \approx \frac{1}{J} \left[ \tau(\hat{\mathbf{F}}^{(ij)}) - \tau(\mathbf{F}) \right] \quad (3.69)$$

where  $J$  is the determinant of the deformation gradient, and  $\hat{\mathbf{F}}^{(ij)} = \mathbf{F} + \Delta\mathbf{F}^{(ij)}$ . For each perturbation of equation (3.69), six independent components of  $\mathbb{C}^{(ij)}$  are determined. Combining these 6x1 arrays creates the required 6x6 material Jacobian for a 3D simulation. A flowchart of this process is shown in Figure 3.4.

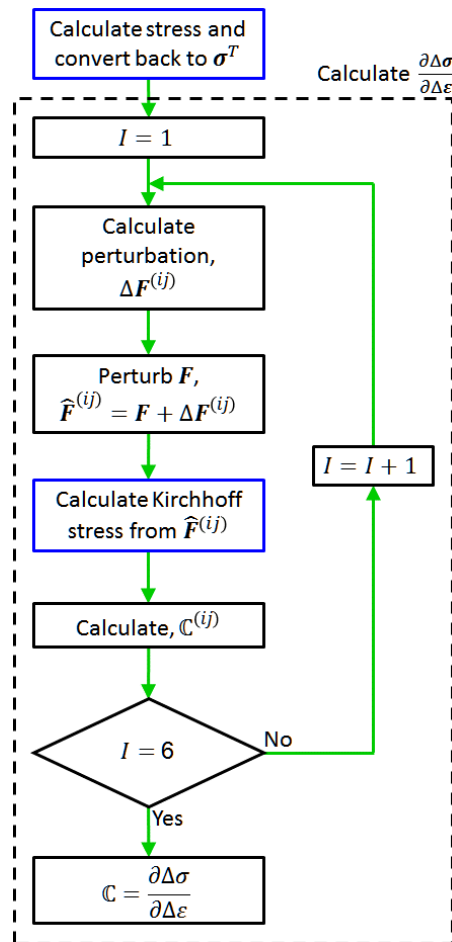


Figure 3.4: Flowchart of the perturbation method for obtaining a numerical approximation of the material Jacobian at an integration point.

## 3.5 References

JAFARI BIDHENDI, A. & KORHONEN, R. K. 2012. A Finite Element Study of Micropipette Aspiration of Single Cells: Effect of Compressibility. *Comput Math Method M*, 2012, 192618.

- MIEHE, C. 1996. Numerical computation of algorithmic (consistent) tangent moduli in large-strain computational inelasticity. *Computer Methods in Applied Mechanics and Engineering*, 134, 223-240.
- NOLAN, D. R., GOWER, A. L., DESTRADE, M., OGDEN, R. W. & MCGARRY, J. P. 2014. A robust anisotropic hyperelastic formulation for the modelling of soft tissue. *Journal of the Mechanical Behavior of Biomedical Materials*, 39, 48-60.
- OFEK, G., NATOLI, R. M. & ATHANASIOU, K. A. 2009. In situ mechanical properties of the chondrocyte cytoplasm and nucleus. *J Biomech*, 42, 873-7.
- SUN, W., CHAIKOF, E. L. & LEVENSTON, M. E. 2008. Numerical approximation of tangent moduli for finite element implementations of nonlinear hyperelastic material models. *J Biomech Eng*, 130, 061003.
- VAUGHAN, T. J., MULLEN, C. A., VERBRUGGEN, S. W. & MCNAMARA, L. M. 2015. Bone cell mechanosensation of fluid flow stimulation: a fluid-structure interaction model characterising the role integrin attachments and primary cilia. *Biomech Model Mechanobiol*, 14, 703-18.

# **4 On the role of the actin cytoskeleton and nucleus in the biomechanical response of spread cells**

## **4.1 Introduction**

The micropipette aspiration (MA) technique is used extensively to study the mechanical behaviour of single cells (Hochmuth, 2000). However, primarily due to the technical complexity of performing MA on cells adhered to a substrate or extracellular matrix (ECM), the MA technique has largely been limited to the investigation of un-adhered cells suspended in media. Previous experimental MA studies have focused on suspended endothelial cells (Sato et al., 1987b, Sato et al., 1990, Sato et al., 1996), suspended chondrocytes (Trickey et al., 2006, Trickey et al., 2000, Trickey et al., 2004, Guilak et al., 1999, Jones et al., 1999, Ohashi et al., 2006, Pravin Kumar et al., 2012), suspended stem cells (Tan et al., 2008, Yu et al., 2010, Ribeiro et al., 2012), and suspended fibroblasts (Thoumine and Ott, 1997a, Zhou et al., 2010). Critically, in suspended cells a fibrillous contractile actin cytoskeleton is not developed (Sato et al., 1987b, Reinhart-King et al., 2005, Haghparast et al., 2013). In contrast, cells adhered to a substrate or ECM develop a

highly structured contractile actin cytoskeleton (Munevar et al., 2001, Thoumine and Ott, 1996, Li et al., 2007, Zaleskas et al., 2004, Tan et al., 2003, Lemmon et al., 2005, Tee et al., 2011, Roy et al., 2009). Therefore, the study of un-adhered suspended cells provides limited insight into the behaviour of contractile cells. The development of a robust MA system to investigate the biomechanical behaviour of spread adhered cells, with emphasis on the contribution of the actin cytoskeleton, would represent a significant advance in the field of experimental cell mechanics.

Previous studies have assumed simple viscoelastic constitutive behaviour for cells in order to interpret MA experimental data (Sato et al., 1990, Nawaz et al., 2012, Tozeren et al., 1992). However, such material models fail to consider the underlying biomechanisms of cell response to mechanical stimuli and a number of studies have demonstrated that passive material model parameters must be artificially altered if any experimental parameter is altered (McGarry, 2009, Caille et al., 2002, McGarry and McHugh, 2008, Thoumine et al., 1999), i.e. a unique set of passive material properties cannot be identified for a cell. The significant contribution of the actin cytoskeleton to the mechanical response of cells has been demonstrated in numerous experimental studies (Thoumine and Ott, 1997b, Shao et al., 2000, Nagayama and Matsumoto, 2010, Ofek et al., 2010, Dowling et al., 2012, Trickey et al., 2004). It has recently been demonstrated that a computational cell model must include the key features of remodelling and contractility of the actin cytoskeleton in order to provide a realistic prediction of cell biomechanical response to physical stimuli (McGarry et al., 2009, Dowling et al., 2012, Ronan et al., 2012, Weafer et al., 2013, Ronan et al., 2014). Such advanced modelling techniques have not previously been applied to the simulation of MA of cells. The incorporation of the key bio-chemo-mechanical features of actin cytoskeleton

remodelling and contractility should be of particular importance to the modelling of MA of spread adhered cells which contain a highly developed network of actin stress fibres (SFs).

Significantly advancing on the previous studies of suspended cells, the current chapter develops an experimental technique for the MA of spread adhered cells. In particular, the important role of the actin cytoskeleton is investigated, both in terms of its contribution to the mechanical response of the cell, and in terms of its redistribution in the cytoplasm during MA. Importantly, it is demonstrated that passive viscoelastic models do not provide an accurate prediction of the observed response of spread cells to MA. It is revealed that the use of a fully predictive active bio-chemo-mechanical formulation of SF contractility and remodelling is required to accurately capture the response of spread adhered cells over a range of applied pressures. Finally, experimental-computational quantification of nucleus deformability during MA of spread cells is presented.

## **4.2 Materials and methods**

### **4.2.1 Sample preparation**

Human umbilical vein endothelial cells (HUVEC) were obtained from Promocell (C-14010, Heidelberg, Germany) and grown as per Promocell protocols (Promocell). Cells are seeded onto gridded coverslips (Bellco, 1916-92525, NJ, USA) inside petri dishes. The alpha-numeric grid, photoetched onto the coverslips enables the relocation of specific cells. Cells are allowed to adhere to the substrate for two hours before 3 ml of media is added. The SF networks developed at this time result in a spread adhered cell morphology, consistent with previous studies (Yeung et al., 2005, Reinhart-King et al., 2005). In order to prepare cells in which

the SFs have been disrupted, the media added at this point contains sufficient cytochalasin-D (cytoD) to completely inhibit actin polymerisation (Bio Sciences, Dublin, Ireland). CytoD concentrations (1  $\mu$ M and 2  $\mu$ M) and treatment times ( $\geq$ 30 minutes) used are based on previous studies (Ali et al., 2004, Hayakawa et al., 2008, Cuschleri et al., 2003, Knudsen and Frangos, 1997, Nishitani et al., 2011, Sawyer et al., 2001). To ensure that the actin cytoskeleton is completely depolymerised, the protocol is verified by immuno-fluorescent staining and also by MA of cytoD treated cells (cytoD cells) with varying molarity concentrations. Experiments are performed on all cells  $3\pm 0.5$  hours after reseeding.

#### **4.2.2 Microscopy and visualisation technique**

The prepared cells are loaded into a custom built MA system (Figure 4.1) mounted on a live cell imaging microscope with an environmental chamber (Olympus, IX-51 inverted microscope, Southend, UK). The environmental chamber enables incubation conditions (37°C and 5% CO<sub>2</sub>) to be maintained during MA experiments. In order to monitor MA of cells on flat horizontal substrates using an inverted microscope, a mirror (Thorlabs Ltd., PFSQ10-03-P01, Cambridgeshire, UK) is positioned in contact with the substrate aligned at a 45° angle (Figure 4.1-A). The system facilitates visualisation of the target cell from multiple perspectives during experiments (bottom-up or from the side). The mirror configuration obstructs the microscopes' in-built light source, hence it is necessary to use a separate LED light source to illuminate the area beneath the mirror. It is important to note that incandescent light can overheat cells, leading to necrosis, whereas no heat radiates from the LED source. To utilise the optical path created by the mirror, the focal plane of the objective must be adjusted through the monolayer until the

reflected image of the cells is observed (Figure 4.1-A). Therefore, a long working distance objectives is required in order to obtain usable focal planes.

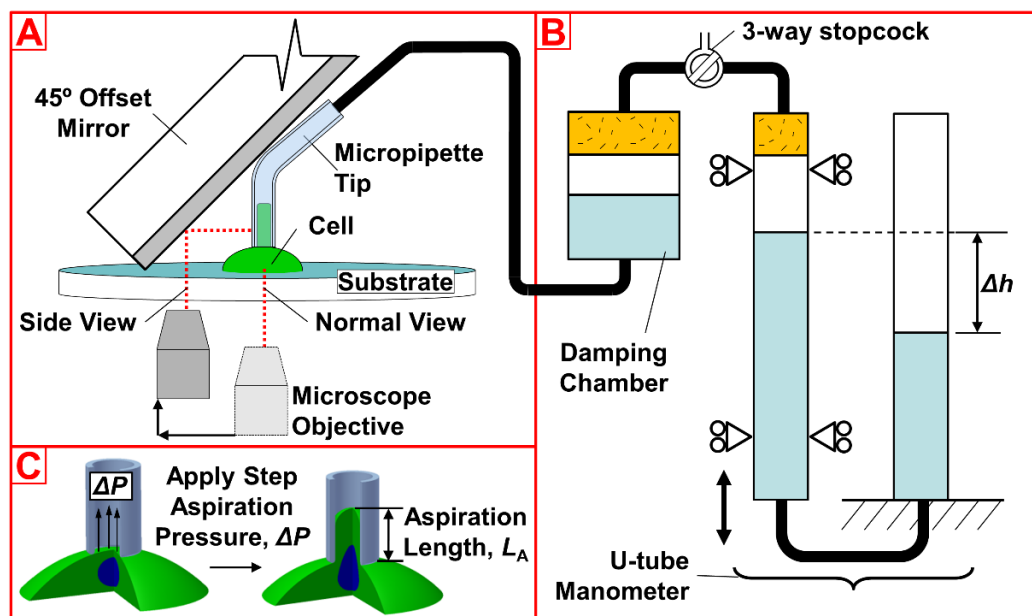


Figure 4.1: (A) MA is visualised using a mirror aligned at  $45^\circ$  to the substrate surface. (B) Pressure is generated using a u-tube manometer and applied instantaneously onto spread adhered cells using a 3-way stopcock. A PBS filled damping chamber minimises pressure fluctuations at the tip of the micropipette. (C) A schematic diagram of adhered cells before and after step application of pressure,  $\Delta P$ . Negative pressure causes deformation of the cell into the micropipette, and aspiration length,  $L_A$ , is measured as a function of time,  $t$ . Note: image is not to scale.

### 4.2.3 Micropipette aspiration rig and data acquisition

Custom designed micropipette tips (TPC, Thebarton, Australia) are attached to a pressure control system and micromanipulator (Sutter Instruments, MM-1, CA, USA) using a modified microelectrode holder (A-M Systems, WA, USA). Micropipettes have a radius of  $5\ \mu\text{m}$  ( $R_{\text{pip}}$ ) and have a  $50^\circ$  bend 1 mm from the tip to facilitate positioning sufficiently close to the  $45^\circ$  aligned mirror. Micropipettes are coated with a siliconising reagent (Sigmacote, SL2, Sigma-Aldrich Ireland Ltd., Arklow) to inhibit cell adhesion. Using the micromanipulator and multiple perspective visualisation capability, the micropipette tip is positioned above the cell. The micropipette is then lowered until contact with the cell surface is

established, leading to a light seal. The aspiration pressure is then applied instantaneously by turning a 3-way stopcock (Figure 4.1-B). Pressure,  $\Delta p$ , is generated by adjusting the height,  $\Delta h$ , of water in the u-tube manometer ( $\Delta h \propto \Delta p$ ), and fluctuations are minimised using a damping chamber that is filled with phosphate buffered saline (PBS). This method of pressure control is similar to a previously described MA system (Sato et al., 1987b). Note that the pressure is

The applied pressure is maintained for 300 s and the cell begins to deform into the micropipette gradually over time. Image sequences are acquired at 2 frames/s at a magnification of 40x, from which the aspiration length,  $L_A$ , is measured using ImageJ software (Schneider et al., 2012). Aspiration length is the distance between the opening of the micropipette tip where the cell enters, and the furthestmost point of the cell inside the micropipette (Figure 4.1-C). Aspiration lengths are normalised by the micropipette diameter ( $L_A/R_{\text{pip}}$ ), and plot as a function of time,  $t$  (in seconds, s). Statistical analysis is performed using Minitab ver. 16 (Minitab Ltd., Coventry, UK). A two-way analysis of variance (ANOVA), with time and pressure as the independent factors, is used with a Tukey HSD test to examine the effect of the pressure variation on control cells. Student t-tests are used to test the significance of cytoD cell results. For all comparisons, statistical significance is declared if  $p < 0.05$ .

#### **4.2.4 Immuno-fluorescent staining**

After 300 s of MA, cells are fixed using a 4% paraformaldehyde solution. Fixed cells are treated with 0.1% triton solution for 5 mins to permeabilise. Cells are then kept in a blocking solution of 10% FBS fetal bovine serum in PBS for 30-60 mins. Rhodamine conjugated phalloidin and Hoechst Dye 33342 (Molecular Probes, Life Technologies, NY, USA) are used to stain the actin filaments and

nucleus, respectively. Washing 3 times with PBS is performed before and after each step. The coverslips containing cells are prepared for confocal imaging by mounting on glass slides. Prolong Gold Antifade Reagent (Molecular Probes, Life Technologies, NY, USA) is used to preserve staining quality and samples are kept below 4°C before obtaining fluorescent images. An Andor Revolution spinning disk confocal microscope (Yokogawa CSU-X1 Spinning disk unit & Olympus IX81 microscope) is used to image fluorescently stained samples. The cell of interest is found by returning to the recorded location on the coverslip's alphanumeric grid using phase-contrast before z-stacks images of the aspirated cell are obtained at 60x magnification (unless otherwise specified). Two image channels are captured at each plane of focus, using laser excitation of 405 nm to visualise the nucleus and excitation of 564 nm to visualise the actin filaments. A step size of 1  $\mu\text{m}$  is used between each z-plane to a depth sufficient to capture the entire cell. Z-stack images are processed using Andor IQ software version 2.3. 3D kymography based on the captured z-stacks is also performed using Andor iQ software.

#### 4.2.5 Computational methods

A bio-chemo-mechanical framework that considers the biochemistry inherent to SF formation, active contractility, and tension dependant dissociation is used to simulate the actin cytoskeleton in the cytoplasm (Deshpande et al., 2007). Summarising the 3D active SF framework, which is described in full by Deshpande et al. (2007) and Ronan et al. (2012), a first order kinetic equation is used to capture formation and dissociation of SFs:

$$\frac{d\eta}{dt} = [1 - \eta] \frac{Ck_f}{\theta} - \left[1 - \frac{\sigma}{\sigma_0}\right] \eta \frac{k_b}{\theta} \quad (4.1)$$

where  $\eta$  is the non-dimensional activation level of a SF ( $0 \leq \eta \leq 1$ ).  $k_f$  and  $k_b$  are forward and backward reaction rate constants, respectively.  $C$  is an activation signal for SF formation that decays over time ( $C = \exp(-t/\theta)$ ).  $\theta$  is a decay constant for the signal.

To simulate the contractile behaviour of the fibre bundle a Hill-like equation is used:

$$\frac{\sigma}{\sigma_0} = 1 + \frac{\overline{k_v} \dot{\epsilon}}{\eta \dot{\epsilon}_0}; \quad -\frac{\eta}{\overline{k_v}} \leq \frac{\dot{\epsilon}}{\dot{\epsilon}_0} \leq 0 \quad (4.2)$$

where  $\dot{\epsilon}$  is the fibre contraction/extension strain rate. This equation gives fibre tension normalised by the isometric tension level bound by zero and the model parameters,  $\overline{k_v}$  and  $\dot{\epsilon}_0$ . For fibres with a small negative strain, the tension will increase up to the isometric tension level ( $\sigma_0 = \eta \sigma_{max}$ ) at zero strain rate. Fibres with a smaller negative strain rate ( $\dot{\epsilon}/\dot{\epsilon}_0 < -\eta/\overline{k_v}$ ) exhibit zero tension, and those undergoing positive strain rate ( $\dot{\epsilon} > 0$ ), have a constant tension equal to the isometric tension. The active framework is implemented in a *user-defined material subroutine (umat)* in the finite element software Abaqus 6.9 (Simula, Providence, RI, USA). In order to visualise areas of high SF alignment for direct comparison with fluorescent images, the variance parameter ( $\Pi = \eta_{MAX} - \bar{\eta}$ ) is calculated at each integration point and used in Abaqus/CAE contour plots.  $\bar{\eta}$  is the average activation level of all SFs at each point in the cytoplasm ( $\bar{\eta} = \sum_{k=1}^n (\eta_k/n)$ ). To simulate experiments in which SFs have been eradicated, the active formulation is removed from the cytoplasm material make-up, leaving only passive elements in the cell.

A neo-Hookean hyperelastic formulation is used to model the passive non-contractile cytoplasm and nucleus behaviour in the cell. The neo-Hookean stress tensor is given as:

$$\sigma_{ij} = \frac{G}{J} \left( \bar{B}_{ij} - \frac{1}{3} \bar{B}_{kk} \delta_{ij} \right) + K(J - 1) \quad (4.3)$$

where  $G$  and  $K$  are material shear and bulk moduli, respectively, and  $\bar{B}$  is determined from the deformation gradient,  $F$ :

$$\bar{B}_{ij} = \frac{B_{ij}}{J^{2/3}} = \frac{F_{ik} F_{jk}}{(\det(F))^{2/3}} \quad (4.4)$$

Passive viscoelastic material behaviour is modelled using a one term Prony series:

$$G(t) = G \left( 1 - \bar{g}^p \left( 1 - e^{-t/\tau} \right) \right) \quad (4.5)$$

$$K(t) = K \left( 1 - \bar{k}^p \left( 1 - e^{-t/\tau} \right) \right) \quad (4.6)$$

where  $\tau$  is the time constant for the material.  $\bar{g}^p$  and  $\bar{k}^p$  are dimensionless Prony series parameters used in the calculation of long-term shear ( $G(t)$ ) and bulk ( $K(t)$ ) moduli, respectively. The subscripts ‘cyto’ and ‘nucl’ are used to denote passive material properties associated with the cytoplasm and nucleus, respectively.

#### 4.2.6 Finite element model development

Cell base radius ( $R_C$ ), nucleus radius ( $R_N$ ), and cell height ( $H_C$ ) are acquired from fluorescent and brightfield images using ImageJ software and are used to determine cell geometries (Figure 4.2). Cell and nucleus radii are calculated from a sample of measured areas (Figure 4.2-A). Height is measured directly from

brightfield side view images (Figure 4.2-B). An axisymmetric mesh is generated based on geometrical measurements. An axisymmetric rigid body is used for the micropipette and micropipette-cell contact is assumed to be frictionless. It should be noted that for the axisymmetric cell geometry, the full 3D stress tensor is calculated as SFs are not confined to the axisymmetric plane. Further simulations were performed to ensure that the micropipette fillet radius has a minimal affect on computed aspiration length (data not shown). A rigidly bonded interaction between the cell and substrate is assumed.

Before MA is simulated in contractile cells, an equilibrium distribution of SFs is computed in the cell. This initial analysis step represents the seeding of untreated contractile cells on the substrate. This step is not required for cytoD cell simulations. In the next analysis step, the micropipette is moved into a position so that it is just in contact with the cell membrane, and pressure is ramped up linearly over a 5 s period using a user-defined non-uniform distributed load subroutine. In order to mimic experimentally applied loading, pressure is applied to the cell membrane within the micropipette only. The constant pressure is maintained for a further 300 s while deformation occurs. The aspiration length is measured as the distance from the micropipette entrance to the furthestmost point of the cell within the micropipette, similar to experimental methods.

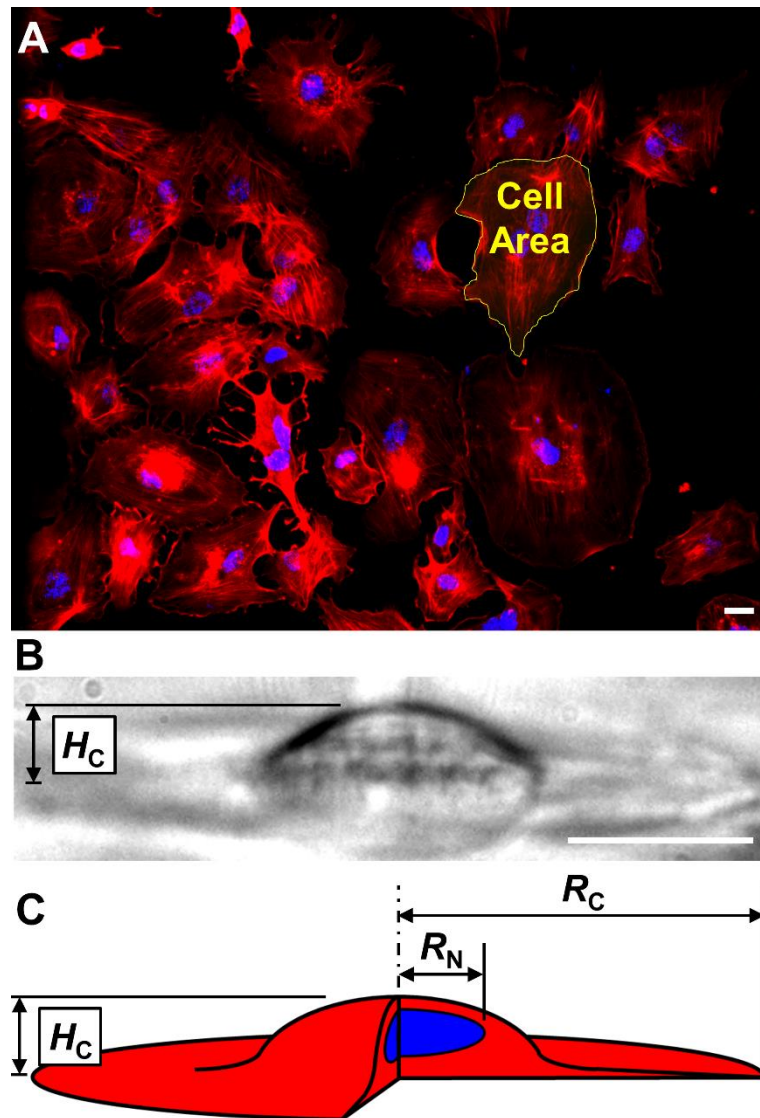


Figure 4.2: To generate cell geometries fluorescent and brightfield images of cells are utilised. (A) By measuring the area of cells and nuclei in fluorescent images, cell base radius ( $R_C$ ) and nucleus radius ( $R_N$ ) can be calculated. (B) Cell height ( $H_C$ ) is measured directly from brightfield images. (C) Diagram of an idealised axisymmetric cell geometry indicating cell height and base radius. Magnification of fluorescent image is 10x. Scale bars = 20  $\mu\text{m}$ .

## 4.3 Results

### 4.3.1 MA of untreated and cytoD treated adhered cells

In Figure 4.3-A, typical experimental images of cytoD treated and untreated cells are shown prior to the application of the aspiration pressure. A spread morphology is observed for untreated contractile cells (Figure 4.3-A(i)) with a highly developed network of SFs (Figure 4.2-A). Treatment with cytoD results in a

break-down of all SFs in the cell, altering the morphology (as illustrated in Appendix A). Prior to aspiration, the measured height of cytoD cells is found to be  $9.2 \pm 2.0 \mu\text{m}$  (Figure 4.3-A(iii)) compared to  $6.8 \pm 1.6 \mu\text{m}$  for untreated cells. This demonstrates that the contractile action of the actin cytoskeleton reduces cell height.

Upon the application of a 100 Pa pressure, the cell aspirates approximately  $5.3 \pm 1.9 \mu\text{m}$  into the micropipette after 300 s, as shown in Figure 4.3-A(ii). Application of a 100 Pa pressure to the cytoD treated cell results in a much higher aspiration length of  $10.8 \pm 2.0 \mu\text{m}$  (Figure 4.3-A(iv)). This demonstrates that the removal of the actin cytoskeleton results in a more deformable cell.

Figure 4.3-B shows normalised aspiration length as a function of time for untreated and cytoD cells. CytoD cell aspiration length is significantly higher than that of an untreated cell ( $p < 0.05$  at all time points); aspiration lengths for cytoD cells are ~2 times higher than untreated cells over the 300 second time span following pressure application. A similar curve shape is observed for both groups, with 70-75% of aspiration occurring within 100 s in all cases. Doubling the cytoD concentration from 1  $\mu\text{M}$  to 2  $\mu\text{M}$  has no statistically significant effect on cytoD aspiration length at any point ( $p > 0.05$ ). The normalised aspiration length as a function of time for experiments in which each cytoD concentration are used are shown in Appendix B.

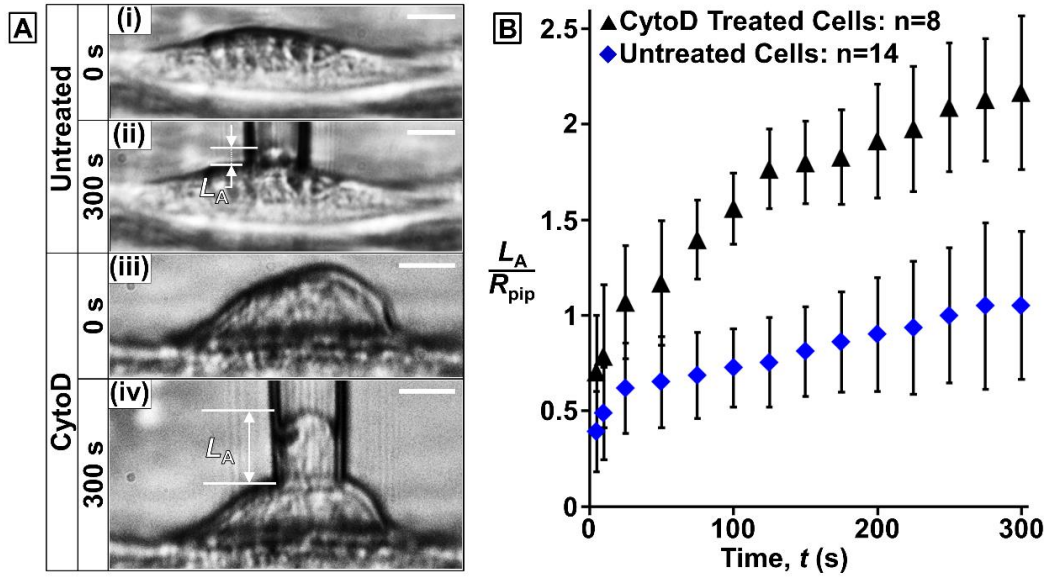


Figure 4.3: (A) Representative brightfield side view images of an adhered untreated contractile cell and a cytoD treated cell are shown. (i) An untreated cell in a sub-confluent monolayer. (ii) Deformation of an untreated cell 300 s after pressure application. (iii) A cytoD treated cell in a sub-confluent monolayer. (iv) Deformation of a cytoD treated cell 300 s after pressure application. (B) Normalised aspiration length is shown as a function of time for cytoD treated and untreated cells. Note that all images and results correspond to a 100 Pa applied pressure. Scale bar = 10  $\mu\text{m}$ .

Table 4.1: Properties for material models used to represent the nucleus and cytoplasm.

	Passive Parameters		Active SF Model Parameters						
Cytoplasm	$G_{cyto}$ (kPa)	$K_{cyto}$ (kPa)	$k_f$	$k_b$	$\sigma_{max}$ (kPa)	$\theta$ (s)	$\bar{k}_v$	$\dot{\epsilon}_0$ ( $\text{s}^{-1}$ )	
	0.026	0.25	1	30	3	70	1	0.003	
Nucleus	$G_{nucl}$ (kPa)	$K_{nucl}$ (kPa)							
	0.07	2.5							

As detailed in Section 4.2.5, cytoD cells are simulated using passive material models. A good fit is established with experimentally measured aspiration data for the cytoD treated cells, as shown in Figure 4.4-A. Hyperelastic material parameters are specified in Table 4.1. Prony series parameters are  $\bar{g}_{cyto}^P = \bar{k}_{cyto}^P = 0.9$  and  $\tau_{cyto} = 20$  s. The contribution of SFs to the mechanical response of untreated cells is simulated via a computational framework that accounts for SF formation, remodelling, and contractility. It is demonstrated in Figure 4.4-A that

the addition of the active framework (in parallel with the passive cytoplasm material behaviour calibrated for the cytoD cell) results in a significant reduction in aspiration length, in agreement with experimental data. Importantly, these active SF model parameters are used, without exception, for all active simulations presented in the current chapter. It should be stressed that the response of the active cell to MA is not achieved by simply calibrating a passive material model; rather, it is achieved by superimposing an active bio-chemo-mechanical framework for SF remodelling and contractility onto the passive material components (calibrated for a cytoD cell above). In essence, Figure 4.4-A demonstrates the ability of the modelling framework to accurately represent the experimentally parsed contribution of the actin cytoskeleton to MA.

In Figure 4.4-B, contour plots of the max principal stresses resulting from simulations are shown. Prior to the application of pressure, significant stresses are computed throughout the cytoplasm of the active cell due to SF contractility (Figure 4.4-B(iii)), whereas the passive cell is in a stress-free state (due to an absence of contractile SFs) (Figure 4.4-B(i)). In Figure 4.4-B(ii) and -B(iv), stress contours in the passive and active cells are shown after a 100 Pa pressure is applied for 60 s. Even though the passive cell is aspirated further into the micropipette, the observed cytoplasm stresses are smaller than in the active cell cytoplasm, showing that the active stresses generated by the SF framework dominate the stress state in the active cell even when applied deformations are large. It should also be noted that the deformed nucleus shape and nucleus stress distribution for the passive cell differs from that of the active cell.

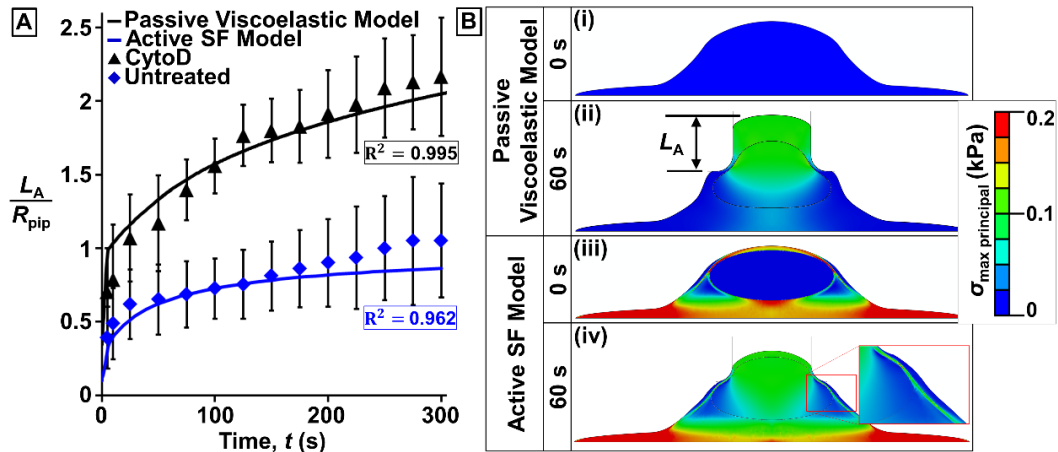


Figure 4.4: (A) Normalised computational and experimental aspiration length as a function of time for untreated and cytoD treated cells subjected to an applied pressure of 100 Pa. (B) Computed distribution of maximum principal stress ( $\sigma_{max\ principal}$ ) in passive and active cell simulations. The passive viscoelastic model is used to simulate cytoD cell response and the active SF model is placed in parallel with the passive viscoelastic model to simulate untreated cell response. (i) Passive model prior to application of applied pressure (stress free reference configuration). (ii) Computed stress state in passive viscoelastic cell 60 s after pressure application. (iii) Stress state in the cell and nucleus prior to application of applied pressure, computed using the active SF model. (iv) Stress state in the cell and nucleus 60 s after pressure application, computed using the active SF model. Insert shows a zoomed image of the stress distribution at the entrance to the micropipette.

### 4.3.2 MA of untreated spread adhered cells over a range of applied pressures

Figure 4.5 shows the normalised experimentally observed aspiration length as a function of time for a range of applied pressures (100 Pa, 500 Pa, and 800 Pa). All tests are performed on untreated contractile cells (it should be noted that full detachment of cytoD treated cells occurred for applied pressures of 500 Pa, whereas untreated cells remain fully adhered for all reported tests). As expected, higher applied pressures result in higher aspiration of the cell into the micropipette. Computational simulations using the active SF framework are also shown in Figure 4.5-A. The active model provides accurate predictions of cell aspiration length for the range of pressures considered experimentally. It is critical to note that active cell model parameters calibrated in Figure 4.4 are used for all simulations presented in Figure 4.5-A. In contrast to the active model, the passive viscoelastic model for the cytoplasm does not provide accurate predictions, as shown in Figure 4.5-B. This

simplified viscoelastic model parameters are fitted to provide a reasonable prediction of the 100 Pa experimental data. However, highly inaccurate results are computed for simulation of the cell response to applied pressures 500 Pa and 800 Pa. This important result clearly demonstrates the inadequacy of passive cell models which ignore the biomechanical behaviour of the actin cytoskeleton. Finally, unless otherwise stated, it should be noted that nucleus properties of  $G_{nucl} = 0.07$  kPa and  $K_{nucl} = 2.5$  kPa are used in all simulations. The mechanical behaviour of the nucleus is considered further in the following section (Section 4.3.3).

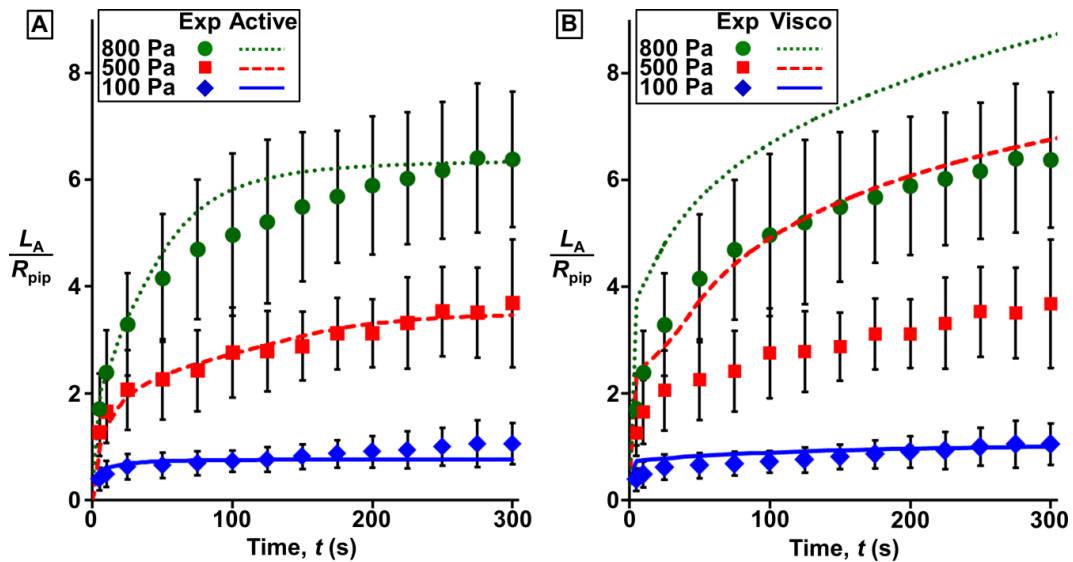


Figure 4.5: Normalised aspiration length as a function of time for untreated cells subjected to a range of applied pressures (100 Pa, 500 Pa, and 800 Pa). Symbols and error bars represent experimental (Exp) results ( $n \geq 10$ ) and lines represent computational predictions. (A) Computed results using the active SF model (Active). (B) Computed results using a passive viscoelastic model (Visco) ( $G_{cyto} = 0.068$  kPa,  $K_{cyto} = 0.67$  kPa,  $\bar{g}_{cyto}^p = \bar{k}_{cyto}^p = 0.9$ ,  $\tau_{cyto} = 40$  s). Experimental results are superimposed in both (A) and (B) for direct comparison with computational predictions.

In Figure 4.6-A(top), a typical brightfield microscopy image of an untreated contractile cell subject to 500 Pa pressure for 300 s is shown. Fluorescent imaging is performed to visualise the actin cytoskeleton and nucleus following MA. By the 3D rendering of z-stacks obtained using confocal microscopy, a side view of a

deformed cell is acquired, as shown in Figure 4.6-A(bottom). It is clear from the side view profile that the nucleus is completely aspirated into the micropipette in the 500 Pa experiment, with SFs being confined to the outer radius of the aspirated section of the cell and the cell base. A computational simulation using the active modelling framework is presented in Figure 4.6-B, showing the predicted deformed cell morphology and SF distribution, again for a 500 Pa MA pressure applied for 300 s. Similar to the experimental image, the entire nucleus is predicted to aspirate into the micropipette. SFs are predicted to extend from the base of the cell into the micropipette. The aspirated SFs are computed near the outer surface of the cell, even in the region below the micropipette where there is no nucleus present (Figure 4.6-B(i)). Inside the micropipette the nucleus occupies the majority of the aspirated volume, with predicted SFs occurring to the sides (Figure 4.6-(ii)) and above (Figure 4.6-B(iii)) the nucleus.

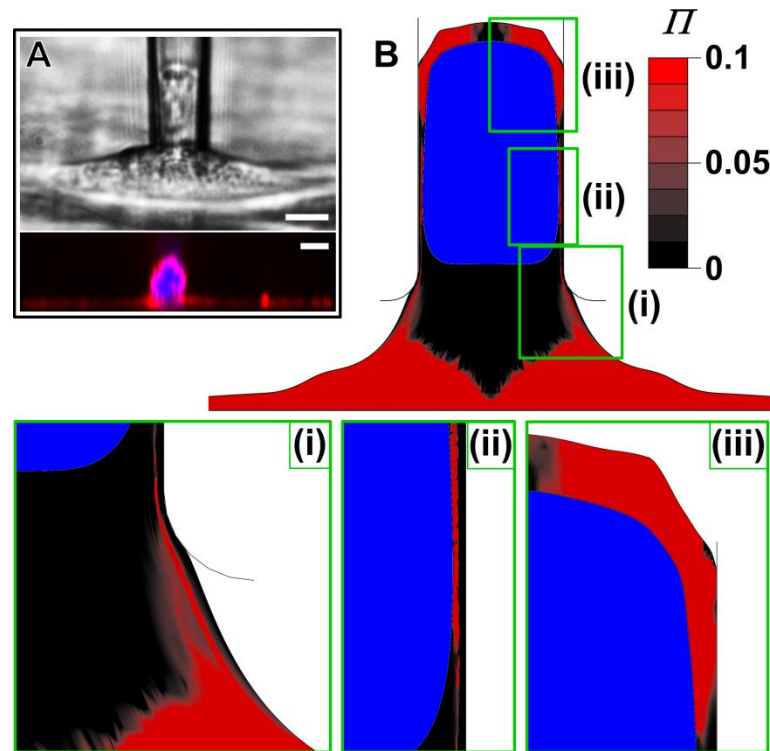
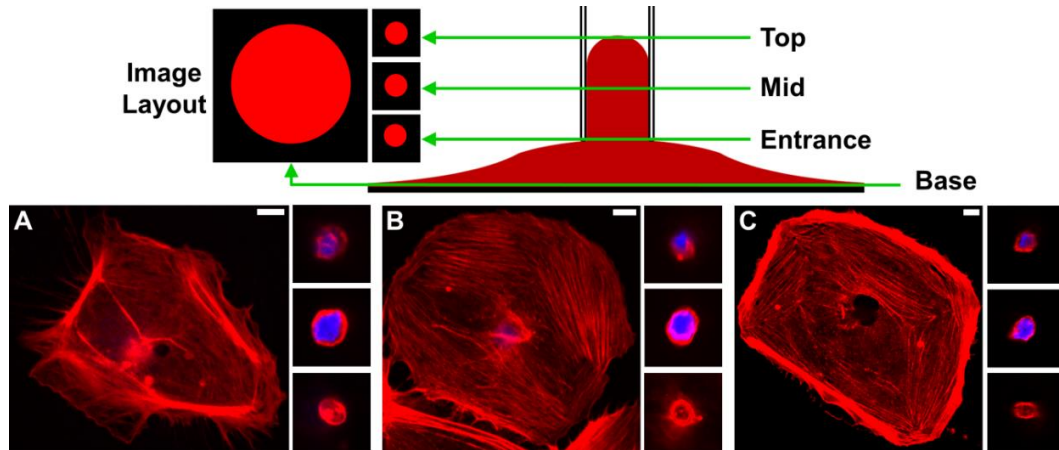


Figure 4.6: (A) Experimental brightfield (top) and 3D rendered fluorescent side view images of aspirated cell (bottom). (B) Computed SF distribution ( $I$ ) in an aspirated cell using the active SF model. Zoomed-in images are shown at: (i) the micropipette entrance; (ii) mid-point of aspirated section; and (iii) top of the aspirated section of the cell. Results shown correspond to a pressure of 500 Pa applied for 300 s. Scale bars = 10  $\mu\text{m}$ .

Further fluorescent images are shown in Figure 4.7; selected z-stacks at four different levels are presented. The base slice in each case shows a significant distribution of SFs near the base of the cell. At the micropipette entrance, fibres are predominantly found at the outer radius of the aspirated portion of the cell. It should be noted that the arrangement of SF at this level is not due to the presence of the nucleus, as the fully aspirated nucleus is positioned above the micropipette entrance in all cases. The aspirated nuclei are surrounded by SFs, as evidenced by the mid aspiration and top of aspiration slices. Out of plane 3D rendered images of two of the aspirated cells are shown in Figure 4.8. Distinct bands of SFs extending vertically in the aspirated portion of the cell can be observed in Figure 4.8-A. Aligned SFs extending into the micropipette entrance are evident in Figure 4.8-B, with a high density of actin in the aspirated section. Kinking or bending of the

aspirated portion can occur due to the fixing and staining protocol performed prior to fluorescent imaging. However, the overall SF distributions are visible from Figures 4.5-4.7 despite this unavoidable experimental drawback.



**Figure 4.7:** Individual z-stack images of aspirated cells fluorescently stained for SFs and nuclei for three cells (A-C). Stacks at the base of the cell (Base), at the micropipette entrance (Entrance), midway along the aspirated section of cell (Mid), and at the top of aspirated section of the cell (Top) are presented. Scale bars = 10  $\mu\text{m}$ .

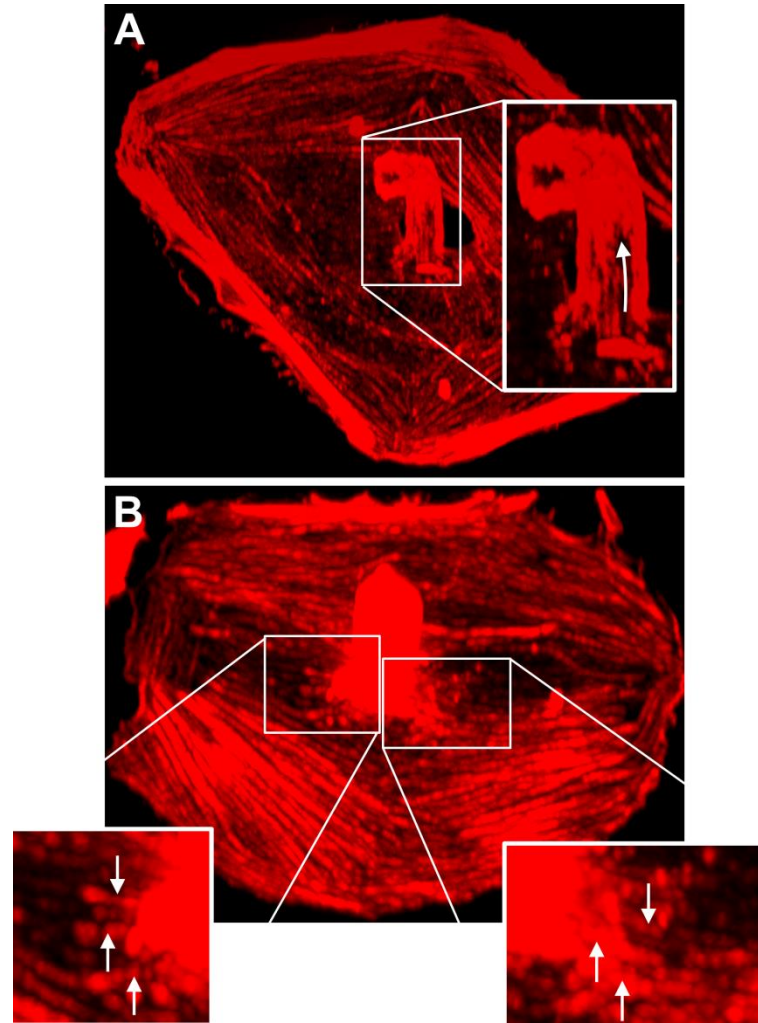


**Figure 4.8:** Out of plane 3D rendered images of the actin cytoskeleton in aspirated cells. (A) Bands of SFs that extend along the aspirated portion of the cell are observed. The arrow in the zoomed-in inset image indicates the direction of the SFs. (B) SFs that extend from the base into the aspirated portion of the cell are indicated in zoomed-in inset images.

### 4.3.3 Investigation of nucleus mechanical behaviour

In all simulations presented above in Sections 4.3.1 and 4.3.2, a nucleus shear modulus of 0.07 kPa and bulk modulus of 2.5 kPa are used. These values are determined from a detailed parametric investigation, as illustrated in Figure 4.9. Simulations are performed for an applied pressure of 500 Pa and corresponding experimental data are reproduced in all plots for comparison. In Figure 4.9-A a parametric investigation of nucleus shear modulus is presented (for a constant bulk modulus of 2.5 kPa). An excellent correlation with experimental results is obtained for a shear modulus 0.07 kPa. An increase in shear modulus from 0.07 to 0.1 kPa

results in a 33% decrease in aspiration length at 300 s, demonstrating that computed aspiration length is highly sensitive to nucleus shear modulus. As is evident in Figure 4.9-A, a change in shear modulus also significantly affects the aspiration rate (slope of the curve), again only a value of 0.07 kPa provides an accurate prediction of experimental results.

In Figure 4.9-B a range of shear moduli is again considered, but for a lower bulk modulus of 0.2 kPa. In this case no value of shear modulus provides an accurate representation of the experimental aspiration curve. For a shear modulus of 0.1 kPa the correct aspiration length is computed at 300 s, but computed values are inaccurate at earlier time points due to an incorrect aspiration rate. It should be noted that, for both the high bulk modulus (Figure 4.9-A) and the low bulk modulus (Figure 4.9-B), the nucleus is computed to fully aspirate into the micropipette only if the shear modulus is less than 0.1 kPa. It should be recalled from the experimental images of Figures 4.5-4.7 that the nucleus fully aspirates into the micropipette for an applied pressure of 500 Pa.

In Figure 4.9-C a range of nucleus bulk moduli is considered while shear modulus is kept at a constant value of 0.14 kPa. In this case no bulk modulus value gives an accurate representation of the experimental aspiration curve. A substantial increase in bulk modulus from 1 kPa to 40 kPa results in only a 12% decrease in aspiration length at 300 s demonstrating that computed aspiration length is relatively insensitive to bulk modulus changes in this range. For a reduction of the bulk modulus to a value less than 1 kPa an increase in aspiration length is computed. However, the computed aspiration rate is not affected by the bulk modulus and is lower than the experimentally observed aspiration rate for a shear modulus of 0.14 kPa considered in Figure 4.9-C. It should also be noted that for this value of shear

modulus, the lowest bulk modulus considered in Figure 4.9-C (0.093 kPa) corresponds to a Poisson's ratio of zero. Therefore, for the given shear modulus (0.14 kPa), full aspiration of the nucleus into the micropipette is not possible, regardless of the bulk modulus used.

In Figure 4.9-D a range of bulk moduli is again considered but for a lower shear modulus of 0.07 kPa. As noted above in Figure 4.9-A, this value of shear modulus in conjunction with a bulk modulus of 2.5 kPa provides a good agreement with the experimental data. However, as is evident in Figure 4.9-D, any value of bulk modulus in the range from 1 kPa to 40 kPa provides a reasonable prediction of the experimental behaviour. For bulk moduli less than 1 kPa computed aspiration lengths are higher than those observed experimentally. However, the computed aspiration rate is insensitive the value of bulk modulus, with all computational curves being parallel to the experimental curve in Figure 4.9-D. Importantly, full aspiration of the nucleus is computed for all simulations reported in Figure 4.9-D.

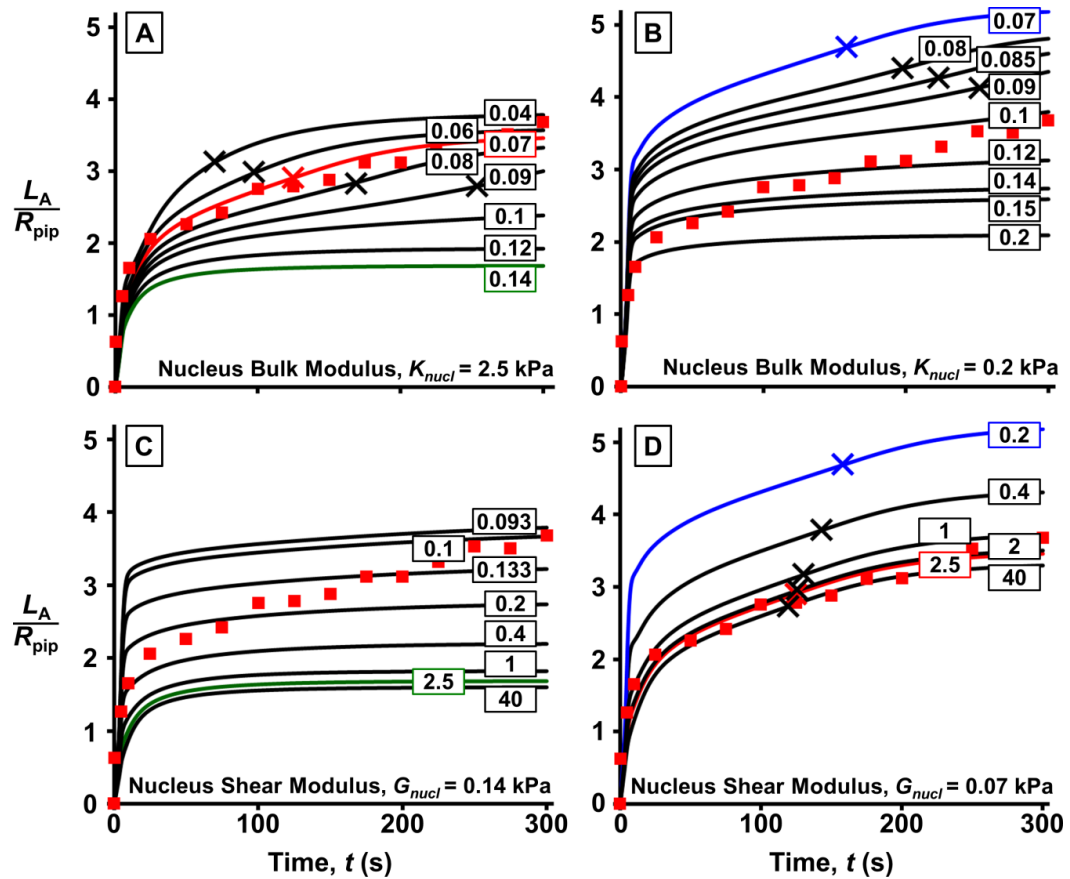
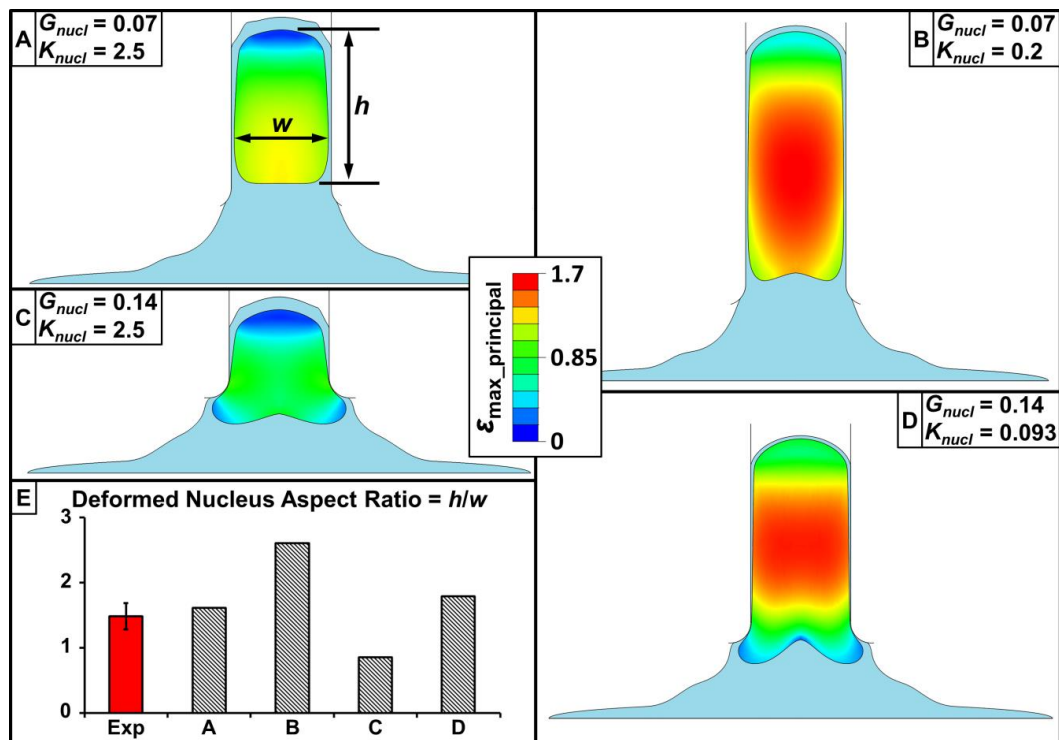


Figure 4.9: Parametric investigation of nucleus material properties. Active SF model is used to simulate the cell response to a 500 Pa applied pressure and different nucleus shear ( $G_{nucl}$ ) and bulk ( $K_{nucl}$ ) modulus values are considered. Normalised aspiration lengths as a function of time are shown and the 500 Pa experimental data is superimposed in all plots (red square data points) for direct comparison with computational results. (A) Shear modulus is varied between 0.04 kPa and 0.14 kPa, with a constant nucleus bulk modulus of 2.5 kPa. (B) Shear modulus is varied between 0.07 kPa and 0.2 kPa with a constant nucleus bulk modulus of 0.2 kPa. (C) Bulk modulus is varied between 0.093 kPa and 40 kPa, with a constant nucleus shear modulus of 0.14 kPa. (D) Bulk modulus is varied between 0.2 kPa and 40 kPa, with a constant nucleus shear modulus of 0.07 kPa. The curve that best fit the 500 Pa experimental data is indicated as the red solid line (found in (A) and (D)), with shear and bulk modulus values of 0.07 kPa and 2.5 kPa, respectively.

Finally, the deformed cell and nucleus morphology following an applied pressure of 500 Pa for 300 s is shown in Figure 4.10-A for the best fit nucleus properties, as determined in Figure 4.9 ( $G_{nucl} = 0.07$  kPa and  $K_{nucl} = 2.5$  kPa). The fully aspirated nucleus is positioned above the entrance to the micropipette, as observed in experimental images (Figure 4.6-A (bottom) and Figure 4.7-(A-C)). The aspect ratio of the deformed nucleus is computed as 1.6, which is within the standard deviation of the experimentally measured value ( $1.5 \pm 0.20$ ) (Figure 4.10-E). As shown in Figure 4.10-B, when the bulk modulus is reduced to 0.2 kPa both

the computed aspiration length (as shown in Figure 4.9-B) and nucleus aspect ratio exceed the values observed experimentally. As shown in Figure 4.10-C and -D the value of shear modulus is excessively high, preventing full aspiration of the nucleus into the micropipette. In addition to predicting incorrect aspiration curves (as shown in Figure 4.9-C), incorrect nucleus aspect ratios are also computed (Figure 4.10-E). In relation to the most accurate prediction of nucleus aspect ratio (Figure 4.10-A), it should be noted that extremely high values of maximum principal strain ( $\sim 130\%$ ) are computed in the nucleus, demonstrating that the cell nucleus is highly deformable. As expected, an inaccurate prediction of cell aspiration length results in an inaccurate prediction of nucleus strain.



**Figure 4.10:** Using the active SF model in the cytoplasm, computed deformation is presented for cells in which different sets of nucleus shear ( $G_{nuc1}$ ) and bulk ( $K_{nuc1}$ ) modulus values are used. Associated normalised aspiration lengths can be found in Figure 4.9. The distribution of the computed maximum principal strain ( $\epsilon_{\max\_principal}$ ) is shown in the deformed cell nuclei. Deformation is shown for simulations in which: (A) the best fit shear and bulk moduli are used in the nucleus (as indicated by the red curve in the nucleus parametric study presented in Figure 4.9); (B) the best fit shear modulus and a relatively low bulk modulus are used in the nucleus; (C) a relatively high shear modulus and the best fit bulk modulus are used in the nucleus; and (D) a relatively high shear modulus is used in the nucleus with a very low bulk modulus. (E) Experimentally (Exp) measured nucleus aspect ratio (mean  $\pm$  standard deviation) and computed results for A-D above.

## 4.4 Discussion

The current chapter presents an investigation of the role of the actin cytoskeleton in the micropipette aspiration (MA) of spread adhered cells. The following key contributions are highlighted: (i) a custom system is developed to allow visualisation of the MA of adhered cells, uncovering the contribution of the actin cytoskeleton to cell aspiration; (ii) it is demonstrated that an active computational framework that incorporates SF remodelling and contractility must be used in order to accurately simulate the MA of untreated cells; and (iii) experimental imaging reveals that the cell nucleus is fully aspirated into the micropipette at higher applied pressures, with corresponding computational simulations demonstrating that the nucleus is highly deformable, undergoing high levels of strain (>100%). These key findings present a significant advance on previous MA studies and to the general understanding of the role of the actin cytoskeleton and nucleus to cell biomechanical behaviour.

A custom MA system for the biomechanical investigation of cells adhered to a substrate is used in the current chapter. Due to the complexity of visualising MA of substrate adhered cells, previous MA studies have focused primarily on cells suspended in media. In particular, suspended endothelial cells (Sato et al., 1987b, Sato et al., 1987a, Sato et al., 1990, Sato et al., 1996), suspended chondrocytes (Jones et al., 1999, Trickey et al., 2000, Trickey et al., 2004, Trickey et al., 2006, Ohashi et al., 2006, Guilak et al., 2000, Pravin Kumar et al., 2012), suspended stem cells (Tan et al., 2008, Yu et al., 2010, Ribeiro et al., 2012), and suspended fibroblasts (Thoumine and Ott, 1997a, Zhou et al., 2010) have been tested using the MA technique. However such studies are of limited value as these cell phenotypes

are typically not found suspended *in vivo*; rather, they adhere to an extra cellular matrix. Moreover, the cytoskeletal structure and biomechanical behaviour of such cells is markedly different when adhered to a substrate, in comparison to the suspended state (Sato et al., 1987b, Reinhart-King et al., 2005, Haghparast et al., 2013). Therefore, the development of an MA system for the investigation of the biomechanical behaviour of cells when adhered to a substrate is of significant value. In an effort to study the mechanical behaviour of spread adhered endothelial cells, Byfield et al. (2004) oriented a micropipette parallel to the substrate, leading to highly localised measurements at the outer edge of the cell-substrate contact region. In order to achieve non-localised measurements representative of whole cell behaviour, a precisely-positioned large diameter micropipette aligned perpendicular to the substrate should be used. In the study of Thoumine et al. (1999) the substrate was rotated by 90° to facilitate visualisation of the aspirated cell. However, using this approach the micropipette can be viewed only from the side, hence precise three-dimensional positioning of the micropipette over the centre of the cell is not possible. Furthermore, relocation of aspirated cells post-aspiration for a confocal microscopy investigation of the stained deformed actin cytoskeleton is not possible using this approach. In the current chapter, a custom designed system that allows for both side and bottom-up views of cells and the micropipette is developed. This facilitates: (i) the precise three-dimensional positioning of the micropipette over the centre of the cell using multiple perspectives; and (ii) the visualisation of the aspirated section of adhered cells using a micropipette aligned perpendicular to the substrate. The system also enables further examination of the actin cytoskeleton of aspirated cells using confocal microscopy.

It is demonstrated in the current chapter that untreated contractile spread adhered cells undergo significantly less aspiration into the micropipette than cells in which the actin cytoskeleton has been chemically inhibited (cytoD cells); therefore, the actin cytoskeleton increases the resistance of cells to MA. Fluorescent staining demonstrates that SFs are stretched into the micropipette during MA. Clearly the tension exerted by aspirated stretched SFs contributes significantly to the mechanical response of the cell. The current chapter demonstrates that MA provides a robust and controlled experimental method of applying a tensile load to *in cyto* actively contractile SFs. Previous efforts to characterise the tensile behaviour of SFs have relied on isolation/extraction of individual SFs from the cell, followed by tensile testing (Kato et al., 1998). It is important to note that isolated/extracted SFs behave as a passive material (Deguchi et al., 2006), neglecting the critically important features of active myosin induced cross-bridge cycling and remodelling. The applicability of the active SF formulation used in the current chapter has been validated for a range of cell phenotypes and loading regimes (McGarry et al., 2009, Ronan et al., 2012). A recent study of single chondrocytes by Dowling et al. (2012) has demonstrated that localised stretching of SFs in tensile regions of the cytoplasm during applied shear significantly influences cell resistance to deformation, with dissociation of the actin cytoskeleton being observed in compressive regions of the cell. Additionally, the studies of Ronan et al. (2012) and Weafer et al. (2013) demonstrate that during parallel plate compression SFs in particular orientations are stretched, again increasing the resistance of cells to deformation. However, unlike applied shear and parallel plate experiments, the MA technique utilised in the current chapter allows for the application of precise tensile loads and accurate monitoring of SF strain rates in the

aspirated section. In summary, the experimental observation of SF deformation under a controlled loading regime provides new insight into the mechanism by which the actin cytoskeleton contributes to the deformation resistance of spread cells. This may inform tissue engineering strategies (Shen et al., 2003, Shieh and Athanasiou, 2003) and may have important implications for new pathologies (Roy et al., 2009, Campbell et al., 2007, Duncan and Turner, 1995). A link between actively generated cell tension and collagen production in a micro-tissue construct has recently been reported (Kural and Billiar, 2014). The experimental-computational approach presented in the current paper provides an advanced understanding of the relationship between externally applied force, SF active contractility, and nucleus deformation. Such a fundamental understanding at a single cell level is critical for the development of next-generation strategies for the precise engineering of tissue constructs. A recent study highlights the ability of the active SF modelling framework to guide the *in vitro* engineering of cardiac tissue (Thavandiran et al., 2013).

Previous studies have used simplified passive models analytical or numerical models of passive homogeneous elastic or viscoelastic cells to interpret experimentally observed aspiration curves (Sato et al., 1990, Theret et al., 1988, Jones et al., 1999, Xinyu et al., 2009, Sato et al., 1996, Byfield et al., 2004, Baaijens et al., 2005, Trickey et al., 2006, Zhou et al., 2005, Zhao et al., 2009, Jafari Bidhendi and Korhonen, 2012, Haider and Guilak, 2002, Haider and Guilak, 2000). Typically such studies report elastic or viscoelastic material parameters based on a curve fit of experimental results. While it could be argued that a viscoelastic model may have some validity for the simulation of a un-adhered suspended cell, which do not contain a network of SFs, the current chapter clearly demonstrates such a simplistic

modelling approach is not appropriate for spread adhered cells. Specifically, it is demonstrated that such a passive material model does not capture the experimentally observed response if the applied pressure is changed. Hence the curve-fitting of viscoelastic material properties to a MA curve is entirely dependent on the applied pressure used experimentally. In addition to the inability of a passive viscoelastic cell model to predict cell aspiration over a range of applied pressures, an earlier study by Thoumine et al. (1999) demonstrates that elastic stiffness and viscosity must be significantly altered as a function of the level of cell spreading. Furthermore, a study by McGarry and McHugh (2008) demonstrates that when the cytoplasm is modelled as a passive viscoelastic, the cell elastic stiffness must be artificially increased as a function of spreading in order to capture *in vitro* cell detachment forces.

In the current chapter an active SF framework is used to investigate the biomechanical role of the actin cytoskeleton during the MA of spread adhered cells. It is demonstrated that the simulation of SF remodelling and contractility throughout the cytoplasm is critical in order to accurately predict experimentally observed cell response to a wide range (100 Pa - 800 Pa) of applied pressures. Furthermore, the predicted distribution of SFs is closely aligned with results of fluorescent images, i.e. SFs stretch along the long axis of the aspirated section of the cell forming a peripheral ring at the inner wall of the micropipette. The stretching of aligned contractile SFs along the axis of the micropipette provides an increased resistance to MA. When SFs are eliminated using the cytoD treatment the reduced resistance to deformation results in significantly increased aspiration length for applied pressures of 100 Pa, and aspiration of the entire cell into the micropipette at higher pressures ( $\geq 500$  Pa). It has been widely established in previous

experimental studies that the actin cytoskeleton remodels during cell spreading, with spread cells exhibiting a highly developed network of contractile SFs (Haghparast et al., 2013, Reinhart-King et al., 2005, Huang et al., 2003, Barreto et al., 2013, Li et al., 2007, Lemmon et al., 2005, Tee et al., 2011). The development of a network of contractile SFs underlies the vast differences in “apparent stiffness” between round and spread cells (Caille et al., 2002, Thoumine et al., 1999, Darling et al., 2008). Furthermore, highly contractile cell phenotypes exhibit a higher apparent stiffness when subjected to cell compression. For example, very high compression forces (~2500 nN) have been reported for spread myoblasts (Peeters et al., 2005) whereas lower compression forces (~360 nN) have been reported for less contractile fibroblasts (Deng et al., 2010). A recent study by Ronan et al. (2012) demonstrates that the active SF model used in the current chapter is capable of capturing the relationship between the level of cell contractility and the compression resistance of spread cells. The current chapter advances on this work, providing a detailed experimental-computational quantitative analysis of the role of SF elongation during cell MA.

The current chapter provides a detailed investigation of nucleus deformation in single spread adhered cells subjected to MA. In the absence of external loading the coupled interaction between the actin cytoskeleton and the cell nucleus has recently been investigated experimentally (Li et al., 2014, Weafer et al., 2013), where it is shown that the contractile action of apical SFs result in changes in nucleus morphology. Building upon this work, the MA technique presented in the current chapter allows for the precise application of force to this key region of the cell, and measurement of the resultant nucleus deformation and stress fibre extension/remodelling. This provides new data for validation and calibration of

constitutive models for the nucleus and surrounding SFs, as presented in the current paper. A high level of nucleus deformation is observed; nuclei are fully aspirated into the micropipette for pressures of 500 Pa or higher, with nucleus strains in excess of 100% being computed. Simulations suggest that complete aspiration of the nucleus into the micropipette occurs only for very low nucleus shear modulus values ( $G_{\text{nucl}} < 0.1$  kPa). Simulating isolated nuclei, Vaziri and Mofrad (2007) also computes a low shear modulus based on experimental data for isolated endothelial cell nuclei (Deguchi et al., 2005) and isolated chondrocyte nuclei (Guilak et al., 2000). However, it should be noted that nucleus mechanical behaviour may be altered by the isolation technique used. It is demonstrated by Guilak et al. (2000) that the long term mechanical properties of nuclei isolated using chemical and mechanical techniques are significantly different. Previous experimental studies of MA of suspended cells also reveal significant nucleus deformation (Pajerowski et al., 2007, Dahl et al., 2005, Rowat et al., 2006, Ribeiro et al., 2012). Furthermore, Pajerowski et al. (2007) report that permanent viscoplastic deformation of the nucleus occurs due lamin A/C and chromatin remodelling. A careful characterisation of nucleus deformation, as presented in the current chapter for spread adhered cells, and in the study of Pajerowski et al. (2007) for suspended cells, is of critical importance as nucleus deformation has been linked to cell mechanotransduction due to the reshaping of nuclear lamina and alterations in chromatin distribution (Dahl et al., 2008, Rowat et al., 2008, Tsukamoto et al., 2000). Direct modulation of nuclear shape has been shown to affect the regulation of type II collagen as well as gene expression (Campbell et al., 2007, Buschmann et al., 1996, Shieh and Athanasiou, 2007, Thomas et al., 2002). Significant deformation of the nucleus has been observed in situ (Henderson et al., 2013, Tsai

et al., 2005), and may have significant implications for in vivo mechanotransduction and cell migration. A high level of deviatoric deformation of the nucleus during MA is computed in the current chapter. Anderson and Knothe Tate (2007) report that such a stress state will result in stem cell differentiation towards an endothelial lineage. The characterisation of nucleus behaviour presented in the current chapter may aid the development and calibration of microfluidic devices for cell sorting (Yamada et al., 2007) and direct cytosolic delivery of transcription factors (Sharei et al., 2013).

Using the system described in the current chapter, a mirror is aligned at  $45^\circ$  in order to provide side view visualisation of cells. However, a limitation of this setup is that the mirror obstructs the light source of the microscope and makes it difficult to manoeuvre the micropipette into position beneath the mirror. In a previous study by Cao et al. (1997), two mirrors are used to obtain side view images of cells subjected to fluid flow. The first mirror redirects light coming downwards from the microscopes light source across the substrate. A second mirror, on the opposite side of the substrate to the first mirror, redirects this light downwards to the microscope objective. Using a similar methodology in the experimental system described in the current chapter would negate the need for a separate light source and custom built micropipettes, and reduce difficulties manoeuvring the micropipette into position. However, custom built mirrors would be required. Another potential limitation of the current chapter is that cells are assumed to be rigidly bonded to the substrate in simulations. In reality, cells are adhered to the substrate, primarily via focal adhesions attachments. In a previous study by Dowling and McGarry (2013), a cohesive zone model is used to investigate cell-substrate adhesion rupture during applied shear. In separate simulations in the

current chapter, the same cohesive zone model and parameters were included and no rupture of the cell from the substrate was predicted (results not shown), in line with experimental observations. Furthermore, the reaction force of the substrate at the end of simulations in the current chapter was negligible. Deshpande et al. (2008) proposed an active framework in which actin cytoskeleton contractility is coupled with traction dependant focal adhesion formation and growth. Such a model could be included to investigate the experimental results. Furthermore, using the experimental platform described in the current chapter, future studies in which the cell is retracted from the substrate post aspiration could be used to investigate the mechanical behaviour of focal adhesion rupture.

The current chapter presents a number of significant advances in the field of experimental and computational single cell biomechanics, providing a platform for several further investigations. Future experiments in which the level of cell spreading is controlled via micro-patterned substrates should be performed to further investigate the relationship between cell geometry and the development of a highly contractile actin cytoskeleton (They et al., 2006, Chen et al., 1998). Furthermore, the role of substrate stiffness and adhesion promoting proteins (Byfield et al., 2009, Solon et al., 2007, Shao et al., 2000) in the biomechanical response of spread adhered cells to MA should be considered. The current technique only allows observation of SFs at the end of aspiration experiments. In order to observe the evolution of the actin cytoskeleton and nucleus deformation during experiments, fluorescent staining could be performed at a number of time points or live imaging techniques could be implemented, for example using F-actin transfection. Live imaging could also allow measurement of intracellular strain in experiments by tracking specific markers such as mitochondria in the cytoplasm

(Knight et al., 2006) or DNA in the nucleus (Henderson et al., 2013). A recent study by Dowling et al. (2012) demonstrates that the mechanical response of cells to applied shear is primarily influenced by the actin cytoskeleton, while the disruption of microtubules and intermediate filaments had a less significant effect on chondrocyte response. A future MA study in which microtubules and intermediate filaments are systematically disrupted would allow for the investigation of the role of these cytoskeletal components in the regulation of nucleus deformation. MA induced membrane and nucleus stretch could be used to examine the enhanced intracellular delivery of macromolecules such as carbon nanotubes, proteins, and siRNA (Sharei et al., 2013).

A custom system that facilitates the visualisation of adhered cells during MA is developed to experimentally investigate the contribution of the actin cytoskeleton to the spread cell biomechanical response. Additionally, computational simulations are performed in order to interpret experimentally observed phenomena. The current experimental-computational investigation uncovers a number of significant findings: (i) The significant contribution of the actin cytoskeleton to cell biomechanical behaviour during MA is demonstrated experimentally; (ii) a passive viscoelastic material model is not capable of capturing experimentally measured aspiration lengths over a range of applied pressures; (iii) an active SF model, including the key features of remodelling and contractility of the actin cytoskeleton, accurately predicts the response the cells over a range of applied pressures and the redistribution and stretching of SFs into the aspirated portion of the cell; and (iv) finally, a detailed experimental-computational investigation of the nucleus mechanical behaviour demonstrates that the nucleus is highly deformable *in cyto*, reaching strain levels in excess of 100% during MA.

These findings represent a significant advancement in the understanding of the characterisation of the biomechanical behaviour of the actin cytoskeleton and cell nucleus.

## Appendix 4.A

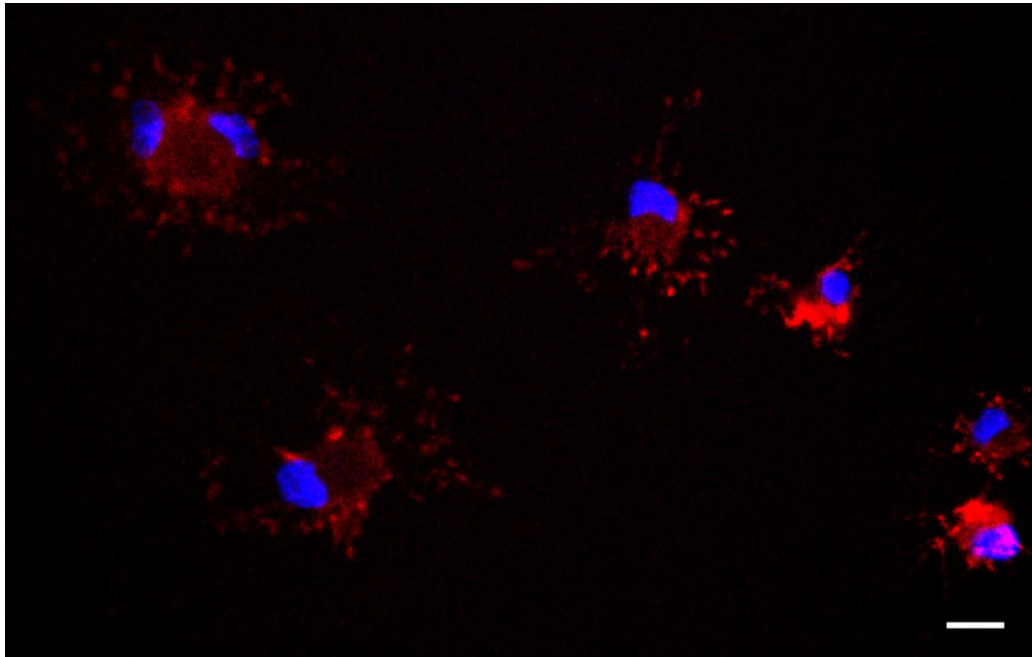


Figure A1: Representative fluorescent image of cytochalasin-D treated cells (cytoD cells) with actin shown in red and nuclei shown in blue. Scale bar = 20  $\mu\text{m}$

## Appendix 4.B

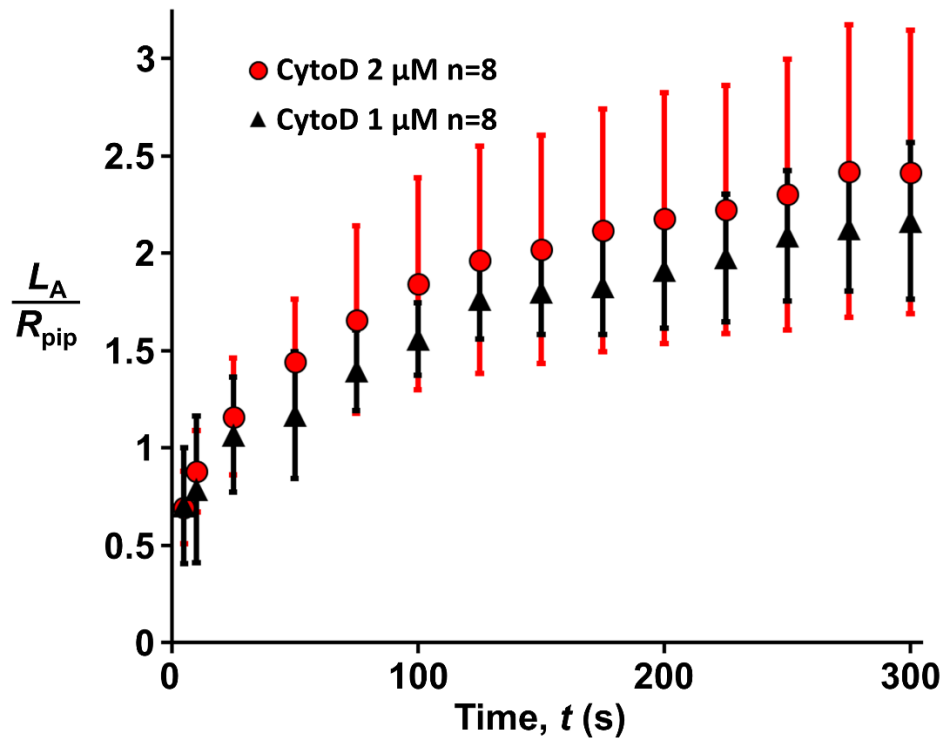


Figure B1: Normalised aspiration length shown as a function of time for cells treated with two different concentrations of cytoD. Note that all results correspond to a 100 Pa applied pressure.

## 4.5 References

- ALI, M. H., PEARLSTEIN, D. P., MATHIEU, C. E. & SCHUMACKER, P. T. 2004. Mitochondrial requirement for endothelial responses to cyclic strain: implications for mechanotransduction. *Am J Physiol Lung Cell Mol Physiol*, 287, L486-96.
- ANDERSON, E. J. & KNOTHE TATE, M. L. 2007. Design of tissue engineering scaffolds as delivery devices for mechanical and mechanically modulated signals. *Tissue Eng*, 13, 2525-38.
- BAAIJENS, F. P. T., TRICKEY, W. R., LAURSEN, T. A. & GUILAK, F. 2005. Large Deformation Finite Element Analysis of Micropipette Aspiration to Determine the Mechanical Properties of the Chondrocyte. *Ann Biomed Eng*, 33, 494-501.
- BARRETO, S., CLAUSEN, C. H., PERRAULT, C. M., FLETCHER, D. A. & LACROIX, D. 2013. A multi-structural single cell model of force-induced interactions of cytoskeletal components. *Biomaterials*, 34, 6119-6126.
- BUSCHMANN, M. D., HUNZIKER, E. B., KIM, Y. J. & GRODZINSKY, A. J. 1996. Altered aggrecan synthesis correlates with cell and nucleus structure in statically compressed cartilage. *J Cell Sci*, 109(Pt 2), 499-508.
- BYFIELD, F. J., ARANDA-ESPINOZA, H., ROMANENKO, V. G., ROTHBLAT, G. H. & LEVITAN, I. 2004. Cholesterol depletion increases membrane stiffness of aortic endothelial cells. *Biophys J*, 87, 3336-3343.

- BYFIELD, F. J., REEN, R. K., SHENTU, T. P., LEVITAN, I. & GOOCH, K. J. 2009. Endothelial actin and cell stiffness is modulated by substrate stiffness in 2D and 3D. *J Biomech*, 42, 1114-9.
- CAILLE, N., THOUMINE, O., TARDY, Y. & MEISTER, J.-J. 2002. Contribution of the nucleus to the mechanical properties of endothelial cells. *J Biomech*, 35, 177-187.
- CAMPBELL, J. J., BLAIN, E. J., CHOWDHURY, T. T. & KNIGHT, M. M. 2007. Loading alters actin dynamics and up-regulates cofilin gene expression in chondrocytes. *Biochem Biophys Res Commun*, 361, 329-334.
- CAO, J., USAMI, S. & DONG, C. 1997. Development of a side-view chamber for studying cell-surface adhesion under flow conditions. *Ann Biomed Eng*, 25, 573-80.
- CHEN, C. S., MRKSICH, M., HUANG, S., WHITESIDES, G. M. & INGBER, D. E. 1998. Micropatterned surfaces for control of cell shape, position, and function. *Biotechnol Prog*, 14, 356-363.
- CUSCHLERI, J., GOURLAY, D., GARCIA, I., JELACIC, S. & MAIER, R. V. 2003. Endotoxin-induced endothelial cell proinflammatory phenotypic differentiation requires stress fiber polymerization. *Shock*, 19, 433-9.
- DAHL, K. N., ENGLER, A. J., PAJEROWSKI, J. D. & DISCHER, D. E. 2005. Power-law rheology of isolated nuclei with deformation mapping of nuclear substructures. *Biophys J*, 89, 2855-64.
- DAHL, K. N., RIBEIRO, A. J. & LAMMERDING, J. 2008. Nuclear shape, mechanics, and mechanotransduction. *Circ Res*, 102, 1307-18.
- DARLING, E. M., TOPEL, M., ZAUSCHER, S., VAIL, T. P. & GUILAK, F. 2008. Viscoelastic properties of human mesenchymally-derived stem cells and primary osteoblasts, chondrocytes, and adipocytes. *J Biomech*, 41, 454-64.
- DEGUCHI, S., MAEDA, K., OHASHI, T. & SATO, M. 2005. Flow-induced hardening of endothelial nucleus as an intracellular stress-bearing organelle. *J Biomech*, 38, 1751-1759.
- DEGUCHI, S., OHASHI, T. & SATO, M. 2006. Tensile properties of single stress fibers isolated from cultured vascular smooth muscle cells. *J Biomech*, 39, 2603-2610.
- DENG, Z., LULEVICH, V., LIU, F. T. & LIU, G. Y. 2010. Applications of atomic force microscopy in biophysical chemistry of cells. *J Phys Chem B*, 114, 5971-82.
- DESHPANDE, V. S., MCMEEKING, R. M. & EVANS, A. G. 2007. A model for the contractility of the cytoskeleton including the effects of stress-fibre formation and dissociation. *Proc Math Phys Eng Sci*, 463, 787-815.
- DESHPANDE, V. S., MRKSICH, M., MCMEEKING, R. M. & EVANS, A. G. 2008. A bio-mechanical model for coupling cell contractility with focal adhesion formation. *Journal of the Mechanics and Physics of Solids*, 56, 1484-1510.
- DOWLING, E. P. & MCGARRY, J. P. 2013. Influence of Spreading and Contractility on Cell Detachment. *Ann Biomed Eng*.
- DOWLING, E. P., RONAN, W., OFEK, G., DESHPANDE, V. S., MCMEEKING, R. M., ATHANASIOU, K. A. & MCGARRY, J. P. 2012. The effect of remodelling and contractility of the actin cytoskeleton on the shear resistance of single cells: a computational and experimental investigation. *J R Soc Interface*, 9, 3469-79.
- DUNCAN, R. & TURNER, C. 1995. Mechanotransduction and the functional response of bone to mechanical strain. *Calcified tissue international*, 57, 344-358.
- GUILAK, F., JONES, W. R., TING-BEALL, H. P. & LEE, G. M. 1999. The deformation behavior and mechanical properties of chondrocytes in articular cartilage. *Osteoarthritis Cartilage*, 7, 59-70.
- GUILAK, F., TEDROW, J. R. & BURGKART, R. 2000. Viscoelastic properties of the cell nucleus. *Biochem Biophys Res Commun*, 269, 781-786.

- HAGHPARAST, S. M. A., KIHARA, T., SHIMIZU, Y., YUBA, S. & MIYAKE, J. 2013. Actin-based biomechanical features of suspended normal and cancer cells. *J Biosci Bioeng*, 116, 380-385.
- HAIDER, M. A. & GUILAK, F. 2000. An axisymmetric boundary integral model for incompressible linear viscoelasticity: application to the micropipette aspiration contact problem. *J Biomech Eng*, 122, 236-244.
- HAIDER, M. A. & GUILAK, F. 2002. An axisymmetric boundary integral model for assessing elastic cell properties in the micropipette aspiration contact problem. *J Biomech Eng*, 124, 586-95.
- HAYAKAWA, K., TATSUMI, H. & SOKABE, M. 2008. Actin stress fibers transmit and focus force to activate mechanosensitive channels. *J Cell Sci*, 121, 496-503.
- HENDERSON, J. T., SHANNON, G., VERESS, A. I. & NEU, C. P. 2013. Direct measurement of intranuclear strain distributions and RNA synthesis in single cells embedded within native tissue. *Biophys J*, 105, 2252-2261.
- HOCHMUTH, R. M. 2000. Micropipette aspiration of living cells. *J Biomech*, 33, 15-22.
- HUANG, W., ANVARI, B., TORRES, J. H., LEBARON, R. G. & ATHANASIOU, K. A. 2003. Temporal effects of cell adhesion on mechanical characteristics of the single chondrocyte. *J Orthop Res*, 21, 88-95.
- JAFARI BIDHENDI, A. & KORHONEN, R. K. 2012. A Finite Element Study of Micropipette Aspiration of Single Cells: Effect of Compressibility. *Comput Math Method M*, 2012, 192618.
- JONES, W. R., PING TING-BEALL, H., LEE, G. M., KELLEY, S. S., HOCHMUTH, R. M. & GUILAK, F. 1999. Alterations in the Young's modulus and volumetric properties of chondrocytes isolated from normal and osteoarthritic human cartilage. *J Biomech*, 32, 119-127.
- KATOH, K., KANO, Y., MASUDA, M., ONISHI, H. & FUJIWARA, K. 1998. Isolation and contraction of the stress fiber. *Mol Biol Cell*, 9, 1919-38.
- KNIGHT, M. M., BOMZON, Z., KIMMEL, E., SHARMA, A. M., LEE, D. A. & BADER, D. L. 2006. Chondrocyte deformation induces mitochondrial distortion and heterogeneous intracellular strain fields. *Biomech Model Mechanobiol*, 5, 180-91.
- KNUDSEN, H. L. & FRANGOS, J. A. 1997. Role of cytoskeleton in shear stress-induced endothelial nitric oxide production. *Am J Physiol*, 273, H347-55.
- KURAL, M. H. & BILLIAR, K. L. 2014. Mechanoregulation of valvular interstitial cell phenotype in the third dimension. *Biomaterials*, 35, 1128-1137.
- LEMMON, C. A., SNIADOCKI, N. J., RUIZ, S. A., TAN, J. L., ROMER, L. H. & CHEN, C. S. 2005. Shear force at the cell-matrix interface: enhanced analysis for microfabricated post array detectors. *Mech Chem Biosyst*, 2, 1-16.
- LI, B., XIE, L., STARR, Z. C., YANG, Z., LIN, J.-S. & WANG, J. H. C. 2007. Development of micropost force sensor array with culture experiments for determination of cell traction forces. *Cell Motil Cytoskeleton*, 64, 509-518.
- LI, Q., KUMAR, A., MAKHIJA, E. & SHIVASHANKAR, G. V. 2014. The regulation of dynamic mechanical coupling between actin cytoskeleton and nucleus by matrix geometry. *Biomaterials*, 35, 961-9.
- MCGARRY, J. P. 2009. Characterization of cell mechanical properties by computational modeling of parallel plate compression. *Ann Biomed Eng*, 37, 2317-25.
- MCGARRY, J. P., FU, J., YANG, M. T., CHEN, C. S., MCMEEKING, R. M., EVANS, A. G. & DESHPANDE, V. S. 2009. Simulation of the contractile response of cells on an array of micro-posts. *Philos Trans A Math Phys Eng Sci*, 367, 3477-3497.
- MCGARRY, J. P. & MCHUGH, P. E. 2008. Modelling of in vitro chondrocyte detachment. *J Mech Phys Solids*, 56, 1554-1565.

- MUNEVAR, S., WANG, Y.-L. & DEMBO, M. 2001. Traction Force Microscopy of Migrating Normal and H-ras Transformed 3T3 Fibroblasts. *Biophys J*, 80, 1744-1757.
- NAGAYAMA, K. & MATSUMOTO, T. 2010. Estimation of single stress fiber stiffness in cultured aortic smooth muscle cells under relaxed and contracted states: Its relation to dynamic rearrangement of stress fibers. *J Biomech*, 43, 1443-1449.
- NAWAZ, S., SÁNCHEZ, P., BODENSIEK, K., LI, S., SIMONS, M. & SCHAAP, I. A. T. 2012. Cell visco-elasticity measured with AFM and optical trapping at sub-micrometer deformations. *PLoS ONE*, 7, e45297.
- NISHITANI, W. S., SAIF, T. A. & WANG, Y. 2011. Calcium signaling in live cells on elastic gels under mechanical vibration at subcellular levels. *PLoS ONE*, 6, e26181.
- OFEK, G., DOWLING, E. P., RAPHAEL, R. M., MCGARRY, J. P. & ATHANASIOU, K. A. 2010. Biomechanics of single chondrocytes under direct shear. *Biomech Model Mechanobiol*, 9, 153-62.
- OHASHI, T., HAGIWARA, M., BADER, D. L. & KNIGHT, M. M. 2006. Intracellular mechanics and mechanotransduction associated with chondrocyte deformation during pipette aspiration. *Biorheology*, 43, 201-14.
- PAJEROWSKI, J. D., DAHL, K. N., ZHONG, F. L., SAMMAK, P. J. & DISCHER, D. E. 2007. Physical plasticity of the nucleus in stem cell differentiation. *Proc Natl Acad Sci USA*, 104, 15619-15624.
- PEETERS, E. A., OOMENS, C. W., BOUTEN, C. V., BADER, D. L. & BAAIJENS, F. P. 2005. Viscoelastic properties of single attached cells under compression. *J Biomech Eng*, 127, 237-43.
- PRAVINCUMAR, P., BADER, D. L. & KNIGHT, M. M. 2012. Viscoelastic cell mechanics and actin remodelling are dependent on the rate of applied pressure. *PLoS ONE*, 7, e43938.
- PROMOCELL. *Endothelial cells (large vessels) - Instruction manual* [Online]. Heidelberg. Available: <http://www.promocell.com/> [Accessed November 2013].
- REINHART-KING, C. A., DEMBO, M. & HAMMER, D. A. 2005. The dynamics and mechanics of endothelial cell spreading. *Biophys J*, 89, 676-689.
- RIBEIRO, A. J., TOTTEY, S., TAYLOR, R. W., BISE, R., KANADE, T., BADYLAK, S. F. & DAHL, K. N. 2012. Mechanical characterization of adult stem cells from bone marrow and perivascular niches. *J Biomech*, 45, 1280-7.
- RONAN, W., DESHPANDE, V. S., MCMEEKING, R. M. & MCGARRY, J. P. 2012. Numerical investigation of the active role of the actin cytoskeleton in the compression resistance of cells. *J Mech Behav Biomed Mater*, 14, 143-57.
- RONAN, W., DESHPANDE, V. S., MCMEEKING, R. M. & MCGARRY, J. P. 2014. Cellular contractility and substrate elasticity: a numerical investigation of the actin cytoskeleton and cell adhesion. *Biomech Model Mechanobiol*, 13, 417-435.
- ROWAT, A. C., LAMMERDING, J., HERRMANN, H. & AEBI, U. 2008. Towards an integrated understanding of the structure and mechanics of the cell nucleus. *Bioessays*, 30, 226-36.
- ROWAT, A. C., LAMMERDING, J. & IPSEN, J. H. 2006. Mechanical properties of the cell nucleus and the effect of emerin deficiency. *Biophys J*, 91, 4649-4664.
- ROY, S., THACHER, T., SILACCI, P. & STERGIOPULOS, N. 2009. Arterial biomechanics after destruction of cytoskeleton by cytochalasin D. *J Biomech*, 42, 2562-2568.
- SATO, M., LEVESQUE, M. J. & NEREM, R. M. 1987a. An application of the micropipette technique to the measurement of the mechanical properties of cultured bovine aortic endothelial cells. *J Biomech Eng*, 109, 27-34.
- SATO, M., LEVESQUE, M. J. & NEREM, R. M. 1987b. Micropipette aspiration of cultured bovine aortic endothelial cells exposed to shear stress. *Arteriosclerosis*, 7, 276-86.

- SATO, M., OHSHIMA, N. & NEREM, R. M. 1996. Viscoelastic properties of cultured porcine aortic endothelial cells exposed to shear stress. *J Biomech*, 29, 461-467.
- SATO, M., THERET, D. P., WHEELER, L. T., OHSHIMA, N. & NEREM, R. M. 1990. Application of the micropipette technique to the measurement of cultured porcine aortic endothelial cell viscoelastic properties. *J Biomech Eng*, 112, 263-8.
- SAWYER, S. J., NORVELL, S. M., PONIK, S. M. & PAVALKO, F. M. 2001. Regulation of PGE(2) and PGI(2) release from human umbilical vein endothelial cells by actin cytoskeleton. *Am J Physiol Cell Physiol*, 281, C1038-45.
- SCHNEIDER, C. A., RASBAND, W. S. & ELICEIRI, K. W. 2012. NIH image to ImageJ: 25 years of image analysis. *Nat Methods*, 9, 671-675.
- SHAO, K.-F., WU, Z.-Z., WANG, B.-C., LONG, M. & CAI, S.-X. 2000. Effects of colchicine and cytochalasin D on the adhesion properties of the HCC onto the collagen IV/laminin coated surface. *Colloids Surf B Biointerfaces*, 19, 55-59.
- SHAREI, A., ZOLDAN, J., ADAMO, A., SIM, W. Y., CHO, N., JACKSON, E., MAO, S., SCHNEIDER, S., HAN, M.-J., LYTTON-JEAN, A., BASTO, P. A., JHUNJHUNWALA, S., LEE, J., HELLER, D. A., KANG, J. W., HARTOULAROS, G. C., KIM, K.-S., ANDERSON, D. G., LANGER, R. & JENSEN, K. F. 2013. A vector-free microfluidic platform for intracellular delivery. *Proc Natl Acad Sci USA*, 110, 2082-2087.
- SHEN, G., TSUNG, H. C., WU, C. F., LIU, X. Y., WANG, X. Y., LIU, W., CUI, L. & CAO, Y. L. 2003. Tissue engineering of blood vessels with endothelial cells differentiated from mouse embryonic stem cells. *Cell Res*, 13, 335-41.
- SHIEH, A. C. & ATHANASIOU, K. A. 2003. Principles of cell mechanics for cartilage tissue engineering. *Ann Biomed Eng*, 31, 1-11.
- SHIEH, A. C. & ATHANASIOU, K. A. 2007. Dynamic compression of single cells. *Osteoarthritis Cartilage*, 15, 328-334.
- SOLON, J., LEVENTAL, I., SENGUPTA, K., GEORGES, P. C. & JANMEY, P. A. 2007. Fibroblast adaptation and stiffness matching to soft elastic substrates. *Biophys J*, 93, 4453-61.
- TAN, J. L., TIEN, J., PIRONE, D. M., GRAY, D. S., BHADRIRAJU, K. & CHEN, C. S. 2003. Cells lying on a bed of microneedles: an approach to isolate mechanical force. *Proc Natl Acad Sci USA*, 100, 1484-9.
- TAN, S. C., PAN, W. X., MA, G., CAI, N., LEONG, K. W. & LIAO, K. 2008. Viscoelastic behaviour of human mesenchymal stem cells. *BMC Cell Biol*, 9, 40.
- TEE, S.-Y., FU, J., CHEN, CHRISTOPHER S. & JANMEY, PAUL A. 2011. Cell Shape and Substrate Rigidity Both Regulate Cell Stiffness. *Biophys J*, 100, L25-L27.
- THAVANDIRAN, N., DUBOIS, N., MIKRYUKOV, A., MASSÉ, S., BECA, B., SIMMONS, C. A., DESHPANDE, V. S., MCGARRY, J. P., CHEN, C. S., NANTHAKUMAR, K., KELLER, G. M., RADISIC, M. & ZANDSTRA, P. W. 2013. Design and formulation of functional pluripotent stem cell-derived cardiac microtissues. *Proc Natl Acad Sci USA*, 110, 4698-4707.
- THERET, D. P., LEVESQUE, M. J., SATO, M., NEREM, R. M. & WHEELER, L. T. 1988. The Application of a Homogeneous Half-Space Model in the Analysis of Endothelial Cell Micropipette Measurements. *J Biomech Eng*, 110, 190-199.
- THERY, M., PEPIN, A., DRESSAIRE, E., CHEN, Y. & BORNENS, M. 2006. Cell distribution of stress fibres in response to the geometry of the adhesive environment. *Cell Motil Cytoskeleton*, 63, 341-55.
- THOMAS, C. H., COLLIER, J. H., SFEIR, C. S. & HEALY, K. E. 2002. Engineering gene expression and protein synthesis by modulation of nuclear shape. *Proc Natl Acad Sci USA*, 99, 1972-1977.

- THOUMINE, O., CARDOSO, O. & MEISTER, J.-J. 1999. Changes in the mechanical properties of fibroblasts during spreading: a micromanipulation study. *Eur Biophys J*, 28, 222-234.
- THOUMINE, O. & OTT, A. 1996. Influence of adhesion and cytoskeletal integrity on fibroblast traction. *Cell Motil Cytoskeleton*, 35, 269-80.
- THOUMINE, O. & OTT, A. 1997a. Comparison of the mechanical properties of normal and transformed fibroblasts. *Biorheology*, 34, 309-26.
- THOUMINE, O. & OTT, A. 1997b. Time scale dependent viscoelastic and contractile regimes in fibroblasts probed by microplate manipulation. *J Cell Sci*, 110 ( Pt 17), 2109-16.
- TOZEREN, A., MACKIE, L. H., LAWRENCE, M. B., CHAN, P. Y., DUSTIN, M. L. & SPRINGER, T. A. 1992. Micromanipulation of adhesion of phorbol 12-myristate-13-acetate-stimulated T lymphocytes to planar membranes containing intercellular adhesion molecule-1. *Biophys J*, 63, 247-58.
- TRICKEY, W. R., BAAIJENS, F. P., LAURSEN, T. A., ALEXOPOULOS, L. G. & GUILAK, F. 2006. Determination of the Poisson's ratio of the cell: recovery properties of chondrocytes after release from complete micropipette aspiration. *J Biomech*, 39, 78-87.
- TRICKEY, W. R., LEE, G. M. & GUILAK, F. 2000. Viscoelastic properties of chondrocytes from normal and osteoarthritic human cartilage. *J Orthop Res*, 18, 891-8.
- TRICKEY, W. R., VAIL, T. P. & GUILAK, F. 2004. The role of the cytoskeleton in the viscoelastic properties of human articular chondrocytes. *J Orthop Res*, 22, 131-9.
- TSAI, J. W., CHEN, Y., KRIEGSTEIN, A. R. & VALLEE, R. B. 2005. LIS1 RNA interference blocks neural stem cell division, morphogenesis, and motility at multiple stages. *J Cell Biol*, 170, 935-45.
- TSUKAMOTO, T., HASHIGUCHI, N., JANICKI, S. M., TUMBAR, T., BELMONT, A. S. & SPECTOR, D. L. 2000. Visualization of gene activity in living cells. *Nat Cell Biol*, 2, 871-8.
- VAZIRI, A. & MOFRAD, M. R. 2007. Mechanics and deformation of the nucleus in micropipette aspiration experiment. *J Biomech*, 40, 2053-62.
- WEAFER, P. P., RONAN, W., JARVIS, S. P. & MCGARRY, J. P. 2013. Experimental and computational investigation of the role of stress fiber contractility in the resistance of osteoblasts to compression. *Bull Math Biol*, 75, 1284-303.
- XINYU, L., YIFEI, W. & YU, S. 2009. Cell Contour Tracking and Data Synchronization for Real-Time, High-Accuracy Micropipette Aspiration. *IEEE T Autom Sci Eng*, 6, 536-543.
- YAMADA, M., KANO, K., TSUDA, Y., KOBAYASHI, J., YAMATO, M., SEKI, M. & OKANO, T. 2007. Microfluidic devices for size-dependent separation of liver cells. *Biomed Microdevices*, 9, 637-645.
- YEUNG, T., GEORGES, P. C., FLANAGAN, L. A., MARG, B., ORTIZ, M., FUNAKI, M., ZAHIR, N., MING, W., WEAVER, V. & JANMEY, P. A. 2005. Effects of substrate stiffness on cell morphology, cytoskeletal structure, and adhesion. *Cell Motil Cytoskeleton*, 60, 24-34.
- YU, H., TAY, C. Y., LEONG, W. S., TAN, S. C. W., LIAO, K. & TAN, L. P. 2010. Mechanical behavior of human mesenchymal stem cells during adipogenic and osteogenic differentiation. *Biochem Biophys Res Commun*, 393, 150-155.
- ZALESKAS, J. M., KINNER, B., FREYMAN, T. M., YANNAS, I. V., GIBSON, L. J. & SPECTOR, M. 2004. Contractile forces generated by articular chondrocytes in collagen-glycosaminoglycan matrices. *Biomaterials*, 25, 1299-1308.

- ZHAO, R., WYSS, K. & SIMMONS, C. A. 2009. Comparison of analytical and inverse finite element approaches to estimate cell viscoelastic properties by micropipette aspiration. *J Biomech*, 42, 2768-73.
- ZHOU, E., QUEK, S. & LIM, C. 2010. Power-law rheology analysis of cells undergoing micropipette aspiration. *Biomech Model Mechanobiol*, 9, 563-572.
- ZHOU, E. H., LIM, C. T. & QUEK, S. T. 2005. Finite Element Simulation of the Micropipette Aspiration of a Living Cell Undergoing Large Viscoelastic Deformation. *Mech Adv Mater Struct*, 12, 501-512.

# 5 Investigation of cell nucleus heterogeneity

## 5.1 Introduction

Numerous studies suggest that nuclei are stiffer than the surrounding cytoplasm (Guilak et al., 2000, Caille et al., 2002, Caille et al., 1998, Maniotis et al., 1997, Jean et al., 2005, Ferko et al., 2007, Deguchi et al., 2007, Ofek et al., 2009a, Knight et al., 2002). In contrast to this finding, Leipzig and Athanasiou (2008) report that cytoplasm and nucleus strains had a 1:1 ratio during compression, suggesting that the stiffness of the cytoplasm and nucleus are similar. However, it should be noted that the extracellular environment in these aforementioned studies is not the same in all cases. It is well known that the “apparent” stiffness of cells can alter due to substrate compliance (Byfield et al., 2009), the level of spreading (Thoumine et al., 1999), and the contractile nature of the cell phenotype in question (Rodriguez et al., 2013, Caille et al., 2002, Peeters et al., 2005, Deng et al., 2010, Ofek et al., 2009b). To overcome this complex factor Deguchi et al. (2005) and Guilak et al. (2000) isolated nuclei from cells before testing. However, it has been suggested that nucleus mechanical behaviour may be altered by the isolation procedure used (Guilak et al., 2000). Simulating experiments of isolated nuclei, Vaziri and Mofrad (2007) compute a shear modulus of 0.008 kPa for the

nucleoplasm of nuclei, which have a stiffer outer shell. Furthermore, previous experimental studies of micropipette aspiration (MA) of suspended cells reveal significant nucleus deformation (Pajerowski et al., 2007, Ribeiro et al., 2012). Pajerowski et al. (2007) report that permanent visco-plastic deformation of the nucleus occurs due to lamin A/C and chromatin remodelling. In summary, the mechanical behaviour of the nucleus has not been definitively characterised in the literature, with a wide range of elastic properties being reported. A detailed and robust methodology for analysis of nucleus biomechanics would represent a considerable contribution to the field of cell mechanics.

In an experimental investigation by Henderson et al. (2013) 3D strain distributions inside the nuclei of single living cells embedded within their native extracellular matrix (ECM) were determined during applied shear strain. During deformation of a cartilage tissue explant, strain is transferred to individual nuclei resulting in submicron displacements. Local deformation gradients were determined from confocal images of nuclear DNA distributions before and after the application of an applied shear loading. 3D distributions of intra-nuclear shear strains were established. Compressive, tensile, and shear strain localisations in the nucleus were shown to be five-fold higher than the macroscopic applied tissue strain. The possibility that intra-nuclear material heterogeneity may result in strain magnification should be investigated through mechanical simulations of the experiments of Henderson et al. (2013)

The current chapter outlines a methodology to construct a heterogeneous finite element model of the chondrocyte nucleus. Greyscale values obtained from confocal z-stacks of the DNA in nuclei within cartilage tissues explants (Henderson et al., 2013) are correlated to shear moduli at each material point in the nucleus

finite element mesh. A representative volume element (RVE) for cartilage tissue, originally developed by Dowling et al. (2013), is adapted to include the heterogeneous nucleus material behaviour. The range of heterogeneous intra-nucleus material properties required to replicate experimentally observed strain distributions is established.

## 5.2 Model development

### 5.2.1 Cartilage representative volume element (RVE)

A previous study by Dowling et al. (2013) developed a RVE for cartilage tissue. A similar RVE is used in the current chapter (Figure 5.1). Full details of RVE development can be found in the study of Dowling et al. (2013). Briefly, an RVE comprising of a chondrocyte cell surrounded by a peri-cellular matrix (PCM) embedded in a cuboidal ECM is modelled. The cuboid has a side dimension of 60  $\mu\text{m}$ , based on observed cell spacing in situ. The nucleus, cell, and PCM are assumed to be spherical with diameters of 7.5  $\mu\text{m}$ , 16  $\mu\text{m}$ , and 22  $\mu\text{m}$ , respectively, again based on experimental observation. It should be noted that dimensions are chosen such that the volume fraction of cells and ECM is representative of cartilage tissue. In the study of Dowling et al. (2013) only half of the overall RVE is simulated due to symmetry. In the current study the nucleus is inhomogeneous in 3D, therefore, simulation of the full RVE, including the entire 3D scanned nucleus, is required.

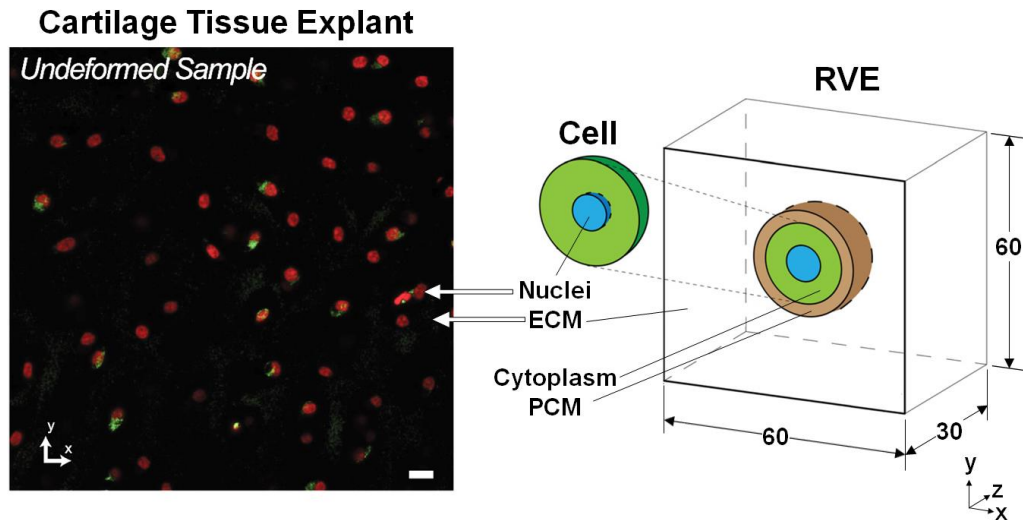


**Figure 5.1:** (A) Confocal image of cartilage tissue explant showing DNA in red and nascent RNA in green. Image adapted from Henderson et al. (2013). Image captured using 60x water immersion objective with a resolution of 1600 x 1600 pixels. Scale bar = 20 μm (B) Schematic of a RVE of cartilage consisting of a single chondrocyte cell surrounded by a PCM embedded in a cuboidal ECM. All dimensions are in μm. Image adapted from Dowling et al. (2013). In A and B, boundary conditions are indicated in red. The bottom of the explant/RVE is rigidly held while the upper surface of the explant/RVE is subjected to 15% shear.

### 5.2.2 Greyscale mapping

Before application of shear deformation in the study of Henderson et al. (2013), image stacks of nucleus DNA from the study of Henderson et al. (2013) were provided by Prof. Corey Neu (Purdue University) and co-workers. Figure 5.2-A shows the 8 z-stacks of the DNA for a single nucleus in the cartilage explant. Each of the experimentally obtained z-stacks shown in Figure 5.2-A has a resolution of 50x50 pixels. To obtain a full cube of greyscale values, i.e. 50x50x50, 6 pseudo z-stacks between each of the observed z-stacks shown must be generated. It is assumed that the greyscale value of each pixel follows a linear progression from one experimentally obtained z-stack to the next. Therefore, for a pixel at  $i, j$  in the 50x50 image, the greyscale value of the first observed z-stack,  $g_{ij}^1$ , is assumed to follow a linear progression to the corresponding greyscale value in the second observed z-stack (z-stack 8),  $g_{ij}^8$ . Figure 5.2-B gives an example of how the greyscale value varies for a pixel at  $i, j$ . By performing this interpolation on all

50x50 pixels between each observed z-stack, a full 50x50x50 cube of pixel intensities is obtained. Before mapping is performed, a finite element mesh for the spherical nucleus is created using the commercial finite element software Abaqus (DS Simulia, RI, USA). By assuming the diameter of the spherical nucleus is equal to the edge dimension of the cube of pixel intensities, a mesh density is chosen such that the number of finite elements per unit volume is similar to the number of pixels per unit volume in the cube of pixel intensities. The 3D coordinate of the centroid of each element is associated with a corresponding greyscale value in the 3D cube of pixel intensities. Elements are assembled into 10 groups based on greyscale values. Group 1 contains all elements with greyscale values between  $\mathbb{g}_{min}$  and  $\frac{1}{10}(\mathbb{g}_{max} - \mathbb{g}_{min})$ , where  $\mathbb{g}_{max}$  and  $\mathbb{g}_{min}$  are the maximum and minimum greyscale values for the finite element mesh, respectively. Group 2 then contains all elements between  $\frac{1}{10}(\mathbb{g}_{max} - \mathbb{g}_{min})$  and  $\frac{2}{10}(\mathbb{g}_{max} - \mathbb{g}_{min})$ , group 3 then contains all elements between  $\frac{2}{10}(\mathbb{g}_{max} - \mathbb{g}_{min})$  and  $\frac{3}{10}(\mathbb{g}_{max} - \mathbb{g}_{min})$ , and so forth. The pseudo z-stack generation, centroid coordinate calculations, greyscale mapping, and element grouping assignments are performed using scripts written in MATLAB (The Mathworks, Natick, MA). To compare the greyscale map in the finite element mesh to experimentally observed z-stacks, each group in the finite element mesh of the nucleus is assigned a greyscale value so that colour ranges from black in group 1 to white in group 10. The planes shown in Figure 5.2-C are chosen to correspond with the experimentally observed z-stacks in Figure 5.2-A. A close correlation with the experimentally observed greyscales is obtained.

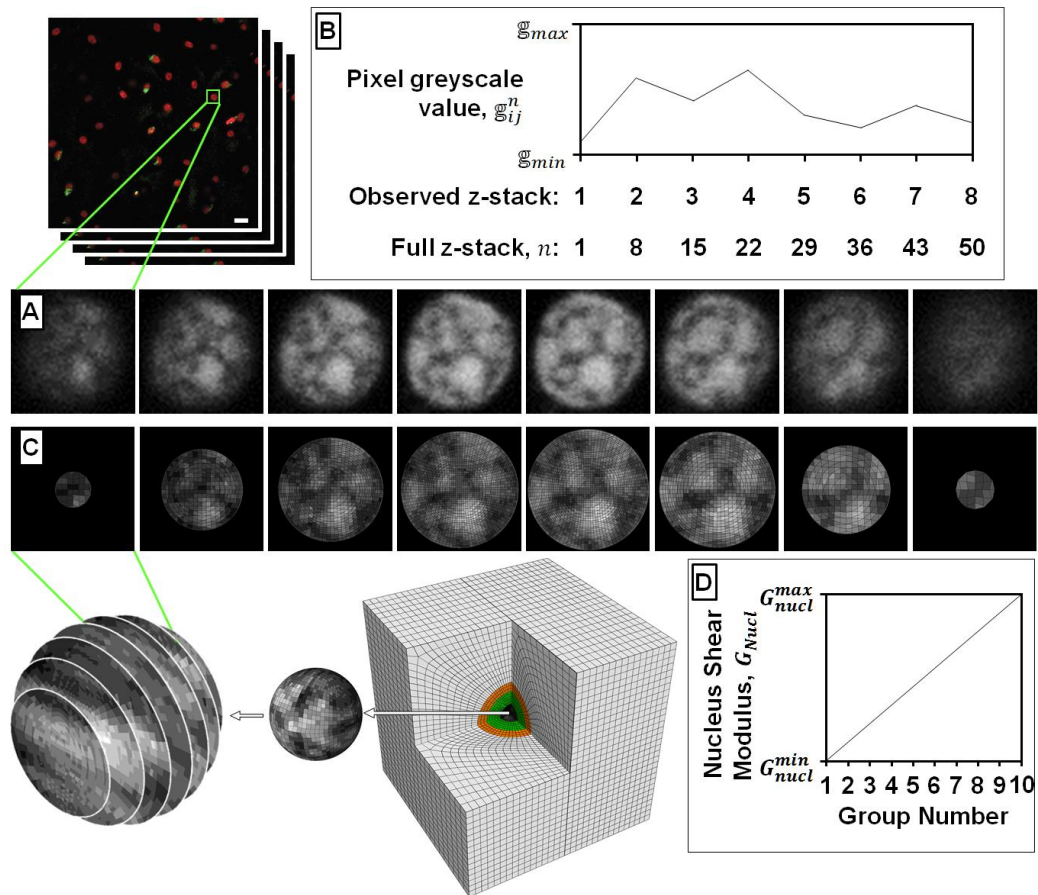


Figure 5.2: (A) A representation of image stacks of a cartilage tissue explant. Greyscale images of a single nucleus from each confocal z-stack showing DNA intensity. Scale bar = 20  $\mu\text{m}$ . Z-stacks for the single nucleus were provided by Prof. Corey Neu (Purdue University) and co-workers. (B) Graphical representation of linear interpolation between observed greyscale values. (C) Corresponding slices of the nucleus in the finite element RVE. The contour plot illustrates assigned material sections ranging from stiff (light) to compliant (dark). (D) Graphical representation of shear modulus assignment to each group.

### 5.2.3 Material properties

For full details on material properties of the ECM, PCM, and cell cytoplasm the reader is referred to the study of Dowling et al. (2013). Briefly, the ECM and PCM are modelled using an isotropic Neo-Hookean hyperelastic constitutive formulation. The shear and bulk moduli are 0.4 MPa and 2.0 MPa, respectively. The mechanical behaviour of the cytoplasm is described by the active stress fibre modelling framework as described in Chapter 4. Parameters for the active modelling framework were determined previously using force data obtained by applying shear loading to single chondrocytes (Dowling et al., 2012). In the current

chapter, the nucleus mechanical behaviour is modelled using Neo-Hookean hyperelasticity. However, specific material properties are assigned to each individual element in the nucleus mesh based on the greyscale value associated with each element. As illustrated in Figure 5.2-D, each nucleus greyscale group (as defined in Section 5.2.2) is assigned a shear modulus such that values range linearly from a minimum value in group 1,  $G_{nucl}^{min}$ , to a maximum value in group 10,  $G_{nucl}^{max}$ . In the current chapter, values ranging from  $G_{nucl}^{min} = 0.03$  kPa to  $G_{nucl}^{max} = 2$  kPa are used. In line with the findings of Chapter 4, a ratio of bulk modulus to shear modulus ( $K_{nucl}/G_{nucl}$ ) of  $\sim 30$  is used, enforcing a condition of near incompressibility throughout the nucleus.

#### **5.2.4 Boundary conditions**

To replicate the 15% shear strain applied to the cartilage explants in the experiments of Henderson et al. (2013), displacement boundary conditions are applied to the upper surface of the RVE. The bottom surface of the cartilage explant and the RVE are rigidly fixed in all directions. Images of the tissue explant, RVE, and nuclei before and after shear deformation are shown in Figure 5.3.

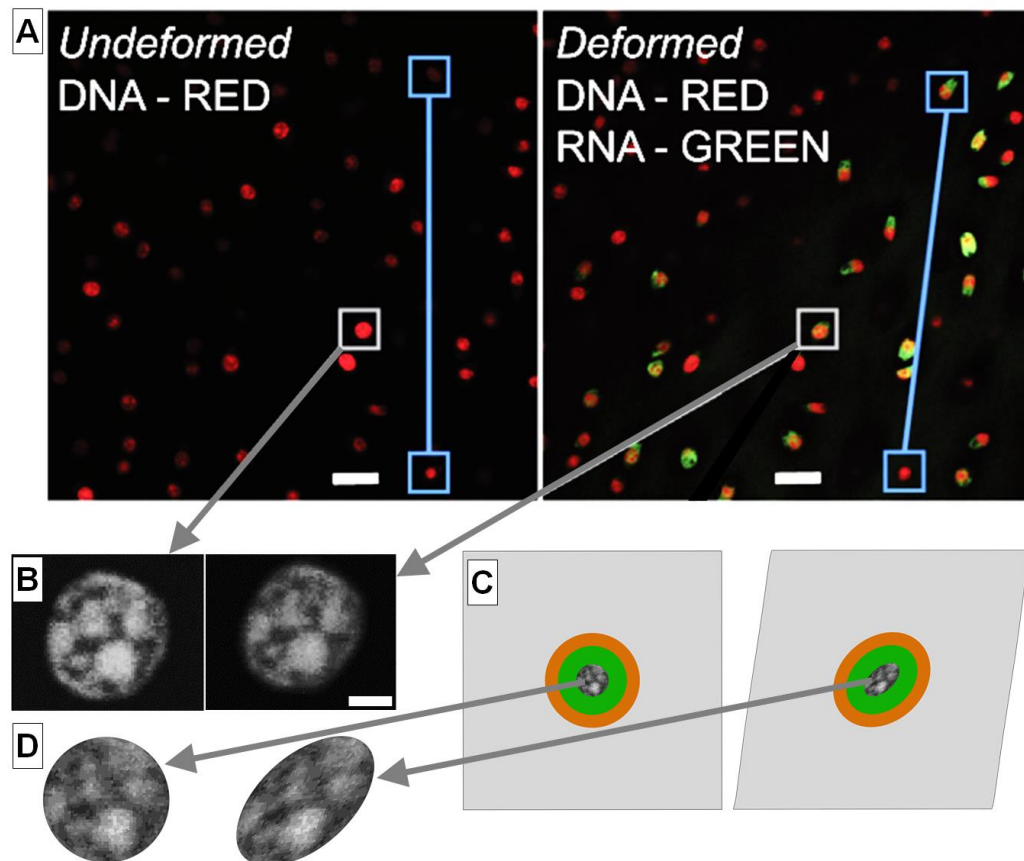


**Figure 5.3:** (A) Undeformed and deformed confocal image of cartilage tissue explant showing DNA in red and nascent RNA in green. The blue line indicates the relative motion between two nuclei in the explant before and after shear deformation. Scale bar = 20  $\mu\text{m}$ . (B) Greyscale confocal image of a DNA in a single nucleus before and after shear deformation. Scale bar = 2  $\mu\text{m}$ . (C) Mid-section of the RVE before and after shear deformation. Each colour represents a specific material as outlined in Figure 5.1. (D) Finite element mesh of undeformed and deformed nucleus showing assigned material sections ranging from stiff (light) to compliant (dark). For all A-D undeformed configurations are shown in left panels and deformed configurations are shown in right panels. A and B adapted from Henderson et al. (2013).

## 5.3 Model predictions

Computed RVE and nucleus deformations are shown in Figure 5.3-C and -D. Both the cell and its nucleus deform into an ellipsoidal shape. The predicted displacement of high concentration DNA regions of the nucleus (white regions) can clearly be seen in Figure 5.3-D. In Figure 5.4 experimentally observed shear strains in the nucleus are shown are compared to computed shear strain distributions. For each contour plot the shear strain along a linear path through the centre of the nucleus is plotted (right-most panels).

In Figure 5.4-A, experimentally observed regions of high strain align generally with darker regions of Figure 5.2-A. In Figure 5.4-B, the computational prediction of nucleus strain is shown. Strain gradients generally correlate with the experimentally observed values. In particular, the large region of low strain in the lower right region of the nucleus is accurately captured. The strain path for the computational contour plot of Figure 5.4-B does not follow the same trends as that observed experimentally in Figure 5.4-A.

During greyscale mapping, the experimental z-stacks are mapped onto a perfect sphere. Greyscale values at transitional regions at the edge of the nucleus are very low. Therefore, greyscale mapping at transitional regions at the edge of the nucleus model may result in very low stiffness's occurring at peripheral regions of the finite element mesh. To overcome this, an outer shell layer of the nucleus is assigned maximum shear modulus ( $G_{nucl}^{max}$ ) for the prediction shown in Figure 5.4-C. The predicted strain gradients generally correlate with the experimentally observed contour plot, similar to Figure 5.4-B. However, the addition of stiffened shell elements improves prediction of the experimentally observed strain path in Figure 5.4-A.

In Figure 5.4-D a homogenous nucleus is assumed and properties previously calibrated in Chapter 4 are used. While the overall nucleus deformation to an ellipsoid is similar to that predicted by the heterogeneous models in Figure 5.4-B and -C, the strain distribution within the nucleus is relatively uniform. Clearly the assumption of a homogeneous nucleus prohibits the prediction of localised strain concentrations observed experimentally.

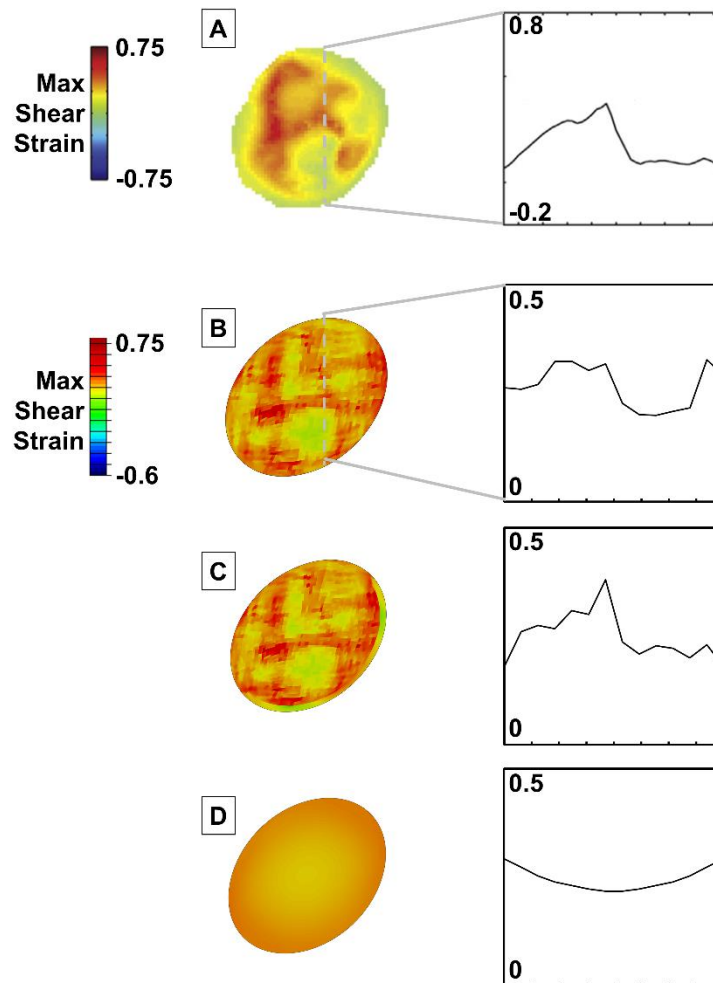


Figure 5.4: Nucleus deformation and contours plots of max shear: (A) experimentally observed by Henderson et al. (2013); (B) predicted during simulations in which a heterogeneous nucleus model is used; (C) during simulations in which a shell layer is added to the heterogeneous nucleus model; and (D) simulations in which a homogenous nucleus is assumed. It should be noted that a deformation scale factor of 0.5 is used for the computational contour plots

## 5.4 Discussion

In the current chapter 3D experimental images from the study of Henderson et al. (2013) are used to construct a heterogeneous model of the chondrocyte nucleus of an in situ chondrocyte. Greyscale values are used to assign the shear modulus of each element in the finite element mesh. To replicate experimental loading, the chondrocyte is placed in a cartilage ECM. The cytoplasm of the cell is modelling using the active modelling framework described in Chapter 4. Active modelling parameters for chondrocytes were determined by Dowling et al. (2012). Assuming

an extremely high stiffness is used for regions of highly compacted DNA ( $G_{nucl}^{max} = 2$  kPa) and extremely low stiffness is used for spaces devoid of DNA ( $G_{nucl}^{min} = 0.03$  kPa), with linear interpolation of intermediate grey scale shear moduli, predicted intra-nucleus strain distributions are reasonably similar to the highly heterogeneous strain state observed experimentally by Henderson et al. (2013). Henderson et al. (2013) observed that regions of low DNA have a high RNA concentration. Therefore, simulations presented in this chapter suggest that RNA is highly deformable. In contrast, DNA appears to be highly undeformable.

The heterogeneous image based nucleus model represents a significant advance in numerical techniques to quantify nucleus deformation. Previous studies have modelled the nucleus as a homogenous isotropic continuum material (Caille et al., 2002, Ronan et al., 2014, Mullen et al., 2014, Deguchi et al., 2007). However, the current chapter demonstrates that a highly inaccurate prediction of the local intra-nucleus strain state is obtained if material heterogeneity is not considered. The accurate prediction of nucleus deformation is a key step in understanding mechanotransduction. Previous studies have demonstrated the link between nucleus deformation and regulation of type II collagen as well as gene expression (Roca-Cusachs et al., 2008, Thomas et al., 2002, Campbell et al., 2007, Buschmann et al., 1996, Shieh and Athanasiou, 2007), possibly due to the reshaping of nuclear lamina and alterations in chromatin distribution (Dahl et al., 2008, Rowat et al., 2008, Tsukamoto et al., 2000). Using a geometrically accurate 3D model of osteocytes, Verbruggen et al. (2012) demonstrated that the cell experiences localised strain amplifications due to ECM projections and the presence of a PCM. It was suggested that these strain amplifications are an important mechanism in osteocyte mechanobiology (Adachi et al., 2008). The computational investigation of the

current chapter suggests that nucleus heterogeneity could also be a means by which strain amplification mechanisms promote mechanotransduction.

The model results presented in this chapter suggest that the range of shear moduli within the nucleus span two orders of magnitude, resulting in nucleus strains that are five times higher than applied tissue strains. This large range of shear moduli within a single nucleus may explain the conflicting reports of macroscale nucleus stiffness in the literature. For example, in previous MA studies (Pajerowski et al., 2007, Deguchi et al., 2005, Guilak et al., 2000, Zhou et al., 2005), and Chapter 4 of this thesis, the apparent shear modulus of a homogeneous nucleus ranges in values from 0.07-1 kPa. In investigations of cell and nucleus mechanical response to unconfined compression (Caille et al., 2002, Ofek et al., 2009a), the apparent shear modulus of a homogeneous nucleus ranges from 0.16-8.33kPa. Vaziri and colleagues modelled the nucleus as a highly compliant nucleoplasm (with a shear modulus of 0.008 kPa) surrounded by very stiff lamina and membrane regions to accurately predict AFM indentation results (Vaziri et al., 2006) and MA results (Vaziri and Mofrad, 2007). Therefore, values reported for nucleus shear properties range over three orders of magnitude in the literature. The nucleus may be perceived to be highly deformable under shear type loading, such as MA. However, under hydrostatic type loading the nucleus may be perceived to be highly undeformable, due to a high bulk modulus. The high bulk moduli used in the current chapter are based on evidence reported in Chapter 4 and on microscopic image analysis performed by Avalos et al. (2011).

A potential limitation of the current chapter is that the shear modulus of each element is assumed to be directly proportional to its associated greyscale value. Even with the high stiffness assigned to the outer shell region in Figure 5.4-C,

predicted strain at the nucleus periphery is still much higher than the experimentally observed result. However, a good prediction of strain is obtained in the more compliant regions. This suggests that a linear proportionality of nucleus stiffness to greyscale intensity may need to be modified to an exponential type relationship in order to more closely capture the experimental observations. Previous studies reported that the nucleus is viscoelastic (Vaziri and Mofrad, 2007, Guilak et al., 2000, Zhou et al., 2005). Another potential limitation in the current chapter is that the nucleus is assumed to be hyperelastic. The deformation applied by Henderson et al. (2013) is monotonic and DNA distribution is observed at two time points, once before and once after applied shear deformation. Therefore, viscous effects cannot be determined from the published experimental tests. A third intra-nucleus 3D image could be taken at a later time point to investigate viscoelastic stress relaxation/creep. Alternatively, imposing the applied tissue shear at different loading rates could be considered. Non-recoverable plastic deformation of the nucleus during large strain loading has also been observed at extremely large levels of deformation (Pajerowski et al., 2007). However, another limitation of the experimental results used in the current chapter is that it is not clear if the elastic limits are being approached/exceeded. If the cartilage explant is returned to the undeformed configuration after applied shear, the strain distribution at this point could be compared to the initial undeformed strain distribution to investigate non-recoverable intra-nuclear strain.

In conclusion, the current chapter considers the highly heterogeneous strain distribution of chondrocyte nuclei in cartilage explants subjected to shear deformation (Henderson et al., 2013). A heterogeneous model of the chondrocyte nucleus is constructed based on 3D images of Henderson et al. (2013) and placed

in an RVE that consists of a chondrocyte cytoplasm and cartilage ECM. Simulations reveal that a very large range of intra-nuclear shear moduli (ranging over two orders of magnitude) provides a reasonable prediction strain heterogeneity and strain magnification observed in experiments.

## 5.5 References

- ADACHI, T., SATO, K., HIGASHI, N., TOMITA, Y. & HOJO, M. 2008. Simultaneous observation of calcium signaling response and membrane deformation due to localized mechanical stimulus in single osteoblast-like cells. *Journal of the Mechanical Behavior of Biomedical Materials*, 1, 43-50.
- AVALOS, P. G., REICHENZELLER, M., EILS, R. & GLADILIN, E. 2011. Probing compressibility of the nuclear interior in wild-type and lamin deficient cells using microscopic imaging and computational modeling. *J. Biomech.*, 44, 2642-2648.
- BUSCHMANN, M. D., HUNZIKER, E. B., KIM, Y. J. & GRODZINSKY, A. J. 1996. Altered aggrecan synthesis correlates with cell and nucleus structure in statically compressed cartilage. *J Cell Sci*, 109(Pt 2), 499-508.
- BYFIELD, F. J., REEN, R. K., SHENTU, T. P., LEVITAN, I. & GOOCH, K. J. 2009. Endothelial actin and cell stiffness is modulated by substrate stiffness in 2D and 3D. *J Biomech*, 42, 1114-9.
- CAILLE, N., TARDY, Y. & MEISTER, J. J. 1998. Assessment of Strain Field in Endothelial Cells Subjected to Uniaxial Deformation of Their Substrate. *Annals of Biomedical Engineering*, 26, 409-416.
- CAILLE, N., THOUMINE, O., TARDY, Y. & MEISTER, J.-J. 2002. Contribution of the nucleus to the mechanical properties of endothelial cells. *J Biomech*, 35, 177-187.
- CAMPBELL, J. J., BLAIN, E. J., CHOWDHURY, T. T. & KNIGHT, M. M. 2007. Loading alters actin dynamics and up-regulates cofilin gene expression in chondrocytes. *Biochem Biophys Res Commun*, 361, 329-334.
- DAHL, K. N., RIBEIRO, A. J. & LAMMERDING, J. 2008. Nuclear shape, mechanics, and mechanotransduction. *Circ Res*, 102, 1307-18.
- DEGUCHI, S., MAEDA, K., OHASHI, T. & SATO, M. 2005. Flow-induced hardening of endothelial nucleus as an intracellular stress-bearing organelle. *J Biomech*, 38, 1751-1759.
- DEGUCHI, S., YANO, M., HASHIMOTO, K., FUKAMACHI, H., WASHIO, S. & TSUJIOKA, K. 2007. Assessment of the mechanical properties of the nucleus inside a spherical endothelial cell based on microtensile testing. *Journal of Mechanics of Materials and Structures*, 2, 1087-1102.
- DENG, Z., LULEVICH, V., LIU, F. T. & LIU, G. Y. 2010. Applications of atomic force microscopy in biophysical chemistry of cells. *J Phys Chem B*, 114, 5971-82.
- DOWLING, E. P., RONAN, W. & MCGARRY, J. P. 2013. Computational investigation of in situ chondrocyte deformation and actin cytoskeleton remodelling under physiological loading. *Acta Biomater*, 9, 5943-55.
- DOWLING, E. P., RONAN, W., OFEK, G., DESHPANDE, V. S., MCMEEKING, R. M., ATHANASIOU, K. A. & MCGARRY, J. P. 2012. The effect of remodelling and contractility of the actin cytoskeleton on the shear resistance of single cells: a computational and experimental investigation. *J R Soc Interface*, 9, 3469-79.

- FERKO, M. C., BHATNAGAR, A., GARCIA, M. B. & BUTLER, P. J. 2007. Finite-element stress analysis of a multicomponent model of sheared and focally-adhered endothelial cells. *Ann Biomed Eng*, 35, 208-23.
- GUILAK, F., TEDROW, J. R. & BURBKART, R. 2000. Viscoelastic properties of the cell nucleus. *Biochem Biophys Res Commun*, 269, 781-786.
- HENDERSON, J. T., SHANNON, G., VERESS, A. I. & NEU, C. P. 2013. Direct measurement of intranuclear strain distributions and RNA synthesis in single cells embedded within native tissue. *Biophys J*, 105, 2252-2261.
- JEAN, R. P., CHEN, C. S. & SPECTOR, A. A. 2005. Finite-element analysis of the adhesion-cytoskeleton-nucleus mechanotransduction pathway during endothelial cell rounding: axisymmetric model. *J Biomech Eng*, 127, 594-600.
- KNIGHT, M. M., VAN DE BREEVAART BRAVENBOER, J., LEE, D. A., VAN OSCH, G. J. V. M., WEINANS, H. & BADER, D. L. 2002. Cell and nucleus deformation in compressed chondrocyte–alginate constructs: temporal changes and calculation of cell modulus. *Biochimica et Biophysica Acta (BBA) - General Subjects*, 1570, 1-8.
- LEIPZIG, N. D. & ATHANASIOU, K. A. 2008. Static compression of single chondrocytes catabolically modifies single-cell gene expression. *Biophys J*, 94, 2412-22.
- MANIOTIS, A. J., CHEN, C. S. & INGBER, D. E. 1997. Demonstration of mechanical connections between integrins, cytoskeletal filaments, and nucleoplasm that stabilize nuclear structure. *Proc Natl Acad Sci USA*, 94, 849-854.
- MULLEN, C. A., VAUGHAN, T. J., VOISIN, M. C., BRENNAN, M. A., LAYROLLE, P. & MCNAMARA, L. M. 2014. Cell morphology and focal adhesion location alters internal cell stress. *Journal of The Royal Society Interface*, 11.
- OFEK, G., NATOLI, R. M. & ATHANASIOU, K. A. 2009a. In situ mechanical properties of the chondrocyte cytoplasm and nucleus. *J Biomech*, 42, 873-7.
- OFEK, G., WILTZ, D. C. & ATHANASIOU, K. A. 2009b. Contribution of the cytoskeleton to the compressive properties and recovery behavior of single cells. *Biophys J*, 97, 1873-82.
- PAJEROWSKI, J. D., DAHL, K. N., ZHONG, F. L., SAMMAK, P. J. & DISCHER, D. E. 2007. Physical plasticity of the nucleus in stem cell differentiation. *Proc Natl Acad Sci USA*, 104, 15619-15624.
- PEETERS, E. A., OOMENS, C. W., BOUTEN, C. V., BADER, D. L. & BAAIJENS, F. P. 2005. Mechanical and failure properties of single attached cells under compression. *J Biomech*, 38, 1685-93.
- RIBEIRO, A. J., TOTTEY, S., TAYLOR, R. W., BISE, R., KANADE, T., BADYLAK, S. F. & DAHL, K. N. 2012. Mechanical characterization of adult stem cells from bone marrow and perivascular niches. *J Biomech*, 45, 1280-7.
- ROCA-CUSACHS, P., ALCARAZ, J., SUNYER, R., SAMITIER, J., FARRE, R. & NAVAJAS, D. 2008. Micropatterning of single endothelial cell shape reveals a tight coupling between nuclear volume in G1 and proliferation. *Biophys J*, 94, 4984-95.
- RODRIGUEZ, M. L., MCGARRY, P. J. & SNIADOCKI, N. J. 2013. Review on cell mechanics: experimental and modeling approaches. *Appl Mech Rev*, 65, 060801.
- RONAN, W., DESHPANDE, V. S., MCMEEKING, R. M. & MCGARRY, J. P. 2014. Cellular contractility and substrate elasticity: a numerical investigation of the actin cytoskeleton and cell adhesion. *Biomech Model Mechanobiol*, 13, 417-435.
- ROWAT, A. C., LAMMERDING, J., HERRMANN, H. & AEBI, U. 2008. Towards an integrated understanding of the structure and mechanics of the cell nucleus. *Bioessays*, 30, 226-36.
- SHIEH, A. C. & ATHANASIOU, K. A. 2007. Dynamic compression of single cells. *Osteoarthritis Cartilage*, 15, 328-334.

- THOMAS, C. H., COLLIER, J. H., SFEIR, C. S. & HEALY, K. E. 2002. Engineering gene expression and protein synthesis by modulation of nuclear shape. *Proc Natl Acad Sci USA*, 99, 1972-1977.
- THOUMINE, O., CARDOSO, O. & MEISTER, J.-J. 1999. Changes in the mechanical properties of fibroblasts during spreading: a micromanipulation study. *Eur Biophys J*, 28, 222-234.
- TSUKAMOTO, T., HASHIGUCHI, N., JANICKI, S. M., TUMBAR, T., BELMONT, A. S. & SPECTOR, D. L. 2000. Visualization of gene activity in living cells. *Nat Cell Biol*, 2, 871-8.
- VAZIRI, A., LEE, H. & MOFRAD, M. R. K. 2006. Deformation of the cell nucleus under indentation: Mechanics and mechanisms. *Journal of Materials Research*, 21, 2126-2135.
- VAZIRI, A. & MOFRAD, M. R. 2007. Mechanics and deformation of the nucleus in micropipette aspiration experiment. *J Biomech*, 40, 2053-62.
- VERBRUGGEN, S. W., VAUGHAN, T. J. & MCNAMARA, L. M. 2012. Strain amplification in bone mechanobiology: a computational investigation of the in vivo mechanics of osteocytes. *J R Soc Interface*, 9, 2735-44.
- ZHOU, E. H., LIM, C. T. & QUEK, S. T. 2005. Finite Element Simulation of the Micropipette Aspiration of a Living Cell Undergoing Large Viscoelastic Deformation. *Mech Adv Mater Struct*, 12, 501-512.

# **6 Single cell active force generation under dynamic loading – Overview and analysis of AFM experiments**

## **6.1 Introduction**

### **6.1.1 Declaration of tasks completed**

In this chapter key experimental results on the response of single cells to dynamic loading are presented. This work recently been published by authors P.P. Weafer, N.H. Reynolds, S.P. Jarvis, J.P. McGarry (Acta Biomaterialia, Single cell active force generation under dynamic loading – Part I: AFM experiments, DOI: [10.1016/j.actbio.2015.09.006](https://doi.org/10.1016/j.actbio.2015.09.006)). The precise contribution of Ph.D. candidate Noel Reynolds to this body of experimental work is detailed in this chapter. Key experimental results are also summarised in this chapter. This experimental data provides key input for a novel computational study performed by Ph.D. candidate Noel Reynolds. This companion computational study is presented in Chapter 7 of this thesis, and was recently published by authors Reynolds and McGarry (Acta

Biomaterialia, Single cell active force generation under dynamic loading – Part II: active modelling insights, DOI: [10.1016/j.actbio.2015.09.004](https://doi.org/10.1016/j.actbio.2015.09.004)).

Statement of Contribution to the work presented in the paper by Weafer et al. (2015) and in the current chapter:

- Patrick McGarry designed the study.
- Suzi Jarvis provided AFM facilities and technical support.
- Paul Weafer developed the bespoke AFM system for single cell dynamic loading.
- Paul Weafer performed the experimental tests and obtained the raw data.
- Paul Weafer performed statistical analysis on maximum and minimum forces at steady state.
- Noel Reynolds performed statistical analysis on transient force data and created transient force-deformation loops for untreated contractile cells and cytochalasin-D treated cells.
- Patrick McGarry, Paul Weafer, and Noel Reynolds wrote the paper.

In Section 6.2, key experimental results from the study of Weafer et al. (2015) are presented. Once again, it should be noted that the development and implementation of the experimental technique and the acquisition of the experimental measurements were performed by Paul Weafer (2012). Statistical analysis and post processing of transient force-strain loops was performed by Noel Reynolds as part of the current Ph.D. Thesis. The figures presented in Section 6.2 were prepared by Noel Reynolds using the experimental data obtained by Paul Weafer (2012). The experimental data presented in the current chapter forms the basis and motivation

for the companion computational study presented in Chapter 7 and published by Reynolds and McGarry (2015).

### **6.1.2 Background to AFM cell mechanics experiments**

Single cell mechanical investigations generally entail static/monotonic loading (Lam et al., 2012, Mann et al., 2012, Butler et al., 2002, Caille et al., 2002) or localised AFM indentation (Nawaz et al., 2012, Watanabe-Nakayama et al., 2011). The use of standard AFM tips to indent cells (Roca-Cusachs et al., 2008, Prabhune et al., 2012) results in a highly localised strain field in the region of the cell membrane. Such highly localised measurements performed on the length-scale of sub cellular components is of limited value in characterising whole cell biomechanical behaviour. In an attempt to overcome this, previous studies have performed large number of indentations over the entire cell (Radmacher et al., 1996, Hofmann et al., 1997, Rotsch and Radmacher, 2000, Kelly et al., 2011). However, acquiring data over a large area is time consuming and does not overcome the problem that the applied strain field is primarily restricted to the cell membrane. Furthermore, the non-uniform strain state due to indentation with a sharp tip is not easily determined. Previous studies have replaced sharp AFM tips with spheres of 60  $\mu\text{m}$  diameter or less (Lehenkari et al., 2000, Lulevich et al., 2006, Jaasma et al., 2006, Zimmer et al., 2012, Titushkin and Cho, 2007, Darling et al., 2008) attached to the end of the AFM cantilever. The strain state that results from indentation with such spheres is significantly less localised than that produced by sharp AFM tips. However, the contact region is still much smaller than the spread cell radius and the applied strain is still primarily localised to the membrane region. To overcome this problem Weafer et al. (2012) attached a 150  $\mu\text{m}$  sphere to the AFM cantilever. As this large sphere has a much greater radius than a spread cell, a large cell-sphere

contact area can be achieved, and a reasonably uniform and easily characterised strain state can be applied to the cell via displacement of the AFM cantilever. In the experiments of Weafer et al. (2015) whole cell cyclic deformation is performed using this system, allowing for a highly accurate characterisation of resultant cell forces (accurate to the pico-Newton level). Technical details relating to the modification of the AFM system for whole cell loading are outlined in Weafer et al. (2012), where solutions for altered cantilever bending profile and thermal drift are developed. A schematic of the experimental system is shown in Figure 6.1-A.

A detailed series of tests was performed on osteoblast cells whereby cyclic strain magnitude was altered at the half-way point of each experiment, with the applied loading and unloading strain rates remaining unchanged (Weafer et al., 2015). Whole cell cyclic compression was applied using the modified AFM system. Figure 6.1-B illustrates the applied cyclic deformation. In regime 1 cells were cyclically loaded between 35% and 10% nominal strain for 1 hour. In regime 2 cells were cyclically loaded between 25% and 0% nominal strain for 1 hour. Cells are cyclically loaded at a frequency of 1 Hz for the full duration of the experiment. It should be noted that while strain magnitude is altered between regime 1 and regime 2, the strain rate remains the same for the entire experiment. As shown in Figure 6.1-C, maximum force was recorded when cells were a nominal strain of 35% in regime 1 and 25% in regime 2. Minimum force was recorded when cells are a nominal strain of 10% in regime 1 and 0% in regime 2. Force-strain curves were generated by Noel Reynolds by taking the forces recorded for a single cycle and plotting them against the applied strain (Figure 6.1-D). Key results are summarised in Section 6.2, revealing that patterns of measured forces are dramatically different

for untreated contractile cells in comparison to cells in which the actin cytoskeleton has been disrupted.

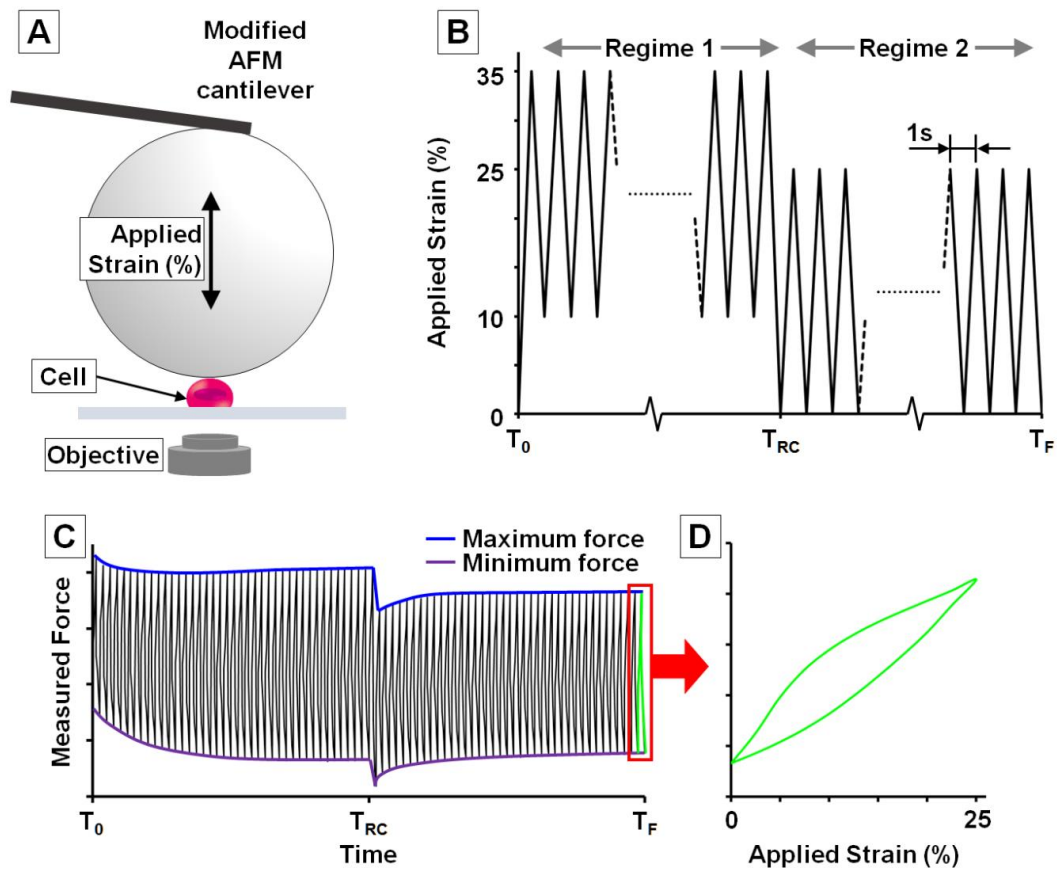


**Figure 6.1:** (A) Schematic of modified AFM cantilever consisting of a flexible cantilever and an attached sphere. (B) Graphical representation of the cyclic deformation experiment. The AFM setup is used to cyclically deform cells at a constant loading and unloading nominal strain rate at a frequency of 1 Hz. In loading regime 1 ( $0 \leq T < T_{RC}$ ), cells are cyclically deformed between 10% and 35%. In loading regime 2 ( $T_{RC} \leq T \leq T_F$ ), cells are cyclically deformed between 0% and 25%. Loading regime 1 starts at  $\epsilon_H = 0\%$ , however, force data collection began from  $\epsilon_H = 10\%$  of the first cycle. (C) Example of measured force indicating maximum and minimum force values. (D) Measure forces from a single cycle are plot against the applied strain to create force-strain curves.

## 6.2 Key experimental results

In Figure 6.2-A, maximum and minimum forces obtained from experiments of untreated cells are shown. It should be noted that a positive force indicates that the cell is resisting compression as the probe displaces downwards during loading and that negative force indicates that the cell is adhered to and resisting probe

retraction during unloading (Figure 6.2-B). The following key observations are made:

- A significant decrease in maximum and minimum force is observed at the onset of cyclic deformation. Forces subsequently stabilise to a steady state.
- For the untreated cells, steady state maximum forces of  $78.1 \pm 19.9$  nN and  $61.6 \pm 15.0$  nN are observed in regime 1 and regime 2, respectively. Steady state minimum forces of  $-70.5 \pm 24.5$  nN and  $-72.0 \pm 25.0$  nN are observed in regime 1 and regime 2, respectively. Therefore, negative (pulling) forces are similar in magnitude to positive (compressive) forces.
- The percentage change in steady state maximum force from regime 1 to regime 2 is  $21.1 \pm 7.8\%$ . A negligible change in steady state minimum force is observed between regimes.

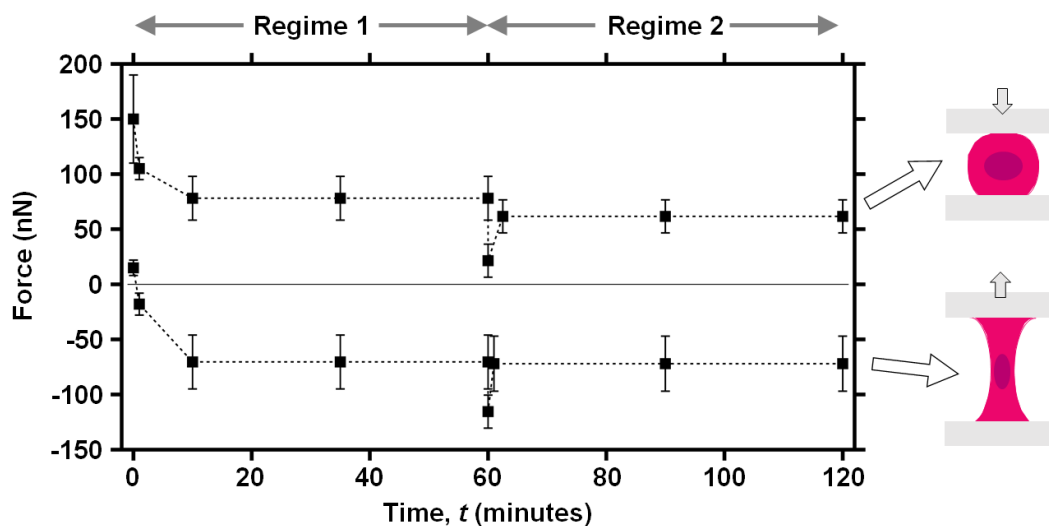


**Figure 6.2:** The maximum and minimum force measured from deformation experiments of untreated cells (average  $\pm$  standard error of the mean,  $n=7$ ). Schematic of a cell resisting compression during probe displaces downwards (top) and during probe retraction (bottom). Raw data obtained by Paul Weafer, [figure creation performed by Ph.D. candidate Noel Reynolds](#).

In Figure 6.3, maximum and minimum forces obtained from experiments of cytoD treated cells are shown and the following key observations are made:

- A significant decrease in maximum and minimum forces is observed at the onset of cyclic deformation. The maximum and minimum forces subsequently stabilise to a steady state.
- For the untreated cells, steady state maximum forces of  $41.3 \pm 7.7$  nN and  $15.7 \pm 4.9$  nN are observed in regime 1 and regime 2, respectively. Steady state minimum forces of  $-11.9 \pm 5.1$  nN and  $-9.5 \pm 5.0$  nN are observed in regime 1 and regime 2, respectively. Therefore, cytoD treated cells provide little resistance to probe retraction (pulling) and strong resistance to loading (pushing).
- A significantly greater maximum force is observed in regime 1 compared to regime 2. The percentage change in steady state maximum force from regime 1 to regime 2 is  $62.0 \pm 6.7\%$ .

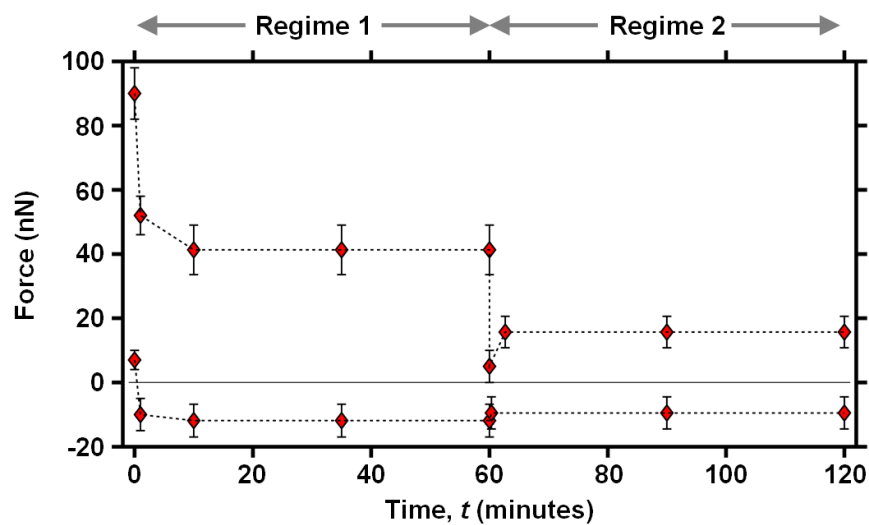


**Figure 6.3: The maximum and minimum force measured from deformation experiments of cytoD treated cells (average  $\pm$  standard error of the mean,  $n=7$ ).. Raw data obtained by Paul Weafer, figure creation performed by Ph.D. candidate Noel Reynolds.**

By comparing data obtained for untreated cells (Figure 6.2-A) to that for cytoD treated cells (Figure 6.3), the following key observations are highlighted:

- Maximum forces are significantly larger for untreated cells compared to cytoD treated cells at all time points.
- Untreated cells provide strong resistance to probe retraction (high minimum forces) whereas cytoD treated cells exert very little pulling force (small minimum forces).
- Between regime 1 and regime 2, maximum steady state force reduces by only  $21.1 \pm 7.8\%$  for untreated cells. The percentage reduction for cytoD treated cells is almost 3-fold higher ( $62.0 \pm 6.7\%$ ) than that for untreated cells. However, the magnitude of force associated with these reductions are similar for both the untreated (16.5 nN) and cytoD treated cells (25.6 nN).
- After 10 minutes the reduction in force from the maximum value obtained in the first cycle is similar for cytoD cells (48.0 nN) and untreated cells (45.0 nN).

Force-strain curves measured for loading cycles at four distinct time points are shown in Figure 6.4. The cycles shown are at the following time points: the initial loading cycle at the start of the experiment; the last loading cycle of regime 1; the first cycle of regime 2 and; the final cycle of regime 2. The following key observations are made:

- The initial loading cycle of regime 1 follows a typical viscoelastic-type loading curve for both the untreated and cytoD treated cells. However, the force recorded for untreated cells significantly higher throughout the cycle, in line with observations of maximum and minimum values.
- For untreated cells the steady state forces gradually increase/decrease between maximum and minimum values during cycling.

- Steady state force-strain curves are extremely similar in both regimes for untreated cells.
- During loading, steady state forces for cytoD treated cells only begin to increase rapidly after the probe has reached ~15% deformation (i.e. 15% applied strain in regime 1 and 25% applied strain in regime 2). During unloading, a rapid decrease in force is observed initially in the first 5% of deformation. The rate of force decrease subsequently reduces.

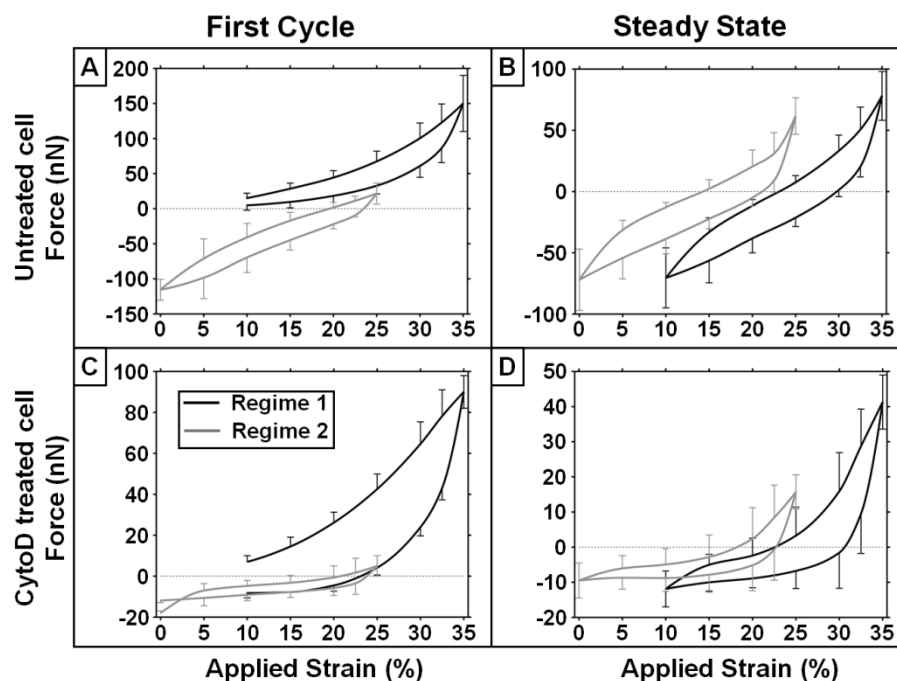


Figure 6.4: Mean  $\pm$  standard error of the mean force-deformation cycles for untreated (A and B) and cytoD (C and D) treated cells. The cycles shown in A and C correspond to the first cycle of regime 1 (black curve) and regime 2 (grey curve). The cycles shown in B and D correspond to steady state cycles of regime 1 (black curve) and regime 2 (grey curve). Raw data obtained by Paul Weafer, data processing and figure creation performed by Ph.D. candidate Noel Reynolds.

## 6.3 Discussion

In the current chapter, the experimental findings of Weafer (2012) are used to construct transient force-deformation loops for both untreated contractile cells and cells treated with cytoD. The following key findings are highlighted:

- (i) Measured forces for the untreated cells are dramatically different to cytoD treated cells, indicating that the contractile actin cytoskeleton plays a critical role in the response of cells to dynamic loading
- (ii) Following a change in applied strain magnitude, while maintaining a constant applied strain rate, the compression force for contractile cells recovers to  $78.9 \pm 7.8\%$  of the steady state force. In contrast, cytoD cell compression forces recover to only  $38.0 \pm 6.7\%$  of the steady state force.
- (iii) Untreated contractile cells exhibit strongly negative (pulling) forces during unloading half-cycles when the probe is retracted. In contrast, negligible pulling forces are measured for cytoD cells during probe retraction.

For untreated cells the steady state force-strain curve in regime 1 is extremely similar to that of regime 2 in terms of (a) the gradual force increase/decrease as the probe progresses through the loading cycle, (b) the patterns of non-linearity, and (c) maximum/minimum force measurements. Significantly increased negative and positive forces are measured for the untreated cells compared to cytoD cells. This suggests that the forces generated by the actin cytoskeleton dominate the response of single cells to dynamic loading. In terms of the minimum force, the strong negative (pulling) force results from active tension generated by actin-myosin cross-bridge cycling. A study by Mitrossilis et al. (2009) demonstrates that isolated myoblasts obey a Hill-type tension-strain rate relationship (Hill, 1938) under quasi-static conditions: higher shortening velocities and lower levels of active tension generation occur when the cell is attached to a flexible cantilever; low shortening velocities and high levels of active tension generation occur when the cell is attached to a stiff cantilever. Additionally, several studies demonstrate that a Hill-type contractility law explains several

experimentally observed cell responses to quasi-static monotonic applied loading: Ronan et al. (2012) demonstrated that more highly contractile cells provide a higher resistance to static compression due to stretching of hoop-type families of stress fibres; Dowling et al. (2012) demonstrated that Hill type behaviour of the actin cytoskeleton of chondrocytes provides accurate predictions of experimental force measurements during monotonic shear loading. The high magnitudes of compression (maximum) force and stretching (minimum) force reported in Weafer et al. (2015) may, in part, be explained through active Hill-type contractility of stress fibre families in the cell cytoplasm.

In terms of the transient behaviour reported in Figure 6.4 above, a gradual increase and decrease in force is observed during loading and unloading half-cycles, respectively. At the end of each half-cycle, the strain rate in the cell instantaneously shifts from a constant positive value (during loading) to a constant negative value (during unloading). If stress fibres in the cell followed a Hill-type contractility law they would instantaneously change from a low tension state to a high (isometric) tension state (or vice versa) upon transition from loading to unloading. This would lead to a step increase/decrease in force at the start of each loading half-cycle. However, this is not observed in the experimental measured force-strain curves reported in the current chapter. Hunter et al. (1998) described a model whereby a history dependent strain rate is used to phenomenologically explain the transient behaviour of cardiac tissue. A similar formulation for the transient active contractility of cells will be examined in Chapter 7 of this thesis.

For cytoD treated cells steady state forces-strain curves in regime 1 are dramatically different to that of regime 2. The high dependence of force on strain magnitude, coupled with the observed stress relaxation and hysteresis in force-

strain curves suggest that cytoD cells may follow a visco-hyperelastic type material behaviour (Chung and Buist, 2012). It was demonstrated in Chapter 4 of this thesis that a visco-hyperelastic formulation is required to characterise the mechanical response of cytoD cells during micropipette aspiration. In the current chapter, the significant 62% reduction in steady state force observed after the applied maximum strain is altered by 10% also suggests that the mechanical behaviour of cytoD cells is highly non-linear. Even following the removal of the actin cytoskeleton, the mechanical behaviour of the remaining material (i.e. the cytoD cell) is complex and requires a rigorous computational analysis in order to provide a meaningful characterisation. Chapter 7 considers the non-linear behaviour of cytoD cells, in addition to the active behaviour of untreated cells under dynamic loading conditions.

## 6.4 References

- BUTLER, J. P., TOLIC-NORRELYKKE, I. M., FABRY, B. & FREDBERG, J. J. 2002. Traction fields, moments, and strain energy that cells exert on their surroundings. *Am J Physiol Cell Physiol*, 282, C595-605.
- CAILLE, N., THOUMINE, O., TARDY, Y. & MEISTER, J.-J. 2002. Contribution of the nucleus to the mechanical properties of endothelial cells. *J Biomech*, 35, 177-187.
- CHUNG, C. W. & BUIST, M. L. 2012. A novel nonlinear viscoelastic solid model. *Nonlinear Analysis: Real World Applications*, 13, 1480-1488.
- DARLING, E. M., TOPEL, M., ZAUSCHER, S., VAIL, T. P. & GUILAK, F. 2008. Viscoelastic properties of human mesenchymally-derived stem cells and primary osteoblasts, chondrocytes, and adipocytes. *J Biomech*, 41, 454-64.
- DOWLING, E. P., RONAN, W., OFEK, G., DESHPANDE, V. S., MCMEEKING, R. M., ATHANASIOU, K. A. & MCGARRY, J. P. 2012. The effect of remodelling and contractility of the actin cytoskeleton on the shear resistance of single cells: a computational and experimental investigation. *J R Soc Interface*, 9, 3469-79.
- HILL, A. V. 1938. The Heat of Shortening and the Dynamic Constants of Muscle. *Philos Trans R Soc Lond B Biol Sci*, 126, 136-195.
- HOFMANN, U. G., ROTSCH, C., PARAK, W. J. & RADMACHER, M. 1997. Investigating the cytoskeleton of chicken cardiocytes with the atomic force microscope. *J Struct Biol*, 119, 84-91.
- HUNTER, P. J., MCCULLOCH, A. D. & TER KEURS, H. E. D. J. 1998. Modelling the mechanical properties of cardiac muscle. *Progress in Biophysics and Molecular Biology*, 69, 289-331.

- JAASMA, M. J., JACKSON, W. M. & KEAVENY, T. M. 2006. Measurement and characterization of whole-cell mechanical behavior. *Annals of biomedical engineering*, 34, 748-758.
- KELLY, G. M., KILPATRICK, J. I., VAN ES, M. H., WEAFFER, P. P., PRENDERGAST, P. J. & JARVIS, S. P. 2011. Bone cell elasticity and morphology changes during the cell cycle. *J. Biomech.*, 44, 1484-1490.
- LAM, R. H., WENG, S., LU, W. & FU, J. 2012. Live-cell subcellular measurement of cell stiffness using a microengineered stretchable micropost array membrane. *Integr Biol (Camb)*, 4, 1289-98.
- LEHENKARI, P. P., CHARRAS, G. T., NYKANEN, A. & HORTON, M. A. 2000. Adapting atomic force microscopy for cell biology. *Ultramicroscopy*, 82, 289-95.
- LULEVICH, V., ZINK, T., CHEN, H. Y., LIU, F. T. & LIU, G. 2006. Cell mechanics using atomic force microscopy-based single-cell compression. *Langmuir*, 22, 8151-8155.
- MANN, J. M., LAM, R. H., WENG, S., SUN, Y. & FU, J. 2012. A silicone-based stretchable micropost array membrane for monitoring live-cell subcellular cytoskeletal response. *Lab Chip*, 12, 731-40.
- MITROSSILIS, D., FOUCHARD, J., GUIROY, A., DESPRAT, N., RODRIGUEZ, N., FABRY, B. & ASNACIOS, A. 2009. Single-cell response to stiffness exhibits muscle-like behavior. *Proceedings of the National Academy of Sciences*, 106, 18243-18248.
- NAWAZ, S., SÁNCHEZ, P., BODENSIEK, K., LI, S., SIMONS, M. & SCHAAP, I. A. T. 2012. Cell visco-elasticity measured with AFM and optical trapping at sub-micrometer deformations. *PLoS ONE*, 7, e45297.
- PRABHUNE, M., BELGE, G., DOTZAUER, A., BULLERDIEK, J. & RADMACHER, M. 2012. Comparison of mechanical properties of normal and malignant thyroid cells. *Micron*, 43, 1267-1272.
- RADMACHER, M., FRITZ, M., KACHER, C. M., CLEVELAND, J. P. & HANSMA, P. K. 1996. Measuring the viscoelastic properties of human platelets with the atomic force microscope. *Biophys J*, 70, 556-67.
- REYNOLDS, N. H. & MCGARRY, J. P. 2015. Single cell active force generation under dynamic loading – Part II: Active modelling insights. *Acta Biomaterialia*, DOI:dx.doi.org/10.1016/j.actbio.2015.09.004.
- ROCA-CUSACHS, P., ALCARAZ, J., SUNYER, R., SAMITIER, J., FARRE, R. & NAVAJAS, D. 2008. Micropatterning of single endothelial cell shape reveals a tight coupling between nuclear volume in G1 and proliferation. *Biophys J*, 94, 4984-95.
- RONAN, W., DESHPANDE, V. S., MCMEEKING, R. M. & MCGARRY, J. P. 2012. Numerical investigation of the active role of the actin cytoskeleton in the compression resistance of cells. *J Mech Behav Biomed Mater*, 14, 143-57.
- ROTSCH, C. & RADMACHER, M. 2000. Drug-induced changes of cytoskeletal structure and mechanics in fibroblasts: an atomic force microscopy study. *Biophys J*, 78, 520-35.
- TITUSHKIN, I. & CHO, M. 2007. Modulation of cellular mechanics during osteogenic differentiation of human mesenchymal stem cells. *Biophysical Journal*, 93, 3693-3702.
- WATANABE-NAKAYAMA, T., MACHIDA, S., HARADA, I., SEKIGUCHI, H., AFRIN, R. & IKAI, A. 2011. Direct detection of cellular adaptation to local cyclic stretching at the single cell level by atomic force microscopy. *Biophys J*, 100, 564-72.
- WEAFFER, P. 2012. *Experimental Investigation of the Response of Osteoblasts to Static and Dynamic Loading using a Modified Atomic Force Microscope*. Ph.D Thesis, National University of Ireland Galway.
- WEAFFER, P. P., MCGARRY, J. P., VAN ES, M. H., KILPATRICK, J. I., RONAN, W., NOLAN, D. R. & JARVIS, S. P. 2012. Stability enhancement of an atomic force microscope for

long-term force measurement including cantilever modification for whole cell deformation. *Rev Sci Instrum*, 83, 093709.

WEAFER, P. P., REYNOLDS, N. H., JARVIS, S. P. & MCGARRY, J. P. 2015. Single cell active force generation under dynamic loading – Part I: AFM experiments. *Acta Biomaterialia*, DOI:dx.doi.org/10.1016/j.actbio.2015.09.006.

ZIMMER, C. C., SHI, L. F., SHIH, Y. P., LI, J. R., JIN, L. W., LO, S. H. & LIU, G. Y. 2012. F-Actin reassembly during focal adhesion impacts single cell mechanics and nanoscale membrane structure. *Science China Chemistry*, 1-11.

# **7 Single cell active force generation under dynamic loading – Active modelling insights**

## **7.1 Introduction**

As summarised in Chapter 6 a novel single cell atomic force microscopy (AFM) experimental investigation uncovers the complex force-strain response of cells to cyclic loading (Weafer et al., 2015). Using a bespoke AFM system (Weafer et al., 2012), force generated by single cells during dynamic loading is measured. Cells in which the actin cytoskeleton is disrupted using cytochalasin-D (cytoD) are also tested. Experimental results reveal that the biomechanical behaviour of untreated contractile cells is fundamentally different to non-contractile cytoD treated cells. The following key findings are uncovered in Weafer et al. (2015) and summarised in Chapter 6:

- Untreated contractile cells are relatively insensitive to changes in applied strain magnitude. In contrast, cells treated with an actin cytoskeleton

inhibitor, cytoD, are shown to be highly sensitive to changes in strain magnitude.

- Untreated contractile cells greatly resist the retraction of the AFM probe during unloading, pulling strongly on the probe. In contrast, cells treated with an actin cytoskeleton inhibitor provide little resistance to AFM probe retraction.
- Untreated contractile cells provide a higher resistance to compression than cells treated with an actin cytoskeleton inhibitor.

The above findings from Weafer et al. (2015) (as summarised in Chapter 6) provide new characterisation of the complexity of single cell response to dynamic loading. However, the biomechanisms underlying such complex behaviour cannot be fully understood without a detailed mechanistic analysis incorporating the key features of active stress generation and remodelling of the actin cytoskeleton. Importantly, the trends outlined above cannot be replicated or explained in terms of passive hyperelastic or viscoelastic material behaviour.

A simplified approach to modelling the behaviour of the actin cytoskeleton commonly entails the ad-hoc placement of pre-stressed beam elements in the cell cytoplasm (Barreto et al., 2013, McGarry and Prendergast, 2004). This approach neglects intercellular processes governing active cytoskeletal contractility and remodelling, and does not allow for the simulation of the multi-axial evolution and stress-generation of the actin cytoskeleton throughout the cell. In contrast, the active model of stress fibre (SF) contractility and remodelling proposed by Deshpande et al. (2007) incorporates the key features of SF formation, dissociation, and contractility. The extension of this active SF framework to a fully predictive 3D finite element (FE) setting (Ronan et al., 2012) allowed for the simulation of

complex multi-axial patterns of SF morphology and contractility (Ronan et al., 2014), with complex experimental tests being accurately simulated under quasi-static conditions, e.g. non-linear force-deformation behaviour of chondrocytes under direct shear (Dowling et al., 2012), and the response of spread adhered endothelial cells to micropipette aspiration (Chapter 4).

This active 3D framework has not previously been used to simulate single cell dynamic loading experiments. Here a computational investigation of the experimental results reported in Chapter 6 is presented. Simulations reveal that different families of SFs generate tension during probe pulling and probe pushing, resulting in elevated forces during both unloading and loading half-cycles, respectively. Additionally, it is shown that a “fading memory” strain rate contractility model is required to replicate the transient behaviour of cells under dynamic loading. Furthermore, results highlight that passive visco-hyperelastic material models cannot accurately simulate the dynamic behaviour of contractile cells.

## **7.2 Materials and Methods**

### **7.2.1 Modelling the bio-chemo-mechanical behaviour of the actin cytoskeleton**

#### *7.2.1.1 Fibre activation level and tension*

As briefly described in Chapter 4, a bio-chemo-mechanical model is used to simulate signal induced SF formation, active SF contractility, and tension dependant SF dissociation. Originally proposed by Deshpande et al. (2007) and implemented in a predictive 3D framework by Ronan et al. (2012), a description of

the key features of the model is provided here. Formation and dissociation of SFs are described using a first order kinetic equation:

$$\frac{d\eta(\phi, \omega)}{dt} = [1 - \eta(\phi, \omega)]Ck_f - \left[1 - \frac{\sigma_f(\phi, \omega)}{\sigma_0(\phi, \omega)}\right]\eta(\phi, \omega)k_b \quad (7.1)$$

where  $\eta$  is the non-dimensional activation level of a fibre ( $0 \leq \eta \leq 1$ ) and  $k_f$  and  $k_b$  are forward and backward reaction rate constants, respectively.  $\theta$  is the decay constant. The first term in the first order kinetic equation captures fibre formation via a spatially uniform signal in the cytoplasm,  $C$ , that is typically represented as an exponent ( $C = \exp(-t_s/\theta)$ ) governed by the decay constant,  $\theta$ , and the time since the most recent signal,  $t_s$  (Figure 7.1-A). The second term describes SF dissociation when the fibre tension is lower than the isometric tension,  $\sigma_f < \sigma_0$  (Figure 7.1-B). The fibre isometric tension is proportional to the fibre activation level, such that  $\sigma_0 = \eta\sigma_{MAX}$ , where the model parameter,  $\sigma_{MAX}$ , is the isometric tension of a fully activated fibre ( $\eta = 1$ ).

Fibre tension,  $\sigma_f$ , is related to the fibre axial strain rate,  $\dot{\epsilon}_f$ , via a linearised approximation of the Hill tension-velocity relationship (Deshpande et al., 2007):

$$\frac{\sigma_f}{\sigma_0} = 1 + \frac{\bar{k}_v}{\eta} \frac{\dot{\epsilon}_f}{\dot{\epsilon}_0}; \quad -\frac{\eta}{\bar{k}_v} \leq \frac{\dot{\epsilon}_f}{\dot{\epsilon}_0} \leq 0, \quad (7.2)$$

where  $\bar{k}_v$  is the reduction in stress upon increasing the shortening strain rate,  $\dot{\epsilon}_f$ , by  $\dot{\epsilon}_0$ . As described by equation (7.2) (and Figure 7.1-C), during fibre shortening (negative strain rate) fibre tension decreases linearly from the isometric tension (at zero strain rate) to zero tension at a strain rate of  $-\eta\dot{\epsilon}_0/\bar{k}_v$ . Fibre tension remains

at zero for strain rates less than  $-\eta\dot{\epsilon}_0/\bar{k}_v$ . Finally, when subjected to positive (lengthening) strain rates, fibres yield at the isometric tension,  $\sigma_0$ .

### 7.2.1.2 Fading Memory of Fibre Strain Rate

The SF model outlined in Section 7.2.1.1 has recently been shown to accurately predict the response of contractile cells to externally applied shear deformation (Dowling et al., 2012, Dowling and McGarry, 2013), parallel-plate compression (Weafer et al., 2013, Ronan et al., 2012), micropipette aspiration (Chapter 4), and spreading on 2D elastic substrates (Ronan et al., 2014). All of these aforementioned studies investigate the cell response under static conditions or during single monotonic applied load (such loading is commonly referred to as “static loading”). In contrast, the current chapter considers dynamic cyclic loading applied at a frequency of 1 Hz for a duration of two hours. In order to provide enhanced predictions of actin-myosin contractility under dynamic conditions, here the SF contractility model presented in Section 7.2.1.1 is modified to incorporate dynamic effects. Based on empirical observations for cardiac muscle (Hunter et al., 1998) under dynamic conditions, a history dependant fibre strain rate is defined as:

$$h_f = \sum_{-\infty}^t \int A e^{-\alpha(t-\tau)} \dot{\epsilon}_m(\tau) d\tau \quad \dot{\epsilon}_m = \begin{cases} \dot{\epsilon}_f & \dot{\epsilon}_f \leq 0 \\ 0 & \dot{\epsilon}_f > 0 \end{cases} \quad (7.3)$$

where  $\dot{\epsilon}_f(\tau)$  is the instantaneous fibre strain rate and  $A$  and  $\alpha$  are material parameters. To include fading memory effects in the active SF model, the Hill contractility equation is modified so that now:

$$\frac{\sigma_f}{\sigma_0} = 1 + \frac{\bar{k}_v h_f}{\eta \dot{\epsilon}_0}; \quad -\frac{\eta}{\bar{k}_v} \leq \frac{h_f}{\dot{\epsilon}_0} \leq 0, \quad (7.4)$$

Full details of the numerical technique used to calculate the history dependant strain rate,  $h_f$ , from the actual strain rate,  $\dot{\epsilon}_f$ , is described in section 7.2.2.2. An example of  $h_f$  calculated from  $\dot{\epsilon}_f$  is graphically illustrated in Figure 7.2-A. A motivation for the incorporation of this fading memory contractility law will be presented in Section 7.3.3.2.

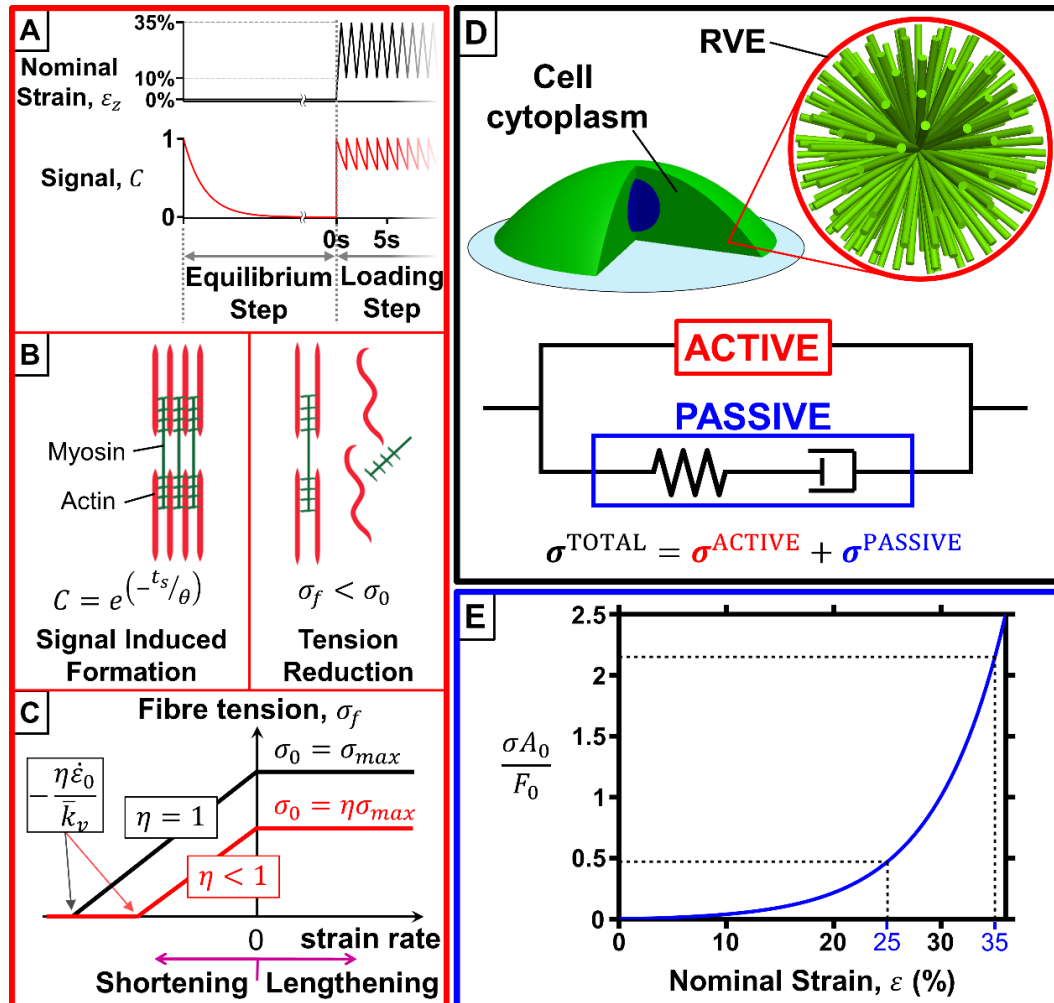


Figure 7.1: (A) Graphical representation of the deformation induced exponentially decaying signal activated at the onset of each loading cycle. Prior to the onset of applied deformation an equilibrium step is simulated to compute the initial distribution of SFs. (B) Illustration of signal dependant SF assembly and tension dependant SF dissociation. (C) Graphical illustration of the linearised approximation of the Hill tension-velocity relationship. (D) Equations 1-4 are solved in 240 discrete directions at every integration point in the cytoplasm, providing a fully predictive framework for computation of the 3D SF distribution in the cell. The total stress tensor is obtained by summation of the active and passive stress tensors. (E) Uniaxial stress-strain curve for the hyperelastic formulation used to simulate the passive components of the cell cytoplasm.

## 7.2.2 Numerical implementation

### 7.2.2.1 Fibre remodelling and contractility

In order to predict the distribution of SFs throughout the cell, the fibre remodelling and contractility equations are solved in 240 discrete directions at every integration point in the cytoplasm. At each integration point the fibre activation level in any one of these 240 directions depends on the local stress state and the signal intensity. This provides a fully predictive framework to determine the inhomogeneous three dimensional SF distribution throughout the cytoplasm. The representative volume element (RVE) is defined as a sphere containing fibres that are equally distributed in 3D space (Figure 7.1-D). The strain rate experienced by each fibre is calculated from the overall strain rate of the integration point, and used to determine the fibre tension,  $\sigma_f$ .

The contribution of the tension in each fibre is numerically integrated over the volume,  $V$ , to determine an overall active stress tensor for the RVE:

$$\boldsymbol{\sigma}^{ACTIVE} = \sigma_{ij}^A = \frac{1}{V} \int_V \sigma_f(\omega, \phi) m_i m_j dV \quad (7.5)$$

where  $m_i m_j$  describes the arbitrary orientation of a fibre. The active stress tensor is then added to the passive stress tensor to obtain the total stress tensor at the integration point:

$$\boldsymbol{\sigma}^{TOTAL} = \boldsymbol{\sigma}^{PASSIVE} + \boldsymbol{\sigma}^{ACTIVE} \quad (7.6)$$

### 7.2.2.2 Fading memory model

In this section, the numerical implementation of the fading memory contractility formulation is outlined. As described by Ronan et al. (2012), the

original SF model has been previously implemented as a *user-defined material subroutine* (UMAT) in the commercial FE software Abaqus 6.13 (Simula, Providence, RI, USA).

A perturbation method to determine a numerical approximation of the material Jacobian is implemented in the UMAT. Described in full by Sun et al. (2008), the perturbation methods is summarised in Section 3.4.2.

In order to introduce the fading memory in a FE setting, the integral must be solved numerically. The integral is approximated using the trapezoidal rule:

$$h_f = \frac{A}{2} \sum_{i=2}^n [e^{-\alpha(t-t_i)} \dot{\epsilon}_{m,i} + e^{-\alpha(t-t_{i-1})} \dot{\epsilon}_{m,i-1}] [t_i - t_{i-1}] \dot{\epsilon}_{m,i} \quad (7.7)$$

$$= \begin{cases} \dot{\epsilon}_{f,i} \dot{\epsilon}_{f,i} \leq 0 \\ 0 \quad \dot{\epsilon}_{f,i} > 0 \end{cases}$$

where  $n$  is the number of history points recorded,  $t$  is the current time, and  $t_i$  and  $\dot{\epsilon}_{f,i}$  are the time and fibre strain rate associated with the history point,  $i$ , respectively. As illustrated in Figure 7.2-B, the history points are the time intervals,  $t_{int}$ , back from the current time,  $t$ , until a specified history time,  $t_{hist}$ , is reached.  $t_{hist}$  and  $t_{int}$  used in the current numerical scheme are restricted for computational efficiency, as discussed later in this section.

Due to the unfeasibility of storing the strain rate for each of the 240 fibre directions in the RVE at every history point, only the strain rate tensor is stored (6 strain rate components per history point) in UMAT state dependant variables (SDVs). The individual fibre strain rates must be recalculated from the integration point strain rate at every history point per stress calculation. For further computational efficiency, the history of strain rates stored into SDVs is limited by

a user defined time,  $t_{hist}$  (Figure 7.2-B). Therefore, only strain rates between the current time,  $t$ , and  $t - t_{hist}$  are stored for use in the calculation. The history time chosen is based on the exponent,  $\alpha$ , such that the oldest contribution (and therefore, any older contribution) to the numerically integrated fibre strain rate,  $h_f$ , is negligible ( $e^{-\alpha(t-(t-t_{hist}))} \dot{\epsilon}_m \approx 0$ ). Furthermore, the strain rate histories are stored only at user defined time intervals,  $t_{int}$ . Once an interval is reached, the strain rates at the oldest history point ( $t - t_{hist}$ ) are replaced with the strain rates at the new interval. Before inclusion into the UMAT, the robustness of this numerical time-integration is rigorously tested. In Figure 7.2-C, for an  $\alpha = 5$ , it is clearly demonstrated that an insufficient history time ( $t_{hist} = 0.2$  s) results in a fading memory strain rate that exhibits a step change each time the oldest history point is dropped (i.e.  $e^{-\alpha(t-(t-t_{hist}))} \dot{\epsilon}_m \neq 0$ ), yielding a bad numerical approximation. It is further illustrated that history times of 0.7 s or greater are sufficient for the approximation when  $\alpha = 5$ . In Figure 7.2-D, a range of numerically approximated fading memory strain rates are shown for different time interval values when  $\alpha = 5$  and  $t_{hist} = 2$  s. It is clearly shown that the time interval must be sufficiently small ( $t_{int} \leq 0.05$  s) for the integral to be accurately approximated. Any increase in the history time or decrease in the time interval has negligible effect on the numerical approximation of fibres fading memory strain rate,  $h_f$ .

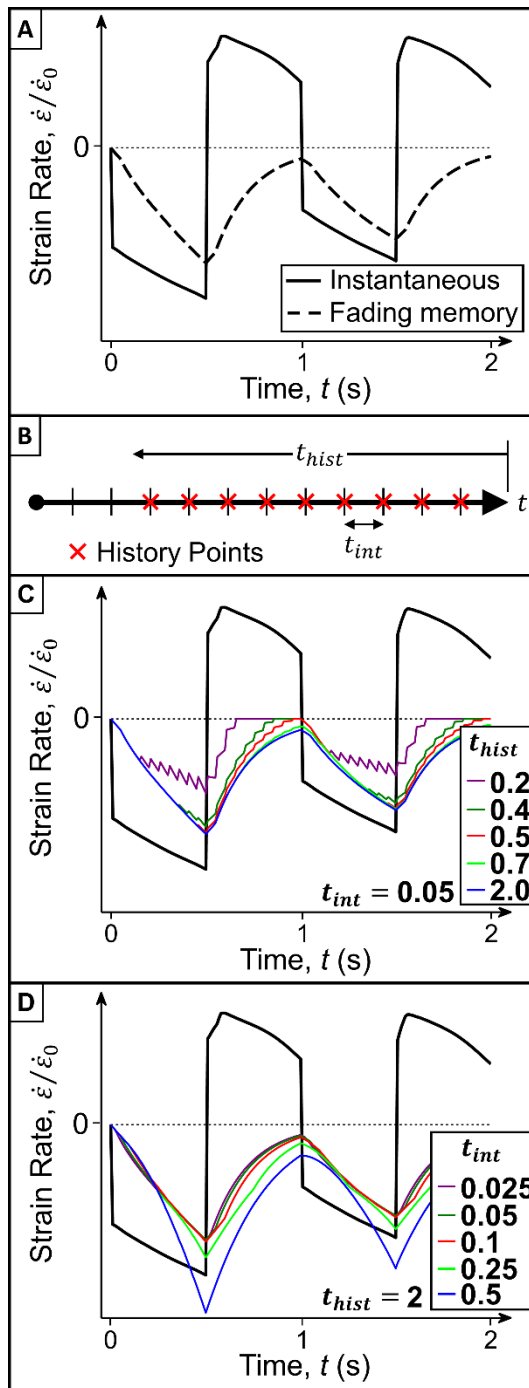


Figure 7.2: (A) Plot of instantaneous applied fibre strain rate,  $\dot{\epsilon}_f$ , (solid line) with corresponding time integrated fading memory strain rate,  $h_f$ , (dashed line). (B) Illustration of history time,  $t_{hist}$ , and time interval,  $t_{int}$ , parameters on a timeline. (C) Parametric study of history time,  $t_{hist}$ . (D) Parametric study of time interval,  $t_{int}$ , used. All time parameters are in seconds. Based on this parametric study, a  $t_{hist}$  of 2 s and a  $t_{int}$  of 0.05 s were used in all further simulations.  $A$  and  $\alpha$  values of 1 and 5, respectively, were also used throughout.

### 7.2.3 Characterising the Passive Response of CytoD Treated Cells during Cyclic Deformation

Passive non-contractile components of the cell cytoplasm are modelled using a non-linear visco-hyperelastic formulation (Figure 7.1-E). The passive stress computed by the reduced-polynomial hyperelastic component is given as:

$$\begin{aligned}\boldsymbol{\sigma}^{PASSIVE} &= \sigma_{ij}^P \\ &= \sum_{m=1}^n \left[ C_{m0} \frac{2}{J} \left( \bar{B}_{ij} - \frac{1}{3} \bar{B}_{kk} \delta_{ij} \right)^m \right. \\ &\quad \left. + \frac{1}{D_m} (J - 1)^{2m} \right]\end{aligned}\quad (7.8)$$

where  $n = 3$ ,  $\delta_{ij}$  is the Kronecker delta, and  $C_{10}$ ,  $C_{20}$ ,  $C_{30}$ ,  $D_1$ ,  $D_2$ , and  $D_3$  are material parameters. The isochoric left Cauchy-Green deformation tensor,  $\bar{\mathbf{B}}$ , is determined from the deformation gradient,  $\mathbf{F}$ :

$$\bar{B}_{ij} = \frac{B_{ij}}{J^{2/3}} = \frac{F_{ik} F_{jk}}{(\det(\mathbf{F}))^{2/3}} \quad (7.9)$$

Viscous behaviour of the passive components of the cell are incorporated via a one-term Prony series:

$$C_{m0}(t) = C_{m0} \left( 1 - \bar{g}^p \left( 1 - e^{-t/\tau^p} \right) \right) \quad (7.10)$$

$$D_i(t) = \frac{D_i}{1 - \bar{k}^p \left( 1 - e^{-t/\tau^p} \right)} \quad (7.11)$$

where  $\bar{g}^p$  and  $\bar{k}^p$  are dimensionless Prony series parameters for isochoric and dilatational behaviour, respectively ( $0 \leq (\bar{g}^p, \bar{k}^p) < 1$ ), and  $\tau^p$  is the time constant

for the formulation. This non-linear visco-hyperelastic material model is used to simulate the mechanical response of the passive components of the cell, i.e. all components of the cell excluding SFs. Therefore the contribution of non-contractile components of the cell, such as intermediate filaments, microtubules, nucleus, cytosol, and other cytoplasm organelles, are treated as non-linear visco-hyperelastic. To calibrate the passive parameters, the force measurements for cytoD cells reported in Chapter 6/Weafer et al. (2015) are used. CytoD is an actin polymerisation inhibitor that eradicates contractile SFs, leaving only a passive non-contractile components in the cell. The calibrated visco-hyperelastic model is used in parallel with an active the framework for SF remodelling and contractility (Figure 7.1-D) described in sections 7.2.1 and 7.2.2.

#### **7.2.4 FE modelling of cyclic loading**

In order to understand the key mechanical features of cell response to applied dynamic loading an idealised cell geometry is assumed, whereby a relatively uniform stress and strain state occurs in the cell. Realistic and complex geometries are not considered until Section 7.3.5, once a fundamental mechanistic understanding has been established. The idealised axisymmetric cell geometry is shown in Figure 7.3-B. A quadrant represents an idealised cell with a radius,  $r_0$ , and height,  $h_0$  (Figure 7.3-A). An axisymmetric rigid body is used to represent the substrate and a rigidly bonded cell-substrate interaction is assumed. The cell is also assumed to be permanently adhered to the probe. Therefore, the z-displacement of the nodes on the symmetry plane is governed by the loading regime applied by the probe (Figure 7.3-C). Nodes on the symmetry plane are unconstrained in the R-direction. It is critical to note that for the RVE described above in Section 7.2.2.1,

SFs are not confined to the axisymmetric plane. Therefore, a full 3D stress tensor is calculated.

After the signal is induced in contractile cell analyses, SFs are allowed to reach an equilibrium distribution before initiation of loading. The interaction between actively generated SF tension and the passive material leads to the ‘hourglass-like’ shape observed in Figure 7.3-A. The equilibrium step is only required for simulations of an untreated contractile cell. For simulations of cells in which SFs and contractility have been inhibited using cytoD, the quadrant is a rectangular shape (or the entire cell has a cylindrical shape) before application of dynamic loading. In the next analysis step, z-displacement is introduced at the symmetry plane of the cell to mimic the experimentally applied nominal strain,  $\epsilon_z$  (Figure 7.3-C). The z-displacement at the symmetry plane is half that applied at the probe, where displacement at the probe is  $u_z$  ( $u_z = \epsilon_z \times h_0$ ). Cells are cyclically deformed at a constant loading and unloading strain rate at a frequency of 1 Hz (Figure 7.3-C). Similar to experiments presented in Chapter 6, dynamic loading is applied for a total of 120 minutes ( $T_F$ ) with a change in loading regime implemented after 60 minutes ( $T_{RC}$ ). In loading regime 1 ( $T_0 \leq t \leq T_{RC}$ ), cells are cyclically deformed between a maximum and minimum compressive strain of 35% and 10%, respectively. In loading regime 2 ( $T_{RC} \leq t \leq T_F$ ), cells are cyclically deformed between a maximum and minimum compressive strain of 25% and 0%, respectively. It is important to note that even though the strain magnitude is altered by 10% between regimes 1 and 2, the peak-to-peak strain amplitudes in each regime are identical (25%). Therefore, the unloading and loading strain rate remains the same in both regimes.

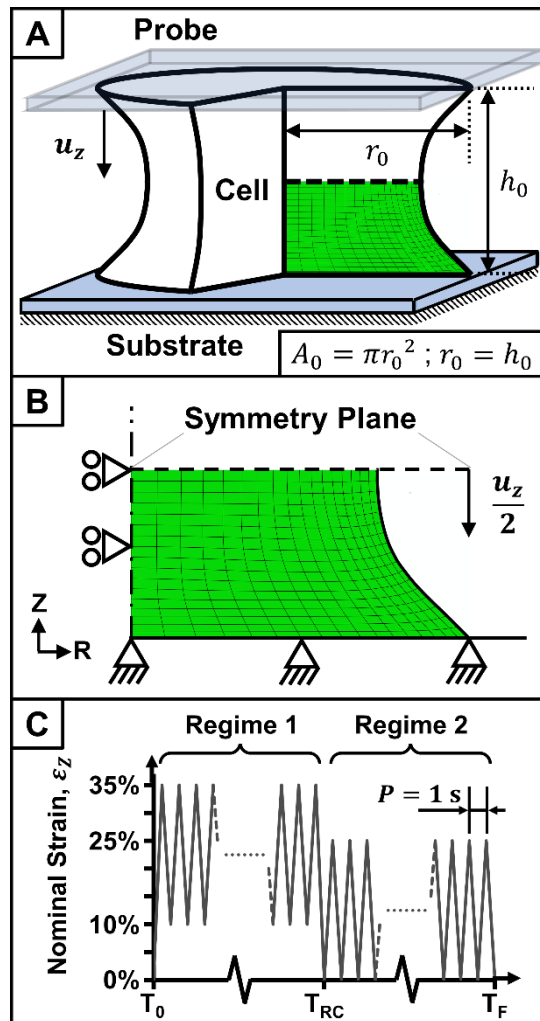


Figure 7.3: (A) Idealised cell geometry, highlighting an axisymmetric quadrant used for dynamic simulations. (B) Boundary conditions used for strain controlled loading on the symmetry plane and cell-substrate/cell-probe rigidly bonded interfaces. (C) Graphical representation of the nominal strain,  $\epsilon_z$ , applied over the course of FE simulations.

Measured dimensions from experimental cell images Weafer et al. (2015) are used to construct a realistic geometry. The undeformed configuration is shown in Figure 7.10-A, with a cell height,  $H_C$ , of  $8.6 \mu\text{m}$  and an outer radius,  $R_C$ , of  $29 \mu\text{m}$ . The cell nucleus has a height,  $H_N$ , of  $6.1 \mu\text{m}$  and a radius,  $R_N$ , of  $5.8 \mu\text{m}$ . The geometry is subject to a similar loading regime as the idealised cell model above. At the end of the first loading half-cycle, a section at the top of the cell comes in contact with the probe, and is assumed to adhere. Firstly, passive properties of the cytoplasm and nucleus for this realistic cell geometry are calibrated using experimentally measured forces for cytoD cells. Based on the detailed investigation

of passive cell material properties reported by in Chapter 4, nucleus stiffness is assumed to be 2.75 higher than the cytoplasm. The nucleus and cytoplasm are assumed to be nearly incompressible.

In results sections, the colour coded vector plots are used to illustrate SF orientations and tension throughout the cell body (ParaView (Henderson et al., 2004)). It should be noted while a 2D axisymmetric geometry is used (Figure 7.3-B) – the evolution of SFs in 3D space is illustrated by plotting SF vectors in distinct orientations on separate planes in 3D space (as shown by the example in Figure 7.4), in order to clearly emphasise the 3D nature of the predictions presented in this paper. Finally, while a mesh sensitivity study reveals that 1600 elements are required to achieve a converged solution in the idealised cell model, only 700 SF vectors are shown in each plane for clarity.

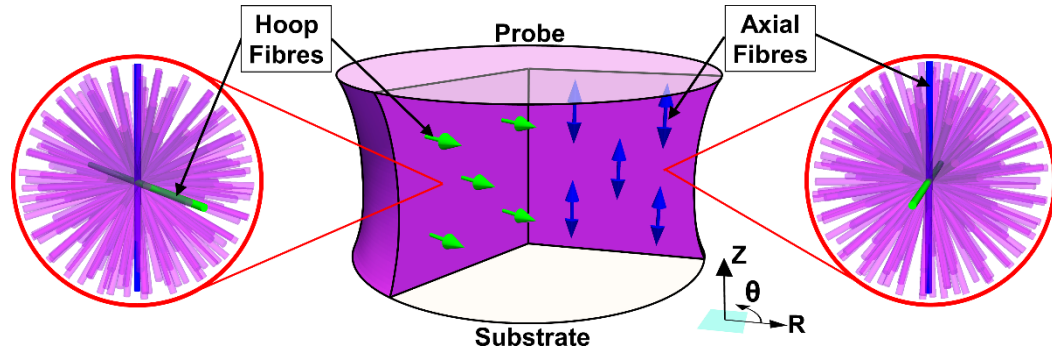


Figure 7.4: Schematic illustrating orientations of axial and hoop orientated fibres.

## 7.3 Results

### 7.3.1 Visco-hyperelastic modelling of cytoD treated cells

In Figure 7.5-A computed results for cytoD treated cells are presented. It should be recalled, cytoD is an actin polymerisation inhibitor that eradicates SFs and contractility in the cell, therefore cytoD treated cells are simulated merely as a

non-linear visco-hyperelastic material (as detailed in Section 7.2.3) and the active SF model is not included. Computed maximum forces (at mid-cycle when the cell is compressed) and minimum forces (the negative pulling forces when the probe is fully retracted at the end of a loading cycle) are plotted in Figure 7.5-A. Experimentally measured forces are also shown for comparison. As the idealised geometry considered in section 7.2.4 is arbitrarily chosen, non-dimensional material properties are presented in Table 7.1. Calibrated material properties are not presented until Section 7.3.5 where a realistic cell geometry, based on experimental images, is simulated. Note that the idealised cell model is assumed to be almost incompressible. As shown in Figure 7.5-A, a close correlation with the experimentally measured maximum and minimum forces is established for the cytoD cells. In the first 10 minutes of regime 1 maximum force is predicted to decrease from 90.0 nN to 41.3 nN and the minimum force decreases from 7.0 nN to -11.9 nN, exhibiting a viscoelastic stress-relaxation, as expected. The model also captures the steady state behaviour observed during the final 50 minutes of regime 1. At the regime change ( $T_{RC} = 60$  minutes), there is a significant reduction in the computed maximum force followed by a relatively rapid increase to a steady state during the following 2.7 minutes. The model predicts that the steady state maximum force in regime 2 (15.7 nN) is significantly lower than that computed during regime 1 (41.3 nN). Computed forces (both maximum and minimum) are extremely close to the experimentally measured values throughout regime 1 and regime 2. The non-linear visco-hyperelastic material model captures the strong dependence of cytoD cells on strain magnitude: A 29% reduction in applied axial strain from regime 1 (max strain = 35%) to regime 2 (max strain = 25%) results in a 62% (41.3 nN to 15.7 nN) reduction in steady state maximum force.

**Table 7.1: Normalised passive visco-hyperelastic material properties used for idealised cell geometry. Note that  $A_0$  is the undeformed cell cross sectional area,  $F_0$  is the maximum force in the first cycle of cytoD treated cell experiments, and  $P$  is the loading period. Normalised  $\sigma_{MAX}$  parameter used in active simulations is also shown.**

$\frac{C_{10}A_0}{F_0}$	$\frac{C_{20}A_0}{F_0}$	$\frac{C_{30}A_0}{F_0}$	$\bar{g}^p$	$\tau^p/P$	$\frac{\sigma_{MAX}A_0}{F_0}$
0.035	0.252	0.398	0.43	0.25	2.1

As well as providing a close correlation with the experimentally measured maximum and minimum forces, the non-linear visco-hyperelastic model yields excellent prediction of the force-strain loops during individual loading cycles (Figure 7.5-B to -E). In Figure 7.5-B, a force decrease between the start and the end of the first cycle of regime 1 is observed in experiments. In the first cycle of regime 2, a slight increase in force is measured between the start and the end of the cycle, causing the curve to overlap itself. The visco-hyperelastic model provides a good prediction of the experimentally observed trends in the first cycle of both regimes (Figure 7.5-D) – including the force change between the start and end of the cycles and the non-linearity of the loading and unloading curves. As observed in Figure 7.5-E, the model also provides a good prediction of the experimentally observed steady state force-strain loops (Figure 7.5-C). In summary, the non-linear visco-hyperelastic model provides an accurate prediction of the maximum and minimum forces as well as the force-strain curves for cytoD treated cells undergoing cyclic compression.

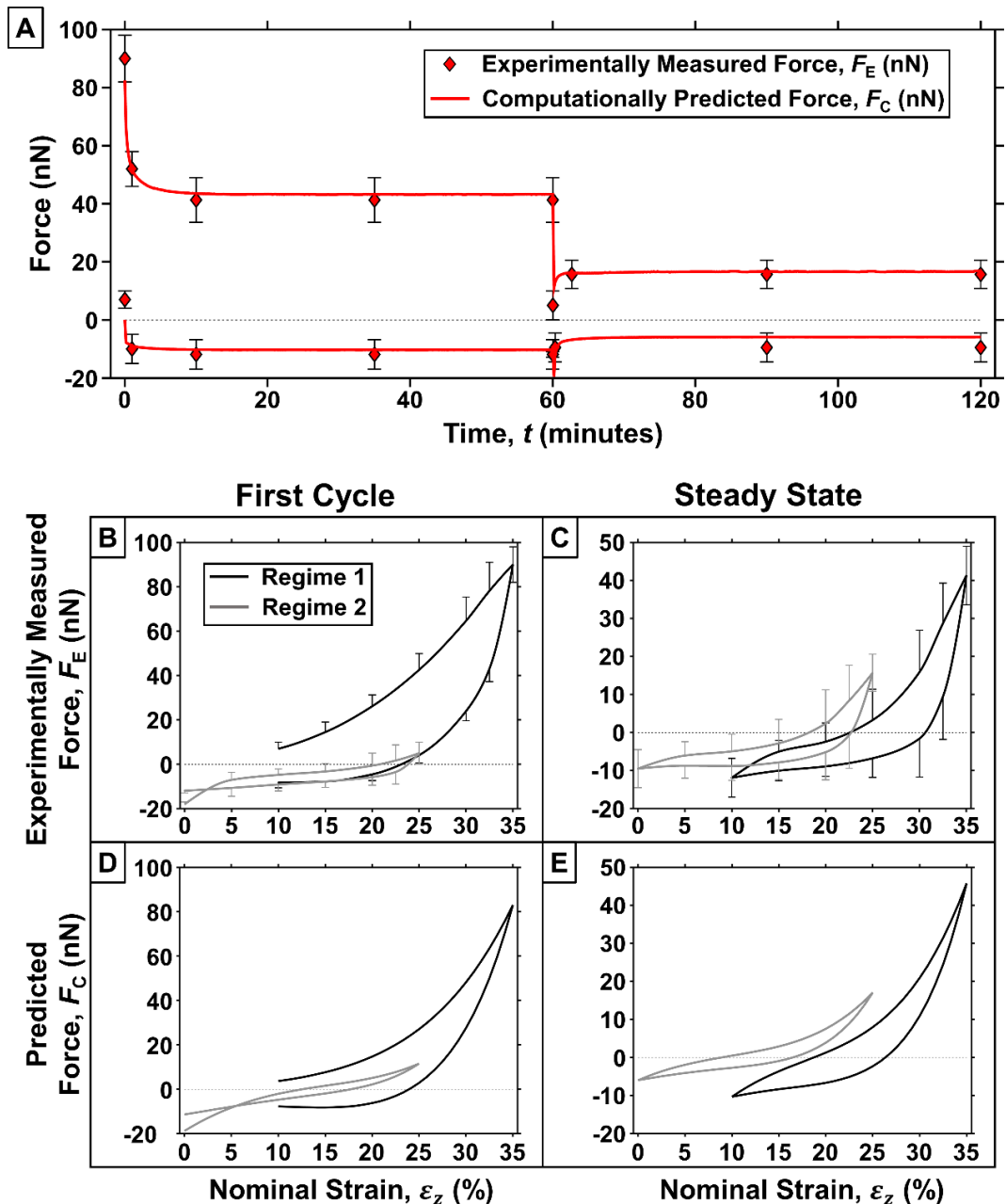


Figure 7.5: (A) The maximum and minimum force measured from deformation experiments of cytoD treated cells (average  $\pm$  standard error of the mean,  $n=7$ ) and predicted using a passive material model in FE simulations. Maximum force is measured when the probe is at compressive strain of 35% and 25% in regime 1 and regime 2, respectively. Minimum force is recorded when the probe is at compressive strain of 10% and 0% for regime 1 and regime 2, respectively. (B) The force measured during the first cycle after the onset of cyclic deformation ( $T_0$ ) and after the regime change ( $T_{RC}$ ). (C) The force measured during the last cycle of regimes 1 and 2. For clarity in (B) and (C), the error bars are only shown in the positive direction during loading (upper section of the curves) and in the negative direction during unloading (lower section of the curves). It should be noted that the standard error of the mean is plus and minus the average value at each point. An in-depth analysis and discussion of the trends observed during cyclic deformation experiments are available in Weafer et al. (2015). Figures (B) and (C) are reproduced from Chapter 6 of this thesis for comparison purposes. (D) The force predicted during the first cycle after the onset of cyclic deformation ( $T_0$ ) and after the regime change ( $T_{RC}$ ). (E) The force predicted during the last cycle of regimes 1 and 2.

### 7.3.2 Active SF modelling of untreated cells

#### 7.3.2.1 Predicting the maximum and minimum forces

The response of untreated contractile cells to dynamic loading is simulated by placing the active bio-chemo-mechanical framework for SFs (Section 7.2.1) in parallel with the passive visco-hyperelastic model (Section 7.2.3). At any integration point in the cytoplasm the stress tensor is obtained through addition of the passive and active stress tensors (equation (7.6)). It should be noted that visco-hyperelastic model parameters determined are retained in all simulations. Predicted maximum and minimum forces for this combined active-passive model are shown in Figure 7.6-A. A strong correlation with experimental results (included for comparison) can be observed. The active tension in axially orientated SF and in circumferentially orientated hoop SFs through a deformation cycle are shown in Figure 7.7. The key features captured by the active model are as follows:

- A significant minimum (negative) pulling force is computed by the active-passive model (Figure 7.6-A). Steady state pulling forces of -72.3 nN and -74.7 nN are computed in regime 1 and regime 2, respectively. These high magnitude (negative) pulling forces occur due to the stretching of axially orientated SFs when the probe is retracted during unloading half-cycles, as shown in the right panels of Figure 7.7 (summarised in Figure 7.6-C). When undergoing a positive strain during the unloading half-cycle these axial fibres yield, generating a tension equal to the isometric value ( $\eta\sigma_{max}$ ). During loading half-cycles axial fibres shorten at a high negative strain rate, so that no tension is generated, as shown in the right panels of Figure 7.7. It should be recalled that negligible pulling forces are computed/observed for passive cytoD treated cells (Figure 7.5).

- The steady state maximum (compression) forces in regime 1 (78.1 nN, see Figure 7.6-A) are significantly higher than that computed/observed for passive cytoD cells (41.3 nN, see Figure 7.5). This computed increase in steady state maximum force is due to the stretching of circumferentially oriented hoop SFs when the cell is compressed during loading half-cycles, as shown in the left panels of Figure 7.7 (summarised in Figure 7.6-B). The additional work required to stretch hoop SFs at isometric tension ( $\eta\sigma_{max}$ ) results in an increase in applied force required to compress the cell.
- In loading regime 2, where the applied strain rate remains unchanged but the applied strain magnitude is different from regime 1, the model accurately captures the experimentally observed ~21% reduction in steady state maximum force (from  $78.1\pm 19.9$  nN in regime 1 to  $61.5\pm 15.0$  nN in regime 2), as shown in Figure 7.6-A. Additionally, only a slight change in steady state minimum pulling force is predicted, again corresponding closely to experimental measurements (from  $-70.5\pm 24.5$  nN in regime 1 to  $-72.0\pm 25.0$  in regime 2). As the applied strain rate (both unloading and loading) is unchanged following the regime change, the SF contribution to the maximum and minimum forces are not significantly altered. The ~21% reduction in maximum steady state forces occurs due to the contribution of the passive visco-hyperelastic component of the model. The magnitude of force reduction is similar to that computed for the fully passive cell (see Figure 7.5), but the percentage reduction is much smaller, due to the dominance of the active SF generated stresses over the passive visco-hyperelastic stresses.

In summary, the results presented in Figure 7.7 demonstrate that two distinctive groupings of fibres contribute to the active force generation in order to replicate experimentally measured forces: axial fibres generate the tension required to provide a high resistance to probe retraction during unloading half-cycles; and hoop fibres generate tension during loading half-cycles, resulting in a high resistance to cell compression. It is not possible to explain the experimentally observed increase in loading and unloading forces compared to cytoD cells without considering the distinctive contributions of axial and hoop fibres.

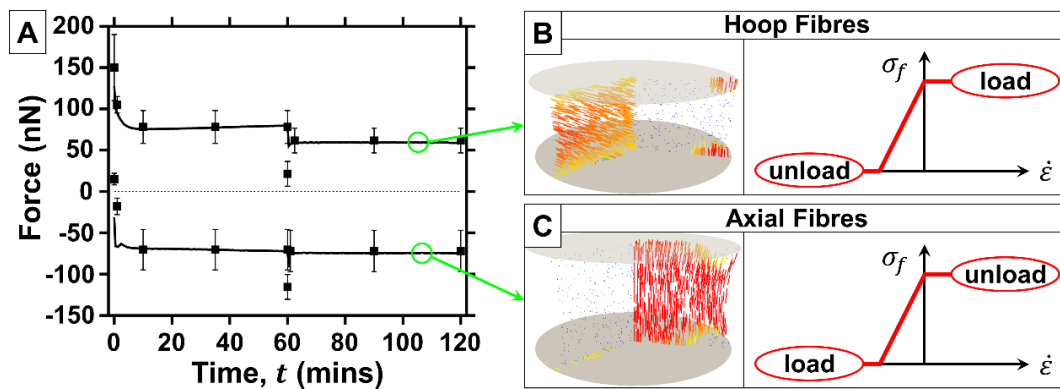


Figure 7.6: (A) Maximum and minimum force predicted using an active SF framework. Maximum and minimum force measured from deformation experiments of untreated cells (average  $\pm$  standard error of the mean,  $n=7$ ) are reproduced for comparison. (B) Illustration of hoop fibre contribution during loading half-cycles (cell compression), including a representation of fibre tension from the Hill-type contractility law. (C) Illustration of axial fibre contribution during unloading half-cycles (cell stretching). For the static Hill-type contractility model,  $k_f$  and  $k_b$  values of 10 and 5 are used, respectively. For a fixed  $\dot{\epsilon}_0$  of 0.003 s,  $\bar{k}_v$  values ranging from 0.01 to 2 yielded similar results (not shown) due to the strain rate applied.

### 7.3.3 Modelling the transient behaviour of SFs during cyclic loading

#### 7.3.3.1 Inaccurate transient behaviour predicted by Hill model

Figure 7.6 shows that the active-passive model accurately predicts both maximum forces at the end of loading half-cycles and the minimum forces at the end of loading half-cycles. Predictions uncover the key role played by axial SFs during unloading and hoop SFs during loading. However, an examination of the computed force-strain loops (Figure 7.8-B) during a single cycle illustrates a

deficiency in the model to capture experimentally observed transient SF contractility during cyclic loading (Figure 7.8-A). The active model predicts discrete jumps in force at the start of each loading and unloading half-cycle, both in regime 1 and in regime 2. During unloading half-cycles axial oriented SFs are stretched at (approximately) the applied strain rate as the probe is retracted (Figure 7.7-inset), hence these axial SFs exert a near constant isometric tension throughout the entire unloading half-cycle, resulting in a nearly constant minimum force of  $\sim 50$  nN. When the loading half-cycle begins the strain rate applied to axial fibres becomes negative and they cease generating tension. However, the strain rate on the hoop fibres increases and they immediately generate tension at the start of the loading half-cycle. This results in a discrete jump in probe force from  $\sim 70$  nN to a positive value of  $\sim 10$  nN, indicating that the compression applied by the probe during the loading half-cycle is instantaneously resisted by the hoop fibres. As the strain rate on the hoop SFs increases during the loading half-cycle a significant number of fibres enter the isometric tension/stretching regime, with the result that the probe force increases during the loading half-cycle. The passive visco-hyperelastic component also contributes to this increase, so that the force at the end of the loading half-cycle is  $\sim 70$  nN during steady state 1. However, at the start of the unloading half-cycle, hoop SFs immediately cease generating tension, axial fibres immediately generate isometric tension, and the probe force immediately reduces from  $\sim 70$  nN to  $\sim 10$  nN. It should be noted that even though the applied nominal strain rate is constant during a half-cycle, the strain rate in each fibre at every point in the cell will not be the same, nor will they necessarily be constant. For example, the strain rate in the hoop fibres is generally lower than in the axial

fibres. Additionally, when hoop fibres are lengthening, axial fibres are, in general, shortening, and *vice versa*.

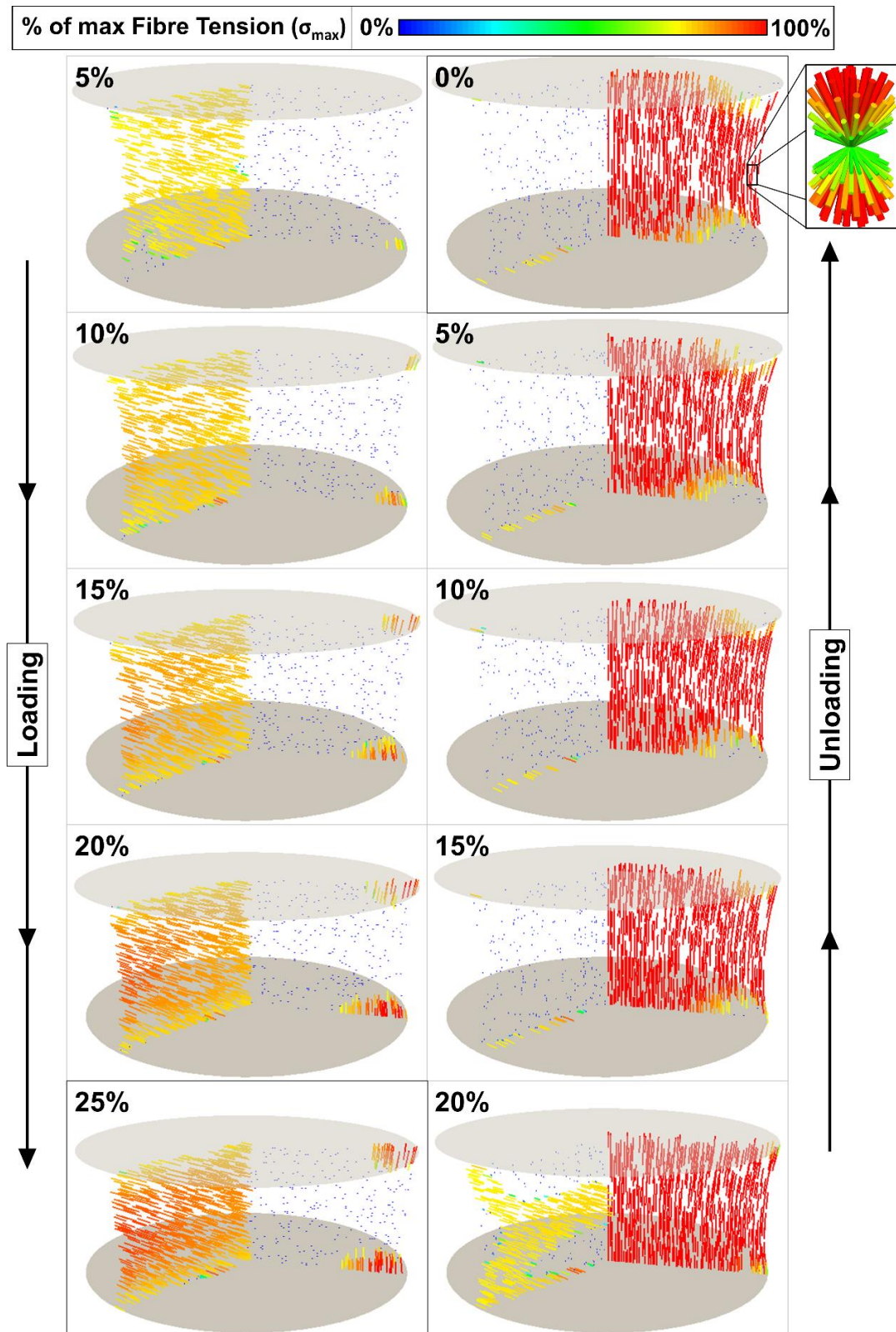


Figure 7.7: Hoop and axial fibre tension at a selection of applied nominal strains during a complete loading cycles in regime 2 using the Hill-type contractility law. An animation can be found in online Supplementary Appendix B ([dx.doi.org/10.1016/j.actbio.2015.09.004](https://dx.doi.org/10.1016/j.actbio.2015.09.004)). Inset panel illustrates the full distribution of fibre tension at a single integration point during cell stretching.

Clearly the transient behaviour computed in Figure 7.8-B is not at all similar to that observed experimentally (Figure 7.8-A), where the probe force gradually increases from  $\sim 70.5$  nN at the end of an unloading half-cycle to  $\sim 70$  nN at the end of the loading half-cycle, with a moderate amount of hysteresis. The failure of the SF model to predict such gradual changes in probe force during a loading cycle is due to the fibre strain rate in the Hill contractility relationship (equation (7.2)); the instantaneous strain rate discretely jumps from a positive value to a negative value immediately upon the switching from unloading to loading (Figure 7.6-B and -C). This results in the binary switching on/off of tension in a SF during a loading cycle.

### 7.3.3.2 *Improved transient behaviour predicted by fading memory model*

The inaccurate prediction of transient changes in cell force during dynamic loading shown in Figure 7.8-B suggests that SF tension is not a simple function of the instantaneous strain rate, as assumed by the Hill equation (equation (7.2)). The steady state maximum and minimum forces can be accurately predicted by the Hill equation, but the step change in cell force upon a change from loading to unloading is not consistent with the experimental observations of Chapter 6. Here it is suggested that the strain rate experienced by a SF is not immediately equal to the instantaneous material strain rate at the start of a loading half-cycle. Rather, the SF strain rate gradually approaches the instantaneous material strain rate. Motivated by modelling approaches for cardiac tissue, a “fading memory” formulation is used to phenomenologically represent the gradually diminishing difference between the SF strain rate and the instantaneous material strain rate over the duration of a loading half-cycle. In Figure 7.8-C, the steady state force-strain loops computed for regime 1 and regime 2 are shown. A greatly improved prediction of the transient changes in force during individual cycles is obtained, characterised by a gradual

increase/decrease between maximum and minimum values. Very similar force profiles are computed in regime 1 and regime 2, which is consistent with experimental measurements. The predicted hysteresis is similar to experimental results; the computed areas between the steady state loading and unloading curves are computed as 776.9 nN in regime 1 and 769.5 nN in regime 2; these values compare well with experimentally observed hysteresis, with measured areas of 588.5 nN and 516.1 nN between loading and unloading curves in regime 1 and regime 2, respectively. In contrast, areas of 2300.0 nN and 2104.2 nN are computed by the original Hill model, as shown in Figure 7.8-B. Overall, Figure 7.8-C clearly demonstrates that predictions of transient changes in active cell force during dynamic loading are significantly improved by the insertion of a history dependent “fading memory” strain rate, in place of the instantaneous applied strain rate, in the Hill contractility equation.

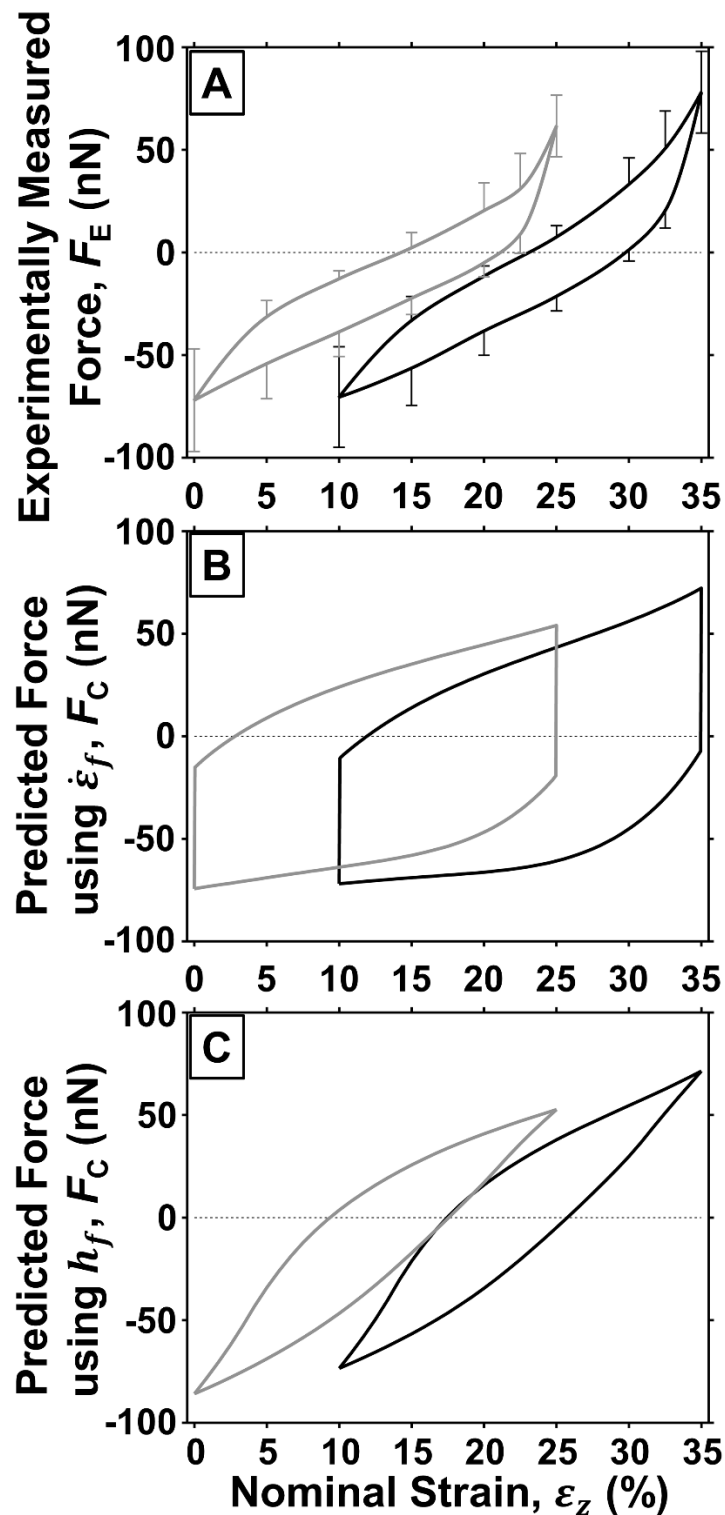


Figure 7.8: (A) Experimentally measured force during the last cycle of regimes 1 and 2. For clarity, the error bars are only shown in the positive direction during loading (upper section of the curves) and in the negative direction during unloading (lower section of the curves). It should be noted that the standard error of the mean is plus and minus the average value at each point. An in-depth analysis and discussion of the trends observed during cyclic deformation experiments are presented in Weafer et al. (2015). (B) The force predicted using the Hill active contractility model during the last cycle of regimes 1 and 2. (C) The force predicted using the fading memory active model during the last cycle of regimes 1 and 2.

### 7.3.4 Axial and hoop fibre behaviour during dynamic simulation

In Figure 7.9, the evolution of hoop and axial fibre tension during a single regime 2 steady state cycle is shown for a simulation in which the fading memory model is used. Steady state force response implies an equilibrium configuration of SFs has been achieved in the cell, both in regime 1 and regime 2. While some SF remodeling may occur during individual cycles, this is phenomenologically represented by the fading memory model. During loading half-cycles (left panels of Figure 7.9) the tension in hoop fibres throughout the central region of the cytoplasm gradually increases during the loading half-cycle (during which the probe compresses the cell). At an applied compressive strain of 5% the majority of hoop fibres generate only ~50% of the maximum possible fibre tension ( $\sigma_{max}$ ). However, the tension in these fibres eventually increases over the course of the loading half-cycle, reaching values of ~95-100% of maximum tension at the end of the cycle (applied strain of 25%). A small number of hoop fibres, localised to the regions near the substrate and probe surfaces, generate maximum tension throughout the cycle. Axial fibres do not generate tension during loading half-cycles.

During the unloading half-cycle (when the probe is retracted from the substrate) the tension in axial fibres gradually increases from ~0% of the maximum value at the onset of unloading (20% applied axial strain) to a value of  $\sim 0.5\sigma_{max}$  by the end of the loading half-cycle when the applied axial strain has reduced to 0% (right panels of Figure 7.9). It is this gradual increase in tension in axial SFs during unloading, in addition to the gradual increase in tension in hoop SFs during loading, which results in the gradual change in probe force shown in Figure 7.8-C. The gradual evolution of fibre tension predicted by the fading memory strain rate shown

in Figure 7.9 is in sharp contrast with the binary switching on/off of SF tension of Figure 7.7 predicted by using the instantaneous strain rate in the Hill curve.

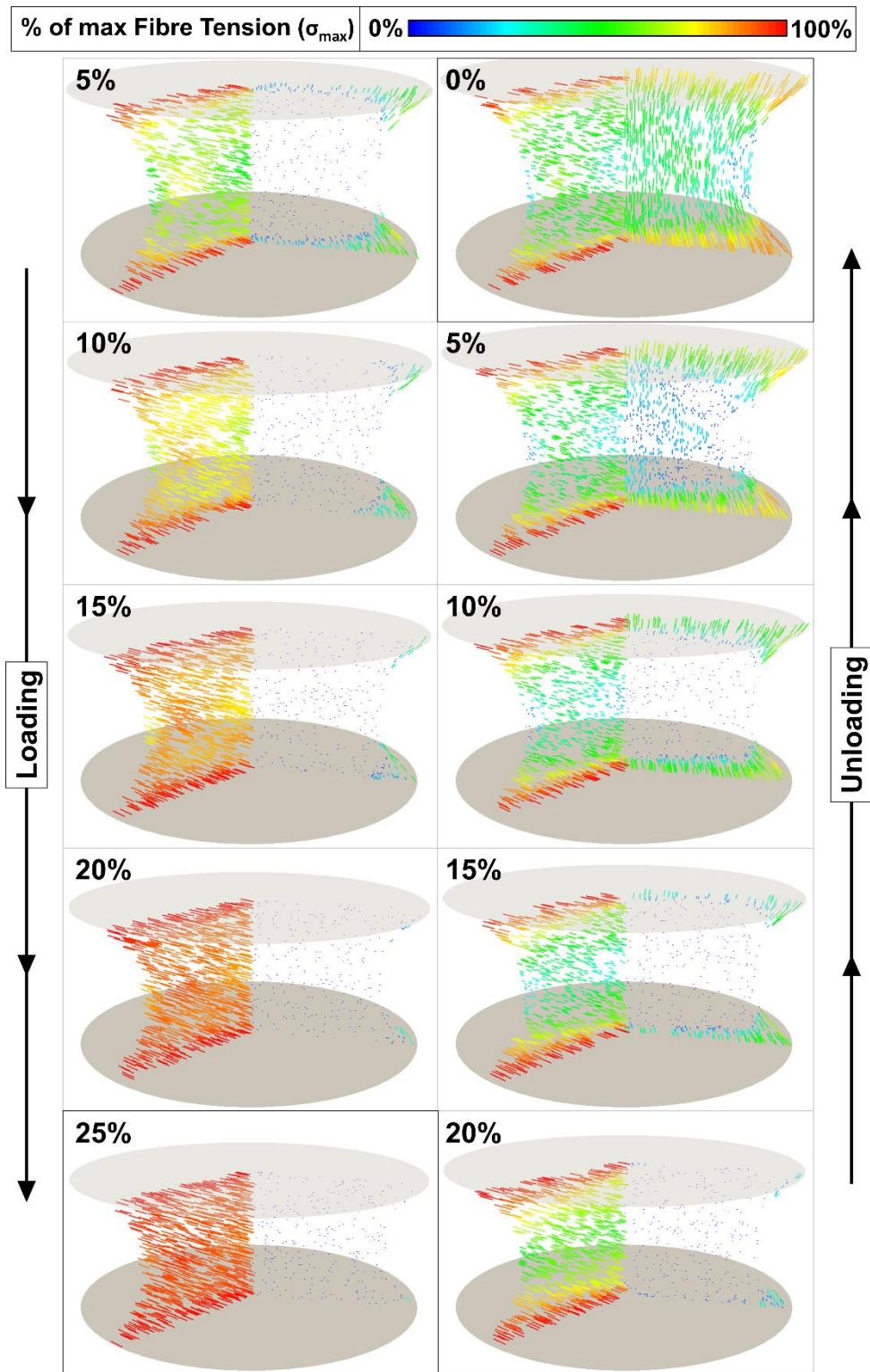


Figure 7.9: Hoop and axial fibre tension computed using the fading memory contractility model. A selection of applied nominal strains during a complete loading cycles in regime 2 are shown. An animation can be found in online Supplementary Appendix C ([dx.doi.org/10.1016/j.actbio.2015.09.004](https://dx.doi.org/10.1016/j.actbio.2015.09.004)). Fading memory contractility model parameters,  $k_f$ ,  $k_b$ ,  $\varepsilon_0$ , and  $\bar{k}_v$  have values of 10, 1, 0.003 s, and 0.01 are used, respectively. The  $\sigma_{MAX}A_0/F_0$  value for fading memory is 4.2.

### 7.3.5 Modelling a realistic cell geometry

Passive properties of the cytoplasm and nucleus for the realistic cell geometry are calibrated and shown in Table 7.2. At the end of the first loading half-cycle, the section at the top of the cell that comes in contact with the probe is computed to have contact area of  $\sim 113 \mu\text{m}^2$ . Addition of the active SF component of the model provides an accurate prediction of the increased pushing and pulling forces for untreated cells, both in regime 1 and regime 2, as shown in Figure 7.10-B. The underlying mechanisms for the elevated pulling and pushing forces are the same as those computed for the idealised cell geometry in Section 7.3.2, i.e. different and distinct families are stretched in the loading and unloading half-cycles. However, as can be seen in Figure 7.10-D, due to the complex realistic cell geometry, the fibres that resist unloading by pulling on the probe are not oriented in a perfectly axial direction. Rather, they are aligned at  $\sim 45^\circ$  to the stretching direction in a localised peri-nuclear region, extending from the base to the probe. These fibres are predicted to actively generate a tensile stress of  $\sim 3\text{kPa}$  during unloading half-cycles. Additionally  $\sim 90^\circ$  (axial) fibres extend from the top (apex) of the nucleus to the probe, but this group of fibres are predicted to contribute less to the active cell pulling force than the  $\sim 45^\circ$  peri-nuclear fibres. During loading half-cycles hoop fibres localised to the peri-nuclear region are stretched (Figure 7.10-C), thus resulting in an elevated resistance to probe pushing. These hoop fibres are predicted to generate a tension of  $\sim 1\text{kPa}$  of tension; this results in a 1.9 fold increase in compression resistance, as observed experimentally between cytoD treated and untreated cells (41.3 nN up to 78.1 nN in regime 1). Clearly due to presence of the nucleus, and due to the complex cell geometry, fibre distributions are inhomogeneous. However, similar to the idealised geometries of Section 7.3.2,

distinctly different groups of fibres are predicted to resist probe pulling and probe pushing.

**Table 7.2: Passive hyperelastic material properties used to model the passive behaviour of the cytoplasm and nucleus for the realistic cell geometry. Prony series parameters used to model viscous effects and maximum actively generated tension for SFs,  $\sigma_{max}$ , are also specified.**

	$C_{10}$ (kPa)	$C_{20}$ (kPa)	$C_{30}$ (kPa)	$\bar{g}^p$	$\tau^p$ (s)	$\sigma_{max}$ (kPa)
Cytoplasm	0.006	0.038	0.064	0.6	0.25	22
Nucleus	0.016	0.6	0.25	0.6	0.25	-

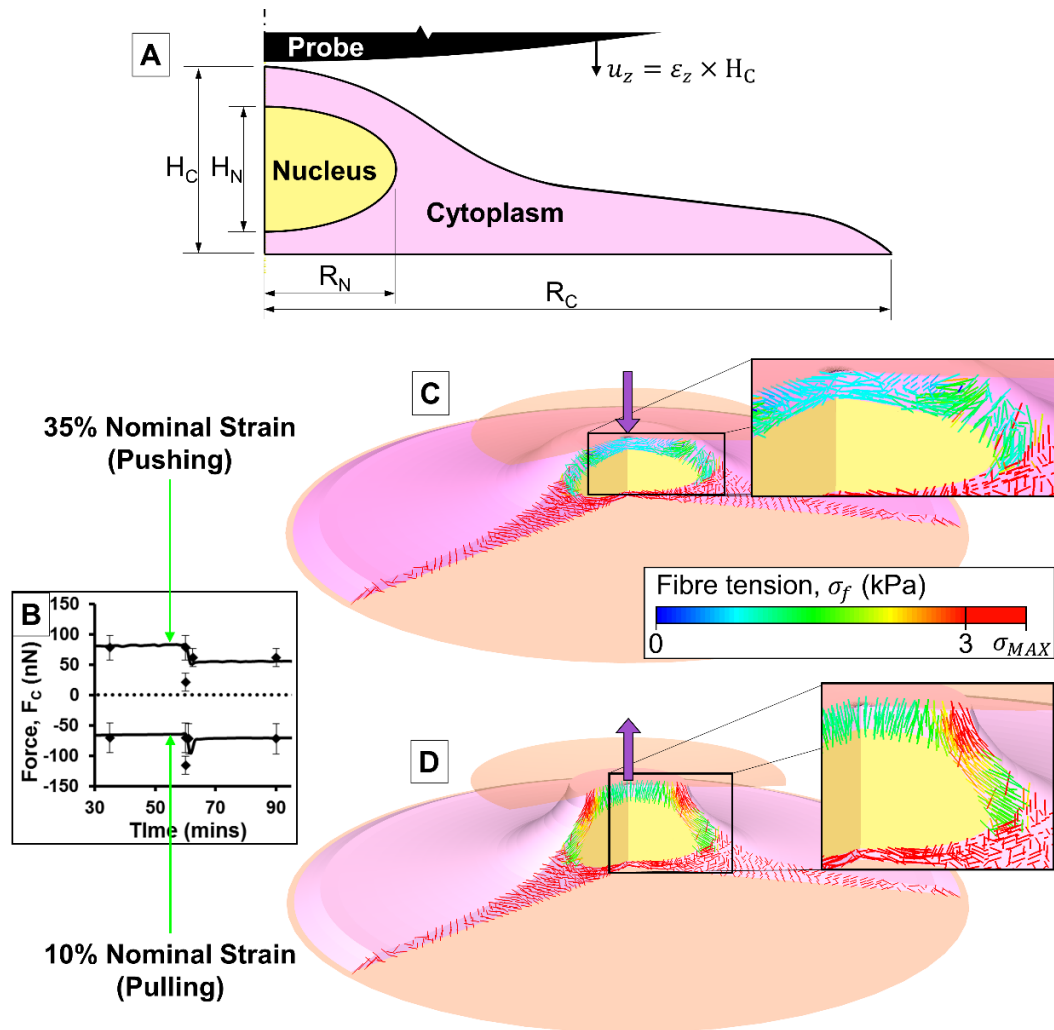


Figure 7.10: (A) Dimensions for realistic cell geometry based on experimental images of Weafer et al. (2015). (B) Force predicted using the realistic cell geometry. Data is shown for 30 minutes before and after the regime change and experimental data is reproduced for comparison. (C) Cell deformation and fibre tension vector plot at the end of a loading half-cycle in regime 1. (D) Cell deformation and fibre tension vector plot at the end of an unloading half-cycle in regime 1. Note that vector plots show the direction of the fibre exhibiting the highest tension level,  $\sigma_f$ , in each RVE at every integration point in the FE mesh. Vector colour indicates the fibre tension.

## 7.4 Discussion

In the current chapter, a computational model that provides a coherent insight into the mechanics underlying the complex response of cells undergoing dynamic loading, as observed in the experimental component of two-part investigation (Chapter 6 and in Weafer et al. (2015)), is presented. The following key contributions are highlighted:

- (i) Cells in which the actin cytoskeleton has been chemically eradicated can be accurately simulated using a non-linear visco-hyperelastic material model.
- (ii) The very high negative and positive forces observed for untreated contractile cells at maximum and minimum applied strain, respectively, occurs due to the contribution of specific fibre families during unloading and loading. Specifically, for idealised cell geometries axial fibres exert active tension during unloading, producing strong resistance to probe retraction, whereas hoop fibres extend during compression during loading half-cycles, adding further resistance to the compressive action of the probe.
- (iii) A fading memory SF contractility model provides an improved prediction of transient force-strain loops for untreated contractile cells in comparison to a static Hill-type contractility model.
- (iv) While complex distributions of SFs are predicted in realistic cell geometries, the key mechanisms of active force generation in axial-type fibres during probe retraction (unloading) and hoop-type fibres during probe compression (loading) is found to accurately capture experimental results.

The increased resistance to probe retraction (unloading) due to active tension generation by axial fibre is not altogether surprising. Previous experiments on single cells by have demonstrated cell tension under static conditions (Thoumine and Ott, 1997, Mitrossilis et al., 2009, Fernández et al., 2006). The current two-part investigation (Chapters 6 and 7) represents an advance on such studies in terms of (i) measuring cell pulling forces under dynamic loading conditions with precise

deformation and force measurement, (ii) parsing the contribution of active tension generation by cell SFs from the passive contribution of the cytoplasm and nucleus, (iii) new insight into SF biomechanics through an active computational framework. The measurements of Mitrossilis et al. (2009) demonstrate that cell contractility follows a Hill-type tension-strain rate relationship under static conditions. However, the computational model demonstrates that such a contractility formulation captures only the peak loading and unloading forces under static conditions. It is then demonstrated that a fading memory formulation must be used to capture experimentally observed transient force-strain loops. The transient contractility law used here is a modification of the empirically based formulation by Hunter et al. (1998) for cardiac tissue contractility. As explained in Section 7.3.3.2, this transient formulation is a phenomenological representation of the “catching-up” of the apparent SF strain rate with the applied strain rate. The finding that the fading memory formulation should account for a history dependent integration of negative (shortening) strain rates and not of positive (lengthening) strains suggests that the remodelling rates of SFs are highly dependent on the applied strain rate. However, a potential limitation of the current chapter is that the fading memory model is a phenomenological description of the stress fibre history dependant strain rate. Future work should focus on the development of binding and unbinding kinetics at the level of actin-myosin cross-bridges in order to provide an enhanced insight into the biophysical processes underlying the transience of SF contractility under dynamic loading.

Our experiments and simulations establish that active tension generation by SFs accounts for the very high pulling forces during probe retraction (unloading). However, the related finding that SFs also increase the resistance to dynamic

compression (probe pushing) is more subtle and perhaps less obvious. Experiments of Chapter 6 suggest that active SFs tension in untreated contractile cells increases the loading/compression force by a factor of 1.9 compared to cytoD treated cells which lack SFs. In the current chapter, models demonstrate that this increase occurs due to the stretching of hoop-type SFs when the probe compresses the cell, hence increasing the work required to deform the cell. A review of the experimental literature on the static compression of cells uncovers the trend that contractile cell phenotypes with well-developed SFs are more resistant to static compression than non-contractile cells. Highly contractile myoblasts (Peeters et al., 2005) require much higher force to compress to 70% strain (~2500 nN) than less contractile fibroblasts (~300 nN) (Deng et al., 2010) or endothelial cells (~750 nN) (Caille et al., 2002). Compression forces of only ~80 nN have been reported for chondrocytes, a phenotype that does not exhibit well-formed SFs. As SFs do not exert tension for high shortening strain rates, following a Hill-type law under static conditions (Mitrossilis et al., 2009), it is therefore reasonable to expect that SFs oriented orthogonal to the direction of applied compressive strain must be stretched during compression, resulting in a higher compression force.

In the current chapter, a non-linear visco-hyperelastic material model provides an excellent prediction of the mechanical response of cytoD treated cells during whole cell cyclic compression. The dramatic (~62%) reduction in steady state compression force following a change from the 35% applied compression strain of regime 1 to the 25% applied compression strain of regime 2 is explained by the non-linear stress-strain relationship of the passive components of the cell. When SFs are added to the model this reduction in compression force between regime 1 and regime 2 is dwarfed by the active SF contribution, which is dependent

on strain rate but independent of strain magnitude, and hence is not affected by the regime change. The precise and novel understanding of cell response to the interconnected but distinct mechanical stimuli of strain magnitude and strain rate, presented in the current chapter, should be of interest to the tissue engineering community. To date a mechanistic approach to the selection of mechanical stimuli in bioreactors has not been established, with most studies relying on a trial-and-error approach for the identification of appropriate loading regimes. Furthermore, from a modelling viewpoint, this chapter demonstrates that passive visco-hyperelastic models should only be used for non-contractile cytoD treated cells, further supporting the findings of the static shear loading and micropipette aspiration experiments of Dowling et al. (2012) and Chapter 4, respectively.

A potential limitation of the current chapter is that only the contribution of the actin cytoskeleton is investigated. Other cytoskeleton components, such as microtubules (MTs) and intermediate filaments (IFs), have been specifically considered. In a recent study by our group, Dowling et al. (2012) demonstrated that the mechanical response of cells to shear is primarily influenced by the actin cytoskeleton. Dowling et al. (2012) also investigated the contribution of MTs and IFs, demonstrating that these cytoskeletal components have a very minor contribution to the mechanical response of cells in comparison to the actin cytoskeleton. Furthermore, Dowling et al. (2012) clearly demonstrated that the contributions of MTs and IFs to the mechanical response of cells are simply hyperelastic in nature. Therefore, in the model presented in the current thesis, MT and IF contributions to the mechanical response of the cell are captured by the passive non-linear visco-hyperelastic component. The ability of this formulation to accurately simulate the force response of cytoD treated cells confirms beyond any

doubt that MT and IF contributions are passive. The complex non-elastic elevated pushing and pulling forces measured in untreated cell experiments are exclusively due to the SFs and not due to MTs and IFs. Therefore, based on previous findings from our group, the current chapter is focused on the contribution of the actin cytoskeleton, and the experiments of Chapter 6/Weafer et al. (2015) firmly demonstrate their dominant and non-hyperelastic role.

The novel insights gained from the experiments and simulations presented in this current two-part investigation (Chapters 6 and 7) can be extended to improve current strategies for the control of cell mechanotransduction, both in-vitro and in-vivo. Accurate prediction of transfer of ECM stress to the cell cytoskeleton and nucleus cannot be achieved without a fundamental understanding of the biomechanics of active cell tension generation under dynamic loading conditions. The fields of cartilage tissue engineering and bone tissue engineering have been significantly limited by the absence of a coherent mechanistic understanding of the role of passive and active cell resistance to applied loading. The single cell experimental-computational approach presented here provides new information on the distinct response of the cell to dynamic strain rate and strain magnitude, revealing the intricate resistance to applied stretching and compression by distinct families of SFs. The accurate understanding of multi-axial active stress generation in cells will allow for new predictions of the transfer of applied loading to the cell nucleus. Previous experimental studies suggest a link between nucleus deformation and mechanotransduction (Thomas et al., 2002, Campbell et al., 2007, Henderson et al., 2013, Lammerding et al., 2007, Tojkander et al., 2012). Furthermore, advances in in-situ imaging techniques (e.g. Henderson et al. (2013)) will provide key experimental data for extension of the current modelling strategy to predict

alterations in nucleus strain and chromatin reorganisation in cells embedded in 3D extra-cellular-matrices (Dowling et al., 2013).

## 7.5 References

- BARRETO, S., CLAUSEN, C. H., PERRAULT, C. M., FLETCHER, D. A. & LACROIX, D. 2013. A multi-structural single cell model of force-induced interactions of cytoskeletal components. *Biomaterials*, 34, 6119-6126.
- CAILLE, N., THOUMINE, O., TARDY, Y. & MEISTER, J.-J. 2002. Contribution of the nucleus to the mechanical properties of endothelial cells. *J Biomech*, 35, 177-187.
- CAMPBELL, J. J., BLAIN, E. J., CHOWDHURY, T. T. & KNIGHT, M. M. 2007. Loading alters actin dynamics and up-regulates cofilin gene expression in chondrocytes. *Biochem Biophys Res Commun*, 361, 329-334.
- DENG, Z., LULEVICH, V., LIU, F. T. & LIU, G. Y. 2010. Applications of atomic force microscopy in biophysical chemistry of cells. *J Phys Chem B*, 114, 5971-82.
- DESHPANDE, V. S., MCMEEKING, R. M. & EVANS, A. G. 2007. A model for the contractility of the cytoskeleton including the effects of stress-fibre formation and dissociation. *Proc Math Phys Eng Sci*, 463, 787-815.
- DOWLING, E. P. & MCGARRY, J. P. 2013. Influence of Spreading and Contractility on Cell Detachment. *Ann Biomed Eng*.
- DOWLING, E. P., RONAN, W. & MCGARRY, J. P. 2013. Computational investigation of in situ chondrocyte deformation and actin cytoskeleton remodelling under physiological loading. *Acta Biomater*, 9, 5943-55.
- DOWLING, E. P., RONAN, W., OFEK, G., DESHPANDE, V. S., MCMEEKING, R. M., ATHANASIOU, K. A. & MCGARRY, J. P. 2012. The effect of remodelling and contractility of the actin cytoskeleton on the shear resistance of single cells: a computational and experimental investigation. *J R Soc Interface*, 9, 3469-79.
- FERNÁNDEZ, P., PULLARKAT, P. A. & OTT, A. 2006. A Master Relation Defines the Nonlinear Viscoelasticity of Single Fibroblasts. *Biophysical journal*, 90, 3796-3805.
- HENDERSON, A., AHERNS, J. & LAW, C. 2004. The ParaView Guide. In: KITWARE (ed.). Clifton Park, NY, USA: Kitware.
- HENDERSON, J. T., SHANNON, G., VERESS, A. I. & NEU, C. P. 2013. Direct measurement of intranuclear strain distributions and RNA synthesis in single cells embedded within native tissue. *Biophys J*, 105, 2252-2261.
- HUNTER, P. J., MCCULLOCH, A. D. & TER KEURS, H. E. D. J. 1998. Modelling the mechanical properties of cardiac muscle. *Progress in Biophysics and Molecular Biology*, 69, 289-331.
- LAMMERDING, J., DAHL, K. N., DISCHER, D. E. & KAMM, R. D. 2007. Nuclear Mechanics and Methods. In: YU-LI, W. & DENNIS, E. D. (eds.) *Methods in Cell Biology*. Academic Press.
- MCGARRY, J. G. & PRENDERGAST, P. J. 2004. A three-dimensional finite element model of an adherent eukaryotic cell. *Eur Cell Mater*, 7, 27-33; discussion 33-4.
- MITROSSILIS, D., FOUCHARD, J., GUIROY, A., DESPRAT, N., RODRIGUEZ, N., FABRY, B. & ASNACIOS, A. 2009. Single-cell response to stiffness exhibits muscle-like behavior. *Proceedings of the National Academy of Sciences*, 106, 18243-18248.
- PEETERS, E. A., OOMENS, C. W., BOUTEN, C. V., BADER, D. L. & BAAIJENS, F. P. 2005. Mechanical and failure properties of single attached cells under compression. *J Biomech*, 38, 1685-93.

- RONAN, W., DESHPANDE, V. S., MCMEEKING, R. M. & MCGARRY, J. P. 2012. Numerical investigation of the active role of the actin cytoskeleton in the compression resistance of cells. *J Mech Behav Biomed Mater*, 14, 143-57.
- RONAN, W., DESHPANDE, V. S., MCMEEKING, R. M. & MCGARRY, J. P. 2014. Cellular contractility and substrate elasticity: a numerical investigation of the actin cytoskeleton and cell adhesion. *Biomech Model Mechanobiol*, 13, 417-435.
- SUN, W., CHAIKOF, E. L. & LEVENSTON, M. E. 2008. Numerical approximation of tangent moduli for finite element implementations of nonlinear hyperelastic material models. *J Biomech Eng*, 130, 061003.
- THOMAS, C. H., COLLIER, J. H., SFEIR, C. S. & HEALY, K. E. 2002. Engineering gene expression and protein synthesis by modulation of nuclear shape. *Proc Natl Acad Sci USA*, 99, 1972-1977.
- THOUMINE, O. & OTT, A. 1997. Time scale dependent viscoelastic and contractile regimes in fibroblasts probed by microplate manipulation. *J Cell Sci*, 110 ( Pt 17), 2109-16.
- TOJKANDER, S., GATEVA, G. & LAPPALAINEN, P. 2012. Actin stress fibers--assembly, dynamics and biological roles. *J Cell Sci*, 125, 1855-64.
- WEAFER, P. P., MCGARRY, J. P., VAN ES, M. H., KILPATRICK, J. I., RONAN, W., NOLAN, D. R. & JARVIS, S. P. 2012. Stability enhancement of an atomic force microscope for long-term force measurement including cantilever modification for whole cell deformation. *Rev Sci Instrum*, 83, 093709.
- WEAFER, P. P., REYNOLDS, N. H., JARVIS, S. P. & MCGARRY, J. P. 2015. Single cell active force generation under dynamic loading – Part I: AFM experiments. *Acta Biomaterialia*, DOI:dx.doi.org/10.1016/j.actbio.2015.09.006.
- WEAFER, P. P., RONAN, W., JARVIS, S. P. & MCGARRY, J. P. 2013. Experimental and computational investigation of the role of stress fiber contractility in the resistance of osteoblasts to compression. *Bull Math Biol*, 75, 1284-303.

# **8 Investigation of cell behaviour in biaxially and uniaxially constrained tissues subjected to cyclic deformation**

## **8.1 Introduction**

A growing interest in the biomechanical behaviour of cells seeded in 3D culture has emerged in recent years. Mechanical priming strategies have been developed in an ongoing drive to engineer tissues with increased functional viability (Berry et al., 2003, Billiar et al., 2005, Cummings et al., 2004, Isenberg and Tranquillo, 2003, Seliktar et al., 2000, Mauck et al., 2000, Mauck et al., 2003). Previous studies demonstrate that the application of 3D substrate stretch can up-regulate gene expression, promote differentiation, cause cell orientation redistribution, increase proliferation, and increase extracellular matrix synthesis (Campbell et al., 2007, Gabbay et al., 2006, Foolen et al., 2014, Berry et al., 2003). Given that cells actively respond to loading in the 3D microenvironment, it is important to develop a fundamental mechanistic understanding of the effects of mechanical conditioning on 3D synthetic tissue constructs. Therefore, the

development of a robust system that can apply different uniaxial and biaxial deformation regimes to engineered hydrogel constructs, while measuring the active and passive force, would represent a significant advance in the field of engineered tissue mechanics.

Stretching of 2D substrates containing semi-confluent cell monolayers reveals that stress fibres (SFs) exhibit stretch avoidance (Kaunas et al., 2005, Barron et al., 2007, Wang et al., 2001, Neidlinger-Wilke et al., 2001). Stretch avoidance of cells in 3D culture has also been reported during cyclic loading of collagen hydrogels in which cells have been embedded (Foolen et al., 2014). However, it has been more commonly reported that, in 3D culture, SF distributions remain unchanged during cyclic deformation (Wille et al., 2006, Foolen et al., 2012, Wakatsuki and Elson, 2002, Zhao et al., 2013, Lee et al., 2008, Nieponice et al., 2007, Gauvin et al., 2011). In numerous studies cell contractile force response during applied stretch was parsed by uniaxially straining untreated cell-seeded hydrogel constructs in conjunction with testing using chemical agents to remove the actin cytoskeleton (Wille et al., 2006, Zhao et al., 2013, Zhao et al., 2014, Wagenseil et al., 2004, Wakatsuki et al., 2000, Wakatsuki et al., 2001). However, due to the complexity of imposing a biaxial strain state on a hydrogel construct while measuring forces during cyclic stretching, to date force measurement during dynamic loading has been limited to uniaxial strain fields.

In the current chapter a novel experimental system for measurement of cell and tissue forces during uniaxial and biaxial stretching is developed. Cells and intracellular SF arrangements are shown to be highly polarised in the case of both uniaxially and biaxially constrained tissues. However, the cells/SF population is shown to be randomly aligned/unaligned within biaxially constrained tissues. In

contrast the cell/SF population is shown to be highly aligned in the case of uniaxially constrained tissues. Force measurements for biaxial tissues subjected to equi-biaxial cyclic stretching are compared to forces measured for uniaxially stretched tissues. It is revealed that the SF distribution in tissue constructs has an important influence on the measured forces. An active SF framework (as described in Chapter 7) is used to simulate biaxial and uniaxial experiments. It is revealed that in-plane stress uniaxiality results in aligned SF distributions, whereas stress biaxiality results in randomly aligned SF distributions.

## 8.2 Materials and methods

### 8.2.1 Sample preparation

Human cardio-myocytes (HCM), obtained from Promocell (C-14010, Heidelberg, Germany), are grown as per Promocell protocols. Before creating the collagen-cell solution, Teflon moulds, stainless steel hangers, and raisers are autoclaved and prepared in ethanol cleaned UV-sterilised petri dishes. The base of the petri dishes are coated with a siliconising reagent to inhibit cell adhesion (Sigmacote, SL2, Sigma–Aldrich Ireland Ltd., Arklow). Collagen-cell solution is made using 10X phosphate buffered saline (PBS), 1 M Sodium Hydroxide (NaOH), 1 mg/mL rat tail collagen type I solution (supplied by Dimitrios Zeugolis, NUIG, as part of collaboration on project), and cells suspended in standard growth media (Promocell, C22170, Heidelberg, Germany) supplemented with an additional 10% foetal calf serum (FCS). The final solution contains a collagen concentration of 0.2mg/mL and a homogenous distribution of  $1 \times 10^6$  cells/mL and is at a physiological pH and ionic strength (Figure 8.1-A). Appropriate volumes are made so that the initial height,  $H_0$ , of the collagen-cell solution in the mould is 3 mm

(Figure 8.1-B). Once the solution is added to the mould, the sample is carefully placed in an incubator (37°C, 5% CO<sub>2</sub>, and 90% humidity) for 1 hour to form a gel. A sufficient amount of HCM growth media is added to the petri dish to ensure the gel is completely submerged. The entire mould, which contains the gelled collagen-cell solution, is raised slightly from the surface of the petri dish using stainless steel raisers. This prevents adhesion of the gel to the petri dish and ensures that media is free to flow beneath the mould. Therefore, the cell laden gel is fully engulfed with growth media during incubation. After 2 days of incubation, cell mediated tension results in gel contraction (Figure 8.1-C). These contractile gels are referred to as “tissues”. Further samples are created using no cells. They are fabricated using the same moulds and quantities of PBS, collagen, and media as that used to create tissue samples. Cell free samples are gelled by incubating at 37° for 1 hour, however, they do not require 2 days of incubation before testing as exhibit the same appearance and mechanical response (results not shown). These cell free constructs are hereon referred to as ‘hydrogels’.

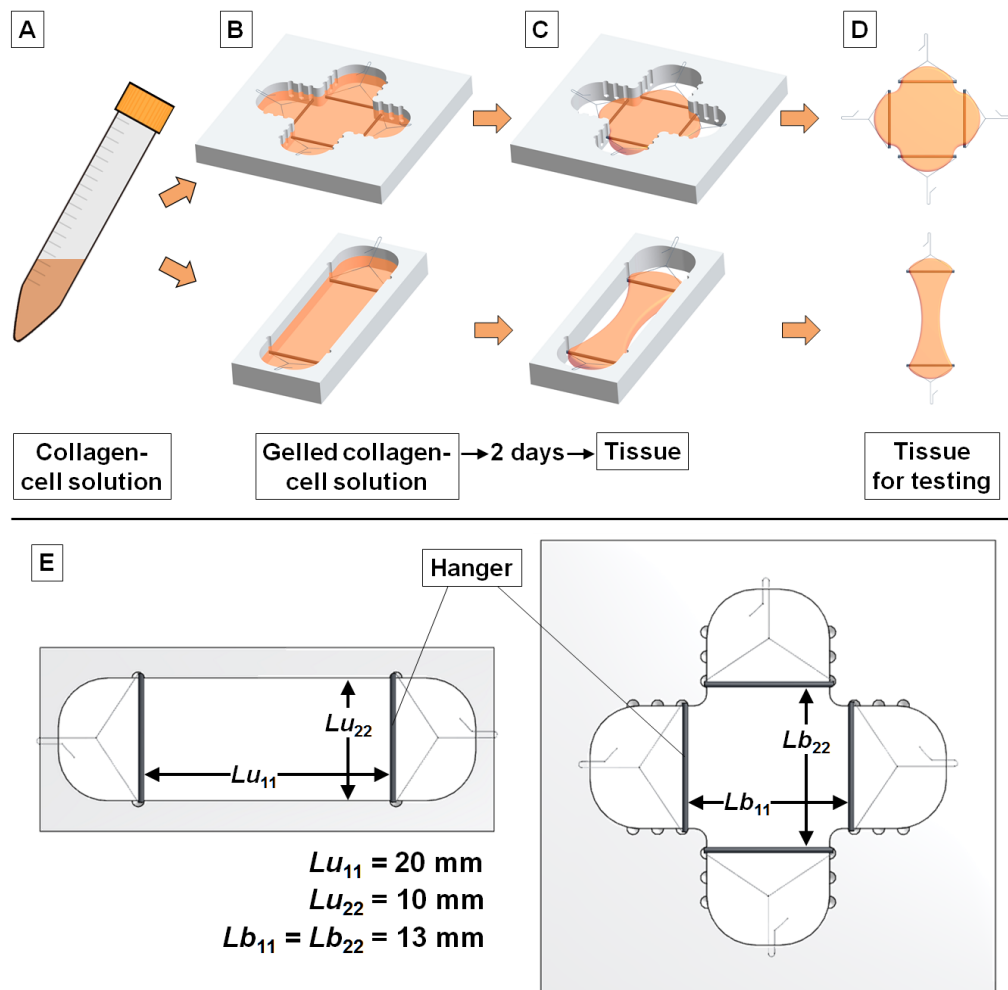


Figure 8.1: Schematic representation of sample preparation. (A) Collagen-cell solution is prepared in a falcon tube. (B) Collagen-cell solution is transferred into the mould and allowed to gel in the incubator at 37°C, 5% CO<sub>2</sub>, and 90% humidity. (C) The mould and gelled collagen-cell solution are raised from the substrate, submerged in media, and incubated for a further 2 days before testing. (D) The tissue is removed from the mould and transferred to the modified biaxial test machine for experimentation. The same procedure is used to prepare both biaxial (upper panels of B-D) and uniaxial (lower panels of B-D) specimens. (E) Key dimensions for the uniaxial (left) and biaxial (right) moulds.

## 8.2.2 Testing system and experiments

Significant modifications are made to a biaxial tensile tester (Zwick/Roell, Ulm, Germany) in order to perform the cyclic experiments on tissues. In order to measure bi-directional force, two load cell transducers (AE801, Kronex, CA, USA) are wired to a custom built circuit that provides the relevant excitation voltage and amplification of the output signal (See Section 0: Appendix B). Digitisation, calibration, and data acquisition of the output signal are performed using a

CompactRIO and LabVIEW software (National Instruments, TX, USA). The force measurement setup provides force readouts with an accuracy in the sub-mN range.

After 2 days of incubation tissues are imaged before being transferred to the modified test machine. Due to the contractile effects of the embedded cells, gels shrink during the 2 day incubation period to form “tissues”. Contraction is prevented in certain directions during this period by fixing the position of hangers in the mould. After releasing hangers from the mould the tissues immediately spring/contract inwards. After loading into the modified test machine, manual adjustments are made to return the tissue to its original “mould” geometry (Figure 8.1-D). It should be noted that the tissue remains submerged in growth media at all times. After loading into the modified test machine, the sample is allowed to stabilise for 30 minutes before experimentation. After an initial loading step to 20% nominal strain in the first second, sinusoidal cyclic deformation is applied to the tissue between 10-20% nominal strain at a frequency of 1 Hz for 2 hours (Figure 8.2-E). After 1 hour, 5  $\mu$ M cytochalasin-D (cytoD) is added to the surrounding growth media to disrupt contractile SFs in tissues. It should be noted that the loading strain is applied uni-directionally for uniaxial specimens and bi-directionally for biaxial specimens (Figure 8.2-D). Uniaxial specimens are free to contract laterally at all times. During experiments, force is recorded at 40 samples per second. Key readings are subjected to statistical significance testing. Statistical analysis is performed using GraphPad (GraphPad, CA, USA). A student *t*-test is used to examine key measurements. For all comparisons, statistical significance is declared if  $p < 0.05$ . Significant differences between groups are indicated in figures by \* $p < 0.05$  and \*\*  $p \leq 0.005$ .

### 8.2.3 Immuno-fluorescence

Tissues are fixed by submerging them in 4% paraformaldehyde solution for 20 minutes. Fixed tissues are treated with 0.1% triton solution for 5 min to permeabilise. Fluorescein Isothiocyanate Labelled (FITC) phalloidin and 4',6-diamidino-2-phenylindole (DAPI), dilactate (Sigma–Aldrich Ireland Ltd., Arklow) are used to stain the actin filaments and nuclei, respectively. Washing 3 times with PBS is performed between each step. Samples are slightly agitated on a rotation plate during each step to assist penetration of reagents throughout the tissues. Samples are mounted in Prolong Gold Antifade Reagent (Molecular Probes, Life Technologies, NY, USA) to preserve staining quality and kept below 4°C before imaging. An Andor Revolution spinning disk confocal microscope (Yokogawa CSU-X1 Spinning disk unit & Olympus IX81 microscope) is used to image fluorescently stained samples. To investigate the SF distribution, representative fluorescent z-stack images are obtained at 5 regions of biaxial and uniaxial tissues before and after experiments. Two image channels are captured at each plane of focus, using laser excitation of 405 nm to visualise the nucleus and excitation of 495 nm to visualise the actin filaments. A step size of 2  $\mu\text{m}$  is used between each z-plane. Complete z-stack image sets are grouped into a single image using maximum intensity.

In order to quantify the SF orientation distribution in the tissues the length and angle of  $\sim 100$  SFs/ $\text{mm}^2$  are manually measured from the fluorescent images at key regions of interest using ImageJ software (Schneider et al., 2012). SFs are grouped by their angles to the nearest 15° increment between -90° and 90° (-90°, -75°, -60°, -45°, -30°, -15°, 0°, 15°, 30°, 45°, 60°, 75°, and 90°). For example, all fibres with angles between 7.5° and -7.5° are grouped to the 0° angular group. The

length of all SFs within each angular group is summed to determine the total length of all SFs occurring at that angle. SF length is then averaged at angles where geometrical symmetry occurs in the tissue (i.e.  $90^\circ$  and  $-90^\circ$ ,  $75^\circ$  and  $-75^\circ$ , etc.). The SF length in each angular group is normalised by the maximum length. Therefore, the most dominant SF direction for the fluorescent image has a normalised non-dimensional length of 1. The normalised lengths of each angular group are presented as circular histograms to illustrate the regularity of SFs occurring at each orientation. These circular histogram plots are referred to as the normalised SF orientation distributions.

#### 8.2.4 Finite element (FE) modelling

FE simulations of the experiments are performed to investigate the effectiveness of the active SF framework, described in Chapter 7, for modelling the behaviour of tissue constructs. A visco-hyperelastic constitutive formulation, as implemented in the previous chapter to describe the passive mechanical behaviour of cells, is used in the current chapter for hydrogels. To simulate the contractility of the actin cytoskeleton in cells in tissue constructs, the active fading memory formulation described in the previous chapter is added in parallel to the visco-hyperelastic model. Passive material properties are listed in Table 8.1. A Poisson's ratio,  $\nu$ , of 0.3 is used in all simulations. In a previous study, a ratio of  $(\sigma_{max}/E) = 25$  was determined for cardiomyocyte tissue constructs (Thavandiran et al., 2013), where  $E$  is the Young's modulus for the passive material such that:  $E = 4C_{10}(1 + \nu)$ . A similar ratio is used in the current chapter. All other parameters are similar to those used in Chapter 7. It should be noted that remodelling is limited in the dynamic step of simulations.

Due to geometric symmetry, only one-eighth of the overall tissue is simulated (Figure 8.2-B). An FE mesh of the tissues section is generated (Figure 8.2-C) and boundary conditions are imposed based on experimental tests (Figure 8.2-D). Initially, an equilibrium step is performed in simulations to represent the 2 day incubation period in experiments. After the signal is induced in contractile tissue analysis, SFs are allowed to reach an equilibrium state before initiation of cyclic loading. The interaction between actively generated SF tension and the passive material leads to significant contraction of the tissues as shown in (Figure 8.2-D). In the next analysis step, displacement is introduced at the hangers to mimic the experimentally applied nominal strain,  $\epsilon_L$  (Figure 8.2-E). After an initial loading step to 20% nominal strain in the first cycle, sinusoidal cyclic deformation is applied to the tissue between 10-20% nominal strain at a frequency of 1 Hz for 2 hours (Figure 8.2-E).

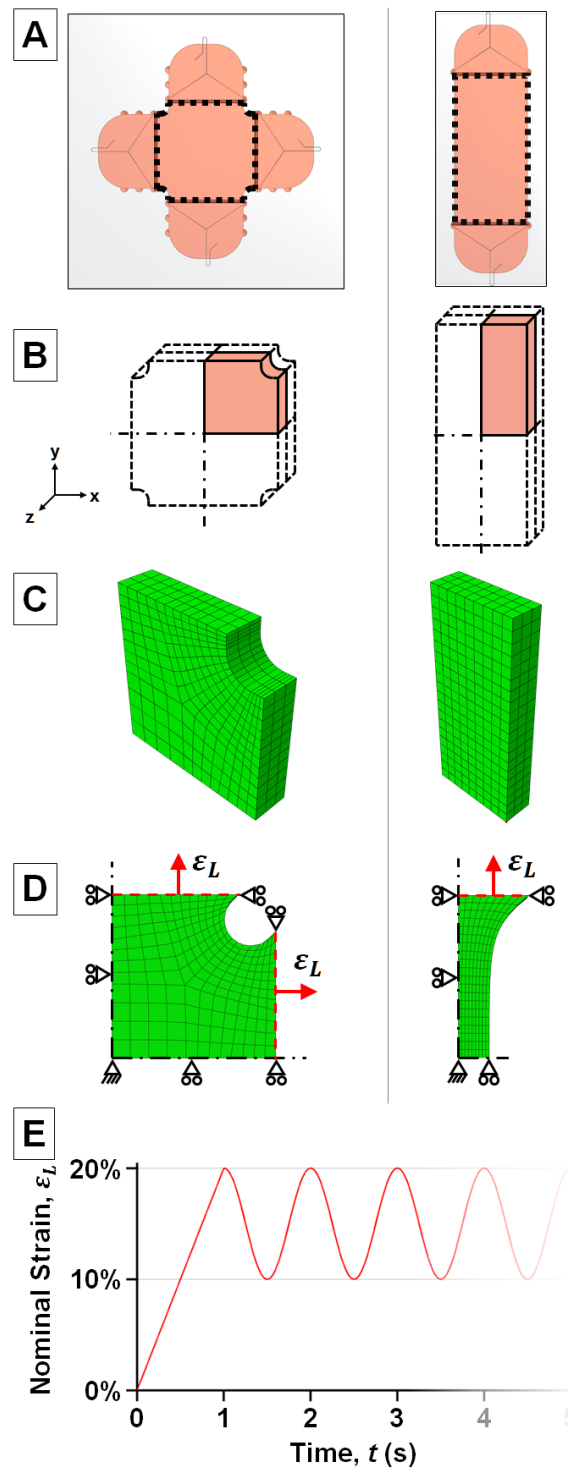


**Figure 8.2:** Schematic of mesh generation and boundary conditions used in simulations. (A) Schematic of the collagen-cell gel in the mould before contraction. For simulations, only the region bound by the hangers is considered (highlighted by dotted lines). (B) Due to geometrical symmetry, the region considered is reduced to a quadrant. The quadrant is also halved in the z-plane. (C) A 3D FE mesh is generated for the region. (D) Deformation after symmetry boundary conditions are applied and the collagen-cell gel is subjected to the SF equilibrium step. During the equilibrium step loading boundaries (highlighted by dashed red lines) are held at zero strain,  $\epsilon_L = 0$ . (E) Nominal loading strain,  $\epsilon_L$ , applied to the contracted collagen-cell gel (tissue) at the loading boundaries (highlighted in (D)) for the first 5 seconds of the dynamic loading step.

**Table 8.1: Modelling parameters.**

	$C_{10}$ (kPa)	$C_{20}$ (kPa)	$C_{30}$ (kPa)	$\bar{g}^p$	$\tau^p$ (s)
Passive	0.24	0.09	0.01	0.8	300

### 8.2.5 FE modelling outputs

In order to investigate the stress state in the tissue, a non-dimensional effective measure of in-plane stress uniaxiality is described as:

$$\hat{S} = \frac{\sigma_{max}^p - \sigma_{min}^p}{\sigma_{max}^p} \quad (8.1)$$

$\sigma_{max}^p$  and  $\sigma_{min}^p$  are the maximum and minimum principal stresses in the plane of applied stretch, respectively, of the Cauchy stress tensor,  $\sigma_{ij}$ . It should be noted that the out of plane stress component is zero. Therefore, the stress state in the tissue is perfectly uniaxial if  $\sigma_{min}^p = 0$ , giving an effective stress of  $\hat{S} = 1$ . On the other hand if  $\sigma_{max}^p = \sigma_{min}^p$ , the in-plane stress state is perfectly biaxial, giving  $\hat{S} = 0$ . Colour coded vector plots are used to illustrate SF distribution at the centre of the tissues (ParaView (Henderson et al., 2004)).

## 8.3 Results

### 8.3.1 Experimental results

#### 8.3.1.1 Collagen-cell gel contraction

After gelling the collagen-cell solution samples are incubated for 2 days before testing to form “tissues”. During this 2 day period cell processes penetrate the collagen matrix and endogenous force generated by crossbridge cycling of the SFs leads to gel contraction. In Figure 8.3 a quantitative analyses of the deformation

of uniaxial and biaxial tissues is shown. In uniaxial tissues the width of specific sections along the length are measured (Figure 8.3-A). For each measurement a significant reduction from the baseline (day 0) width is observed (Figure 8.3-B). Mid-way between the opposing hangers a minimum width of  $W_M = 4.3 \pm 0.3$  mm is measured. This dramatic reduction in sample width correlates to a large negative nominal strain (-57%) in the lateral direction. The width gradually increases from the centre section to  $4.5 \pm 0.3$  mm at  $W_3$  (3 mm from the mid-way section),  $5.3 \pm 0.4$  mm at  $W_2$  (6 mm from the mid-way section), and  $7.3 \pm 0.5$  mm at  $W_1$  (9 mm from the mid-way section). On the hanger contractile forces reduce the width of the sample to  $8.6 \pm 0.5$  mm ( $W_H$ ). Deformation of the biaxial tissue during static incubation is characterised by the change in the distance,  $L_C$ , indicated in Figure 8.3-C. In the absence of contractility  $L_C = 1.707$  mm.

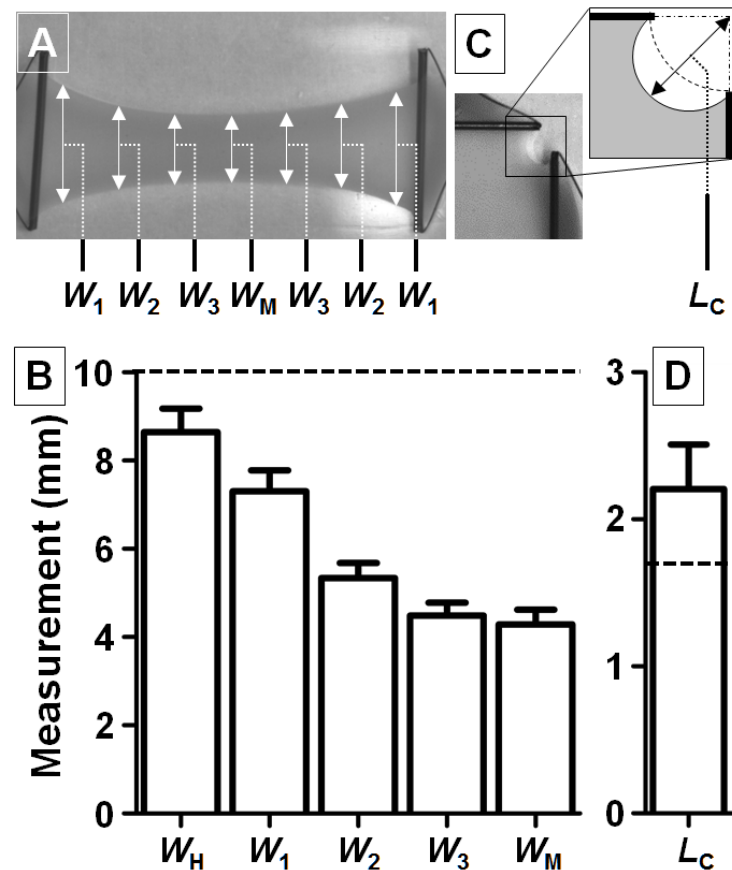


Figure 8.3: Measurements of contractility mediated deformation of biaxial and uniaxial specimens after 2 days of static incubation. (A) Contracted uniaxial tissue indicating regions at which width measurements are made. Distance between regions is 3 mm. Region  $W_1$  is 1 mm from the hangers. Note that width measurements are also made at the hangers,  $W_H$ . (B) Plot of measurements (mean  $\pm$  standard deviation,  $n=6$ ) for the uniaxial tissues at each section. (C) Quadrant of a contracted biaxial tissue indicating the corner length,  $L_C$ , measured after 2 days. (D) Measurement of the corner length,  $L_C$ , of the biaxial tissue (mean  $\pm$  standard deviation,  $n=6$ ). In (B) and (D), baseline (day 0) measurements are indicated by dashed lines.

### 8.3.1.2 Maximum force measurements

In Figure 8.4 the maximum force measured during cyclic deformation experiments is shown. It should be recalled that ‘tissues’ contain cells, and have been incubated for 2 days so allow cell mediated contractility to reach an equilibrium state before cyclic testing. ‘Hydrogels’ contain no cells and, therefore, do not require incubation and do not contain contractility. Maximum force is recorded when tissue and hydrogels are at a maximum applied nominal strain of 20%. At the end of the initial loading cycle (Figure 8.4-C), uniaxial maximum force is  $18.5 \pm 6.7$  mN and biaxial maximum force is  $22.1 \pm 6.6$  mN in tissues. For

hydrogels (Figure 8.4-C), these measurements are  $7.3 \pm 1.0$  mN and  $14.9 \pm 3.3$  mN for the uniaxial and biaxial specimens, respectively. It should be noted that for the first cycle the ratio of biaxial to uniaxial force drops from 2.04 for hydrogels to 1.20 for tissues. A significant decrease in maximum force is recorded for both uniaxial (Figure 8.4-A) and biaxial (Figure 8.4-B) specimens at the onset of cyclic deformation. The maximum force subsequently stabilises to a steady state after  $\sim 10$  minutes for tissues and  $\sim 5$  minutes for hydrogels. A steady state force is observed for the remainder of experiments. For tissues, uniaxial maximum force reduces to  $4.4 \pm 1.5$  mN and biaxial maximum force reduces to  $6.0 \pm 1.2$  mN after 60 minutes cyclic loading (Figure 8.4-E). For hydrogels (Figure 8.4-G) lower forces of  $1.2 \pm 0.4$  mN and  $2.5 \pm 0.7$  mN are measured for the uniaxial and biaxial specimens, respectively. Therefore, the ratio of biaxial to uniaxial steady state measured force is 2.08 for hydrogels, compared to 1.36 for tissues. In the histograms shown in Figure 8.4 only specific time points are presented. However, it should be noted that for cell laden tissues the biaxial forces are on average 1.30 times higher than the uniaxial forces. For hydrogels, which contain no cells, measured biaxial forces are on average 1.75 times higher than measured uniaxial forces. This is simply due to the fact that the biaxial specimen is a stiffer structure due to its highly constrained geometry (Nolan and McGarry, 2016). When cells are introduced the ratio of measured biaxial to uniaxial tissue force is significantly reduced to 1.30. After addition of cytoD in tissue experiments, forces recorded for uniaxial and biaxial tissues reduced to  $2.9 \pm 1.2$  mN and  $4.1 \pm 0.7$  mN, respectively, demonstrating the significant contribution of active cell force to measured forces in untreated contractile tissues for both biaxial and uniaxial specimens.

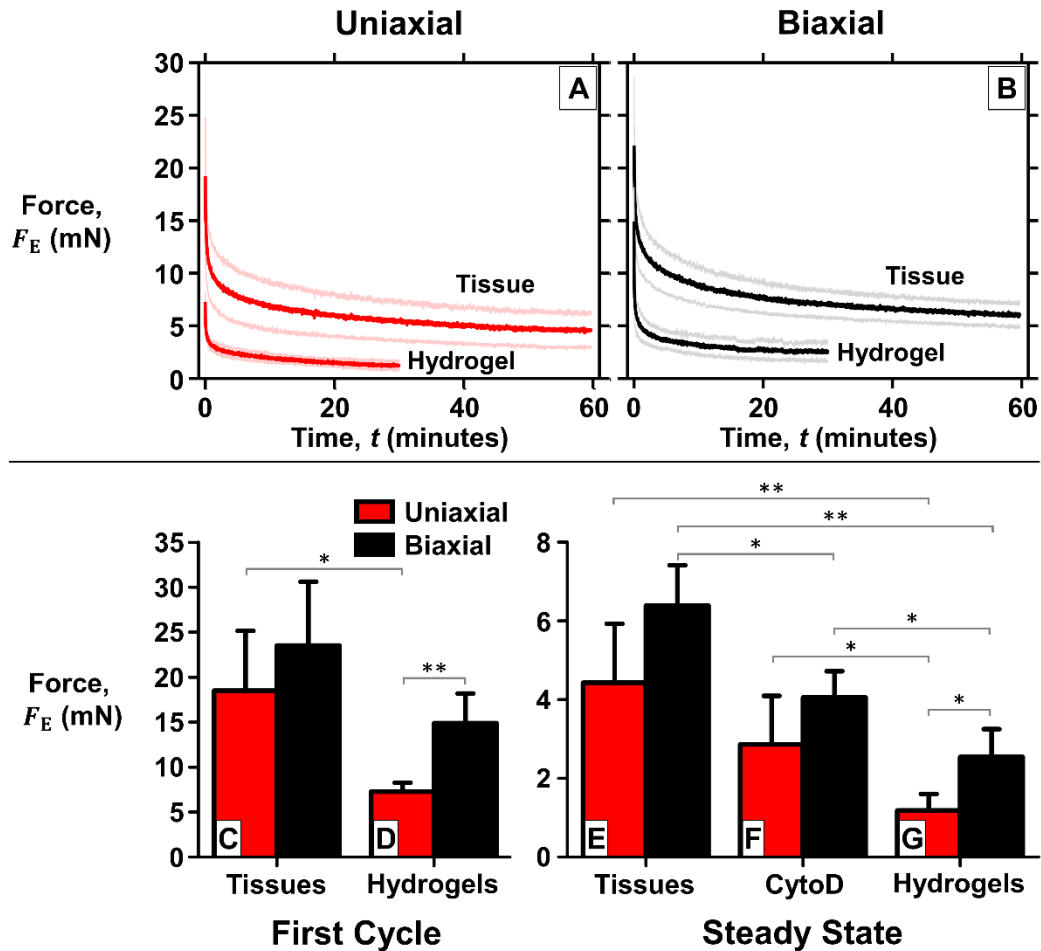


Figure 8.4: The maximum force measured from cyclic deformation experiments of: (A) uniaxial collagen tissues and hydrogels (Mean (red curve)  $\pm$  standard deviation (pink curves),  $n=6$ ) and (B) biaxial collagen tissues and hydrogels (Mean (black curve)  $\pm$  standard deviation (grey curves),  $n=6$ ). The force measurement from uniaxial and biaxial deformation experiments at the end of the initial loading cycle for (C) tissues and (D) hydrogels. (E) Force measurement after 60 minutes of cyclic loading of (E) tissues and (F) 60 minutes after the addition of cytoD. (G) Force measurement after 30 minutes of cyclic loading of hydrogels. Note that maximum force is recorded when samples are at maximum stretch of 20% nominal strain.

### 8.3.1.3 Fluorescent Images

In Figure 8.5 and Figure 8.6, fluorescent images of uniaxial and biaxial tissues are shown, respectively. Five specific regions of interest are imaged in each tissue to investigate the SF distribution before (pre) and after (post) cyclic deformation experiments. In Figure 8.5 and Figure 8.6 (-A and -B), the darkened portions to the left of the images exhibit low fluorescence due to the presence of the hanger in these regions. In Figure 8.5 and Figure 8.6 (-A and -C), the edge of the

tissue is indicated by the abrupt absence of fluorescence in the upper portions of the images. It should be noted that fluorescent images shown in Figure 8.5 and Figure 8.6 are generated by combining multiple z-stack images. Therefore, the out-of-plane directionality of SFs is not clear in 2D images. Examination of 3D rendered image z-stacks reveals that SFs do indeed preferentially align in the 2D plane shown in Figure 8.5-Figure 8.7, with very little out-of-plane directionality. A representative example of an animated 3D rendered z-stack of Figure 8.5-E (pre) can be found in online supplementary material at the following web address: "[j.mp/3D-rendered-Zstack](http://j.mp/3D-rendered-Zstack)". It should be recalled that tissues are free to deform in the out-of-plane direction. Therefore, tension reduction results in SF dissociation in this direction.

Before the application of cyclic stretch to uniaxial tissues, it is qualitatively clear that the tissue exhibits a preferential alignment of SFs longitudinally between the two opposing hangers, particularly in Figure 8.5-C to D (pre). This is unsurprising given that hangers are fixed in the axial direction, and therefore SF tension is supported in this direction. The absence of a lateral constraint (parallel to the hangers as indicated in Figure 8.5) in the tissue leads to SF dissociation in the lateral direction. Furthermore, a high concentration of SFs is observed in the tissue before cyclic stretching. Following cyclic stretching, a very similar SF distribution and concentration is observed in the uniaxial tissue (Figure 8.5-C to D (post)). This suggests that cyclic deformation of the 3D tissue maintains SFs parallel to the stretch direction, in contrast to the well-known behaviour of cells on 2D substrates undergoing similar loading conditions (Kaunas et al., 2005, Barron et al., 2007, Wang et al., 2001). A deviation from this trend is observed near the hangers. In Figure 8.5-A, SFs predominantly align tangential to the edge of the tissue in both

cases. However, further away from the tissue edge, SFs begin to align closer to the stiff hanger post experimentation (Figure 8.5-A (post)). This trend of localised alignment of SFs parallel to the hanger is also evident in Figure 8.5-B following cyclic stretching. A random distribution of fibres is observed before experiments in this region (Figure 8.5-B (Pre)). Realignment of SFs at the tissue-hanger interface occurs due to cyclic stretching.

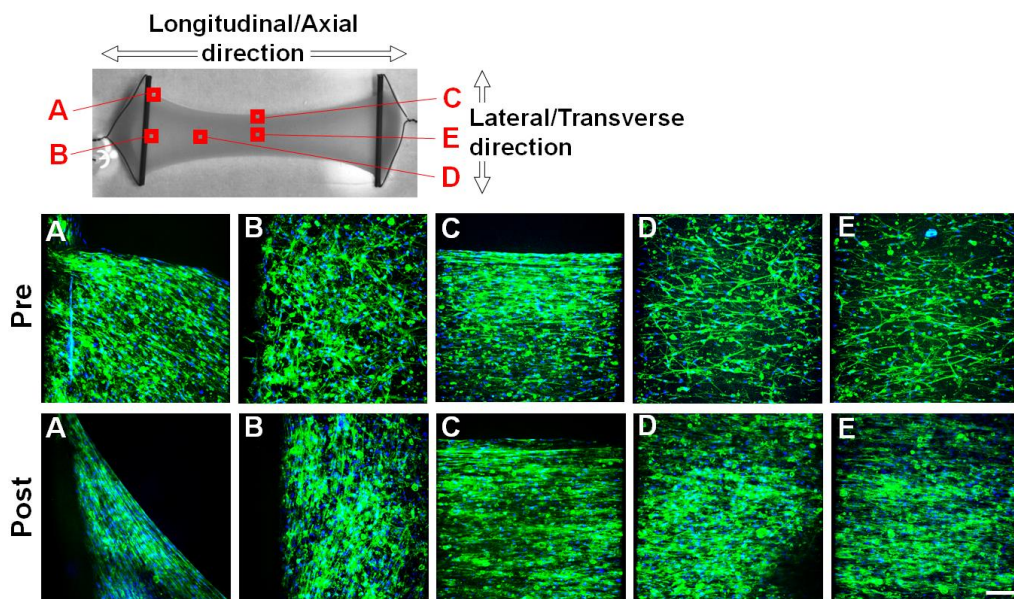


**Figure 8.5: Fluorescent images of the uniaxial tissues. Actin is labelled with green and nuclei are blue. The maximum intensity of multiple z-stacks are combined to create images at the following regions: (A) the edge of the tissue-hanger interface region, (B) the middle of the tissue-hanger interface region, (C) the edge of the tissue between the two opposing hangers, (D) a region mid-way between the hanger and the centre of the tissue, and (E) the centre of the tissue. Scale bar = 250  $\mu\text{m}$ .**

In Figure 8.6-D and E, it is clearly shown that SFs are randomly oriented throughout the majority of the biaxial tissue pre-experimentation. Before cyclic stretching a very high concentration of long SFs is also observed. Post-cyclic deformation an extremely similar SF distribution and concentration is observed (Figure 8.6-D and E (post)). It should be recalled that an unchanged SF arrangement is also observed in uniaxial tissues pre- and post-cyclic stretching. Therefore, biaxial experiments further suggest that cyclic deformation of the 3D tissues

supports SF maintenance. During the initial 2 day incubation period before the application of cyclic load tissue contraction is observed in the corner region between neighbouring hangers (Figure 8.3-C), as noted previously in section 8.3.1.1. However, fluorescent images shown in Figure 8.6-C reveal that this inward contraction only affects the SF distribution in a highly localised corner region. Similar to the uniaxial tissue, a more complex SF distribution is observed in the tissue-hanger interface region in biaxial tissues. In Figure 8.6-A (pre) highly aligned SFs at the edge of the tissue protrude from the hanger at  $45^\circ$ . The tension supported between two neighbouring hangers is key to this behaviour, where the tangentially aligned fibres are observed along the edge of the tissue, as observed in Figure 8.6-C (pre). Similar SF distributions are observed post application of cyclic stretching.

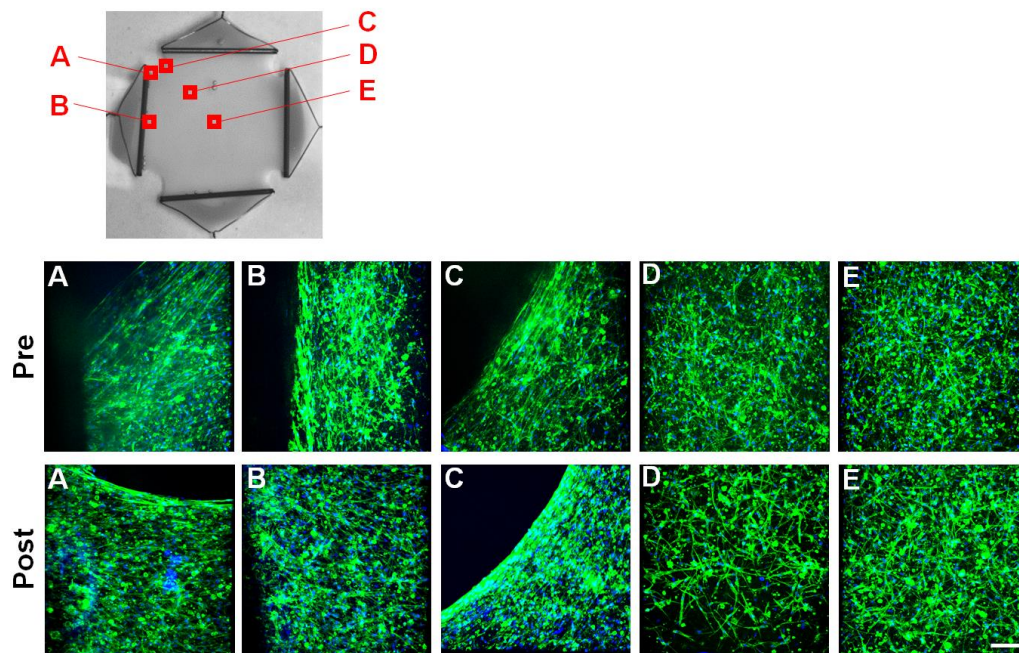


**Figure 8.6:** Fluorescent images of the biaxial tissues. Actin is labelled with green and nuclei are blue. The maximum intensity of multiple z-stacks are combined to create images at the following regions: (A) the edge of the hanger- tissue interaction region, (B) the middle of the hanger- tissue interaction region, (C) the edge of the tissue between two neighbouring hangers, (D) a region mid-way between the edge and the centre of the tissue, and (E) the centre of the tissue. Scale bar = 250  $\mu\text{m}$ .

In Figure 8.7, a quantitative analysis of SF distribution in two key regions of uniaxial and biaxial tissues is presented. In the uniaxial tissue, SFs distribution at the edge mid-way between the two opposing hangers (Figure 8.7-A) and in the very centre (Figure 8.7-B) is analysed pre- and post-cyclic stretching. In the uniaxial tissue the extremely strong SF alignment, as observed in Figure 8.5, is quantitatively confirmed. In Figure 8.7-A and -B, while SFs are strongly aligned between the rigid hangers before stretching (pre), 48% of SFs are not directly aligned in the longitudinal ( $0^\circ$ ) direction, with 38% of SFs aligned at  $\sim 15^\circ$ . Interestingly, the proportion of these non-axial SFs (at  $15^\circ$  and  $30^\circ$ ) greatly decreases after the cyclic stretching (22%), demonstrating that moderate SF realignment occurs due to cyclic stretching. In biaxial tissues the strong alignment observed at the corner edge is quantified in Figure 8.7-C. No pronounced differences between polar plots pre- and post-cyclic deformation are observed. In the centre region of biaxial tissues, a random distribution of SFs is measured both before and after cyclic stretching (Figure 8.7-D).

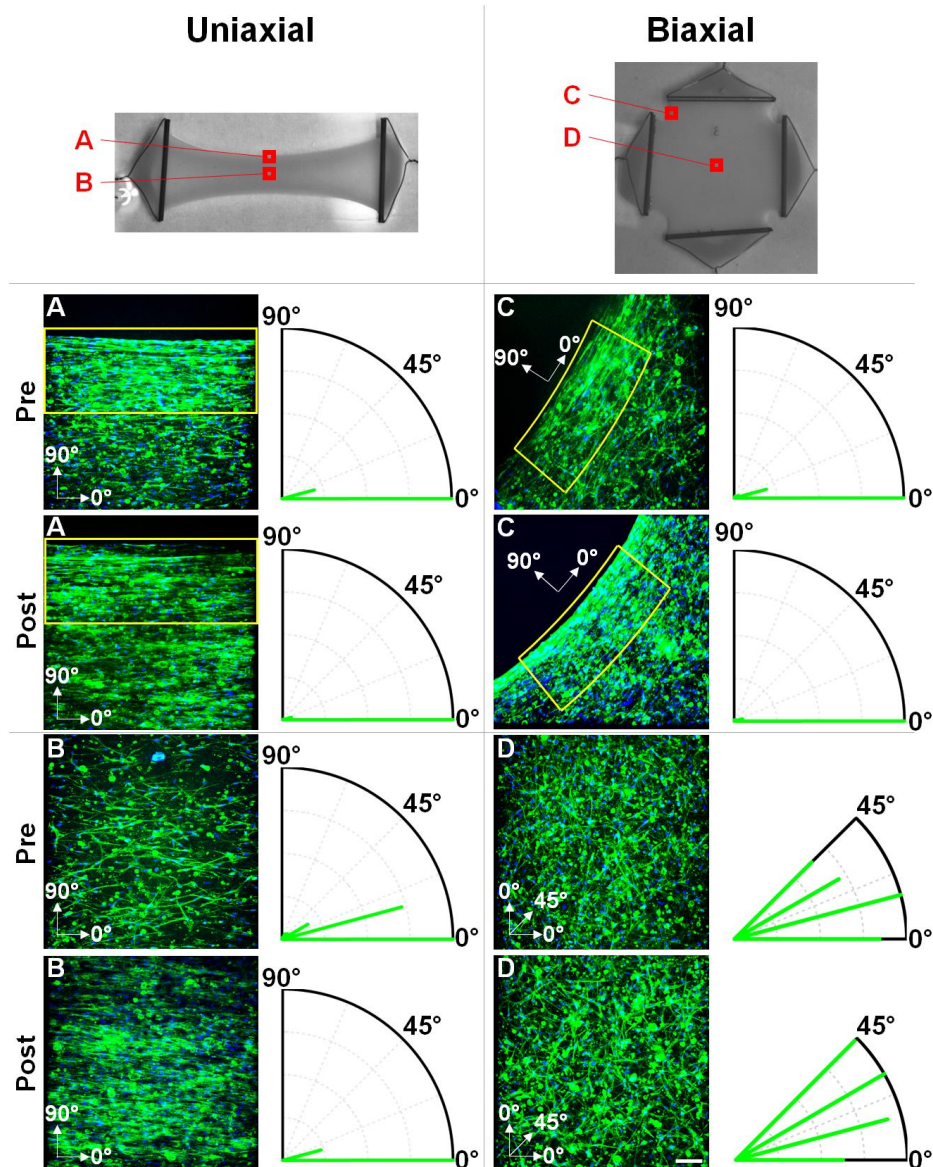


Figure 8.7: Fluorescent images and associated normalised SF orientation distribution at specific regions of uniaxial and biaxial tissues are shown. Actin is labelled with green and nuclei are blue. In the uniaxial specimens, normalised SF orientation distribution is measured from fluorescent images obtained pre- and post-experimentation at: (A) the edge of the tissue mid-way between the two opposing hangers, and (B) the absolute centre of the tissue. In the biaxial specimens, normalised SF orientation distribution is measured from fluorescent images obtained pre- and post-experimentation at: (C) the edge of the tissue between two neighbouring hangers, and (D) the centre of the tissue. In (C),  $0^\circ$  SFs are those that align tangentially to the edge of the specimen. In (A) and (C), only a limited region of interest considered (outlined in yellow). The regions of interest for uniaxial and biaxial specimens have a depth of  $300\ \mu\text{m}$  and  $500\ \mu\text{m}$  from the edge, respectively. Note that in (D), geometrical symmetry occurs in the quadrant, therefore, only a half-quadrant is shown. Scale bar =  $250\ \mu\text{m}$ .

### 8.3.2 Computational results

In Figure 8.8-A and -B contour plots of the non-dimensional effective uniaxial stress invariant,  $\hat{S}$ , (as detailed in section 8.2.5) after simulation of the

initial equilibrium step are shown. In the uniaxial tissue in Figure 8.8-A a highly uniaxial stress state is predicted throughout the majority of the tissue ( $\hat{S} = 1$ ). The corresponding predicted SF distribution is highly aligned in the maximum principal direction, i.e. the longitudinal direction. In contrast, a highly biaxial stress state ( $\hat{S} = 0$ ) is predicted throughout the majority of the biaxial tissue (Figure 8.8-B). A biaxial SF distribution is predicted by the model in these regions as SF tension is supported in all directions. In contrast to the central region of the biaxial tissue, corner regions experience a highly uniaxial stress state ( $\hat{S} = 1$ ). In the case of both the uniaxial and biaxial tissues, no significant SFs are predicted in the out-of-plane direction. The absence of constraints in the out-of-plane direction, coupled with cell contractility, leads to a significant reduction in thickness of the tissues during the equilibrium step. The highly negative (shortening) strain rate coupled leads to the prediction of dissociation of out-of-plane SFs, in accordance with equation 7.1. In summary, aligned SFs are predicted to align in the maximum principal direction when the local stress state is highly uniaxial in nature ( $\hat{S} \approx 1$ ). In contrast, a biaxial distribution of SFs is predicted where the local stress state is non-uniaxial ( $\hat{S} \approx 0$ ).

In Figure 8.8-C and -D computed deformation of the uniaxial and the biaxial tissues after the equilibrium step are quantified and compared to experimental measurements at a number of sections along the longitudinal axis of the tissue. The interaction between actively generated SF tension and the passive material leads to the prediction of lateral contraction of the uniaxial tissues as no constraints are provided in this direction (Figure 8.8-A). This results in SF dissociation in the lateral direction as only the passive stiffness of the hydrogel provides support for a very low level of SF tension. For each measurement, a significant reduction from the baseline width is observed, in strong agreement with

experimental observations. The deformation of the biaxial tissue is characterised by the deformation of the free edge at the specimen corners ( $L_C$ ), as shown in Figure 8.8-D (refer to Figure 8.3-C for definition of  $L_C$ ). Once again a close agreement between computational predictions and experimental measurements is obtained.

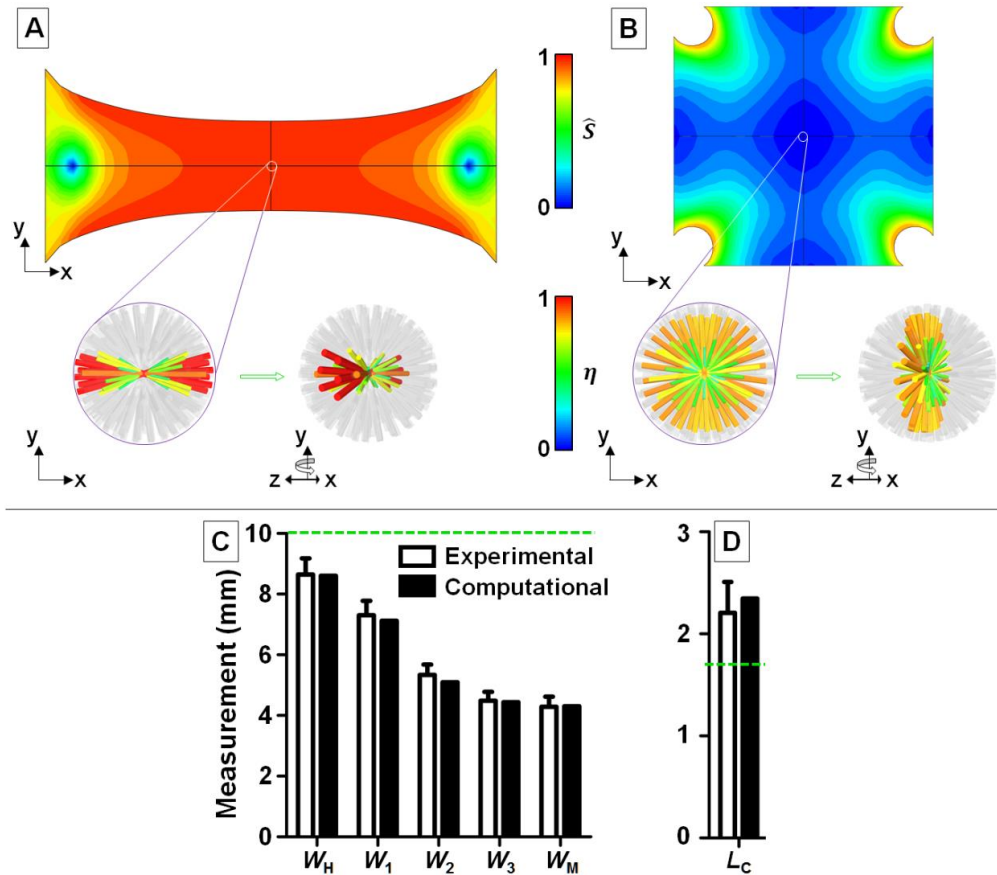


**Figure 8.8:** (A) Contour plot of stress uniaxiality obtained at the end of the equilibrium step during simulations of uniaxial experiments. (B) Contour plot of stress uniaxiality obtained at the end of the equilibrium step during simulations of biaxial experiments. In (A) and (B), vector plots show the full distribution of SF activation at a single integration point at the centre of the FE mesh. Two fields of view are shown to illustrate the full 3D distribution of SFs. (C) Measurements of uniaxial width at specific sections (refer to Figure 8.3-(A)) after simulation of the equilibrium step. (D) Measurement of the corner length,  $L_C$ , of the biaxial tissue after simulation of the equilibrium step (refer to Figure 8.3-(C)). In (C) and (D), experimental results are reproduced from Figure 8.3 for comparison purposes and baseline values are indicated by dashed green lines. Note that baseline values refer to the experimental measurements of gels at day 0 (before cell mediated tissue contraction) and measurements of the un-deformed geometry in simulations (before the initial equilibrium step)

In Figure 8.8-E, maximum force predicted after 60 minutes of dynamic loading is presented. At 20% nominal strain, the computed force for uniaxially and biaxially stretched hydrogels is 1.2 mN and 2.4 mN, respectively. This is in close

agreement with the experimentally measured values of  $1.2 \pm 0.4$  mN and  $2.5 \pm 0.7$  mN. For the uniaxial tissue the computed force of 4.6 mN is in close agreement with experimentally measured value of  $4.4 \pm 1.5$  mN. However, for the biaxial tissue the computed force of 9.9 mN is significantly higher than the experimentally measured value of  $6.4 \pm 1.0$  mN. Therefore, while a good prediction of experimentally observed SF distributions, tissue deformation, and uniaxial steady state force is achieved in simulations, an inaccurate prediction of the biaxial force is computed.

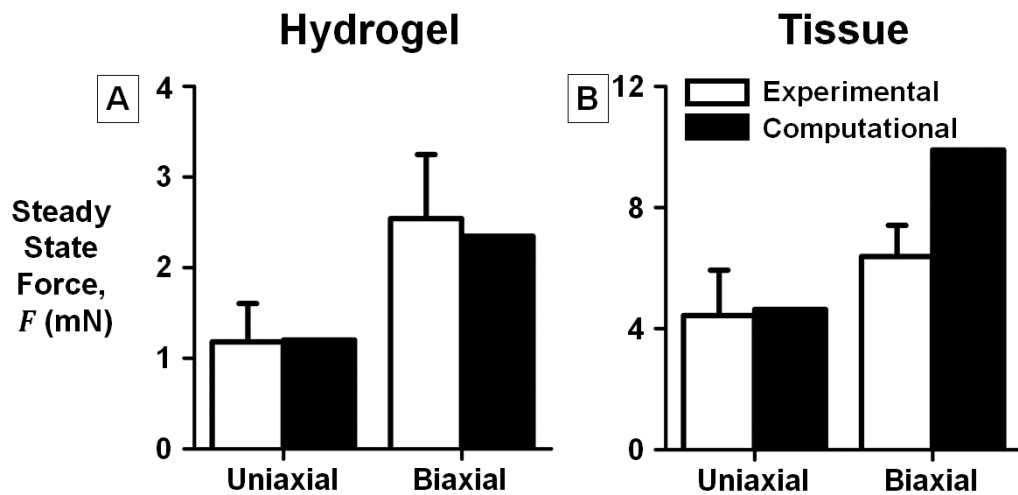


Figure 8.9: Steady state force predicted for (A) hydrogels and (B) tissues. Experimental results are reproduced from Figure 8.4 for comparison purposes.

## 8.4 Discussion

The current chapter presents an investigation of the role of the actin cytoskeleton in the response of cell laden uniaxial and biaxial tissue constructs. The following key contributions from the current chapter are highlighted:

- A novel experimental system for measurement of tissue and cell forces during applied biaxial and uniaxial cyclic stretching is developed. Previous systems have been limited to uniaxial cyclic stretching.

- Stress uniaxiality ( $\hat{S} = 1$ ) results in highly aligned SF distributions, whereas stress biaxiality ( $\hat{S} = 0$ ) results in randomly aligned SF distributions. In both cases individual cells and SFs are highly polarised.
- Significant tissue deformation occurs due to cell contractility, particularly in uniaxially constrained tissues. Active cell force is also shown to contribute significantly to the measured tissue force during biaxial and uniaxial cyclic stretching.
- Due to the highly aligned and coordinated SF distribution in uniaxial tissues, measured forces are not significantly different from biaxial tissues, despite the higher structural stiffness of the biaxial construct.

In hydrogels which contain no cells the ratio of measured force for the biaxial specimen to that for the uniaxial specimen is  $\sim 1.75$ . When cells are seeded into the tissue this ratio decreases to 1.3 (with the same cell density being used for uniaxial and biaxial tissues). The high ratio of 1.75 for hydrogels containing no cells results entirely from the fact that the biaxially constrained tissue is a stiffer structure (see Nolan and McGarry (2016) for a comprehensive mechanical assessment of biaxial testing). A simple FE model treating the hydrogel as a passive hyperelastic material provides reasonable agreement with the experimentally observed ratio of 1.75. The reduction in the ratio of biaxial to uniaxial measured force when cells are seeded in the tissue can be explained as follows. In uniaxial tissues all SFs are highly aligned in the axial direction, hence the cumulative cell contribution to measured force is fully aligned concentrated in this direction. In contrast, SFs are randomly aligned in biaxial tissues and the contractile action of the highly polarised cells is dispersed over  $360^\circ$  in the plane between rigid hangers. Therefore, the cumulative “cell force” measured by each load cell in the biaxial tissue is lower

than that recorded for uniaxial tissues. In other words, each tissue contains the same density of highly polarised cells, but in the case of the uniaxial tissue all cells are aligned in the same direction and actively generating force in this direction. It has been previously reported that a uniaxial stress state improved the performance and maturation state of in vitro engineered cardiac tissue (Thavandiran et al., 2013). The current chapter suggests that cardiomyocyte tissue constructs should be constrained uniaxially in order to achieve highly coordinated cumulative active force generation.

In the current chapter, a very similar distribution of SFs is observed in tissues before and after the application of cyclic loading. It is well-known that cells exhibit stretch avoidance on 2D substrates undergoing cyclic deformation (Kaunas et al., 2005, Barron et al., 2007, Wang et al., 2001, Neidlinger-Wilke et al., 2001). This response has also been observed for cells in 3D culture (Foolen et al., 2014). However, in the case of uniaxially constrained tissues, it is more commonly reported that SFs align in the longitudinal (constrained) direction, both before and after cyclic stretching (Foolen et al., 2012, Zhao et al., 2013, Wille et al., 2006, Lee et al., 2008, Nieponice et al., 2007, Gauvin et al., 2011). It is well known that cells orient in the direction of maximal stiffness under static conditions (Bischofs and Schwarz, 2003). Moreover, strong cell alignment has been observed on 1D fibrils and on grooved 2D substrates due to “contact guidance” (Teixeira et al., 2003, Doyle et al., 2009). A previous study of uniaxially constrained tissues has demonstrated a collagen fibril alignment that corresponds with cell alignment patterns (Rubbens et al., 2009). Furthermore, it has been demonstrated that parallel alignment of collagen fibril becomes more pronounced during cyclic straining (Rubbens et al., 2009). Foolen et al. (2012) suggested previously that the

maintenance of SF alignment of cells in 3D culture parallel to the direction of cyclic loading is possibly due to the dominant effect of contact guidance of intra-tissue collagen fibrils. In the study of Foolen et al. (2012), tissues that were originally biaxially constrained were subjected to a uniaxial cyclic stretch. If the collagen density was “high” (1.5 mg/mL), the random SF distribution observed before cyclic loading was maintained in cells encapsulated in the core of the tissues. However, in tissues with a “low” collagen density (0.45 mg/mL), SFs exhibited stretch avoidance. Furthermore, SFs at the top and bottom surfaces exhibited stretch avoidance in all cases. In the current chapter, tissues (with collagen densities lower than the “low” collagen density of Foolen et al. (2012)) that are originally biaxially constrained were subjected to a biaxial stretch regime. A similar SFs orientation and intensity is observed before and after stretching. On 2D substrates, significant SF dissociation is observed in all directions in cells undergoing a similar loading pattern (Wang et al., 2001). The system described in the current chapter provides a useful tool for investigations of SF orientation redistribution during cyclic stretch. A potential limitation of the technique described in the current chapter is that collagen fibril direction cannot be directly controlled. However, electrospinning techniques could be used to directly manipulate collagen fibrils orientation to investigate the effect of contact guidance on cell alignment in tissues constructs (Baker et al., 2008, Li et al., 2006, Zeugolis et al., 2008). Experimental results presented in the current chapter reveal, for the first time, that the actin distribution in cardiomyocytes cultured in 3D remains relatively unchanged during uniaxial and biaxial cyclic loading. Results also reveal that active cell force generation is significant in both biaxial and uniaxial cyclic stretching experiments.

The current chapter presents a novel experimental system to investigate the mechanical behaviour of engineered tissue constructs. Precise uniaxial and biaxial cyclic deformation is applied to tissue constructs while measuring force at a milli-Newton level. In previous studies, the contractile behaviour of cell laden tissue constructs has been investigated (Legant et al., 2009, Kural and Billiar, 2014, West et al., 2013). However, these studies examined tissue contractility in static culture, neglecting the mechanical behaviour during applied load. Additionally, the mechanical response of tissues constructs has been quantified during monotonic and cyclic tensile loading (Berry et al., 2003, Seliktar et al., 2000, Wagenseil et al., 2003). In these studies, the mechanical contribution of cells to the measured force was not quantified using cytoD or similar inhibitors of active contractility. Zhao et al. (2013) fabricated contractile uniaxial collagen tissues on two opposing deformable microposts. By magnetically displacing a bead attached to one micropost, cyclic loading was applied to the tissues while the force was estimated by measuring the deflection of the opposing micropost. In the study of Wakatsuki et al. (2000), a system whereby tissue rings were fabricated for loading into a custom stretching rig is described. The force generated by the tissues rings during static contraction and during cyclic stretch was measured, in a similar fashion to the system described in the current chapter. In the studies of Zhao et al. (2013) and Wakatsuki et al. (2000), the mechanical contribution of cells during tissue stretch was quantified by comparing the force response of untreated tissues to tissues treated to disrupt the actin cytoskeleton. Furthermore, a similar technique is implemented to parse the response of the actin cytoskeleton in later studies (Wakatsuki et al., 2001, Wille et al., 2006). However, it should be noted that these aforementioned studies are confined to uniaxial loading. Wagenseil et al. (2004)

developed a system which investigated the anisotropic mechanical behaviour of collagen tissue vessels using a “pressure-diameter, force-length” test system. Vessels were either inflated to set diameters or axially stretched while the internal pressure, axial force, external diameter, and overall length were measured. It should be noted that in Wagenseil et al. (2004), tissues vessels were fabricated on rigid mandrels and, therefore, could only be engineered to exhibit circumferential or axial cell alignment before testing. Furthermore, the application of internal pressure and axial deformation was mutually exclusive. The system described in the current chapter represents a significant advancement on previously described methods. In particular, the novel experimental system developed in the current chapter facilitates: (i) performing testing on a broad range of tissue constructs with different engineered parameters, such as, collagen density and cell seeding density; (ii) the application cyclic loading regimes to tissues; (iii) independent controlling of deformation in both stretching directions during biaxial testing; (iv) independent measurement of force in both stretching direction during biaxial testing; and (v) conducting immuno-fluorescent investigations of tissues before and after testing.

As stated previously, by using a computational model for actin cytoskeleton remodelling and contractility, an accurate prediction of SF distribution is obtained. Importantly, fibre dissociation in unconstrained directions is correctly predicted for the uniaxial tissues, and also in localised regions near the tissue hangers in the biaxial case. Furthermore, this approach builds upon the studies of Thavandiran et al. (2013) and Legant et al. (2009), where the SF distribution of tissues under static multi-axial conditions is accurately simulated. However, in the aforementioned studies, the actively generated force was not measured experimentally or predicted computationally. In the current chapter, the active force generated during dynamic

load experiments is computed and compared to experimental measurements. While accurate predictions of cell force are obtained for uniaxial cyclic stretching, the active SF model provides an inaccurate prediction of the biaxial force measurements. It should be recalled that the computational model was developed for single cell applications. Therefore, it is assumed that globular actin is abundantly available throughout the entire continuum. It then follows that SF formation can occur in all directions and at any point. However, it is observed experimentally that a finite number of cells exist in the tissues and these individual cells are highly polarised, with each cell exhibiting a preferential alignment. This is not captured by the model, which predicts that cells will exhibit a biaxial distribution of SFs in a region with a biaxial stress state. In reality, cardiomyocytes are observed to remain polarised, but randomly aligned in such regions. The SF model therefore over predicts the active force generation of biaxial tissues. The prediction is correct for the uniaxial tissue, simply because the model predicts a uniaxial distribution of SFs, and hence a high level of cell alignment, as observed in experiments; i.e. the polarised cell/SF distribution is captured by the model only in regions where the stress state is uniaxial. Recent models do not have this limitation, as they have described the macroscopic cell mediated contractile stress as a function of the volume fraction of cells in the tissue (Wagenseil and Okamoto, 2007). Furthermore, cells in tissues have been assumed to be rod shaped with a characteristic length and orientation (Zahalak et al., 2000). However, these models have not been implemented in 3D, focusing only on uniaxial 1D idealisations. To overcome this limitation to enable the simulation of a tissue environment in 3D using the model described in the current thesis, slight modifications to consider a finite cell density and preferential cell alignment must be implemented.

Furthermore, the passive material response could be adjusted from the isotropic visco-hyperelastic formulation used in the current chapter to an anisotropic model that considers collagen fibril realignment during cyclic stretching. A recent anisotropic hyperelastic model by Nolan et al. (2014), which considers collagen fibre contribution during isochoric and hydrostatic deformation, could be readily implemented. In summary, the work carried out in the current chapter highlights a shortcoming in the active cell model to accurately predict force response at a tissue level for multi-axial stress states.

In conclusion, in the current chapter a novel experimental system for measurement of tissue and cell forces during applied biaxial and uniaxial cyclic stretching is developed. Experiments reveal that stress uniaxiality results in highly aligned SFs and cells throughout the tissue, whereas stress biaxiality results in randomly aligned SF distributions. In the case of both uniaxial and biaxially constrained tissues cells and SFs are highly polarised. Significant tissue deformation occurs due to cell contractility, particularly in the lateral direction of uniaxially constrained tissues. The force measured during biaxial cyclic stretching is only  $\sim 1.30$  times higher than that for uniaxial cyclic stretching. The total cell force contribution is coordinated in axial direction in the case of uniaxial cyclic stretching. The contractile action of the same concentration of cells is randomly distributed in biaxial tissues. Finally, the current chapter presents a first attempt at implementing the active SF framework for simulation of forces generated during cyclic loading of tissue constructs. It is revealed that minor modifications must be made to the SF framework to accurately predict active cell traction in regions of biaxial stress state.

## Appendix 8.A

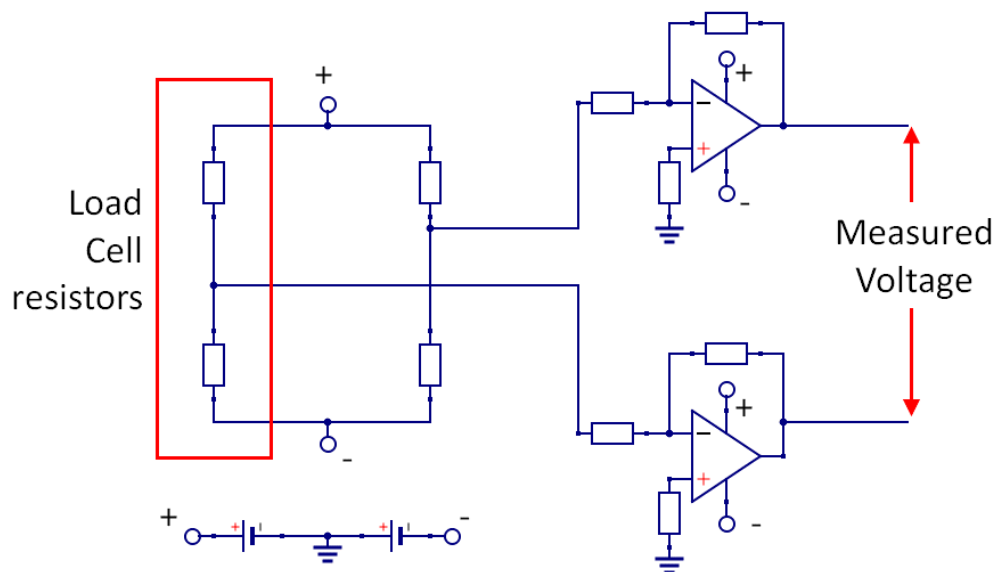


Figure 1.A: Schematic of Wheatstone bridge and voltage amplification circuit.

## 8.5 References

- BAKER, B. M., GEE, A. O., METTER, R. B., NATHAN, A. S., MARKLEIN, R. A., BURDICK, J. A. & MAUCK, R. L. 2008. The potential to improve cell infiltration in composite fiber-aligned electrospun scaffolds by the selective removal of sacrificial fibers. *Biomaterials*, 29, 2348-2358.
- BARRON, V., BROUGHAM, C., COGHLAN, K., MCLUCAS, E., O'MAHONEY, D., STENSON-COX, C. & MCHUGH, P. E. 2007. The effect of physiological cyclic stretch on the cell morphology, cell orientation and protein expression of endothelial cells. *J Mater Sci Mater Med*, 18, 1973-81.
- BERRY, C. C., SHELTON, J. C., BADER, D. L. & LEE, D. A. 2003. Influence of external uniaxial cyclic strain on oriented fibroblast-seeded collagen gels. *Tissue Eng*, 9, 613-24.
- BILLIAR, K. L., THROM, A. M. & FREY, M. T. 2005. Biaxial failure properties of planar living tissue equivalents. *J Biomed Mater Res A*, 73, 182-91.
- BISCHOFFS, I. B. & SCHWARZ, U. S. 2003. Cell organization in soft media due to active mechanosensing. *Proceedings of the National Academy of Sciences*, 100, 9274-9279.
- CAMPBELL, J. J., BLAIN, E. J., CHOWDHURY, T. T. & KNIGHT, M. M. 2007. Loading alters actin dynamics and up-regulates cofilin gene expression in chondrocytes. *Biochem Biophys Res Commun*, 361, 329-334.
- CUMMINGS, C. L., GAWLITTA, D., NEREM, R. M. & STEGEMANN, J. P. 2004. Properties of engineered vascular constructs made from collagen, fibrin, and collagen-fibrin mixtures. *Biomaterials*, 25, 3699-706.
- DOYLE, A. D., WANG, F. W., MATSUMOTO, K. & YAMADA, K. M. 2009. One-dimensional topography underlies three-dimensional fibrillar cell migration. *The Journal of Cell Biology*, 184, 481-490.

- FOOLEN, J., DESHPANDE, V. S., KANTERS, F. M. & BAAIJENS, F. P. 2012. The influence of matrix integrity on stress-fiber remodeling in 3D. *Biomaterials*, 33, 7508-18.
- FOOLEN, J., JANSSEN-VAN DEN BROEK, M. W. & BAAIJENS, F. P. 2014. Synergy between Rho signaling and matrix density in cyclic stretch-induced stress fiber organization. *Acta Biomater*, 10, 1876-85.
- GABBAY, J. S., ZUK, P. A., TAHERNIA, A., ASKARI, M., O'HARA, C. M., KARTHIKEYAN, T., AZARI, K., HOLLINGER, J. O. & BRADLEY, J. P. 2006. In vitro microdistraction of preosteoblasts: distraction promotes proliferation and oscillation promotes differentiation. *Tissue Eng*, 12, 3055-65.
- GAUVIN, R., PARENTEAU-BAREIL, R., LAROUCHE, D., MARCOUX, H., BISSON, F., BONNET, A., AUGER, F. A., BOLDUC, S. & GERMAIN, L. 2011. Dynamic mechanical stimulations induce anisotropy and improve the tensile properties of engineered tissues produced without exogenous scaffolding. *Acta Biomater*, 7, 3294-301.
- HENDERSON, A., AHERNS, J. & LAW, C. 2004. The ParaView Guide. In: KITWARE (ed.). Clifton Park, NY, USA: Kitware.
- ISENBERG, B. C. & TRANQUILLO, R. T. 2003. Long-term cyclic distention enhances the mechanical properties of collagen-based media-equivalents. *Ann Biomed Eng*, 31, 937-49.
- KAUNAS, R., NGUYEN, P., USAMI, S. & CHIEN, S. 2005. Cooperative effects of Rho and mechanical stretch on stress fiber organization. *Proceedings of the National Academy of Sciences of the United States of America*, 102, 15895-15900.
- KURAL, M. H. & BILLIAR, K. L. 2014. Mechanoregulation of valvular interstitial cell phenotype in the third dimension. *Biomaterials*, 35, 1128-1137.
- LEE, E. J., HOLMES, J. W. & COSTA, K. D. 2008. Remodeling of Engineered Tissue Anisotropy in Response to Altered Loading Conditions. *Annals of biomedical engineering*, 36, 1322-1334.
- LEGANT, W. R., PATHAK, A., YANG, M. T., DESHPANDE, V. S., MCMEEKING, R. M. & CHEN, C. S. 2009. Microfabricated tissue gauges to measure and manipulate forces from 3D microtissues. *Proc Natl Acad Sci U S A*, 106, 10097-102.
- LI, W.-J., COOPER JR, J. A., MAUCK, R. L. & TUAN, R. S. 2006. Fabrication and characterization of six electrospun poly( $\alpha$ -hydroxy ester)-based fibrous scaffolds for tissue engineering applications. *Acta Biomaterialia*, 2, 377-385.
- MAUCK, R. L., SOLTZ, M. A., WANG, C. C., WONG, D. D., CHAO, P. H., VALHMU, W. B., HUNG, C. T. & ATESHIAN, G. A. 2000. Functional tissue engineering of articular cartilage through dynamic loading of chondrocyte-seeded agarose gels. *J Biomech Eng*, 122, 252-60.
- MAUCK, R. L., WANG, C. C., OSWALD, E. S., ATESHIAN, G. A. & HUNG, C. T. 2003. The role of cell seeding density and nutrient supply for articular cartilage tissue engineering with deformational loading. *Osteoarthritis Cartilage*, 11, 879-90.
- NEIDLINGER-WILKE, C., GROOD, E. S., WANG, J.-C., BRAND, R. A. & CLAES, L. 2001. Cell alignment is induced by cyclic changes in cell length: studies of cells grown in cyclically stretched substrates. *J Orthop Res*, 19, 286-93.
- NIEPONICE, A., MAUL, T. M., CUMER, J. M., SOLETTI, L. & VORP, D. A. 2007. Mechanical stimulation induces morphological and phenotypic changes in bone marrow-derived progenitor cells within a three-dimensional fibrin matrix. *J Biomed Mater Res A*, 81, 523-30.
- NOLAN, D. R., GOWER, A. L., DESTRADE, M., OGDEN, R. W. & MCGARRY, J. P. 2014. A robust anisotropic hyperelastic formulation for the modelling of soft tissue. *Journal of the Mechanical Behavior of Biomedical Materials*, 39, 48-60.

- NOLAN, D. R. & MCGARRY, J. P. 2016. On the correct interpretation of measured force and calculation of material stress in biaxial tests. *Journal of the Mechanical Behavior of Biomedical Materials*, 53, 187-199.
- RUBBENS, M. P., DRIESSEN-MOL, A., BOERBOOM, R. A., KOPPERT, M. M. J., VAN ASSEN, H. C., TERHAAR ROMENY, B. M., BAAIJENS, F. P. T. & BOUTEN, C. V. C. 2009. Quantification of the Temporal Evolution of Collagen Orientation in Mechanically Conditioned Engineered Cardiovascular Tissues. *Annals of Biomedical Engineering*, 37, 1263-1272.
- SCHNEIDER, C. A., RASBAND, W. S. & ELICEIRI, K. W. 2012. NIH image to ImageJ: 25 years of image analysis. *Nat Methods*, 9, 671-675.
- SELIKAR, D., BLACK, R. A., VITO, R. P. & NEREM, R. M. 2000. Dynamic mechanical conditioning of collagen-gel blood vessel constructs induces remodeling in vitro. *Ann Biomed Eng*, 28, 351-62.
- TEIXEIRA, A. I., ABRAMS, G. A., BERTICS, P. J., MURPHY, C. J. & NEALEY, P. F. 2003. Epithelial contact guidance on well-defined micro- and nanostructured substrates. *J Cell Sci*, 116, 1881-92.
- THAVANDIRAN, N., DUBOIS, N., MIKRYUKOV, A., MASSÉ, S., BECA, B., SIMMONS, C. A., DESHPANDE, V. S., MCGARRY, J. P., CHEN, C. S., NANTHAKUMAR, K., KELLER, G. M., RADISIC, M. & ZANDSTRA, P. W. 2013. Design and formulation of functional pluripotent stem cell-derived cardiac microtissues. *Proc Natl Acad Sci USA*, 110, 4698-4707.
- WAGENSEIL, J. E., ELSON, E. L. & OKAMOTO, R. J. 2004. Cell orientation influences the biaxial mechanical properties of fibroblast populated collagen vessels. *Ann Biomed Eng*, 32, 720-31.
- WAGENSEIL, J. E. & OKAMOTO, R. J. 2007. Modeling cell and matrix anisotropy in fibroblast populated collagen vessels. *Biomech Model Mechanobiol*, 6, 151-62.
- WAGENSEIL, J. E., WAKATSUKI, T., OKAMOTO, R. J., ZAHALAK, G. I. & ELSON, E. L. 2003. One-dimensional viscoelastic behavior of fibroblast populated collagen matrices. *J Biomech Eng*, 125, 719-25.
- WAKATSUKI, T. & ELSON, E. L. 2002. Reciprocal interactions between cells and extracellular matrix during remodeling of tissue constructs. *Biophysical Chemistry*, 100, 593-605.
- WAKATSUKI, T., KOLODNEY, M. S., ZAHALAK, G. I. & ELSON, E. L. 2000. Cell mechanics studied by a reconstituted model tissue. *Biophysical Journal*, 79, 2353-2368.
- WAKATSUKI, T., SCHWAB, B., THOMPSON, N. C. & ELSON, E. L. 2001. Effects of cytochalasin D and latrunculin B on mechanical properties of cells. *J Cell Sci*, 114, 1025-36.
- WANG, J. H. C., GOLDSCHMIDT-CLERMONT, P., WILLE, J. & YIN, F. C. P. 2001. Specificity of endothelial cell reorientation in response to cyclic mechanical stretching. *Journal of Biomechanics*, 34, 1563-1572.
- WEST, A. R., ZAMAN, N., COLE, D. J., WALKER, M. J., LEGANT, W. R., BOUDOU, T., CHEN, C. S., FAVREAU, J. T., GAUDETTE, G. R., COWLEY, E. A. & MAKSYM, G. N. 2013. Development and characterization of a 3D multicell microtissue culture model of airway smooth muscle. *Am J Physiol Lung Cell Mol Physiol*, 304, L4-16.
- WILLE, J., ELSON, E. & OKAMOTO, R. 2006. Cellular and Matrix Mechanics of Bioartificial Tissues During Continuous Cyclic Stretch. *Annals of Biomedical Engineering*, 34, 1678-1690.
- ZAHALAK, G. I., WAGENSEIL, J. E., WAKATSUKI, T. & ELSON, E. L. 2000. A cell-based constitutive relation for bio-artificial tissues. *Biophys J*, 79, 2369-81.
- ZEUGOLIS, D. I., KHEW, S. T., YEW, E. S., EKAPUTRA, A. K., TONG, Y. W., YUNG, L. Y., HUTMACHER, D. W., SHEPPARD, C. & RAGHUNATH, M. 2008. Electro-spinning of

pure collagen nano-fibres - just an expensive way to make gelatin? *Biomaterials*, 29, 2293-305.

ZHAO, R., BOUDOU, T., WANG, W. G., CHEN, C. S. & REICH, D. H. 2013. Decoupling cell and matrix mechanics in engineered microtissues using magnetically actuated microcantilevers. *Adv Mater*, 25, 1699-705.

ZHAO, R., CHEN, C. S. & REICH, D. H. 2014. Force-driven evolution of mesoscale structure in engineered 3D microtissues and the modulation of tissue stiffening. *Biomaterials*, 35, 5056-5064.

# 9 Concluding remarks and future perspectives

## 9.1 Summary of key contributions

The combined experimental-computational approaches provide new insights into the mechanical response of cells to their dynamic extra-cellular microenvironment. The novel investigations presented in this thesis are achieved by: (i) developing custom systems to conduct novel experiments on cells and tissue constructs; and (ii) advancing on previous state-of-the-art computational models to provide coherent mechanistic interpretations of experimentally observed behaviour. Key contributions of this thesis to the field of cell biomechanics are summarised below.

### **Chapter 4 and 5:**

- Advancing on previous micropipette aspiration (MA) studies, which are largely limited to the investigation of suspended cells (Hochmuth, 2000), a novel experimental technique is developed to perform MA on spread adhered cells.
- Using the novel MA system, the dominant contribution of the actin cytoskeleton to cell biomechanical behaviour is demonstrated. It is clearly

shown that the implementation of a 3D active stress fibre model is required to accurately predict the response the cells over a range of applied MA pressures.

- A detailed experimental-computational investigation reveals that the nucleus is highly deformable *in cyto*, reaching strain levels in excess of 100% during MA.
- Guided by results for nucleus mechanical properties, a follow-on computational investigation in situ chondrocytes reveals that nuclei are highly heterogeneous with localised intra-nuclear shear moduli ranging over two orders of magnitude.

#### **Chapter 6 and 7:**

- By using a previously described Hill-type 3D active stress fibre contractility model, simulations reveal that the actin cytoskeleton has a dominant role in the response of cells to cyclic loading. In particular, it is demonstrated that: circumferentially aligned SF bundles are stretched during unconfined compression, causing a very high resistance to probe pushing force; axially aligned SFs resist tensile loading, causing very high pulling force during probe retraction.
- It is demonstrated that a fading memory SF contractility formulation is required to replicate transient behaviour of untreated cells during cyclic loading.
- A non-linear visco-hyperelastic material model provides an excellent prediction of the mechanical response of cytoD treated cells during whole cell cyclic compression.

**Chapter 8:**

- Advancing on previous mechanical investigations of engineered tissue constructs, a novel experimental system is developed for measurement of cell and tissues forces during uniaxial and biaxial cyclic stretching.
- Force measurements from biaxial tissue stretching are only ~1.30 times greater than that during uniaxial tissue stretching. This ratio for passive hydrogels, which do not contain cells, is ~1.75. It is revealed that the lower ratio observed for tissues is due to the fact that the total cell force contribution is coordinated in stretching direction in uniaxial tissues. In biaxial tissues the contractile action of the same concentration of cells is randomly distributed.
- Using the active modelling framework it is shown that stress uniaxiality results in cell/SF alignment in tissues, whereas stress biaxiality leads to an unaligned SF distribution. The modelling framework over-predicts the total cell force generation under biaxial conditions.

## 9.2 Future perspectives

As presented in Chapter 4, the MA system provides a robust testbed for a detailed investigation of nucleus mechanical response in cyto. The investigation of nuclei, which still inhabit the cell cytoplasm, is beneficial as previous studies have demonstrated that nucleus mechanical behaviour may be altered by isolation techniques (Guilak et al., 2000). It has been suggested that the nucleus behaves as a viscoelastic material (Vaziri and Mofrad, 2007). Moreover, it has been shown that cell nuclei exhibit a visco-plastic response during large scale deformation (Pajerowski et al., 2007). In these aforementioned studies, and in the detailed

investigation of nucleus bulk mechanical properties presented in Chapter 4, the nucleus is assumed to be a homogenous continuum. However, previous studies strongly indicate that the nucleus is highly heterogeneous (Rowat et al., 2005, Henderson et al., 2013, Vaziri and Mofrad, 2007). Chapter 5 considers the highly heterogeneous strain distribution of chondrocyte nuclei in cartilage explants before and after shear deformation (Henderson et al., 2013). It is revealed that intra-nuclear shear moduli range over two orders of magnitude, based on greyscale intensities from fluorescent z-stacks of DNA. However, Pajerowski et al. (2007) reported reshaping of the lamin A/C and alteration in the chromatin distribution during deformation. Therefore, while mapping nucleus stiffness properties based on greyscale values of fluorescent images is useful for characterising the mechanical behaviour of pre-compacted DNA, the underlying process governing DNA assembly/bundling, such as protein dynamics (Misteli, 2001), are not identified. Using the system and techniques developed in Chapters 4 and 5, characterisation of the intra-nuclear biomechanical behaviour of single cells could be performed. The direct application of force to the nucleus region of single adhered cells using the MA system, in combination with techniques for direct measurement of intra-nuclear strain distributions (Henderson et al., 2013) would provide useful data for detailed characterisation of the inhomogeneous nucleus biomechanical behaviour. Such characterisation of the nucleus is of critical importance, as alterations in nuclear lamina and chromatin distribution during cell deformation has been linked to cell mechanotransduction (Dahl et al., 2008, Rowat et al., 2008, Tsukamoto et al., 2000).

Previous studies have observed that, in the absence of external loading, SFs stretch over the nucleus in cells seeded on 2D substrates (Li et al., 2014, Weafer et

al., 2013). The fluorescent images in Chapter 4 reveal that during MA SFs that extend from the base of the cell continue into the micropipette (along the periphery of the aspirated section) and around the nucleus. Using the active SF modelling approach it is revealed that fibres, which were initially stretched over the nucleus before aspiration, become aspirated into the micropipette during simulations. Therefore, simulations suggest that apical SFs observed before aspiration are the same as those observed to extend into the micropipette at the end of aspiration. A further investigation in which live imaging of the actin cytoskeleton would be useful to monitor the behaviour of these SFs during MA experiments for comparison with computational predictions. A similar live imaging technique would also be useful for experimental validation of the computational results presented in Chapter 7. Using the active modelling framework it is revealed that specific families of stress fibres resist certain modes of deformation during cyclic loading. A live imaging technique coupled with the AFM system described in Chapter 6 could be used to confirm these predictions. Live imaging could also allow measurement of intracellular strain during experiments by tracking specific markers such as mitochondria in the cytoplasm (Knight et al., 2006) or DNA in the nucleus (Henderson et al., 2013). However, it should be noted that GFP actin transfection has been known to alter the mechanical response of cells (Pravincumar et al., 2012).

In Chapters 6 and 7, it is revealed that the biomechanical response of untreated contractile cells is largely independent of the applied strain magnitude. Untreated cell force-deformation curves, maximum forces, and minimum force remain relatively unchanged after the applied strain is reduced by 10%. In other words, results show that if the applied strain rate remains unchanged, the force behaviour of untreated cells also remains relatively unchanged. This strongly

suggests that cells which contain the active contractile machinery of the actin cytoskeleton are highly dependent on the strain rate. In order to investigate this suggestion, a follow-on study should be performed in which untreated contractile cells are subjected to cyclic loading at different strain rates. Previous studies have demonstrated that cell mechanical behaviour is dependent on the rate of strain application (Lee et al., 2010, Hsu et al., 2010, Wille et al., 2006, Mitrossilis et al., 2009) and rate of force application (Pravincumar et al., 2012). Using the MA technique, Pravincumar et al. (2012) reported different stiffness properties for suspended chondrocytes subjected to different rates of monotonic increase of aspiration pressure. To perform a similar investigation on adhered cells, the MA system developed in Chapter 4 could be used. Furthermore, cyclic application of aspiration pressure could be used to investigate cell response to dynamic force changes. In Chapter 6, a constant strain rate is used for all experiments. Strain rate dependence of cell forces in tissue constructs was demonstrated by Wille et al. (2006). Fibroblast cells were seeded in collagen scaffolds and cyclically stretched at constant strain rates. The active contribution of the cells was isolated and it was demonstrated that lower strain rates resulted in higher steady state forces following several hours of cyclic deformation. However, in the study of Wille et al. (2006), stretching was limited to the axial direction. The robust experimental system developed in Chapter 6 could be used to apply different stretching strain rates to biaxial tissues. Moreover, strain rates in each direction in biaxial loading could be changed from the 1:1 ratio of Chapter 8 to investigate the effect of different multi-axial strain rates on force generation. Investigating the effect of strain rates in different directions could be used for careful development of the active modelling

framework so that accurate predictions of contractile forces at the tissue level can be obtained.

Further to testing tissues over a range of strain rates, the experimental protocol of Chapter 8 could be altered to investigate a number of other variations, such as strain magnitudes, collagen density, cell density, cell type, engineered collagen/cell alignments, and pre-aligned tissues. It was demonstrated in Chapter 6/7 that single cells are relatively unaffected by alterations in strain magnitude. However, the dependence of engineered tissue constructs to strain magnitude has not been widely reported. A similar loading pattern to that imposed on single cells in Chapter 6/7 could be performed at the tissue level using the system developed in Chapter 8 to investigate this. Reorientation of the actin cytoskeleton of cells encapsulated in collagen tissue constructs was reported to be dependant of the collagen concentration (Foolen et al., 2014). However, it has been more prominently reported that cells align between rigid and dynamic constrains (Foolen et al., 2012, Zhao et al., 2013, Wille et al., 2006, Lee et al., 2008, Nieponice et al., 2007, Gauvin et al., 2011). The maintenance of SF alignment of cells in 3D culture parallel to the direction of cyclic loading is possibly due to the dominant effect of contact guidance of intra-tissue collagen fibrils (Rubbens et al., 2009, Teixeira et al., 2003, Doyle et al., 2009). The system developed in Chapter 8 could be used for further investigation of cell orientation and contact guidance in tissue constructs. Significantly advancing an investigation of this type, preferential orientations of collagen fibrils could be directly manipulated using electrospinning techniques (Zeugolis et al., 2008, Baker et al., 2008, Li et al., 2006). In Chapter 8, force measurements for uniaxially stretched tissues which were constrained in the uniaxial direction during cell seeding is reported. Due to the coordinated alignment

of cells in the uniaxial direction, it is assumed that these tissues are highly anisotropic. However, force measurement in the lateral direction was not performed. Using the novel experimental system developed in Chapter 8, different tissues configurations can be tested by varying mould dimensions and hanger placement. For example, to stretch uniaxially constrained tissues in the lateral direction, the collagen-cell solution could be gelled in a configuration similar to the biaxial tissues. Rather than constraining all hangers in the mould, a free boundary could be imposed in one direction. This would result in a uniaxial-type tissue with hangers available for stretching in the lateral direction. Further investigations, such as those outlined above, could be used to guide mechanical priming strategies for engineering tissues with increased functional viability (Berry et al., 2003, Billiar et al., 2005, Cummings et al., 2004, Isenberg and Tranquillo, 2003, Seliktar et al., 2000, Mauck et al., 2000, Mauck et al., 2003).

In Chapter 7, the history dependent behaviour of the actin cytoskeleton in response to dynamic loading is captured using a fading memory model (Hunter et al., 1998). The fading memory model was developed to phenomenologically represent the transient behaviour of cardiac tissue under dynamic conditions. In terms of the actin cytoskeleton, the fading memory model is considered as a representation of localised stress fibre remodelling. A recent study by Vigliotti et al. (2015) proposes a thermodynamically motivated framework for stress fibre dependence on stress, strain, and strain rate. Vigliotti et al. (2015) describes a stress fibre as a series of actin/myosin functional units. During shortening if the functional units in the stress fibre become too highly contracted (shortened) they exhibit a low energy state. In order for the stress fibre to continue exhibiting contractility functional units must be discarded back into the cytoplasm. In contrast, more

functional units must be added for the stress fibre to continue exhibiting contractility during lengthening. Functional units consist of an organised structure of actin filaments,  $\alpha$ -actin, and phosphorylated myosin that must be formed in the cytoplasm before addition into a stress fibre. Furthermore, as a new functional unit enters a stress fibre new bonds must be formed before contractility is generated. Therefore, generating and adding new functional units during lengthening is significantly more time consuming than simply removing them during shortening. This addition/removal of functional units, or localised remodelling of the stress fibre, may provide an explanation for the fact that the fading memory formulation is not dependent on positive strain rates (or localised addition of functional units to the stress fibre), whereas it is a function of negative strain rates (or localised removal of functional units from the stress fibre). Future work should focus on the development of binding and unbinding kinetics at the level of actin-myosin cross-bridges in order to provide an enhanced insight into the biophysical processes underlying the transience of SF contractility under dynamic loading.

### 9.3 References

- BAKER, B. M., GEE, A. O., METTER, R. B., NATHAN, A. S., MARKLEIN, R. A., BURDICK, J. A. & MAUCK, R. L. 2008. The potential to improve cell infiltration in composite fiber-aligned electrospun scaffolds by the selective removal of sacrificial fibers. *Biomaterials*, 29, 2348-2358.
- BERRY, C. C., SHELTON, J. C., BADER, D. L. & LEE, D. A. 2003. Influence of external uniaxial cyclic strain on oriented fibroblast-seeded collagen gels. *Tissue Eng*, 9, 613-24.
- BILLIAR, K. L., THROM, A. M. & FREY, M. T. 2005. Biaxial failure properties of planar living tissue equivalents. *J Biomed Mater Res A*, 73, 182-91.
- CUMMINGS, C. L., GAWLITTA, D., NEREM, R. M. & STEGEMANN, J. P. 2004. Properties of engineered vascular constructs made from collagen, fibrin, and collagen-fibrin mixtures. *Biomaterials*, 25, 3699-706.
- DAHL, K. N., RIBEIRO, A. J. & LAMMERDING, J. 2008. Nuclear shape, mechanics, and mechanotransduction. *Circ Res*, 102, 1307-18.
- DOYLE, A. D., WANG, F. W., MATSUMOTO, K. & YAMADA, K. M. 2009. One-dimensional topography underlies three-dimensional fibrillar cell migration. *The Journal of Cell Biology*, 184, 481-490.

- FOOLEN, J., DESHPANDE, V. S., KANTERS, F. M. & BAAIJENS, F. P. 2012. The influence of matrix integrity on stress-fiber remodeling in 3D. *Biomaterials*, 33, 7508-18.
- FOOLEN, J., JANSSEN-VAN DEN BROEK, M. W. & BAAIJENS, F. P. 2014. Synergy between Rho signaling and matrix density in cyclic stretch-induced stress fiber organization. *Acta Biomater*, 10, 1876-85.
- GAUVIN, R., PARENTEAU-BAREIL, R., LAROUCHE, D., MARCOUX, H., BISSON, F., BONNET, A., AUGER, F. A., BOLDUC, S. & GERMAIN, L. 2011. Dynamic mechanical stimulations induce anisotropy and improve the tensile properties of engineered tissues produced without exogenous scaffolding. *Acta Biomater*, 7, 3294-301.
- GUILAK, F., TEDROW, J. R. & BURBKART, R. 2000. Viscoelastic properties of the cell nucleus. *Biochem Biophys Res Commun*, 269, 781-786.
- HENDERSON, J. T., SHANNON, G., VERESS, A. I. & NEU, C. P. 2013. Direct measurement of intranuclear strain distributions and RNA synthesis in single cells embedded within native tissue. *Biophys J*, 105, 2252-2261.
- HOCHMUTH, R. M. 2000. Micropipette aspiration of living cells. *J Biomech*, 33, 15-22.
- HSU, H. J., LEE, C. F., LOCKE, A., VANDERZYL, S. Q. & KAUNAS, R. 2010. Stretch-Induced Stress Fiber Remodeling and the Activations of JNK and ERK Depend on Mechanical Strain Rate, but Not FAK. *PLoS One*, 5.
- HUNTER, P. J., MCCULLOCH, A. D. & TER KEURS, H. E. D. J. 1998. Modelling the mechanical properties of cardiac muscle. *Progress in Biophysics and Molecular Biology*, 69, 289-331.
- ISENBERG, B. C. & TRANQUILLO, R. T. 2003. Long-term cyclic distention enhances the mechanical properties of collagen-based media-equivalents. *Ann Biomed Eng*, 31, 937-49.
- KNIGHT, M. M., BOMZON, Z., KIMMEL, E., SHARMA, A. M., LEE, D. A. & BADER, D. L. 2006. Chondrocyte deformation induces mitochondrial distortion and heterogeneous intracellular strain fields. *Biomech Model Mechanobiol*, 5, 180-91.
- LEE, C. F., HAASE, C., DEGUCHI, S. & KAUNAS, R. 2010. Cyclic stretch-induced stress fiber dynamics - dependence on strain rate, Rho-kinase and MLCK. *Biochem Biophys Res Commun*, 401, 344-9.
- LEE, E. J., HOLMES, J. W. & COSTA, K. D. 2008. Remodeling of Engineered Tissue Anisotropy in Response to Altered Loading Conditions. *Annals of biomedical engineering*, 36, 1322-1334.
- LI, Q., KUMAR, A., MAKHIJA, E. & SHIVASHANKAR, G. V. 2014. The regulation of dynamic mechanical coupling between actin cytoskeleton and nucleus by matrix geometry. *Biomaterials*, 35, 961-9.
- LI, W.-J., COOPER JR, J. A., MAUCK, R. L. & TUAN, R. S. 2006. Fabrication and characterization of six electrospun poly( $\alpha$ -hydroxy ester)-based fibrous scaffolds for tissue engineering applications. *Acta Biomaterialia*, 2, 377-385.
- MAUCK, R. L., SOLTZ, M. A., WANG, C. C., WONG, D. D., CHAO, P. H., VALHMU, W. B., HUNG, C. T. & ATESHIAN, G. A. 2000. Functional tissue engineering of articular cartilage through dynamic loading of chondrocyte-seeded agarose gels. *J Biomech Eng*, 122, 252-60.
- MAUCK, R. L., WANG, C. C., OSWALD, E. S., ATESHIAN, G. A. & HUNG, C. T. 2003. The role of cell seeding density and nutrient supply for articular cartilage tissue engineering with deformational loading. *Osteoarthritis Cartilage*, 11, 879-90.
- MISTELI, T. 2001. Protein Dynamics: Implications for Nuclear Architecture and Gene Expression. *Science*, 291, 843-847.
- MITROSSILIS, D., FOUCHARD, J., GUIROY, A., DESPRAT, N., RODRIGUEZ, N., FABRY, B. & ASNACIOS, A. 2009. Single-cell response to stiffness exhibits muscle-like behavior. *Proceedings of the National Academy of Sciences*, 106, 18243-18248.

- NIEPONICE, A., MAUL, T. M., CUMER, J. M., SOLETTI, L. & VORP, D. A. 2007. Mechanical stimulation induces morphological and phenotypic changes in bone marrow-derived progenitor cells within a three-dimensional fibrin matrix. *J Biomed Mater Res A*, 81, 523-30.
- PAJEROWSKI, J. D., DAHL, K. N., ZHONG, F. L., SAMMAK, P. J. & DISCHER, D. E. 2007. Physical plasticity of the nucleus in stem cell differentiation. *Proc Natl Acad Sci USA*, 104, 15619-15624.
- PRAVINCUMAR, P., BADER, D. L. & KNIGHT, M. M. 2012. Viscoelastic cell mechanics and actin remodelling are dependent on the rate of applied pressure. *PLoS ONE*, 7, e43938.
- ROWAT, A. C., FOSTER, L. J., NIELSEN, M. M., WEISS, M. & IPSEN, J. H. 2005. Characterization of the elastic properties of the nuclear envelope. *Journal of the Royal Society Interface*, 2, 63-69.
- ROWAT, A. C., LAMMERDING, J., HERRMANN, H. & AEBI, U. 2008. Towards an integrated understanding of the structure and mechanics of the cell nucleus. *Bioessays*, 30, 226-36.
- RUBBENS, M. P., DRIESSEN-MOL, A., BOERBOOM, R. A., KOPPERT, M. M. J., VAN ASSEN, H. C., TERHAAR ROMENY, B. M., BAAIJENS, F. P. T. & BOUTEN, C. V. C. 2009. Quantification of the Temporal Evolution of Collagen Orientation in Mechanically Conditioned Engineered Cardiovascular Tissues. *Annals of Biomedical Engineering*, 37, 1263-1272.
- SELIKTAR, D., BLACK, R. A., VITO, R. P. & NEREM, R. M. 2000. Dynamic mechanical conditioning of collagen-gel blood vessel constructs induces remodeling in vitro. *Ann Biomed Eng*, 28, 351-62.
- TEIXEIRA, A. I., ABRAMS, G. A., BERTICS, P. J., MURPHY, C. J. & NEALEY, P. F. 2003. Epithelial contact guidance on well-defined micro- and nanostructured substrates. *J Cell Sci*, 116, 1881-92.
- TSUKAMOTO, T., HASHIGUCHI, N., JANICKI, S. M., TUMBAR, T., BELMONT, A. S. & SPECTOR, D. L. 2000. Visualization of gene activity in living cells. *Nat Cell Biol*, 2, 871-8.
- VAZIRI, A. & MOFRAD, M. R. 2007. Mechanics and deformation of the nucleus in micropipette aspiration experiment. *J Biomech*, 40, 2053-62.
- VIGLIOTTI, A., RONAN, W., BAAIJENS, F. P. T. & DESHPANDE, V. S. 2015. A thermodynamically motivated model for stress-fiber reorganization. *Biomechanics and Modeling in Mechanobiology*, 1-29.
- WEAFER, P. P., RONAN, W., JARVIS, S. P. & MCGARRY, J. P. 2013. Experimental and computational investigation of the role of stress fiber contractility in the resistance of osteoblasts to compression. *Bull Math Biol*, 75, 1284-303.
- WILLE, J., ELSON, E. & OKAMOTO, R. 2006. Cellular and Matrix Mechanics of Bioartificial Tissues During Continuous Cyclic Stretch. *Annals of Biomedical Engineering*, 34, 1678-1690.
- ZEUGOLIS, D. I., KHEW, S. T., YEW, E. S., EKAPUTRA, A. K., TONG, Y. W., YUNG, L. Y., HUTMACHER, D. W., SHEPPARD, C. & RAGHUNATH, M. 2008. Electro-spinning of pure collagen nano-fibres - just an expensive way to make gelatin? *Biomaterials*, 29, 2293-305.
- ZHAO, R., BOUDOU, T., WANG, W. G., CHEN, C. S. & REICH, D. H. 2013. Decoupling cell and matrix mechanics in engineered microtissues using magnetically actuated microcantilevers. *Adv Mater*, 25, 1699-705.